TECHNISCHE UNIVERSITÄT MÜNCHEN
Institut für Photogrammetrie und Kartographie
Lehrstuhl für Methodik der Fernerkundung

Phase Unwrapping of Multi-Channel Synthetic Aperture Radar Data: Application to the TanDEM-X Mission

Marie Lachaise

Vollständiger Abdruck der von der Ingenieurfakultät Bau Geo Umwelt der Technischen Universität München zur Erlangung des akademischen Grades eines

Doktor-Ingenieurs (Dr.-Ing.)

genehmigten Dissertation.

Vorsitzender: Univ.-Prof. Dr.-Ing. Uwe Stilla

Prüfer der Dissertation:

1. Univ.-Prof. Dr.-Ing. habil. Richard H.G. Bamler
2. Hon.-Prof. Dr. rer. nat. Michael Eineder
3. Prof. Giampaolo Ferraioli, Ph.D.
   Università Parthenope, Napoli, Italien

Die Dissertation wurde am 18.06.2015 bei der Technischen Universität München eingereicht und durch die Ingenieurfakultät Bau Geo Umwelt am 25.09.2015 angenommen.

Abstract

Synthetic Aperture Radar Interferometry allows to measure accurately geometric parameters of the Earth such as its surface topography. However, this one can be recovered only after having restored the continuity of the *interferometric phase*. This is the aim of the *phase unwrapping (PU)* procedure, which estimates the integer number of cycles to add to the measured *wrapped* phase. Phase unwrapping is a challenging task and its results have dramatic effects on the overall accuracy of the restored topography. The conversion of the phase cycles to height (the height of ambiguity) is ruled by the length of the interferometric baseline. Multiple interferograms or *channels* of different baselines may be combined to ease the problem.

The TanDEM-X mission has the primary objective to generate in a short time a global Digital Elevation Model (DEM) of 10 m absolute vertical accuracy and 2 m relative height accuracy. In order to achieve this goal, the whole land mass has been mapped at least twice from the same geometry but with different baselines. Dense forested regions and mountainous terrain have been acquired a third time with smaller baselines. The success of the TanDEM-X mission is absolutely dependent on the accuracy of the final DEM and therefore on the reliability of the phase unwrapping algorithm. Hence, a robust and versatile PU method, which is in accordance with the acquisition concept, is necessary.

The main contribution of this thesis is the design and development of a new method which combines bistatic high-resolution interferometric data in order to perform a correct and accurate phase unwrapping on a huge amount of data. The Dual-Baseline Phase Unwrapping Correction (DB-PUC) framework addresses this challenge by correcting errors that occurred during the single-baseline PU procedure. It benefits from the additional information available through the *differential interferogram* and the *stereo-radargrammetric phase*. The *differential interferogram* stems from the demodulation of the two interferograms with respect to each other and provides a third information with a higher height of ambiguity, which is easier to unwrap. It is used to correct the ambiguity bands of the misestimated unwrapped phases. The *stereo-radargrammetric phase* is derived from the (small) local parallactic shifts of the SAR images in the slant range direction. It is an absolute measurement of the surface topography but of lower resolution. This phase enables the assessment of the *differential* unwrapped phase and the correction of its potential errors region-wise.

Within this work, the proposed method has been compared with relevant phase unwrapping algorithms from the literature. Results on examples illustrating typical challenges, namely the noise, surface discontinuities and geometrical distortions issues, have been assessed. It is shown that the DB-PUC framework outperforms the evaluated algorithms. Its multi-level approach makes it flexible, computationally efficient and well adapted to deal with the various PU errors scenarios. Last but not least, the region-wise correction of the integer number of cycles misestimated during the single-baseline phase unwrapping allows it to be less sensitive to noise and possible temporal changes.

The DB-PUC framework is used during the operational processing (or re-processing) of the TanDEM-X acquisitions, which are used for the generation of the final global DEM. The second global coverage has been unwrapped with the proposed approach with a success rate of 96.5%. For the other 3.5%, available data are not of sufficient quality, have unfavourable height of ambiguity (HoA) ratios and/or exhibit significant terrain changes due to different climatic conditions.

The final TanDEM-X DEM is being generated from the corrected height maps. It surpasses all the specifications in absolute and relative vertical and horizontal accuracies. Therefore, it demonstrates the success of the proposed method.

Kurzfassung

Synthetic Aperture Radar (SAR) Interferometrie erlaubt die genaue Messung geometrischer Parameter der Erdoberfläche wie z.B. ihrer Topographie. Jedoch ist eine genaue Rekonstruktion der Höheninformation nur möglich, wenn die Kontinuität der ursprünglich zyklischen interferometrischen Phase sichergestellt ist. Dies ist das Ziel von Algorithmen zur Phasenabwicklung (phase unwrapping, PU), welche die ganzzahligen Zyklen schätzen, die zu den gemessenen, "aufgewickelten" (wrapped) Phasenwerten hinzugefügt werden müssen. Phase unwrapping ist eine herausvordernde Aufgabe und die Qualität der Resultate hat eine dramatischen Effekt auf die Genauigkeit der abgeleiteten Topographie. Die Konversion von Phasenzyklen zu Höhen (die Höhenmehrdeutigkeit) ist abhängig von der Länge der interferometrischen Basislinien. Mehrere Interferogramme (bzw. Kanäle) verschiedener Basislinie, können kombiniert werden, um dieses Problem zu lösen.

Die TanDEM-X Mission hat als primäres Ziel, in kurzer Zeit ein globales Digitales Höhenmodell (Digital Elevation Model, DEM) mit 10 m absoluter und 2 m relativer Höhengenauigkeit aus interferometrischen Radardaten zu erstellen. Um dies zu erreichen, wurde die gesamte Landfläche der Erde mindestens zweimal unter gleichen geometrischen Aufnahmebedingungen abgedeckt, jedoch mit jeweils unterschiedlichen Basislinien. Regionen dichter Vegetation sowie gebirgige Gebiete wurden noch zusätzlich mit kleineren Basislinien erfasst. Der Erfolg der TanDEM-X Mission steht und fällt mit der Genauigkeit des finalen DEMs und somit mit der Zuverlässigkeit des Phase Unwrapping Algorithmus. Daher ist eine robuste und flexible PU Methode notwendig, die im Einklang mit dem Aufnahmekonzept die Daten korrekt verarbeitet.

Der Hauptbeitrag der vorliegenden Arbeit ist der Entwurf und die Entwicklung einer neuen Methode, welche bi-statische, hoch-auflösende interferometrische Daten kombiniert, um ein korrektes und exaktes Phase Unwrapping für eine extrem große Datenmenge durchzuführen. Das System für eine Phase Unwrapping Korrektur mittels zweier Basislinien (Dual-Baseline Phase Unwrapping Correction, DB-PUC) geht diese Herausforderung an, in dem es einen Mechanismus schafft, PU-Fehler, die aus der Verarbeitung der Daten nur einer Basislinie entstehen, vor der Weiterverarbeitung zu korrigieren. Es nutzt dafür die zusätzlichen Informationen des *differentiellen Interferogramms* und der *stereo-radargrametrischen Phase*. Das *differentielle Interferogramm* stammt aus der gegenseitigen Demodulation der zwei unterschiedlichen Phasen und liefert somit eine Zusatzinformation mit einer höheren Höhenmehrdeutigkeit, die sich wesentlich leichter abwickeln lässt. Sie wird benutzt, um die Mehrdeutigkeit der Zyklen der falsch geschätzten Phase zu korrigieren. Die *stereo-radargrammetrische Phase* wird aus der (geringen) parallaktischen Verschiebung der zwei SAR-Bilder, die das Interferogramm bilden, gewonnen. Es ist eine absolute, aber schlechter aufgelöste Messung der topographischen Höhe. Diese Phase ist frei von Mehrdeutigkeiten und ermöglicht so die Beurteilung der Genauigkeit der abgewickelten differentiellen Phase und gegebenenfalls eine Korrektur möglicher PU-Fehler in einzelnen Regionen.

In dieser Arbeit wird die entwickelte Methode mit den relevanten PU-Algorithmen der Literatur verglichen. Analysiert wurden die Ergebnisse für einige Beispiele, welche die typischen Herausforderungen die für reale Daten bewältigt werden müssen, illustrieren; das wären insbesondere Phasenrauschen, Diskontinuitäten in der Topographie sowie geometrische Störungen. Es ergibt sich, dass der DB-PUC Ansatz alle evaluierten Algorithmen in der Qualität der Resultate übertrifft. Sein Mehr-Ebenen Aufbau macht ihn flexibel, numerisch effizient und hervorragend an die unterschiedlichsten Fehlerszenarien angepasst. Nicht zuletzt ist die regionenweise Korrektur von falsch geschätzten ganzzahligen Zyklusnummern der abgewickelten Phasen einer einzelnen Basislinie ist wesentlich weniger anfällig für das Rauschsignal und mögliche zeitliche Veränderungen.

Der DB-PUC Ansatz wird in der operationellen Verarbeitungskette der TanDEM-X Aufnah-

men zur Erzeugung des globalen Höhenmodells eingesetzt. Er wird ebenfalls zur nachträglichen Korrektur von Daten, die zunächst mit nur einer Abdeckung verarbeitet werden mussten, benutzt. Die zweite globale Abdeckung wurde so mit Hilfe der ersten Abdeckung verarbeitet und erreicht dabei eine Erfolgsquote von 96,5% in der Konsistenz der PU-Resultate. Bei den restlichen 3,5% sind die verfügbaren Daten meist von unzureichender Qualität und/oder haben ein ungünstiges Verhältnis der jeweiligen Höhenmehrdeutigkeiten. Auch sind es oftmals signifikante Änderungen der in den beiden Abdeckungen gemessenen Höhe durch unterschiedliche saisonale und klimatische Bedingungen, die eine Kombination der Daten vereiteln.

Das bis heute erstellte finale Produkt der TanDEM-X Mission, dass aus diesen korrigierten Höhendaten erstellt wurde, übertrifft in allen Aspekten die ursprünglichen Spezifikationen an Höhengenauigkeit und demonstriert den Erfolg der Methode unter schwierigen Bedingungen.

Contents

List of abbreviations

pdf	probability density function
1B-PU	single-baseline phase unwrapping
AAD	Absolute Ambiguity Deviation
CoSSC	Coregistered Single-look Slant-range Complex
CRLB	Cramér-Rao Lower Bound
DB-PUC	Dual-Baseline Phase Unwrapping Correction
DEM	Digital Elevation Model
DLR	German Aerospace Center
GC-TV	Graph-Cuts Total Variation
GMRF	Gaussian Markov Random Field
HoA	height of ambiguity
ICESat	Ice, Cloud and land Elevation Satellite
InSAR	Synthetic Aperture Radar Interferometry
ITP	Integrated TanDEM-X Processor
MAP	Maximum A Posteriori
MCF	Minimum Cost Flow
MCP	Mosaicking and Calibration Processor
MLE	Maximum Likelihood Estimate
NMAD	Normalised Median Absolute Deviation
PU	phase unwrapping
SAR	Synthetic Aperture Radar
SNR	signal-to-noise ratio
SRTM	Shuttle Radar Topographic Mission
TanDEM-X	TerraSAR-X add-on for Digital Elevation Measurement
TDM	TanDEM-X mission
TDX	TanDEM-X satellite
TMSP	TerraSAR Multimode SAR Processor
TSX	TerraSAR-X satellite

List of symbols

B	baseline
$B_\perp$	effective baseline, perpendicular component of B
c_0	speed of light, $c_0 = 299792458$ m/s
c	considered channel in C possible channels
C	number of channels
$\mathbf{C}$	complex covariance matrix
f_0	radar carrier frequency
f_{RS}	range sampling frequency
h	actual terrain height
$\hat{h}$	estimated height
$\hat{h}^d$	— from the *differential interferogram*
$\hat{h}^m$	— from the *master* interferogram
$\hat{h}^s$	— from the *slave* interferogram
$h_{2\pi}$	height of ambiguity (HoA)
$h^d_{2\pi}$	— of the *differential interferogram*
$h^m_{2\pi}$	— of the *master* interferogram
$h^s_{2\pi}$	— of the *slave* interferogram
H	master/active sensor altitude
k	integer ambiguity band ($k \in \mathbb{Z}$)
k_{off}	true ambiguity band of the absolute phase offset
k^d_{off}	— of the *differential* phase
k^m_{off}	— of the *master* phase
k^s_{off}	— of the *slave* phase
k_{PU}	true ambiguity band to be solved during the phase unwrapping (PU) procedure
k^d_{PU}	— of the *differential* phase
k^m_{PU}	— of the *master* phase
k^s_{PU}	— of the *slave* phase
$\hat{k}$	estimated ambiguity band
$\hat{k}_{\text{off}}$	estimated ambiguity band of the absolute phase offset
$\hat{k}^d_{\text{off}}$	— of the *differential* phase
$\hat{k}^m_{\text{off}}$	— of the *master* phase
$\hat{k}^s_{\text{off}}$	— of the *slave* phase
$\hat{k}_{\text{PU}}$	ambiguity band estimated during the PU procedure

$\hat{k}^d_{\mathrm{PU}}$	— of the *differential* phase
$\hat{k}^m_{\mathrm{PU}}$	— of the *master* phase
$\hat{k}^s_{\mathrm{PU}}$	— of the *slave* phase
L	number of looks
$\overline{\mathrm{AD}}$	mean of the Ambiguity Deviation to the simulated phase from the SRTM DEM
m_{AD}	median of the Ambiguity Deviation to the simulated phase from the SRTM DEM
N_c	cross-correlation patch size
N_{patches}	number of considered cross-correlation patches
osf	oversampling factor
$\%_{(\mathrm{AD}=0)}$	percentage of correctly unwrapped pixels (Ambiguity Deviation AD=0) w.r.t SRTM DEM
$p(\phi;\gamma)$	interferometric phase probability density function (*pdf*)
$p(\phi;\gamma,L)$	*pdf* of the multi-looked phase
r	coordinate in range direction in a SAR/InSAR image
R	(slant) range
u_i	complex observation i
v	complex interferogram
W_R	range (chirp) bandwidth
$W(\centerdot)$	wrapping operator
α	baseline tilt angle (angle between the horizontal plane and the baseline)
β	hyperparmeters for the Maximum A Posteriori (MAP) estimation
γ	complex coherence
γ^m	— of the *master* interferogram
γ^s	— of the *slave* interferogram
γ^d	*differential coherence*
$\Delta\hat{h}$	estimate of the height difference between $\hat{h}^m$ and $\hat{h}^s$
Δh_N	noise in the estimate of the height difference
$\Delta\chi$	parallectic shift between two SAR images in the slant range direction
$\varepsilon_{k_{\mathrm{off}}}$	error in the estimated ambiguity band of the absolute phase offset, $\varepsilon_{k_{\mathrm{off}}} = \hat{k}_{\mathrm{off}} - k_{\mathrm{off}}$
$\varepsilon^d_{k_{\mathrm{off}}}$	— of the *differential* phase, $\varepsilon^d_{k_{\mathrm{off}}} = \hat{k}^d_{\mathrm{off}} - k^d_{\mathrm{off}}$
$\varepsilon^m_{k_{\mathrm{off}}}$	— of the *master* phase, $\varepsilon^m_{k_{\mathrm{off}}} = \hat{k}^m_{\mathrm{off}} - k^m_{\mathrm{off}}$
$\varepsilon^s_{k_{\mathrm{off}}}$	— of the *slave* phase, $\varepsilon^s_{k_{\mathrm{off}}} = \hat{k}^s_{\mathrm{off}} - k^s_{\mathrm{off}}$
$\varepsilon_{k_{\mathrm{PU}}}$	error in the ambiguity band estimated during the PU procedure, $\varepsilon_{k_{\mathrm{PU}}} = \hat{k}_{\mathrm{PU}} - k_{\mathrm{PU}}$
$\varepsilon^d_{k_{\mathrm{PU}}}$	— of the *differential interferogram*, $\varepsilon^d_{k_{\mathrm{PU}}} = \hat{k}^d_{\mathrm{PU}} - k^d_{\mathrm{PU}}$
$\varepsilon^m_{k_{\mathrm{PU}}}$	— of the *master* interferogram, $\varepsilon^m_{k_{\mathrm{PU}}} = \hat{k}^m_{\mathrm{PU}} - k^m_{\mathrm{PU}}$

$\varepsilon^s_{k_{\mathrm{PU}}}$	— of the *slave* interferogram, $\varepsilon^s_{k_{\mathrm{PU}}} = \hat{k}^s_{\mathrm{PU}} - k^s_{\mathrm{PU}}$
θ	SAR look angle (with respect to nadir)
θ_{inc}	(local) incidence angle
λ	radar signal wavelength
μ	height of ambiguity (HoA) ratio
ξ	compatibility (of the *slave* with the *master* interferograms)
σ_{AD}	standard deviation of the Ambiguity Deviation to the simulated phase from the SRTM DEM
$\sigma_{\Delta h}$	standard deviation of the height difference
σ_{ϕ}	interferometric phase error
$\sigma_{\phi_{\mathrm{rdgr}}}$	standard deviation of the stereo-radargrammetric phase
$\sigma_{\Delta\chi}$	standard deviation of the coregistration shifts $\Delta\chi$
$\sigma_{\Delta\chi_{cc}}$	— obtained with coherent cross-correlation
$\sigma_{\Delta\chi_{ic}}$	— obtained with incoherent cross-correlation
τ	range delay tine (fast time)
ϕ	true absolute interferometric phase, flat Earth phase subtracted ($\phi = \phi_T + \phi_N$)
ϕ^d	— *differential* true phase
ϕ^m	— *master* true phase
ϕ^s	— *slave* true phase
ϕ_0	expected (noise-free) phase used for topography reconstruction, $\phi_0 = \mathrm{E}[\phi]$
ϕ_{flat}	interferometric phase corresponding to a flat Earth
ϕ_N	phase noise
ϕ_{rdgr}	stereo-radargrammetric phase obtained from the parallectic shifts $\Delta\chi$
ϕ^d_{rdgr}	— *differential* stereo-radargrammetric phase
ϕ^m_{rdgr}	— *master* stereo-radargrammetric phase
ϕ^s_{rdgr}	— *slave* stereo-radargrammetric phase
ϕ_T	topographic phase
$\hat{\phi}$	estimated absolute unwrapped phase
$\hat{\phi}^d$	— of the *differential interferogram*
$\hat{\phi}^m$	— of the *master* interferogram
$\hat{\phi}^s$	— of the *slave* interferogram
ψ	observed wrapped phase
ψ^d	— of the *differential interferogram*
ψ^m	— of the *master* interferogram
ψ^s	— of the *slave* interferogram

1 Introduction

1.1 Background

Many scientific, medical or industrial applications such as spectroscopy, Magnetic Resonance Imaging (MRI) or Synthetic Aperture Radar (SAR) use coherent imaging systems. They are able to collect both the backscattered amplitude and phase signals, where the phase depends on the wavelength and the time or travel distance. However, the signal being periodic per nature, only the fraction of the last wave cycle can be measured. An illustration of this problem is depicted in Fig. 1.1 by means of a sinusoidal wave. The returned phase is then constrained to its principal value and exhibits 2π-phase jumps: it is the so-called *wrapped* phase.

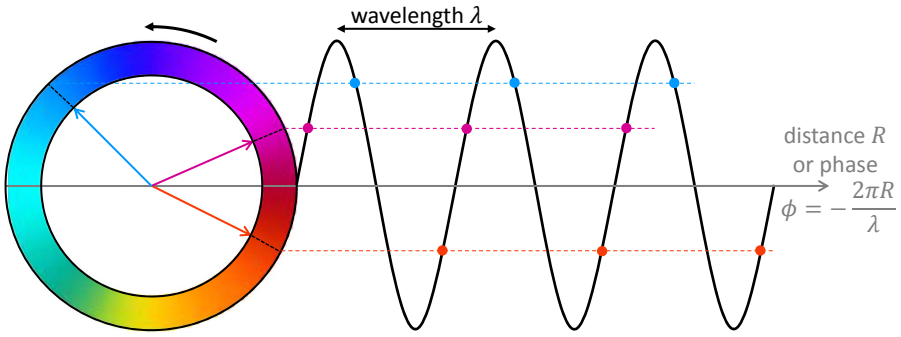

Fig. 1.1. Example of a 2π-periodic signal: the sinusoidal wave. The phase is proportional to the travel distance of the wave and the wavelength. However, the measured phase is circular and only its fractional part can be monitored. The integer number of cycles is thus lost and the acquired phase is wrapped between $-\pi$ and π.

In SAR, the measured phase of a distributed scatterer is generally random and meaningless. Still, two reflected signals can interfere to form an interferogram. In this case, the resulting phase is the difference of both phases and is related to the sensor-target path-length differences. This is the principle of Synthetic Aperture Radar Interferometry (InSAR). The interferometric phase is then exploited to retrieve heights or displacements. Naturally, the interferometric phase is also wrapped. Hence, it is not further valuable as long as its continuous counterpart has not been recovered through the so-called *phase unwrapping (PU)* procedure. Nevertheless, discontinuities from real objects (real phase jumps) but also the possible violation of Shannon's theorem (undersampling) or the presence of noise (both suggesting false phase jumps) complicate the unwrapping procedure. Therefore, PU is challenging and its results have dramatic effects on the overall performance of the aforementioned applications.

InSAR became popular in the last decades of the 20$^{\text{th}}$ century (Zebker and Goldstein, 1986; Goldstein et al., 1988; Massonnet and Rabaute, 1993) thanks to its ability to extract different geophysical information. For example, the wrapped phase difference between two points in an interferogram provides an ambiguous measurement of the relative terrain height. As a result, if the unwrapping process is successful, a topographic map can be generated and, after geocoding, a Digital Elevation Model (DEM). Two-dimensional phase unwrapping grew accordingly to be a primordial research topic in InSAR (and in parallel in MRI).

Many PU methods have been proposed all providing different results (Goldstein et al. (1988); Ghiglia and Romero (1996); Flynn (1997); Costantini (1998); Zebker and Lu (1998) in InSAR and Hedley and Rosenfeld (1992); Adi et al. (2010) in MRI). Nonetheless, no *correct* solution is guaranteed because of the difficulty to discriminate real and false phase jumps. Instead, PU algorithms generate *estimations* of the *true* solution which are the *most likely* according to various criteria. Most of the approaches are based on the integration of the estimated gradients and produce a phase, which is still globally ambiguous. For this reason, a single constant integer number of cycles has to be determined afterwards to obtain the *absolute phase* making terrain

height retrieval possible. Nevertheless, terrain complexity and the need of high accuracy render phase unwrapping almost impossible with only one interferogram. Alternative approaches had to be found.

The idea of combining several phase images taken under different configurations arose instinctively already in the late 90s (Xu et al., 1994; Ghiglia and Wahl, 1994; Jakowatz et al., 1996; Massonnet et al., 1996; Lombardini, 1996; Homer et al., 1997; Schmitt and Wiesbeck, 1997). Indeed, acquired with different *baselines* (different spatial distances between the sensors) or wavelengths, interferograms present distinct fringe patterns (see Fig. 1.2 for an example). In other words, the phase representing the height variation between two pixels is not identical. Furthermore, a phase variation of 2π (a cycle or an ambiguity) is equivalent to a certain height change called the *height of ambiguity (HoA)*, which is inversely proportional to the baseline. In consequence, an interferogram acquired with a high HoA has few fringes and is easier to unwrap (Fig. 1.2 right). Larger baselines, on the contrary, imply more cycles per height and thus more difficulties in the unwrapping process (Fig. 1.2 left). After all, the ensued interferograms are measures of the same physical variable: the topography. On the other hand, for a given phase noise, the height accuracy is directly dependent on the height of ambiguity. Accuracy increases accordingly (or the height noise decreases) with larger baselines. In this way, interferograms with different baselines deliver complementary information. Additionally, their combination facilitates phase unwrapping and, theoretically, is even able to retrieve the absolute phase directly (Eineder and Krieger, 2005).

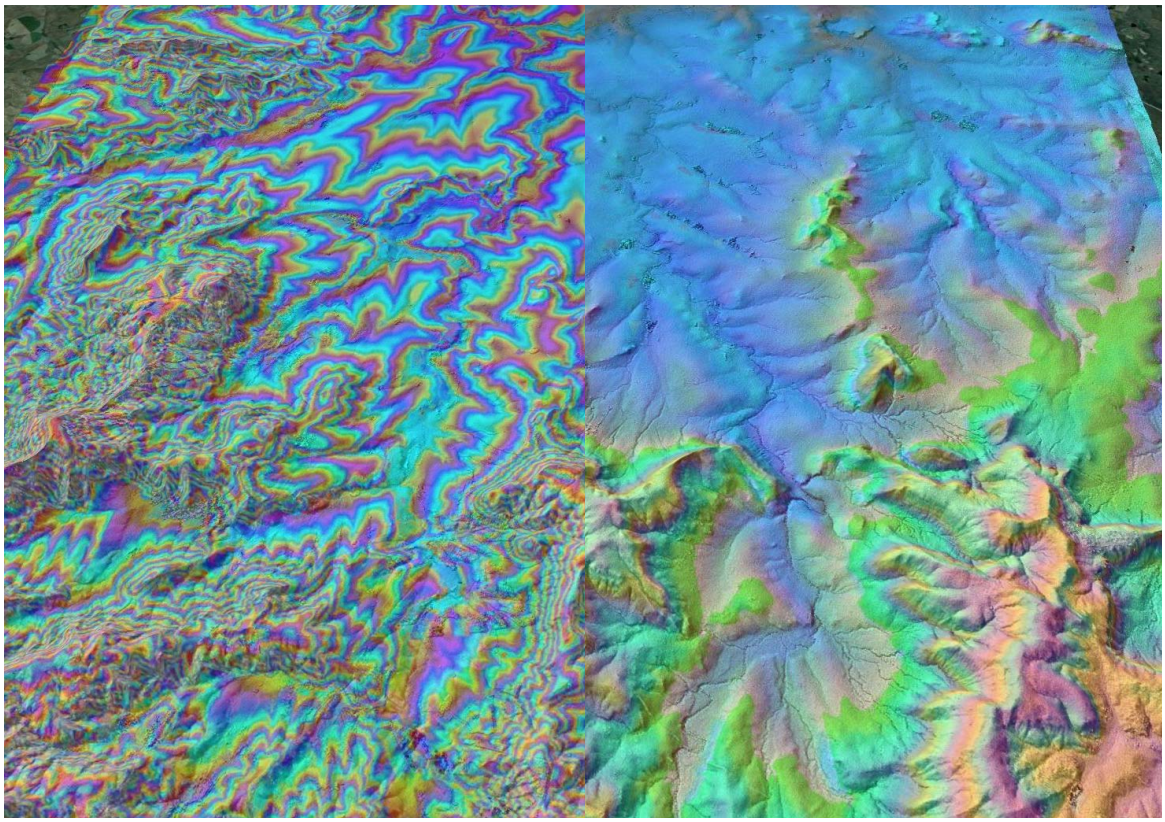

Fig. 1.2. Interferometric phases of the same scene but acquired with different baselines. The wrapped phase depicted on the left side of the scene has a large baseline so that the height accuracy is good but PU difficult. On the other hand, the phase on the right side exhibits less fringes and is thus easier to unwrap but has a lower accuracy.

The topic of this thesis is the *phase unwrapping of multi-channel Synthetic Aperture Radar data and its application to the TanDEM-X mission*. To this end, a new multi-channel phase unwrapping method has been developed. It is robust regarding data diversity (i.e. mapping of the whole landmass with different baselines but same viewing geometry, various coherence and distinct coverages) and computationally efficient to enable operational usage.

1.2 Scientific relevance

A wide range of applications (cartography, navigation, environmental researches, geology, etc.) requires accurate, uniform and up-to-date information about the Earth's topography. As an active sensor, SAR has the capacity for working almost independently of weather conditions (a significant advantage over optical imaging systems). Radar is thus able to provide a global, uniform and reliable data set.

In 2000, the Shuttle Radar Topographic Mission (SRTM) (Rabus et al., 2003; Farr et al., 2007) provided the first global DEM with a posting of 90 m (restricted to latitudes between 57°S and 60°N). However, the need for higher accuracy and higher resolution always increases. Moreover, the latitudinal coverage must be extended. This leads to the necessity of generating a new high-resolution global DEM. For this reason, the TanDEM-X (TerraSAR-X add-on for Digital Elevation Measurement) mission has been designed (Moreira et al., 2004a). The TanDEM-X satellite, together with the TerraSAR-X satellite, form a single-pass bistatic radar interferometer. These two SAR sensors fly in a novel closely controlled HELIX formation allowing precisely adjustable cross-track baselines (see appendix A and Fig. A.1).

The main TanDEM-X mission objective is to generate a three-dimensional model of 12 metres resolution of the whole Earth's landmass, which is consistent, homogeneous in quality and unprecedented in accuracy (10 m absolute vertical accuracy and 2 m relative height accuracy). Figure 1.3 exhibits visually the resolution difference between TanDEM-X and SRTM DEMs. In order to achieve the required accuracy, the whole landmass is mapped twice over two years with the same viewing geometry (Krieger et al., 2007) but with different baselines. These are the multi-channel data considered in this thesis. The first coverage provides a higher HoA to ease PU whereas the second, which is acquired one year later with a larger baseline and shifted beams, yields the full height accuracy at the cost of more demanding phase unwrapping. In addition, mountainous regions are acquired two more times following the same approach but from crossing orbits to fill layover and shadow regions.

No appropriate solution existed at the start of the mission to solve this particular phase unwrapping problem on a global scale. Indeed, it is well-known that, for small HoAs and difficult terrain, PU (with only one interferometric phase) fails. Some algorithms based on Maximum Likelihood Estimate (MLE) or Maximum A Posteriori (MAP) combine multiple interferograms (Eineder, 2003a; Ferraioli et al., 2008) but in the framework of TanDEM-X, only two acquisitions are in general available (more are available for areas exhibiting poor performance). Earlier, specific studies succeeded to unwrap jointly two interferograms with MLE/MAP. However, the two interferometric phases were issued from systems with three antennas (Lombardini, 1998) and consequently did not suffer from temporal changes between them contrary to TanDEM-X interferograms. Therefore, a new multi-channel PU method specific to the mission challenges is absolutely required to enable the generation of the high resolution global TanDEM-X DEM. In contrast to existing algorithms which were designed for ideal stationary data, this thesis deals with real world data and problems. Thus a more robust approach is followed. It consists in correcting the possible errors in the unwrapped phases.

1.3 Objectives and focusses of this thesis

The general goal of this thesis is to combine multi-temporal bistatic high-resolution interferometric data in order to perform a correct and accurate phase unwrapping on a global scale. More particularly,

"a robust and fast multi-channel phase unwrapping algorithm which is reliable, fully automatic and usable operationally for the TanDEM-X mission"

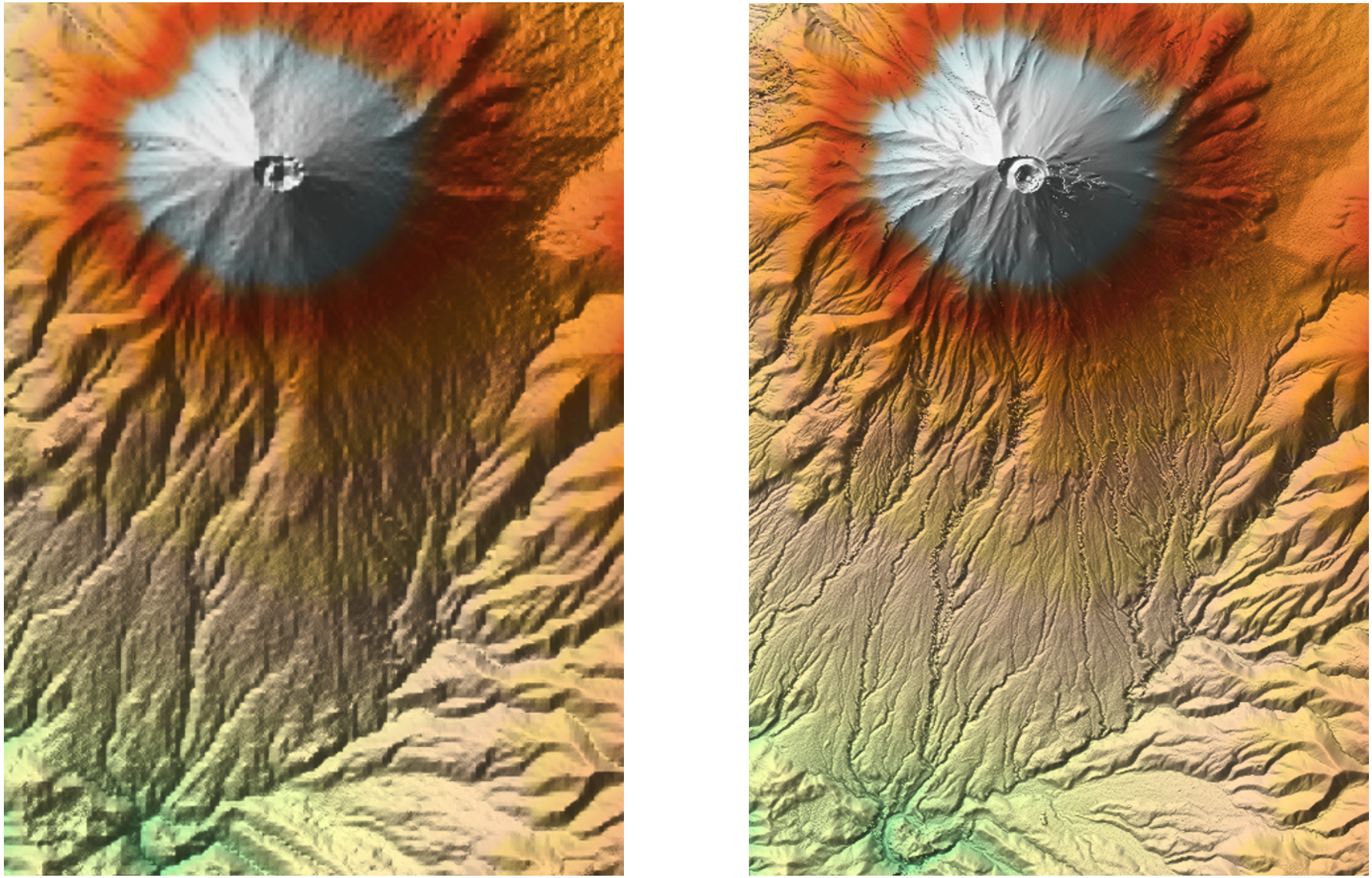

(a) SRTM DEM

(b) TanDEM-X DEM

Fig. 1.3: Comparison of the SRTM and TanDEM-X DEMs of the Misti volcano, Peru. The level of details brought by the new TanDEM-X DEM is clearly visible.

has to be designed, implemented and demonstrated.

Since the success of the TanDEM-X mission is absolutely dependent on a correct phase unwrapping, the following requirements have to be met:

- the algorithm has to work well with a limited data set of heterogeneous quality and coverage;
- it has to be stable and robust; the quality of the results has to be controlled automatically;
- it has to be computationally efficient in order to process more than 400 scenes per day.

Aiming at the design and development of a new multi-channel phase unwrapping concept fulfilling these different requirements, several objectives related to the main goal have to be achieved:

Objective 1: New multi-channel phase unwrapping method

Although many PU algorithms exist, none of the tested ones can successfully unwrap TanDEM-X data on a global scale in a reasonable time (see section 4.3). Therefore, the new multi-channel phase unwrapping approach has to respond to the specific TanDEM-X mission challenges and be adapted to its special acquisition plan. The algorithm has to ensure the delivery of correctly unwrapped data in a limited time.

Objective 2: Robustness and flexibility of the algorithm

The largest part of the world has been acquired twice from the same orbital track (same viewing geometry) but with different beams (different spatial coverage). The algorithm has thus to deal with these interferometric data with different footprints on the Earth. Moreover, the reliability of the outcomes should be independent of the number of available interferograms (at least 2). The algorithm has to be optimised for dual-baseline data with the specified HoA ratio of about 0.7 (see section 4.1). Last but not least, its performance has to be assessed in terms of success rate and accuracy and its limits have to be described.

Objective 3: Make good use of all available independent information

Since the number of InSAR acquisitions is very limited, every additional data produced during the standard TanDEM-X scenes processing (see section 4.2 and appendix B) should be used. Especially, the stereo-radargrammetric parallax measurements provide reliable independent absolute height information. On the contrary, the use of external data such as SRTM has to be avoided to eliminate the risk of introducing external errors.

1.4 Outline of this thesis

This thesis is structured as follows. After a brief recall on SAR and InSAR basics, chapter 2 exposes phase unwrapping causes and principles. Chapter 3 gives an overview of different ways to retrieve the absolute phase and the terrain elevation such as multi-channel PU or stereo-radargrammetry. Chapter 4 describes the different data available in the framework of the TanDEM-X mission and discusses the performances of the several relevant PU algorithms on these data. The proposed multi-channel PU concept, the Dual-Baseline Phase Unwrapping Correction (DB-PUC), which aims to correct potential PU errors fully automatically, is the topic of chapter 5. In chapter 6, practical demonstrations for typical representative terrain and global results of the operational TanDEM-X DB-PUC are analysed. The limitations of the new PU method are also shown. Finally, the conclusion of this thesis and an outlook on further work are given in chapter 7.

2 InSAR and phase unwrapping principles

In this chapter, fundamentals on Synthetic Aperture Radar (SAR) acquisition geometry and on Synthetic Aperture Radar Interferometry (InSAR) that are necessary for the understanding of this thesis are first recalled. In the second part, phase unwrapping (PU) basics and a brief overview of algorithms to unwrap one single phase image are provided.

2.1 Synthetic Aperture Radar and SAR Interferometry

2.1.1 SAR imaging and SAR geometry

A SAR is an active sensor, that transmits microwave pulses to an area of interest and coherently receives the backscattered signal from the target. The use of active microwave radar enables to be independent of weather conditions and day/night time. Two-dimensional images of the Earth's surface are then formed by looking into the series of radar echoes. Curlander and McDonough (1991); Cumming and Wong (2005); Massonnet and Souyris (2008) address extensively the SAR processing. The SAR flight direction defines the *azimuth* axis of the image, while the acquisition direction, perpendicular to the trajectory (and typically in side-looking with a *look angle* θ) is the *(slant) range* axis (see Fig. 2.1). The *range* R, representing the distance between the sensor and the target, is known through the time delay between the emitting and receiving times τ_e and τ_r following $R = (\tau_r - \tau_e)c_0/2$, where c_0 is the speed of light. SAR systems map the 3-D world into a 2-D image in the azimuth-range plane. Terrain topography results in geometric distortions in SAR images (see Fig. 2.1). Terrain slopes directed towards the sensor appear smaller (*foreshortening* and *layover*) while those tilted away appear bigger. When terrain slope is opposed to the radar and too steep, objects are invisible (*shadow*).

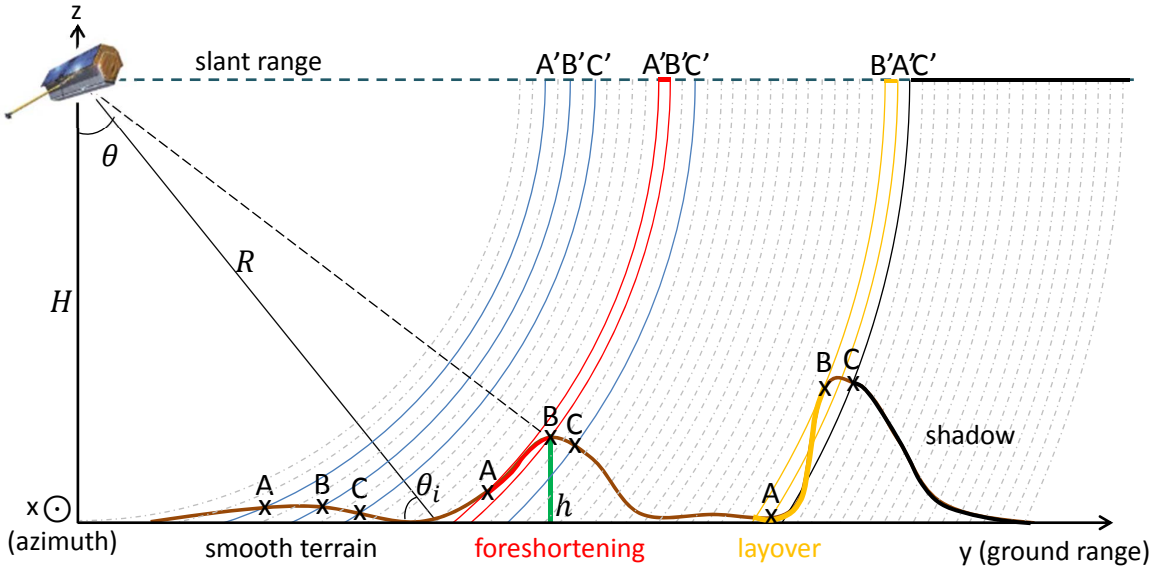

Fig. 2.1. SAR acquisition geometry and geometrical distortions: *smooth terrain* where the three points A, B and C are mapped conventionally to A', B' and C', and the different distortion areas: *foreshortening* where A and B are mapped closer than they really are; *layover* where the top of the mountain B is mapped before its base A; and finally *shadow* where no information can be mapped.

2.1.2 SAR interferometry for terrain mapping

SAR interferometry is a set of methods, which employ two complex-valued SAR images and exploit their phase jointly to derive geometric information about a scene.

Two modes exist:

- *along-track interferometry*: the two SAR sensors fly on the same path with an along-track separation so that a scene is observed from the same point but at different times. It allows to measure movements in the radar line-of-sight such as ocean currents (Goldstein and Zebker, 1987; Romeiser et al., 2010) or moving targets (Raney, 1971; Suchandt and Runge, 2012);
- *across-track interferometry*: the two satellites have different flying paths, almost parallel and look at targets from slightly different positions. Surface topography can be measured (Zebker and Goldstein, 1986; Massonnet and Rabaute, 1993; Bamler and Hartl, 1998; Rosen et al., 2000). Furthermore, surface changes such as deformations can be monitored by means of the *differential interferometric SAR (D-InSAR)*.

2.1.2.1 Across-track interferometry

In this configuration, two SARs map the terrain with slightly different look angles θ_1 and θ_2 as represented in Fig. 2.2. The antennas are separated by a *baseline* B. Its perpendicular component, called *effective baseline* $B_\perp$, defines the sensitivity to height. A large baseline implies fast phase variations difficult to resolve but a smaller separation entails a higher level of noise once the phase is converted to height. Topography measurement with SAR interferometry may seem similar to optical (or stereoscopic) methods. Yet, the latter are based on parallax effect, thus directly based on angle measurements whereas radar measures distances (ranging) through the phase of every pixel (the parallax effect is much smaller, see section 3.2.1).

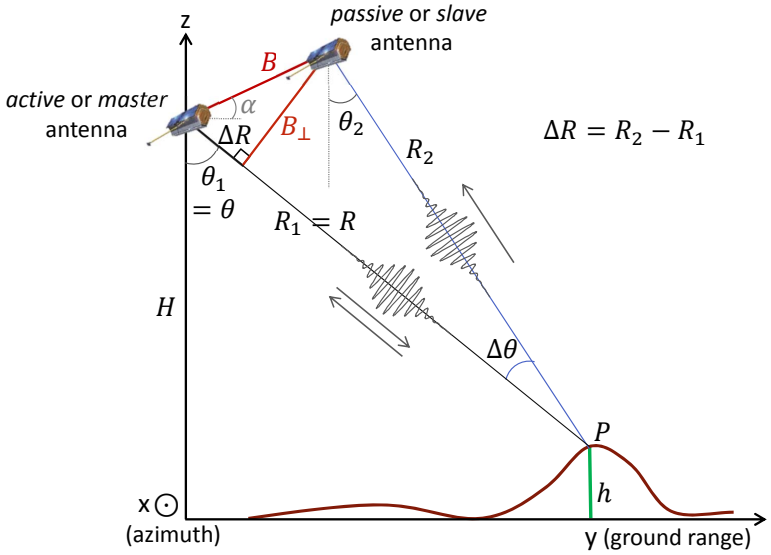

Fig. 2.2. Across-track bistatic interferometric configuration: the master or active antenna emits and receives, whereas the slave or passive sensor only receives (θ_1, R_1 refer to the master antenna and θ_2, R_2 to the slave one).

The SAR images can be obtained in two different acquisition ways:

- in *repeat-pass*, the same antenna acquires a scene at different times to get the various acquisitions, stacks of repeat-pass data enable to monitor ground deformations;
- in *single-pass*, the acquisition system has two (or more) antennas, which either transmit and receive independently within a short time interval (monostatic) or where one antenna transmits and receives and the other only receives (bistatic or multistatic case), temporal decorrelation is then reduced (former case) or even eliminated (latter setup).

Repeat-pass interferometry is widely employed with images from sensors like ERS-1/ERS-2 (Geudtner, 1995; Schwäbisch, 1995), RadarSAT or TerraSAR-X. Single-pass interferometers are mostly airborne systems, but in space, there was the Shuttle Radar Topographic Mission

(SRTM) (Rabus et al., 2003; Farr et al., 2007) and nowadays the TanDEM-X mission (TDM) (Moreira, 2003; Krieger et al., 2007; Zink et al., 2014). Figure 2.2 shows the interferometric principle with two antennas acquiring simultaneously in a bistatic configuration (the default acquisition mode for TDM and the one considered in this thesis). The *active* antenna transmits and then acquires the *master* channel and the *passive* antenna acquires the *slave* image.

2.1.2.2 Interferometric phase

As a coherent imaging system, SAR records both the amplitude and the phase of the received signal as a complex number $u_i = |u_i|e^{j\phi_i}$ where $|u_i|$ is the amplitude, ϕ_i the phase and the subscript i represents either the master ($i = 1$) or the slave ($i = 2$) channel. The notations are largely inspired by Bamler and Hartl (1998). The observed phase value is:

$$\phi_i = -\frac{2\pi R_{total,i}}{\lambda} + \phi_{scat,i} + \phi_{N,i} \tag{2.1}$$

where λ is the radar wavelength, $R_{total,i}$ the sum of the transmitter-target and target-receiver distances, $\phi_{scat,i}$ the phase of the scatterer and $\phi_{N,i}$ the noise phase. In the considered bistatic case (i.e. for TanDEM-X), $R_{total,1} = 2R_1$ and $R_{total,2} = R_1 + R_2$. After image coregistration, the complex interferogram v is formed by calculating:

$$v = u_1 u_2^* = |u_1||u_2|e^{j(\phi_1 - \phi_2)} = |u_1||u_2|e^{j\phi} \tag{2.2}$$

where u_2^* is the complex conjugate of u_2 and $\phi = \phi_1 - \phi_2$ the *interferometric phase*. Considering constant scattering characteristics ($\phi_{scat,1} = \phi_{scat,2}$), the single-pass interferometric phase ϕ is:

$$\phi = -\frac{2\pi(R_1 - R_2)}{\lambda} + \phi_N = \frac{2\pi\Delta R}{\lambda} + \phi_N \tag{2.3}$$

with $\Delta R = R_2 - R_1$. ϕ is the non-ambiguous absolute interferometric phase. It depicts very precisely the slant range difference with an accuracy of a fraction of a wavelength. Nonetheless, it is measurable only in the principal interval $[-\pi; \pi[$ i.e. *modulo* 2π. In this way, the measured or observed phase ψ is:

$$\psi = W(\phi) = \mathrm{mod}\,\{\phi + \pi, 2\pi\} - \pi = \phi - 2\pi k \tag{2.4}$$

where $W(\centerdot)$ is the wrapping operator, $\mathrm{mod}\,\{\centerdot, 2\pi\}$ the modulo-2π operation and $k \in \mathbb{Z}$ the ambiguity band. ψ is *wrapped* and ambiguous exhibiting the so-called *fringes*.

2.1.2.3 Phase to height relation

Several fundamental relations are derived geometrically hereafter with the help of Fig. 2.2. These are only approximate equations to make the understanding easier. Under the assumption that $B \ll R_1, R_2$ (*parallel-ray* approximation, Zebker and Goldstein (1986)), ΔR can be written as:

$$\Delta R \approx B\sin(\theta - \alpha) \tag{2.5}$$

where α is the baseline tilt angle i.e. the angle between the horizontal plane and the baseline. The resulting phase $\phi_{\mathrm{flat}} = -\frac{2\pi}{\lambda}B\sin(\theta - \alpha)$ is the phase representing a flat Earth i.e. it depicts the variation of the line-of-sight across the scene. Let us now consider a target of height $h = H - R\cos\theta$, where H is the altitude of the master antenna. The sensitivity of the interferometric phase ϕ with respect to the terrain height h, the *height sensitivity*, is retrieved by differentiating ϕ, ΔR and h (eqs. (2.3) and (2.5)):

$$\frac{\delta\phi}{\delta h} \approx \frac{-2\pi}{\lambda}\frac{B\cos(\theta - \alpha)}{R\sin\theta} \approx \frac{-2\pi}{\lambda}\frac{B_\perp}{R\sin\theta} \tag{2.6}$$

where $B_\perp = B\cos(\theta - \alpha)$ is the effective baseline. In consequence, a bistatic single-pass configuration has only half the sensitivity of a repeat-pass one. Therefore, it can be seen as a repeat-pass system with half a baseline. Finally, the height corresponding to one ambiguity (or a phase cycle of 2π), the so-called *height of ambiguity (HoA)* $h_{2\pi}$, is obtained by inserting $\delta\phi = 2\pi$ in eq. (2.6):

$$h_{2\pi} = \frac{\lambda R \sin\theta}{B_\perp} \tag{2.7}$$

Observing eqs. (2.6) and (2.7), it becomes clear that the sensitivity of an interferometric system is determined by the effective baseline, the look angle and the wavelength. The *absolute* interferometric phase ϕ can be written as:

$$\phi \approx -\frac{2\pi}{\lambda} B \sin(\theta - \alpha) - \frac{2\pi}{\lambda}\frac{B_\perp}{R\sin\theta} h = \phi_{\text{flat}} - \frac{2\pi}{h_{2\pi}} h = \phi_{\text{flat}} + \phi_T \tag{2.8}$$

ϕ_{flat} is usually removed from the interferometric phase giving the (flattened) *topographic phase* ϕ_T. In practice, ϕ deviates from ϕ_T because of noise and decorrelation effects. Furthermore, only the wrapped phase ψ can be measured. The phase has thus to be unwrapped to recover the absolute phase required for terrain reconstruction. This is further explained in section 2.2.

2.1.3 Statistical description and coherence

2.1.3.1 Interferometric phase statistics

Many scatterers contribute to the response of a single resolution cell to a radar pulse since the cell is typically larger than the radar wavelength and the correlation length of the rough surface (Curlander and McDonough, 1991). Consequently, the observed amplitude and phase result from the coherent sum of the individual signals. Scatterers are called *distributed* or *Gaussian scatterers* if they can be decomposed into a sufficiently high number of random (independent and uncorrelated) sub-scatterers. This holds for low and medium resolution SAR and for scenes containing mostly natural scatterers like forest, soil and rocks, agricultural fields or rough water. In this case, the central limit theorem can be applied and observations can be modelled as *zero-mean complex circular Gaussian random variables* (Goodman, 1963; Bamler and Hartl, 1998). On the contrary, the Gaussian assumption is violated with high-resolution SAR systems or as soon as few dominant scatterers such as artificial objects are present in a resolution cell (see Oliver and Quegan (1999); Frery et al. (1999); Kuttikkad and Chellappa (2000) for alternative statistical models). Nevertheless, the Gaussian model is convenient and acceptable, especially in the context of global terrain mapping.

The bivariate Gaussian distribution of the two SAR images u_1 and u_2 is (Goodman, 1963; Lee et al., 1994; Tough et al., 1995; Bamler and Hartl, 1998):

$$p(\mathbf{w}) = \frac{1}{\pi^2 |\mathbf{C}|} \exp\left(-\mathbf{w}^{*T}\mathbf{C}^{-1}\mathbf{w}\right) \tag{2.9}$$

where $\mathbf{w} = (u_1, u_2)^T$ and $|\mathbf{C}|$ is the determinant of the complex covariance matrix $\mathbf{C}$ defined by:

$$\mathbf{C} = \mathrm{E}\left[\mathbf{w}\mathbf{w}^{*T}\right] = \begin{pmatrix} \mathrm{E}\left[|u_1|^2\right] & \gamma\sqrt{\mathrm{E}\left[|u_1|^2\right]\mathrm{E}\left[|u_2|^2\right]} \\ \gamma^*\sqrt{\mathrm{E}\left[|u_1|^2\right]\mathrm{E}\left[|u_2|^2\right]} & \mathrm{E}\left[|u_2|^2\right] \end{pmatrix} = \begin{pmatrix} \overline{I_1} & \gamma\overline{I} \\ \gamma^*\overline{I} & \overline{I_2} \end{pmatrix} \tag{2.10}$$

where $\overline{I} = \sqrt{\mathrm{E}\left[|u_1|^2\right]\mathrm{E}\left[|u_2|^2\right]}$ is the geometric mean of the expectations of the pixels intensity of the two data sets and γ the complex coherence (or correlation coefficient, see section 2.1.3.2).

From eq. (2.9), the marginal probability density function (*pdf*) of the true interferometric phase $p(\phi;\gamma)$ is derived (Sarabandi (1992); Lee et al. (1994); Tough et al. (1995)):

$$p(\phi;\gamma) = \frac{1-|\gamma|^2}{2\pi}\frac{1}{1-|\gamma|^2\cos^2(\phi-\phi_0)}\left(1+\frac{|\gamma|\cos(\phi-\phi_0)\arccos(-|\gamma|\cos(\phi-\phi_0))}{\sqrt{1-|\gamma|^2\cos^2(\phi-\phi_0)}}\right) \quad (2.11)$$

$p(\phi;\gamma)$ describes how the interferometric phase ϕ differs from the noise-free phase ϕ_0 used for terrain reconstruction because of decorrelation effects. If only an interval centred in ϕ_0 (i.e. $\phi-\phi_0 \in [-\pi,\pi[$) is considered, $\mathrm{E}[\phi] = \phi_0$. Figure 2.3a depicts $p(\phi;\gamma)$ considering different coherences. Usually, a *multi-looking* procedure is applied to denoise the data and to reduce statistical variation. Multi-looking assumes interferogram values inside a small window to be independent and uses them jointly to estimate the phase [1]. The *pdf* of the multi-looked phase estimate $p(\phi;\gamma,L)$ turns into (Lee et al., 1994; Joughin et al., 1994; Tough et al., 1995):

$$p(\phi;\gamma,L) = \frac{\Gamma(L+1/2)(1-|\gamma|^2)^L|\gamma|\cos(\phi-\phi_0)}{2\sqrt{\pi}\,\Gamma(L)(1-|\gamma|^2\cos^2(\phi-\phi_0))^{L+1/2}} + \frac{(1-|\gamma|^2)^L}{2\pi}\,{}_2F_1\left(L,1;1/2;|\gamma|^2\cos^2(\phi-\phi_0)\right) \quad (2.12)$$

where ${}_2F_1$ is the hypergeometric function. Fig. 2.3b shows the influence of the number of looks on $p(\phi;\gamma,L)$. The error or phase standard deviation decreases as the number of looks increases (as depicted in Fig. 2.4a, Just and Bamler (1994)). The phase error approaches the Cramér-Rao Lower Bound (CRLB) (dashed lines in Fig. 2.4a, Rodriguez and Martin (1992)) for high number of looks and coherence:

$$\sigma^2_{\phi,\mathrm{CRLB}} = \frac{1-|\gamma|^2}{2|\gamma|^2 L} \quad (2.13)$$

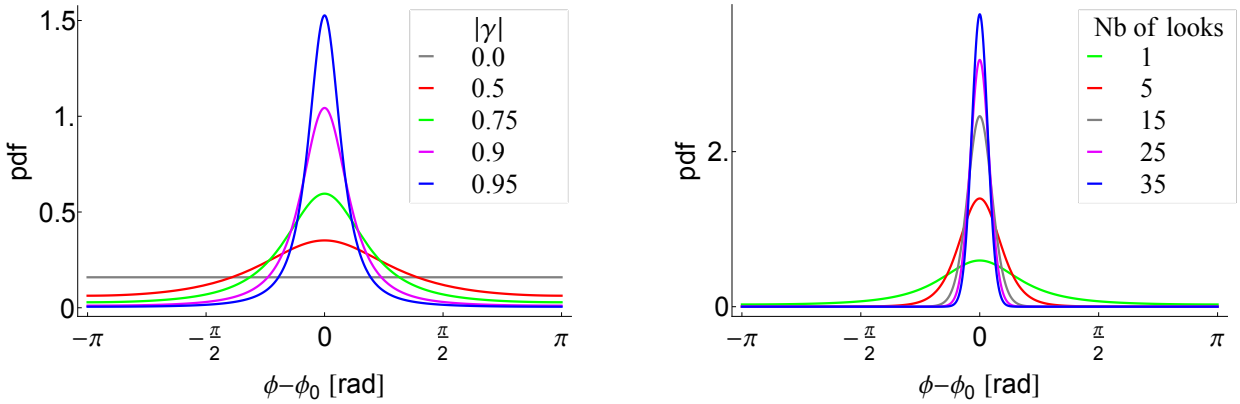

(a) Single-look phase *pdfs* for $|\gamma| = 0, 0.5, 0.75, 0.9, 0.95$

(b) Multi-look phase *pdfs* for 1, 5, 15, 25, 35 looks ($|\gamma| = 0.75$)

Fig. 2.3. Interferometric phase *pdfs* (a) for different coherences and 1 look and (b) for $|\gamma| = 0.75$ and different number of looks. The green curve represents in both plots the *pdf* for $|\gamma| = 0.75$ and 1 look.

2.1.3.2 Coherence coefficient and coherence estimation

The complex coherence γ is defined as the normalised complex cross-correlation of the two SAR images u_1 and u_2 (Papoulis, 1991; Zebker and Villasenor, 1992) and quantifies the similarity between two radar echoes:

$$\gamma = \frac{\mathrm{E}[u_1 u_2^*]}{\sqrt{\mathrm{E}\left[|u_1|^2\right]\mathrm{E}\left[|u_2|^2\right]}} = \frac{\mathrm{E}[v]}{\bar{I}} = |\gamma|\exp(j\phi_0) \quad (2.14)$$

[1] approximating ensemble averages by spatial mean implicitly assumes that pixels have stationary statistics

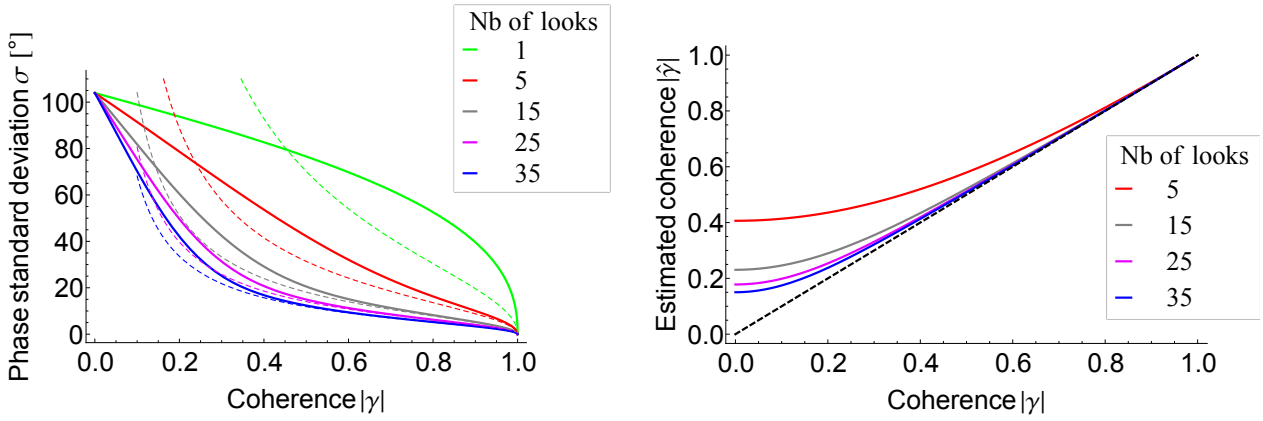

(a) Phase error versus coherence

(b) Estimated coherence versus real coherence

Fig. 2.4. (a) Standard deviation of the interferometric phase (the dashed lines represent the Cramér-Rao bounds) and (b) bias of the estimated coherence for different number of looks and coherences.

The phase of γ is the expected interferometric phase ϕ_0 and its amplitude, the interferometric coherence, is related to the phase noise and quantifies disturbances. $|\gamma|$ can be written as the product of different contributions (Rodriguez and Martin, 1992; Zebker and Villasenor, 1992; Bamler and Just, 1993):

$$|\gamma| = \gamma_{\text{thermal}}\gamma_{\text{spatial}}\gamma_{\text{temp}}\gamma_{\text{coreg}} \tag{2.15}$$

where

- γ_{thermal} represents the influence of the thermal noise reflected by the finite signal-to-noise ratio (SNR) (Just and Bamler, 1994; Zebker and Villasenor, 1992). Other decorrelation sources coming from the system (e.g. quantisation noise) may be included in it;
- γ_{spatial} summarises the decorrelation effects of the signals coming from two different antennas. It is composed from:
  - γ_{geom}, which gives an account of the baseline and geometric decorrelation for flat surfaces due to the difference of both incidence angles (Gatelli et al., 1994). Higher baselines lead to reduced range resolution and to decorrelation (the extreme case of totally uncorrelated images is obtained for the *critical baseline* (Zebker and Villasenor, 1992; Gatelli et al., 1994)). Geometrical decorrelation can be reduced through spectral shift filtering;
  - γ_{vol}, which is the volume decorrelation caused by different penetrations in the scattering medium, it gives a rough estimate of the thickness of the scattering layer. It depends on incidence angles, thus it is also due to the geometry. In TanDEM-X, this is a major issue (De Zan et al., 2013);
  - γ_{DC}, which characterises the loss due to the differences in the Doppler centroids of both acquisitions. This is the azimuth equivalent to the geometrical decorrelation;
- γ_{temp} exhibits the temporal decorrelation when the scatterer properties have changed (relevant in repeat-pass interferometry);
- γ_{coreg} comes from inaccurate coregistration of both images. Error contributions issued from the processing (e.g. interpolation errors in the resampling procedure) may be included in it.

In practice, the estimate of the local coherence is computed by averaging the considered pixel with its neighbours [2]. However, properties of the signal and the imaging system result in biased estimates of the underlying correlation (see Fig. 2.4b and Touzi and Lopes (1996); Touzi et al. (1999); Zebker and Chen (2005)). The two main biases are (1) an underestimation resulting from the presence of residual interferometer fringes, and (2) an overestimation due to the limited

[2] assuming that all the scatterers within the estimation window are independent with identical statistical properties (ergodic process)

sample number used for the estimation. New methods using for example non-local approach (Deledalle et al., 2011) provide a more accurate coherence estimate.

2.2 Phase unwrapping basics

The observed interferometric phase ψ is ambiguous and known only in the principal interval $[-\pi;\pi[$. To derive the terrain height, an estimate $\hat{\phi}$ of the true absolute (flattened) phase ϕ has to be recovered by adding a certain integer number of cycles $\hat{k}$ to ψ:

$$\hat{\phi} = \psi + 2\hat{k}\pi \tag{2.16}$$

This inverse problem is not trivial because it is non-linear and the amount of solutions is infinite. If no further information is considered, there is no safe way to determine which of these solutions is correct. Two possible approaches are worth considering to retrieve $\hat{\phi}$:

- conventional phase unwrapping (PU) methods, which mainly consist in integrating gradients, estimate $\hat{\phi}$ up to a constant integer $\hat{k}_{\text{off}}$ multiple of 2π called *absolute phase offset*:

$$\hat{\phi} = \psi + 2\hat{k}_{\text{PU}}\pi + 2\hat{k}_{\text{off}}\pi \tag{2.17}$$

  where $\hat{k}_{\text{PU}}$ is the ambiguity band retrieved during the PU procedure.
- multi-channel techniques, which extract the absolute phase jointly from several interferograms using the Maximum Likelihood Estimate (MLE) or the Maximum A Posteriori (MAP).

Phase unwrapping is a major research area and many methods have been developed. This section explains first the problem and then describes the usual (single-channel) PU algorithms with an emphasis on Minimum Cost Flow (MCF). The absolute phase retrieval is detailed in chapter 3 with a special focus on multi-channels approaches.

2.2.1 Phase unwrapping principle: gradient integration and residues

2.2.1.1 PU process and path dependence

To solve the PU problem, most algorithms assume that the terrain is (mostly) smooth. In signal theory, it means that the spatial sampling rate is assumed to be high enough in (most parts of) the complex interferogram to avoid aliasing (Nyquist criterion). Accordingly, true phase differences between two adjacent pixels are smaller than π: this is known as the Itoh condition (Itoh, 1982). In this case, PU is straightforward. The difference between two neighbouring pixels is first calculated. If the measured difference is greater than π, then a cycle (2π) is subtracted. On the contrary, if it is lower than $-\pi$, a cycle is added. At this point, the estimated gradients are assumed to be the ones of the true phase. Finally, ambiguities are solved by integrating the gradients along a path from a first pixel chosen arbitrarily to the last pixel (Itoh, 1982). Any estimate $\hat{\phi}$ obtained by adding a phase offset with a constant integer cycle to this unwrapped phase is also a possible solution. The key of phase unwrapping is thus not to estimate the unwrapped phase itself but to estimate the unwrapped phase differences. However, the Itoh condition is not fulfilled in case of noise or surface discontinuity. Consequently, the estimated gradients may be wrong and lead to the addition or subtraction of incorrect multiples of 2π, which propagate to the following pixels. Without any further information, the true phase cannot be recovered. Thus, phase unwrapping is an *ill-posed* problem. In 2-D, a wrong estimation of the gradients renders unwrapping dependent of the integration path. Figure 2.5 illustrates this problem: the wrapped phase (Fig. 2.5a) is unwrapped following two different paths (Fig. 2.5b

and Fig. 2.5c) resulting into two different estimated phases, which can be both considered as correct. Nevertheless, gradients in azimuth and range are dependent and their relationship can be exploited to identify corrupted regions.

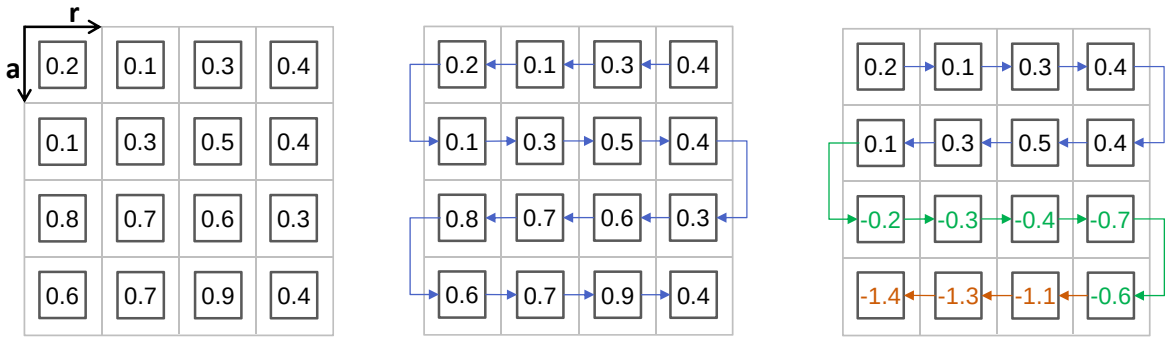

(a) Wrapped phase (b) Unwrapped phase along path 1 (c) Unwrapped phase along path 2

Fig. 2.5. Path dependency in phase unwrapping: from the wrapped phase (a), two distinct unwrapped phases (b) and (c) can be obtained by following two different paths (all values are in cycle, i.e $2\pi \equiv 1$).

2.2.1.2 Gradient estimate and residues

The gradient of the true phase is defined by $\nabla\phi = (\Delta_r\phi, \Delta_a\phi)^T$ where Δ_r and Δ_a are respectively the partial derivatives calculated between adjacent pixels in the range and azimuth directions. A gradient field is conservative, which means that the curl of this 2-D vector field has to be 0:

$$\nabla \times \nabla\phi = \Delta_r\Delta_a\phi - \Delta_a\Delta_r\phi = 0 \tag{2.18}$$

In other words, any integral over a closed loop in the gradient of an unwrapped phase is necessarily zero. However, the estimated gradients $\hat{\nabla}\psi$ of the wrapped phase are also wrapped. $\hat{\nabla}\psi$ may thus differ from $\nabla\phi$ in the presence of noise or undersampling. Therefore, curls may not be equal to 0 anymore rendering the gradient field of the wrapped phase non-conservative. Integration results in path-dependent inconsistencies in the unwrapped phase. To avoid that, Goldstein et al. (1988) suggested to integrate wrapped phase differences on 2×2 neighbouring pixels as depicted in Fig. 2.6a. It is equivalent to calculating the curl:

$$\begin{aligned} \text{res}(r,a) &= W\left(\Delta_r\psi(r,a)\right) + W\left(\Delta_a\psi(r+1,a)\right) - W\left(\Delta_r\psi(r,a+1)\right) - W\left(\Delta_a\psi(r,a)\right) \\ &= \nabla \times \nabla\psi(r,a) = \{-2\pi, 0, 2\pi\} \end{aligned} \tag{2.19}$$

For four pixels, the result can be either 0 i.e. no *residue* is present or $\pm 2\pi$ producing a *positive* or *negative residue*. Figure 2.6b depicts the residues found for the example of Fig. 2.5a.

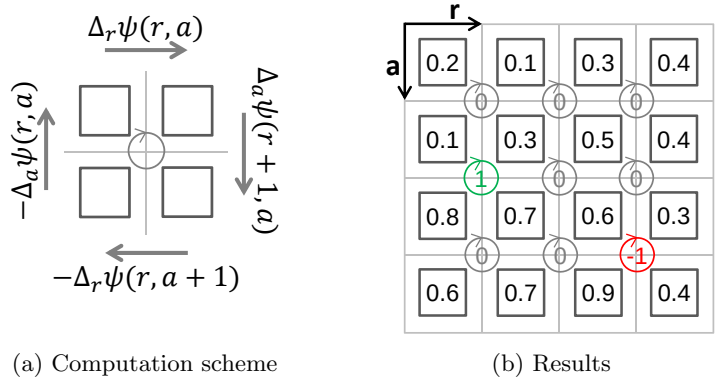

(a) Computation scheme (b) Results

Fig. 2.6. Residues calculation for the example of Fig. 2.5a: two residues found.

Residues are local inconsistencies representing configurations which are physically impossible in the hypothesis that the true phase gradient is conservative (Goldstein et al., 1988). They cause global phase unwrapping errors if not accounted for. A positive residue has to be connected to a negative one with a so-called *branch-cut* (or *residue-cut* or *ghost line*) to cancel each other. After that, any gradients integral over any closed path is 0. Ideally, when residues have a topographical cause, branch-cuts follow the terrain discontinuity.

Gradients could also be estimated through a frequency estimation, a multi-resolution approach or a periodogram.

2.2.2 Conventional 2-D phase unwrapping techniques

The residues and branch-cuts concepts are the basis of all path-following unwrapping methods. Alternatively, minimum-norm algorithms try to minimise the deviation between the estimated unwrapped phase gradients $\nabla\hat{\phi}$ and their wrapped counterparts $\hat{\nabla}\psi$. The following subsections give an overview of these two main algorithm families. A complete explanation of the different techniques can be found in Ghiglia and Pritt (1998) or Gens (2003). At last, statistical PU, which opens the door to the multi-channel PU, is reviewed.

2.2.2.1 Path-following methods (local integration)

Path-following methods rely on placing branch-cuts between residues. Phase gradients are then locally integrated over a path avoiding crossing them so that no integration path can encircle regions with residues. Within these constraints, path independence is guaranteed (Goldstein et al., 1988). The corresponding unwrapped and wrapped phase values are ensured to differ only by an integer number of cycles. This property is called *congruence* and is actually an *a priori* assumption of the PU problem. The real difficulty is thus to match positive with negative residues especially for those due to terrain discontinuities. A wrong choice in the placement of the branch-cuts results in an error which may propagate over the whole phase image (Fornaro et al., 1997). Goldstein et al. (1988) proposed the branch-cut algorithm where positive and negative residues are linked by applying a nearest neighbour strategy. Nevertheless, it often leads to unrealistic branch-cuts placements. Chen and Zebker (2000) proposed an improved weighted version, the *minimum spanning tree*, that ensures a complete coverage. Later on, Chen and Zebker (2002) put forward the SNAPHU (Statistical-cost, Network-flow Algorithm for Phase Unwrapping) algorithm. It poses phase unwrapping as a MAP probability estimation problem.

Network flow formulation and MCF (Costantini, 1998; Flynn, 1997) consider PU as a minimisation problem with integer variables introducing weighting or cost functions (c_r and c_a) associated to every branch-cut. A low cost specifies a probable placement of a branch-cut whereas a high cost indicates an improbable location. Branch-cuts are used to correct phase differences by adding an integer multiple of 2π. The minimisation problem is described by:

$$\min_{d_r d_a} \left\{ \sum_r \sum_a c_r(r,a)|d_r(r,a)| + \sum_r \sum_a c_a(r,a)|d_a(r,a)| \right\} \tag{2.20}$$

where $\mathbf{d}(r,a) = (d_r(r,a), d_a(r,a))^T = \frac{1}{2\pi}\left(\nabla\hat{\phi}(r,a) - \hat{\nabla}\psi(r,a)\right)$ is an estimate of the phase gradient error. The curl of $\mathbf{d}(r,a)$ is the negative of the curl of the estimated gradients of the wrapped phase. It can be seen as a correction on $\hat{\nabla}\psi(r,a)$ applied before the integration. In this way, the non-conservative estimated gradient field is compensated and recovers its conservativeness property. The success of phase unwrapping depends thus on how the residues are linked.

For Costantini's (1998) MCF algorithm, the minimisation of the network of flows defines the placement of every segment of the branch-cuts guided by cost factors. A node represents a wrapped gradient loop integral around a 2×2 square of pixels. Positive or negative residues are the surplus and demand nodes. The flow can travel on arcs connecting neighbouring nodes along paths determined by the cost functions equalising in this way the nodes. The resulting grid-like network (see Fig. 2.7a) contains thus one arc for each phase gradient. Since phase gradients are to be estimated in a PU problem, arcs and the quantities of flow on them play a critical role in the quality of the unwrapping results. Physically, the amount of flow on an arc represents the difference between the unwrapped and wrapped gradients ($\nabla\hat{\phi} - \hat{\nabla}\psi$) while the direction of the flow determines the sign of the difference. As a result, any feasible flow arrangement corresponds uniquely to a valid, residue-free unwrapped solution (Fig. 2.7b).

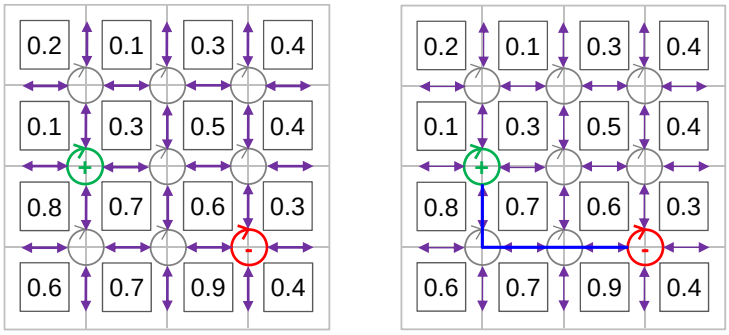

Fig. 2.7. Example of the equivalent network to the phase unwrapping problem of 2.5a: (a) the network itself: positive and negative residues (respectively depicted in green and red) are the supply and demand nodes, neighbouring nodes are connected by arcs or possible flow paths, (b) placement of a possible branch-cut (in blue) discharging the residues.

The only critical point of the MCF is to find physically meaningful cost functions. Special features of the interferogram such as layover, shadow or incoherent areas are generally preferred to position branch-cuts. For this reason, costs generators use local information such as the coherence (Costantini, 1998), the residue density (correlated to the coherence), wrapped phase gradients, or the amplitude of the images (correlated to the topography) (Eineder et al., 1998; Carballo and Fieguth, 2000; Suchandt and Eineder, 2003). The coherence has been found to be always a good helper in guiding the MCF algorithm. Chen and Zebker (2000, 2002) define costs for topography or deformation mapping through statistical models.

The application of network flow methods is however limited because of the required computational power. Eineder et al. (1998) optimised it with respect to memory and speed for the SRTM mission. In the last decade, several works proposed two-step algorithms to parallelise the minimisation problem for large interferograms (Carballo and Fieguth, 2002; Chen and Zebker, 2002; Zhang et al., 2011).

2.2.2.2 Minimum-norm methods (global integration)

Global integration methods are also based on phase gradients. Nevertheless, they try to find an unwrapped phase which minimises the L^p norm of the difference between $\hat{\nabla}\psi$ and $\nabla\hat{\phi}$ (Ghiglia and Romero, 1996):

$$\min_{\hat{\phi}} \left\{ \sum_r \sum_a w_r(r,a) \left| \left(\nabla_r \hat{\phi}(r,a) - \hat{\nabla}_a \psi(r,a) \right) \right|^p + \sum_r \sum_a w_a(r,a) \left| \left(\nabla_r \hat{\phi}(r,a) - \hat{\nabla}_a \psi(r,a) \right) \right|^p \right\} \tag{2.21}$$

where p determines how the differences between $\nabla\hat{\phi}$ and $\hat{\nabla}\psi$ are penalised and $w(r,a)$ are weights comparable to the costs in eq. (2.20). It is a global approach since all samples are

used together to find the solution. However, the congruency property is lost. When $p = 2$, eq. (2.21) becomes the well-known least-squares estimation, which can be unweighted (Fried, 1977; Hudgin, 1977; Ghiglia and Romero, 1994) or weighted (Ghiglia and Romero, 1994, 1996). Like for the MCF, the success of the weighted algorithm depends strongly on how the weights are chosen. Bamler et al. (1998) demonstrated that these approaches (with $p = 2$) underestimate phase gradients and erode the terrain in the presence of residues. Zebker and Lu (1998); Ghiglia and Pritt (1998) confirmed it empirically. Examples of alternative solutions are multi-grid techniques (Pritt, 1996), Green's formulation (equivalent to $p = 2$, Fornaro et al. (1996)), Fourier-domain vector projections (Pritt and Shipman, 1994), bi-orthogonal wavelet transform (Kim and Kim, 2005) or graph-cuts (Bioucas-Dias and Valadão, 2007).

2.2.2.3 Links between local and global integrations

Both apparently diverging families of methods agree that a good solution to PU minimises some error norm. In the late 90s, several links have been found between them:

1. the generalisation to the L^p norm by Ghiglia and Romero (1996) allowed to recognise that local gradients of the solution match well the measured wrapped gradients when $p < 2$. In the limit of p approaches 0 (L^0-norm), the number of discontinuities is minimised. Goldstein et al.'s (1988) residue-cut can thus be seen as an unweigthed minimum L^0-norm algorithm. The gradients of the two unwrapped maps differ only when there is a branch-cut.
2. sophisticated path-following methods like Flynn (1997) or Costantini (1998) actually minimise the L^1-norm. Empirically, L^0 and L^1 algorithms tend to deliver more accurate solutions than L^2 ones (Zebker and Lu, 1998; Ghiglia and Pritt, 1998).
3. Pritt (1997) restored the congruence to the output of least-square solutions and thus transformed the least-square approach more or less into a minimum L^0-norm.
4. Fornaro et al. (1996) show with the Green's formulation that, at a given point, the least-squares estimation is the average of all solutions obtained by simple path-following on radial paths from the point to the boundary.

2.2.2.4 Statistical estimation methods

Statistical approaches rely on a data observation mechanism model in which *a priori* knowledge of the phase may be considered. They are optimal from the information theoretical point of view but cannot ensure the uniqueness of the solution. Coherence properties, phase and amplitude statistics or instrument response can be used in a statistically optimal way in the likelihood term. Prior information about terrain properties (e.g. roughness or fractal dimensions) may constrain the solution. Many works tried to benefit from the statistical estimation: Marroquin and Rivera (1995); Marroquin et al. (1995); Guerriero et al. (1998); Leitao and Figueiredo (1998); Loffeld et al. (2008); Martinez-Espla et al. (2009). Nico et al. (2000) analysed the different existing phase unwrapping algorithms in the context of Bayesian inference and showed the influence of different *priors*. Bioucas-Dias and Leitao (2002) used a Gaussian Markov Random Field (GMRF) to model the absolute phase in their prior. The algorithm simultaneously solves the phase unwrapping problem and smoothes the observations.

Statistical estimation methods open a door to an efficient solution for the PU problem: the multi-channel PU, which uses several interferometric SAR data jointly.

3 Multi-channel interferometry and elevation extraction

Phase unwrapping (PU) is a key procedure to reconstruct a Digital Elevation Model (DEM) from SAR images. Unfortunately, it is not uniquely solvable in the presence of noise or discontinuities. To get around this problem, several interferograms or channels with different baselines or frequencies can be combined. The first part of this chapter gives an overview of the multi-channel PU techniques and more specifically of the multi-baseline approaches. In the second part, alternative methods to get an absolute elevation map are introduced.

3.1 Multi-channel interferometry and phase unwrapping

Multi-channel interferometry combines at least two interferograms of the same scene in order to simplify or even avoid the single-channel integration-based PU. The different channels are acquired from the same viewing geometry either at different frequencies and/or with various baselines. For this reason, multi-channel InSAR takes advantage of the data diversity to significantly increase ambiguity intervals of the interferometric phases. It makes also possible to estimate the unwrapped phase in isolated regions. In this context, the PU problem is addressed on a single phase value basis instead of on a phase difference basis. This section is divided as follows. First, the differences between multi-frequency and multi-baseline interferometry are stated. Then, approaches based on combination of channels are presented followed by statistical estimation methods. Finally, the advantages and drawbacks of these techniques are summarised.

3.1.1 Multi-frequency and multi-baseline interferometry

Multi-frequency interferometry uses 1) SAR image pairs acquired with sensors operating at different frequencies or, 2) interferograms obtained by partitioning the Doppler bandwidth into non-overlapping sub-bands (Pascazio and Schirinzi, 2001, 2002). The interferometric data are statistically independent since they do not overlap in the frequency domain. Nonetheless, in the second case, the bandwidth is narrowed implying a reduction of the spatial resolution so that a trade-off has to be found between the spatial resolution and the number of sub-bands to consider.

Another way to get multiple interferograms is to acquire several SAR images from slightly different look angles so that the image pairs exhibit different baselines. Yet, statistical independence is fulfilled only if the baselines of the cross-interferograms are larger than the critical baseline so that the spectra of the different interferometric pairs do not overlap (Pascazio and Schirinzi, 2002).

The height of ambiguity (HoA) of a specific channel is $h_{2\pi}^c = \frac{\lambda^c R \sin\theta}{B_\perp}$ with $\lambda^c = c_0/f_0^c$ in case of multi-frequency or $h_{2\pi}^c = \frac{\lambda R \sin\theta}{B_\perp^c}$ for multi-baseline interferometry. Short baselines or low frequencies result in higher height error while large baselines or high frequencies can cause greater phase unwrapping problems. Accordingly, multi-channel interferometry provides the solution to tackle both problems by increasing the ambiguity intervals of interferometric phases without degrading the height accuracy.

3.1.2 Phase ambiguity resolution by combining interferograms

Xu et al. (1994) proposed the linear combination and the projection method explained thereafter to unwrap multi-channel interferograms.

3.1.2.1 Linear combination of interferograms

An initial measure of the height is obtained from a short baseline or low frequency interferogram. A first estimate of the ambiguity band is then deduced and later used to resolve phase wraps in the next interferogram. In this way, the height is iteratively determined for every baseline or frequency from highest to lowest HoA leading to an accurate final height estimate (Thompson et al., 1999). For the sake of simplicity, the following demonstration considers only two interferograms A and B, where A has the higher HoA. In the absence of noise, both interferograms deliver the same height estimate $\hat{h}$, which is equal to (eqs. (2.8) and (2.16)):

$$\hat{h} = \frac{h_{2\pi}^A}{2\pi}\left(\psi^A + 2\hat{k}^A\pi\right) = \frac{h_{2\pi}^B}{2\pi}\left(\psi^B + 2\hat{k}^B\pi\right) \tag{3.1}$$

Once $\hat{k}^A$ has been estimated, the ambiguity band $\hat{k}^B$ can be easily figured out as follows:

$$\hat{k}^B = \frac{1}{2\pi}\left(\frac{h_{2\pi}^A}{h_{2\pi}^B}\psi^A - \psi^B\right) + \frac{h_{2\pi}^A}{h_{2\pi}^B}\hat{k}^A = \frac{1}{2\pi}\left(\frac{1}{\mu}\psi^A - \psi^B\right) + \frac{1}{\mu}\hat{k}^A \qquad \in \mathbb{Z} \tag{3.2}$$

where μ is the HoA ratio defined as $\mu = h_{2\pi}^B/h_{2\pi}^A$ (with $h_{2\pi}^B < h_{2\pi}^A$ i.e. $\mu < 1$). Lombardini (1998) called $1/\mu$ the phase Unambiguous Range Magnification (URM) because the combination of two interferograms exhibiting a HoA ratio μ provides a phase estimated modulo $2\pi/\mu$. The smaller μ, the more straightforward it is to retrieve $\hat{k}^B$ from $\hat{k}^A$ and the easier PU is made (Jakowatz et al., 1996; Lanari et al., 1996; Corsini et al., 1997; Schmitt and Wiesbeck, 1997). If the short baseline can be chosen so that it covers the full range of heights present in the scene to be mapped, PU is completely avoided for the interferogram A and ambiguities in interferogram B can be recovered directly (without noise reduction).

Alternatively, if no interferometric pair with a sufficiently high HoA is available, it is possible to combine linearly the two interferograms (Xu et al., 1994). Massonnet et al. (1996) published a similar approach called the Integer Interferometric Combination (IIC). It aims to multiply the interferograms by the integers q^A and q^B before their combination. The resulting interferogram exhibits a HoA $h_{2\pi}^R$ given by:

$$\frac{1}{h_{2\pi}^R} = \frac{q^A}{h_{2\pi}^A} + \frac{q^B}{h_{2\pi}^B} \tag{3.3}$$

where q^A and q^B have to be chosen so that $h_{2\pi}^R$ is greater than both $h_{2\pi}^A$ and $h_{2\pi}^B$ to ease unwrapping. Unfortunately, this method is highly sensitive to noise since any integer combination results in an increase of the noise in the phase (nonetheless, an addition entails a reduction of the equivalent noise in the height domain since $h_{2\pi}^R$ would be smaller). In practice, q^A and q^B have to remain low (and of opposite signs) so that the noise distribution does not exceed one cycle.

3.1.2.2 Projection method

A good means to reduce noise effects is provided by the projection method. The latter relies strongly on the satellite configuration to deduce the behaviour of the phases. From eq. (3.1), the following relation is obtained:

$$\frac{\psi^A + 2\hat{k}^A\pi}{\psi^B + 2\hat{k}^B\pi} = \frac{h_{2\pi}^B}{h_{2\pi}^A} = \mu \tag{3.4}$$

It is clear that ψ^A is a linear function of ψ^B where the HoA ratio μ is the slope of the line segments (with $\mu < 1$). As long as μ is a rational number, the number of segments is finite and

they reconnect in a wrapped sense (see Fig. 3.1 where only few lines are depicted). Theoretically, it is thus possible to expand the unambiguous range just by changing the ratio μ (the smaller μ, the larger the range is). However, points do not lie on the line segments in the presence of noise and have to be projected to the correct line segments (Xu et al., 1994; Wu et al., 2009). As noise increases or line segments get closer, the projection method becomes unreliable. Figure 3.1 depicts the relation between ψ^A and ψ^B for two different HoA ratios, the noise remaining unchanged. For a small μ (Fig. 3.1a), the lines segments are clearly separated and the points can be easily projected to the correct line. In contrast, when μ is higher (Fig. 3.1b), the segments are closer from each other and the points cannot be assigned unequivocally to a specific segment even if the noise level is the same. A cluster analysis as suggested by Yu et al. (2011); Liu et al. (2015) may improve the results.

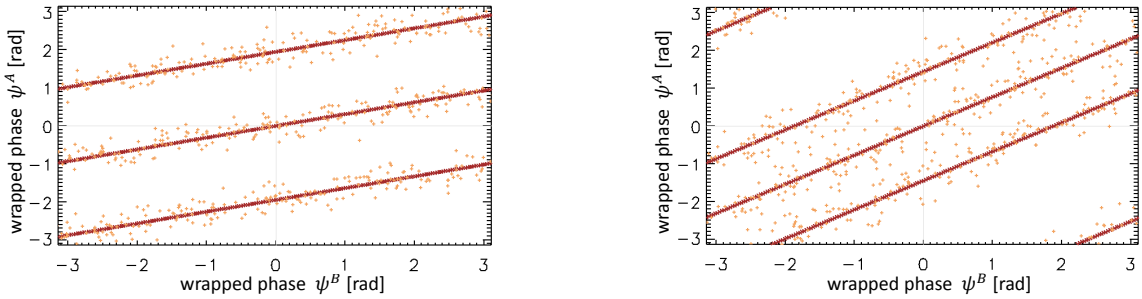

(a) $\mu = 0.31$ (b) $\mu = 0.77$

Fig. 3.1. Relationship between the wrapped phases ψ^A and ψ^B with two different HoA ratios μ but the same low level of noise ($\sigma^A = 0.2$ rad, $\sigma^B = 0.33$ rad). (a) when the HoA ratio is small (here $\mu = 0.31$), the line segments are well separated and points can be projected to the correct line whereas in (b), the lines are closer because of the greater HoA ratio $\mu = 0.77$, in this case, the projection is not anymore straightforward already with little noise.

3.1.3 Statistical estimation of the terrain height

During the last ten to twenty years, most multi-channel approaches have been formulated in a statistical framework (Baselice et al., 2014b). Indeed, estimation theory is an appropriate tool as it allows to deal with uncertainties introduced by the noise. The different interferograms can be combined efficiently in order to retrieve the terrain height (the unknown to be estimated). The objective is thus to find an optimal estimate of the true terrain height according to some (statistical) criterion. Height can be estimated either pixel-wise or by considering the neighbourhood of every pixel. It is presumed that the reader is already familiar with estimation theory. Kay (1993) provides a comprehensive explanation.

3.1.3.1 Pixel-wise height estimation

By replacing the expected noise-free phase ϕ_0 by its equivalent height h (eq. (2.8)) in the multi-looked interferometric phase probability density function (*pdf*) (eq. (2.12)), the single-channel *pdf* $p(\psi^c|h;\gamma^c,L)$ of the measured wrapped phase given the actual height can be written as:

$$p(\psi^c|h;\gamma^c,L) = \frac{\Gamma\left(L+\frac{1}{2}\right)\left(1-|\gamma^c|^2\right)^L|\gamma^c|\cos\left(\psi^c-\frac{2\pi}{h^c_{2\pi}}h\right)}{2\sqrt{\pi}\,\Gamma(L)\left(1-|\gamma^c|^2\cos^2\left(\psi^c-\frac{2\pi}{h^c_{2\pi}}h\right)\right)^{L+1/2}} + \frac{\left(1-|\gamma^c|^2\right)^L}{2\pi}\,{}_2F_1\left(L,1;\frac{1}{2};|\gamma^c|^2\left(\psi^c-\frac{2\pi}{h^c_{2\pi}}h\right)\right) \tag{3.5}$$

where ψ^c, γ^c and $h^c_{2\pi}$ stand respectively for the observed interferometric phase, the coherence and the HoA of the considered channel. Once ψ^c has been observed, $p(\psi^c|h;\gamma^c,L)$ is the likeli-

hood function. It is $h_{2\pi}^c$-periodic and exhibits an infinite number of maxima. The combination of likelihoods of distinct HoAs (i.e. periods) empowers to reduce the number of global maxima. For C independent phase measurements, the joint likelihood is given by:

$$p(\mathbf{\Psi}|h) = \prod_{c=1}^{C} p(\psi^c|h;\gamma^c,L) \tag{3.6}$$

where $\mathbf{\Psi} = (\psi^1, \psi^2, ..., \psi^C)^T$ is the measured wrapped phase data vector related to the considered pixel. Notwithstanding, in the multi-baseline case, observations are usually dependent so that the joint multi-baseline likelihood cannot be obtained through eq. (3.6). Meglio et al. (2006) established a closed form of $p(\mathbf{\Psi}|h)$ for three SAR correlated signals. They showed also that the two interferograms can be assumed as independent as long as the baselines differ significantly. Corsini et al. (1999) and, lately, Baselice et al. (2014a); Schmitt (2014) used the *pdf* of the complex SAR pixel to compute the joint likelihood to counter the dependency problem (at the same time they took benefit of the amplitude in the estimation). In practice, the independence is generally presupposed.

If no further information is considered, the height h is assumed to be a *deterministic* parameter, which can be determined by means of the *classical* estimation theory. The location of the global maximum of the multi-channel joint likelihood function $p(\mathbf{\Psi}|h)$ is called the Maximum Likelihood Estimate (MLE) of the height (Ghiglia and Wahl, 1994; Lombardo and Lombardini, 1997; Pascazio and Schirinzi, 2001; Fornaro et al., 2006):

$$\hat{h}_{\mathrm{MLE}} = \arg\max_h p(\mathbf{\Psi}|h) = \arg\max_h \prod_{c=1}^{C} p(\psi^c|h;\gamma^c,L) \tag{3.7}$$

MLE approaches are able to deal with discontinuities and high sloped areas and they allow to restore the uniqueness of the solution. The MLE is asymptotically unbiased and efficient since it reaches the Cramér-Rao Lower Bound (CRLB) when a large set of data is considered.

Figures 3.2a to 3.2c exhibit the one-look height likelihoods combining up to four interferograms of different HoAs ($h_{2\pi}^1 = 67$ m/cycle, $h_{2\pi}^2 = 50$ m/cycle, $h_{2\pi}^3 = 30$ m/cycle and $h_{2\pi}^4 = 37,5$ m/cycle) of different coherences ($\gamma^1 = \gamma^3 = 0.7$ and $\gamma^2 = \gamma^4 = 0.4$). Starting with only two likelihood functions, the calculated joint likelihood exhibits two global maxima (Fig. 3.2d). A third and eventually a fourth measurements are added to demonstrate the decrease of the number of local and global maxima (Figs. 3.2e and 3.2f). The more channels available, the more reliable the height estimate is. The single-channel likelihoods overlap perfectly at the real height $h = 600$ m implying that the different wrapped phases are equal to their respective wrapped nominal phases ($\psi^c = W(\phi_0^c) = \psi_0^c$). This is an optimum but unrealistic case.

In reality, the measured wrapped phases deviate from ψ_0^c so that the different likelihoods do not superimpose exactly at h as depicted in Fig. 3.3. In this case, the multi-channel likelihoods have totally different shapes and the (global) maxima may be positioned at different ambiguity bands depending on the noise of the different channels (Figs. 3.3d to 3.3f). Consequently, the resulting estimated height image may appear noisy because $\hat{h}_{\mathrm{MLE}}$ may be in different ambiguity bands from one pixel to the next. A large number of interferograms is therefore required to ensure a good terrain reconstruction.

Additional knowledge about the terrain can be used to reduce this effect. Subsequently, the height h of a pixel is seen as a random variable and is modelled by an *a priori* distribution. Such an approach is termed *Bayesian* estimation. According to the Bayes' rule, the joint or the *posterior* probability is proportional to the product of the multi-channel likelihood function given by eq. (3.6) and an appropriate *a priori* distribution. Henceforth, the height estimate is

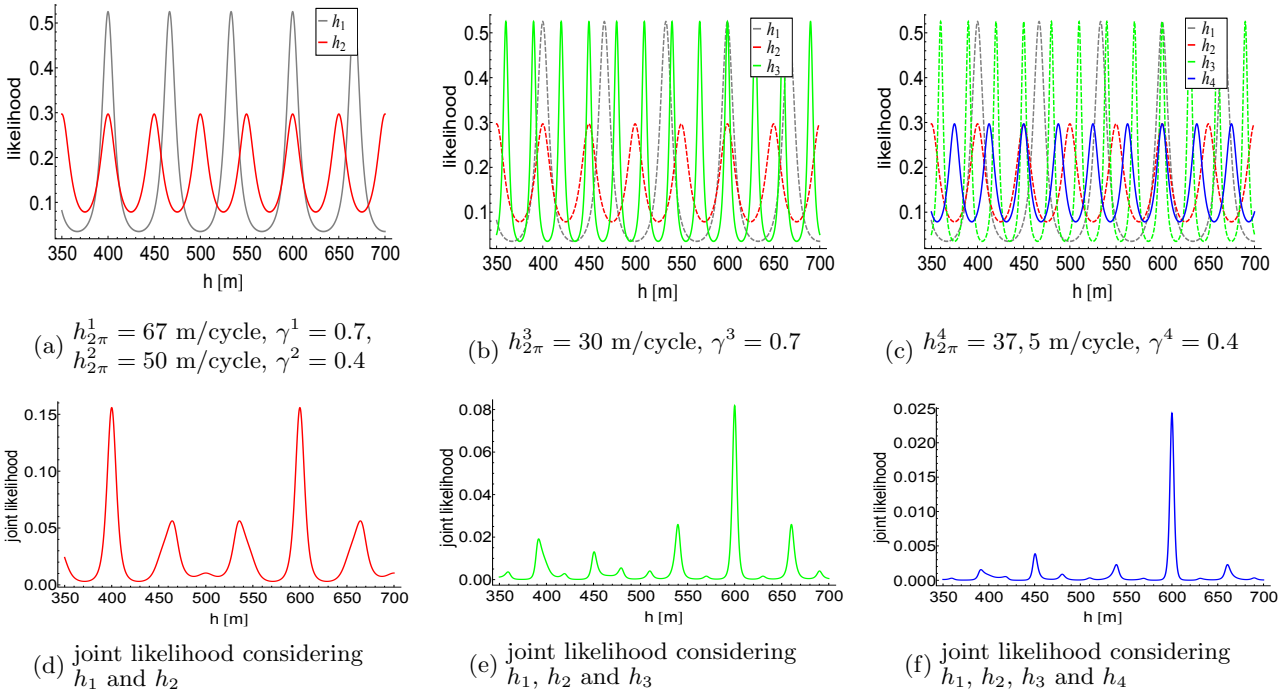

(a) $h^1_{2\pi} = 67$ m/cycle, $\gamma^1 = 0.7$, $h^2_{2\pi} = 50$ m/cycle, $\gamma^2 = 0.4$

(b) $h^3_{2\pi} = 30$ m/cycle, $\gamma^3 = 0.7$

(c) $h^4_{2\pi} = 37,5$ m/cycle, $\gamma^4 = 0.4$

(d) joint likelihood considering h_1 and h_2

(e) joint likelihood considering h_1, h_2 and h_3

(f) joint likelihood considering h_1, h_2, h_3 and h_4

Fig. 3.2. Height likelihood functions: optimum but unrealistic case. Different HoAs ($h^1_{2\pi} = 67$ m/cycle, $h^2_{2\pi} = 50$ m/cycle, $h^3_{2\pi} = 30$ m/cycle and $h^4_{2\pi} = 37,5$ m/cycle) and two coherences ($\gamma^1 = \gamma^3 = 0.7$ and $\gamma^2 = \gamma^4 = 0.4$) are considered. (a,b,c) overplot of the single-channel likelihoods; (d,e,f) multi-channel likelihood function. One channel is added per new pair of plots (2 channels in a,d, 3 in b,e and 4 in c,f). The different wrapped phases are supposed to be equal to the respective wrapped nominal phases so that the single-channel likelihoods overlap perfectly at the actual height $h = 600$ m. The number of global maxima decreases and the first-to-second peak ratio increases by adding new measurements.

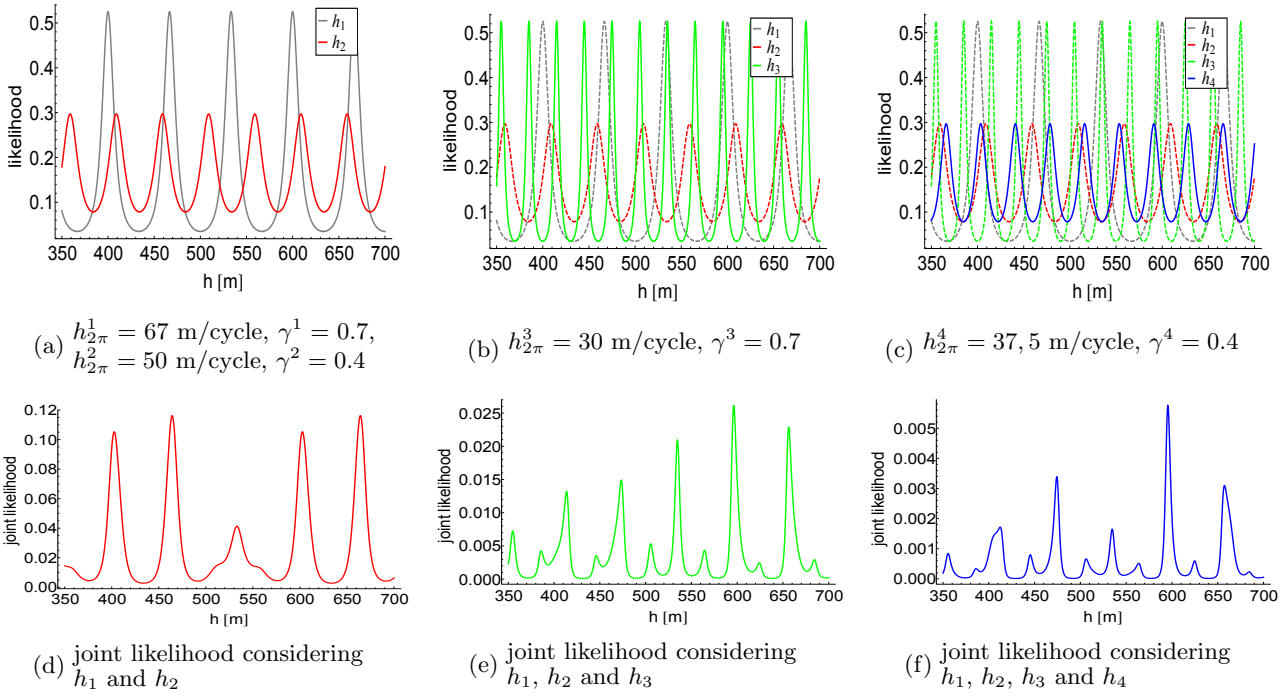

(a) $h^1_{2\pi} = 67$ m/cycle, $\gamma^1 = 0.7$, $h^2_{2\pi} = 50$ m/cycle, $\gamma^2 = 0.4$

(b) $h^3_{2\pi} = 30$ m/cycle, $\gamma^3 = 0.7$

(c) $h^4_{2\pi} = 37,5$ m/cycle, $\gamma^4 = 0.4$

(d) joint likelihood considering h_1 and h_2

(e) joint likelihood considering h_1, h_2 and h_3

(f) joint likelihood considering h_1, h_2, h_3 and h_4

Fig. 3.3. Height likelihood functions: realistic case. Different HoAs ($h^1_{2\pi} = 67$ m/cycle, $h^2_{2\pi} = 50$ m/cycle, $h^3_{2\pi} = 30$ m/cycle and $h^4_{2\pi} = 37,5$ m/cycle) and two coherences ($\gamma^1 = \gamma^3 = 0.7$ and $\gamma^2 = \gamma^4 = 0.4$) are considered. (a,b,c) overplot of the single-channel likelihoods; (d,e,f) joint likelihood function. One channel is added per new pair of plots (2 channels in a,d, 3 in b,e and 4 in c,f). The measured wrapped phases deviate from their respective wrapped true phases so that the *pdfs* do not overlap perfectly at the real height $h = 600$ m. The joint likelihoods exhibit more peaks and at different positions.

the the maximum of the *a posteriori* distribution, which is retrieved through the Maximum A Posteriori (MAP) estimator (Kay, 1993). On a pixel basis, *a priori* knowledge coming from a reference Digital Elevation Model (DEM) (Ferretti et al., 1997; Eineder and Adam, 2005) is usually exploited at least to constrain the range of interest.

3.1.3.2 Approaches using neighbourhood information

Approaches using neighbourhood information take into account that a pixel height is somehow similar to the surrounding heights. Accordingly, like in single-channel PU, it is assumed that the terrain is rather smooth (Ferraiuolo et al., 2004).

In the literature, the prior is mainly modelled as a Gaussian Markov Random Field (GMRF). It is a powerful tool to describe the interaction between neighbours and is well-suited for natural scenes. Geman and Geman (1984); Li (2009) provide complete theoretical information about MRF and GMRF. A local GMRF can be tuned pixel-wise to be applicable to any terrain profile. The considered *a priori* distribution follows (Ferraiuolo et al., 2004):

$$p\left(\mathbf{h};\boldsymbol{\beta}\right) = \frac{1}{Z(\boldsymbol{\beta})}\,\exp\left[-\sum_{n=1}^{N}\sum_{j\in N_n}\left(\frac{\left(h(n)-h(j)\right)^2}{2\beta_{n,j}^2}\right)\right] \tag{3.8}$$

where $Z(\boldsymbol{\beta})$ is the so-called partition function, $\boldsymbol{\beta}$ is the unknown *hyperparameter* vector gathering all $\beta_{n,j}$, N_n is the neighbourhood of the n^{th} pixel and N the number of phase/height samples. Hyperparameters enable the image to be locally described by quantifying the spatial correlation between neighbouring pixels. A high value indicates high height discrepancy whereas low values mean that the neighbours are likely to have a similar height. They balance the regularisation (prior) and the data (likelihood) terms in the maximisation process. The MAP estimate of the terrain height $\hat{\mathbf{h}}_{\mathrm{MAP}}$ is obtained by maximising the posterior distribution or equivalently by minimising the total energy:

$$\begin{aligned}
\hat{\mathbf{h}}_{\mathrm{MAP}} &= \arg\max_{h}\; p(\boldsymbol{\Psi}|\mathbf{h})p\left(\mathbf{h};\boldsymbol{\beta}\right) \\
&= \arg\min_{h}\left[-\sum_{n=1}^{N}\ln\, p(\boldsymbol{\Psi}|h(n)) + \sum_{n=1}^{N}\sum_{j\in N_n}\frac{\left(h(n)-h(j)\right)^2}{2\beta_{n,j}^2}\right] \\
&= \arg\min_{h}\left[E_{\mathrm{data}}(\boldsymbol{\Psi}|\mathbf{h}) + E_{\mathrm{prior}}(\boldsymbol{\Psi};\boldsymbol{\beta})\right]
\end{aligned} \tag{3.9}$$

where $\mathbf{h} = (h(1), h(2), ..., h(N))^T$ is the unknown output image seen as a realisation of the random vector $\mathbf{H}$. Since the GMRF prior restores the smoothness, ambiguity is solved while the noise is reduced (and as a consequence the needed number of interferograms too). The uniqueness of the solution is restored without external constraints.

Hyperparameters have to be estimated. A complete explanation can be found in Ferraiuolo et al. (2004). Usually the Expectation-Maximisation algorithm (Li, 2009) is applied. After that, the different height values have to be calculated. Several algorithms exist (Li, 2009) like the Iterated Conditional Modes (ICM) or the Metropolis algorithms (Ferraiuolo et al., 2004; Ferraioli, 2010). Nonetheless, the computation load is often critical for large size images and the global optimum may not be found so that alternatives using different priors have been proposed.

Ferraioli et al. (2009) suggested a MAP approach where the prior is the Total Variation (TV). TV is well-known in image processing (Rudin et al., 1992) or for SAR image restoration (Denis et al., 2008). It is a non-local model (the hyperparameter is a constant for the whole image)

but it favours neither discontinuity nor smoothness. The TV prior energy is given by:

$$E_{\text{prior}_{\text{TV}}}(\mathbf{\Psi};\beta) = \beta \sum_{n=1}^{N} \sum_{j \in N_n} |h(n) - h(j)| \tag{3.10}$$

The estimation is faster because the hyperparameter β is constant for the whole image. The latter can be determined for example by finding the corner of the *L-curve* (Hansen and O'Leary, 1993; Castellanos et al., 2002). Ferraioli et al. (2009) solved this energy minimisation problem with graph-cuts. This algorithm is more robust with respect to local optima and more efficient computationally. Moreover, it is possible, under certain conditions, to find the global optimum (Ishikawa, 2000). Nevertheless, the memory consumption is considerable: the graph has $N \times K$ nodes and $N \times K^2$ edges, with K being the number of labels i.e. the different height levels. Shabou et al. (2012) used jointly the amplitude and the phase to reconstruct the terrain height.

Lachaise and Bamler (2010); Lachaise et al. (2010) proposed a two-stage multi-baseline PU method where the ambiguity and errors in the gradient estimation are first reduced by means of a MAP estimation. This is performed either separately or jointly through belief propagation on the azimuth and range gradients. Based on these estimates, the Minimum Cost Flow (MCF) algorithm is used in a second step to unwrap the phase accounting for the overall conservative condition of the gradient. This method takes advantage of the fact that a gradient should not be too high except at few places (e.g. in the presence of terrain discontinuities) to constrain the range of possible unwrapped values and reduce the memory consumption. However, this approach is sensitive to noise and cannot solve the unwrapping problem properly with only two interferograms.

Lately, another series of algorithms based on Kalman filters have been proposed (Loffeld et al., 2008; Chirico and Schirinzi, 2013; Osmanoglu et al., 2014).

3.1.4 Main characteristics of the multi-channel approaches

3.1.4.1 Multi-frequency versus multi-baseline

Multi-frequency and multi-baseline configurations are formally compared in Table 3.1. In practice, the configuration is imposed by the acquisition concept.

	Advantages	Drawbacks
Multi-frequency	• frequency is known accurately • statistical independence of the channels	• sub-bands (if used) reduce the spatial resolution • small frequency separation • limited number of channels
Multi-baseline	• possibility to get arbitrary many channels	• baseline knowledge has a limited accuracy • independence is usually not satisfied

Table 3.1. Comparison of multi-frequency and multi-baseline configurations.

3.1.4.2 Advantages and drawbacks of the different approaches

Table 3.2 summarises the pros and cons of the different multi-channel approaches presented in the previous sections namely the interferograms combination, the pixel-wise approaches and the ones using the neighbourhood.

As long as multi-channel methods do not exploit phase gradients (like most single-baseline approaches), they ensure the uniqueness of the solution in the case of piecewise continuous elevation patterns with strong discontinuities (even several π phase jumps between adjacent pixels). MLE and MAP provide the absolute elevation. Ferraiuolo et al. (2009) give a complete

	Advantages	Drawbacks
Interferograms combination	• computationally efficient • usable only with two image pairs	• very sensitive to noise
Pixel-wise (MLE/MAP)	• asymptotically efficient and unbiased • can reconstruct any terrain • parallelisable	• requires lots of data • performance highly dependent on data (coherence, HoA, ...) • no smoothness criterion
Neighbourhood (MAP)	• a priori information with neighbours • less data required	• possibly computationally heavy and time consuming • reconstruction quality depends on terrain slope

Table 3.2. Advantages and drawbacks of the different multi-channel approaches.

analysis of the reconstruction accuracy achieved by the MLE and MAP approaches. Briefly, the accuracy of the MLE depends clearly on the number of images and their baseline configuration. By way of contrast, MAP has difficulties to reconstruct strong slopes.

The MLE can take place in ground range (i.e. include a geocoding part) to directly fuse ascending and descending interferometric data into a DEM (Eineder and Adam, 2005). However, this method is computationally expensive.

3.2 Absolute elevation extraction from SAR data

This section describes three alternative methods to PU that are able to retrieve absolute elevation from SAR data. First, radargrammetry, also applicable under interferometric conditions, is described more deeply since it is of special interest for this thesis. Then, split-band interferometry is shortly explained as it resembles to multi-frequency interferometry previously exposed. Finally, a totally different approach, clinometry or shape-from-shading is briefly mentioned.

3.2.1 Radargrammetry and interferometric stereo-radargrammetry

Quoting Leberl (1990), radargrammetry is *"the technology of extracting geometric object information from radar images"*. Since two images taken from different angles exhibit differences due to the relief and the parallax, height information can be derived by matching the two images. It is the SAR equivalent of photogrammetry in optical imagery and has been largely developed by Leberl et al. (1986); Leberl (1990).

3.2.1.1 Radargrammetry as a SAR stereoscopic method

Stereoscopic methods have been first employed on radar images with the aim of reconstructing terrain elevation by La Prade (1963). From the 1980s on, radargrammetry has been applied to spaceborne SAR systems (Leberl et al., 1986; Toutin, 1995). Toutin and Gray (2000) provide a precise historical overview. More recently, stereo-radargrammetry has been studied with high resolution sensors like RADARSAT-2 (Toutin, 2010) or TerraSAR-X (Raggam et al., 2010) to determine buildings height (Soergel et al., 2009; Dubois et al., 2013) or ships velocity (Duque et al., 2014).

Technique for terrain reconstruction A stereoscopic configuration is similar to the interferometric one but is characterised by a much larger baseline (few hundred kilometres in comparison to only several hundred metres in InSAR, see Fig. 3.4). The sensors A_1 and A_2 form a stereo pair and their *convergence angle* $\Delta\theta_s = \theta_1 - \theta_2$ increases with the baseline B. The displacement due to the different projections of the target P of height h on the ground leads to the terrain induced *stereo-parallax* Δx (assuming a flat Earth for simplification). Δx is the

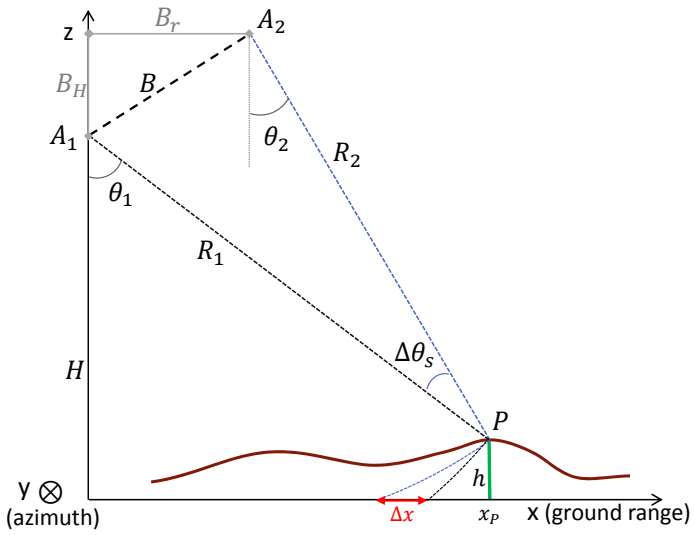

Fig. 3.4. Stereo-radargrammetric acquisition geometry: Δx is the displacement in ground range or shift due to the parallax i.e. the difference between the two projections of the target P with height h on the ground observed by two sensors at different positions.

key to reconstruct the terrain. Δx and $\Delta\theta_s$ play an important role regarding the quality and the accuracy of the terrain reconstruction. Shifts or disparities Δx are usually estimated on detected images (i.e. ground range geometry). Furthermore, shifts accuracy depends strongly on image content.

The key of radargrammetry is to match two radar images by a *registration* process, which aligns the two images viewed from different positions (like in InSAR). The matching of grey-level images is commonly performed using the normalised cross-correlation coefficient (Leberl et al., 1994), the sum of mean normalised absolute difference (Ramapriyan et al., 1986) or alternatively with edge-based matching methods (Méric et al., 2009). Ground response can however vary significantly depending on the illumination angle (contrary to optical systems) and might cause mismatching. Finally, absolute heights are recovered from Δx by means of equations describing the geometry of the flight paths (Leberl, 1990; Méric et al., 2009).

Limits Typical side-looking SAR systems enable only two acquisition configurations (assuming parallel trajectories): both images are taken either from the same side of a scene or from opposite sides. The opposite side stereo configuration allows theoretically better accuracy thanks to the larger baseline providing a higher parallax (Leberl, 1979; Toutin, 1996). However, the stereoscopic angle is de facto wide so that illumination differs strongly and occlusions may appear making the feature matching more complicated. A compromise has to be reached between a better stereo-viewing (small radiometric differences) and a more accurate elevation determination (large parallax). Usually, the same-side acquisition configuration is adopted. Mismatching remains the most significant source of height errors in the reconstructed DEM. Last but not least, ground control points are essential to correct the geometric model of the terrain in order to obtain a reliable DEM.

3.2.1.2 Stereo-radargrammetry applied in an interferometric configuration

The main difference between the interferometric and the (same-side) radargrammetric configurations is the baseline length. In fact, radargrammetric baselines are much larger than the critical interferometric one. An interferometric pair can still be seen from the geometrical point of view as a stereo pair with a very small convergence angle. Another similarity arises during data processing: the coregistration. In radargrammetry, coregistration shifts are geometrically transformed to terrain heights and allow to reconstitute the DEM. As for InSAR, a good coregistration is absolutely required to build an accurate and coherent interferogram without

knowing the target height. Relying on these similitudes, one could think about applying stereo-radargrammetry in an InSAR configuration but is it possible or is the accuracy high enough?

Radargrammetry and InSAR work at different scales. Typical viewing angle differences vary from 5° to 45° in radargrammetry whereas in InSAR, even with a baseline in the order of the critical one, the convergence angle is usually narrower than 1°. The shifts of the image contents between both SAR images are consequently much smaller. Bamler and Eineder (2005) showed that the scale difference between InSAR and radargrammetry is given by the ratio f_0/W_R where W_R is the range (or chirp) bandwidth and f_0 the carrier frequency. TerraSAR-X and TanDEM-X offer ratios of 32 to 100 (W_R = 100 MHz for standard StripMap mode and up to 300 MHz for High-Resolution Spotlight, in X-band with f_0 = 9.65 GHz). As a matter of fact, it is now possible to take advantage of the absolute stereo-radargrammetric measurement to support InSAR in the ambiguity resolution. Moreover, DEMs can be generated following a stereo-radargrammetric approach in an interferometric configuration. An advantage is that the coherent signatures (i.e. speckle and phase) can be used to estimate the shifts. For this reason, the achievable accuracy is much higher than in the radargrammetric case (no image contrast is required). Bamler (2000) introduced the term *interferometric stereo-radargrammetry* because partially coherent complex signals are used to estimate the shifts merging interferometry and stereo-radargrammetry.

Principle Parallactic shifts computed during the coregistration are a measure of the timing differences between both images. Considering that the active satellite sees a target P at $\tau_{P,1} = 2R_{P,1}/c_0$ and the passive one sees it at $\tau_{P,2} = (R_{P,1} + R_{P,2})/c_0$ (bistatic mode), the shifts in slant range $\Delta\chi$ can be written as:

$$\Delta\chi = ((\tau_{P,2} - \tau_{0,2}) - (\tau_{P,1} - \tau_{0,1}))\, f_{\mathrm{RS}} \tag{3.11}$$

where $\tau_{0,1}$ and $\tau_{0,2}$ are the active and passive images reference times and f_{RS} the range sampling frequency. As described in section 2.1.2, the absolute interferometric phase ϕ (eq. (2.3)) is proportional to the slant range difference i.e. to the time delay between both acquisitions:

$$\phi = 2\pi f_0 \Delta\tau_P \tag{3.12}$$

with $\Delta\tau_P = \tau_{P,2} - \tau_{P,1}$. The so-called *stereo-radargrammetric phase* ϕ_{rdgr} is thus:

$$\phi_{\mathrm{rdgr}} = 2\pi f_0 \left(\frac{\Delta\chi}{f_{\mathrm{RS}}} + \Delta\tau_0 \right) \tag{3.13}$$

with $\Delta\tau_0 = \tau_{0,2} - \tau_{0,1}$. It represents the absolute phase retrieved from the stereo-parallaxes.

Coregistration shifts are found using correlation techniques. Existing algorithms are the residual delay estimation from Madsen (1995), speckle tracking from Gray et al. (1998) (specially used for glacier monitoring). Yague-Martinez et al. (2010a) proposed a method which combined both coherent and incoherent cross-correlation to calculate highly precise shifts for the TanDEM-X mission (TDM) (see appendix B.3.2).

Accuracy of the stereo-radargrammetry In the coherent cross-correlation, both the amplitude and the terrain compensated phase are used. On the other hand, incoherent cross-correlation, also known as speckle tracking, correlates only the (detected) amplitude of the signal, discarding the phase information. For this reason, incoherent cross-correlation is a sub-optimum. Bamler (2000); Bamler and Eineder (2005) evaluated and compared the performance of the coherent and incoherent cross-correlations.

It is known that the complex or coherent cross-correlation between images is optimal in the case of Gaussian signals. In other words, if distributed correlated circular Gaussian scatterers

are assumed, maximising the complex cross-correlation between images produces the best estimate (maximum likelihood) for differential shifts. Bamler (2000) demonstrated that the error standard deviation (CRLB) of the shifts $\sigma_{\Delta\chi_{cc}}$ for homogeneous patches is:

$$\sigma_{\Delta\chi_{cc}} = \sqrt{\frac{3}{2N_c}} \frac{\sqrt{1-\gamma^2}}{\pi\gamma} osf^{3/2} \tag{3.14}$$

in units of resolution elements, where 'cc' stands for coherent cross-correlation, N_c is the number of samples in the estimation window and osf the oversampling factor (depicted in green in Fig. 3.5 for $osf = 1$). To compute a correct estimate, systematic non-noise phase differences (such as topographical fringes) have to be removed carefully.

Incoherent cross-correlation accuracy is worse because it depends only on the presence of coherent speckle or features in the patches (even if it is also more robust because it is not affected by possible significant errors in the phase). De Zan (2014) found out that the error deviation of the incoherent shifts $\sigma_{\Delta\chi_{ic}}$ under the assumption of homogeneous patches is:

$$\sigma_{\Delta\chi_{ic}} = \sqrt{\frac{3}{10N_c}} \frac{\sqrt{2+5\gamma^2-7\gamma^4}}{\pi\gamma^2} osf^{3/2} \tag{3.15}$$

where 'ic' stands for incoherent cross-correlation (displayed in purple in Fig. 3.5). Note that before computing incoherent cross-correlation, intensity images have to be oversampled by a factor 2.

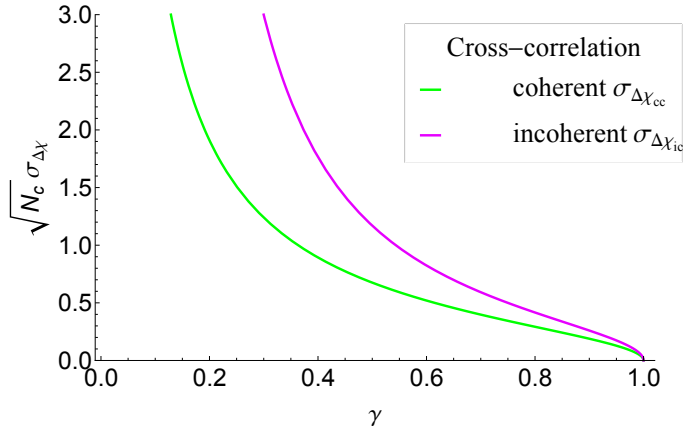

Fig. 3.5. Normalised error of the coherent and incoherent shifts estimations $\sqrt{N_c}\sigma_{\Delta\chi_{cc}}$ and $\sqrt{N_c}\sigma_{\Delta\chi_{ic}}$ respectively in green and purple (with $osf = 1$).

Application: absolute phase offset retrieval A critical stage of an interferometric chain is the absolute phase retrieval once the phase has been unwrapped. Stereo-radargrammetry offers a possibility to find out this offset without the help of external data. Usually, at least one reference point with known position and recognisable in the radar image is necessary to determine this phase offset. It can be also obtained with a reference DEM (used for SRTM mission, Rabus et al. (2003)). A last solution when no external data is available, is to match DEMs from crossing orbits (Rabus et al., 2003).

Comparing eq. (2.17) giving the absolute interferometric phase after PU and eq. (3.13), the absolute phase offset is calculated as follows:

$$2\pi\hat{k}_{\text{off}} = 2\pi f_0 \left(\frac{\Delta\chi}{f_{\text{RS}}} + \Delta\tau_0 \right) - \left(\psi + 2\hat{k}_{\text{PU}}\pi \right) \tag{3.16}$$

Madsen (1995) proposed to compare the interferometric and the stereo-radargrammetric measurements with its *residual delay method*. The absolute phase offset is found by correlating the

master image with the slave image previously resampled with the unwrapped phase. It leads to a biased phase offset estimate in the presence of phase unwrapping errors. In the framework of the TanDEM-X mission, both stereo-radargrammetric and unwrapped interferometric phases are compared in a single step since the coregistration achieves a sufficient accuracy (Rossi et al., 2012) (see section 4.2.2 and appendices B.3.2 and B.3.5 for the technical details of the Integrated TanDEM-X Processor (ITP) implementation). In order to solve the absolute phase offset, the shift estimation accuracy must be smaller than half the wavelength or smaller than $\lambda/2\rho_r = W_R/f_0$ in units of resolution cells where ρ_r is the range resolution (Bamler and Eineder, 2005). It means that the standard deviation $\sigma_{\Delta\chi}$ must be smaller than one third of a phase cycle (supposing Gaussian distribution of the shifts, 99% of the possible values are inside $\pm 3\sigma_{\Delta\chi}$). Thus, the required standard deviation is:

$$\sigma_{\Delta\chi} \leqslant \frac{W_R}{3f_0} \tag{3.17}$$

i.e. about 1/300 of a range resolution for TanDEM-X standard DEM acquisitions. Section 4.2.2 and section B.3.5.3 give a detailed analysis of the accuracy of the interferometric stereo-radargrammetry in for TanDEM-X DEM acquisitions.

3.2.2 Split-band interferometry

Split-band interferometry utilises the carrier frequency dependence of the interferometric phase. The absolute interferometric phase is retrieved using the frequency diversity provided by sub-bands within a wide bandwidth.

In the *Delta-k* method (Madsen and Zebker, 1992; Madsen et al., 1993; Madsen, 1995), the available range bandwidth is subdivided into two bands providing two slightly different interferograms. They can be seen as interferograms acquired at frequencies f_1 and f_2 (see Fig. 3.6).

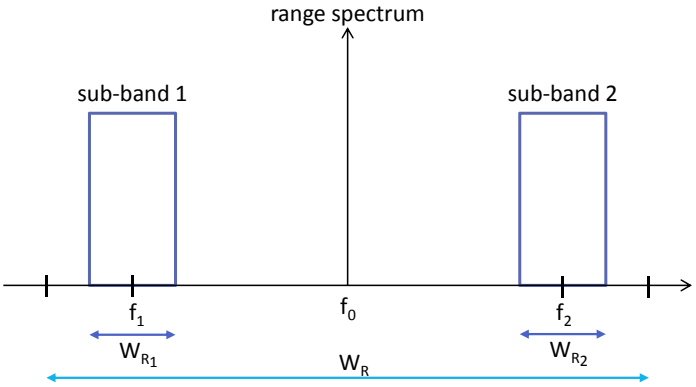

Fig. 3.6. Delta-k method: the received signals are filtered bandpass to have non-overlapping lower and upper sub-bands with bandwidth W_{R_1} and W_{R_2} centred in f_1 and f_2 respectively.

The idea is to exploit the small wavelength dispersion within the range bandwidth to determine the absolute phase constant of an interferogram. This is a similar concept as these presented in section 3.1.2 but in the frequency domain so that only one interferogram is required. The phase difference of the two interferograms corresponds to third interferogram obtained with a system having a carrier frequency which is the difference between the two band centres $f_s = f_2 - f_1$ (Brcic et al., 2009). Since f_s is low, phase unwrapping occurs less frequently. Indeed, the HoA of the obtained differential interferogram is:

$$h^s_{2\pi} = \frac{f_0}{f_2 - f_1} h_{2\pi} \tag{3.18}$$

where $h_{2\pi}$ is the HoA of the full band interferogram. The ambiguity problem is considerably reduced and allows absolute ranging estimation (Ulander and Frolind, 1998). The centre frequencies of the two sub-bands must be chosen carefully since the smaller f_s the more increased is the ambiguity but at the same time, the noise too and the resolution decreased. A trade-off has to be found.

Both the phase of a sub-band and the phase of the differential interferogram, which however contains more noise, can be inputs to an estimation algorithm to recover the absolute phase. Statistical multi-frequency techniques presented in section 3.1.3 and Delta-k both use frequency diversity. However, Delta-k is model free whereas statistical multi-frequency methods use the phase distribution as a model so that their results depend on the correctness of this model.

3.2.3 Radarclinometry

Radarclinometry, called shape-from-shading in the robot vision community, is rather an unknown technique. Its aim is also to reconstruct the relief. Shading is the variation of the brightness in an image resulting from the different reflection because of the various orientations of the surface. In this way, radarclinometry uses shade, shadows and occluded areas to retrieve terrain elevation from a single image. The principle is simple: it estimates the geometric parameters of the imaged ground pixel from the backscattered intensity (Wildey, 1986). However, its application to SAR is not trivial since it is sensitive to the reflective properties of the Earth's surface. Another problem is that shadow and layover regions are correctly reconstructed only if they are caused by vertical structures. As a result, radarclinometry is not able to render accurate heights but rather gives an idea of the relief. This technique is only used empirically when just one SAR image is available.

4 TanDEM-X multi-baseline interferometric data

Before designing a specific phase unwrapping (PU) algorithm for the TanDEM-X mission, it is essential to understand the peculiarities of the received interferometric data and the challenges stemming from them. Therefore, this chapter has two main objectives: 1) it describes the specifics of the TanDEM-X data and 2) it assesses the results of several state-of-the-art PU algorithms. The initial acquisition plan and the key parameters for the dual-/multi-baseline PU are described in the first part as well as the actual acquisition plan and its consequences on the acquired data. In the second part, data available from the interferometric processing by the ITP are introduced. Finally, several common challenging cases for PU are unwrapped with three algorithms from the literature and their results and deficits are discussed.

4.1 TDM acquisition plan and key parameters for the dual-/multi-baseline PU

The aim of the TanDEM-X mission is to generate a global high resolution DEM with a relative height accuracy of 2 m and a maximum absolute height error of 10 m (see appendix A [3]). To fulfil these requirements, a suitable acquisition plan has been conceived following different key parameters to enable dual/multi-baseline PU (see first subsection). However, due to the high volume decorrelation over dense forested areas, this strategy had to be adapted (described in the second subsection) affecting these various parameters (refer to the last subsection).

4.1.1 Original acquisition plan and resulting key parameters

According to initial performance analyses (Krieger et al., 2007), acquisitions with a HoA in the order of 30 to 40 m/cycle are necessary to achieve the expected relative height accuracy of the TanDEM-X DEM. However, such a HoA is likely to cause severe phase unwrapping problems, e.g. for steep terrain or trees. As a consequence, the whole landmass is mapped twice over two years with the same viewing geometry (i.e. incidence angle) but different baselines. The first global mapping has a higher HoA of around 45 to 50 m/cycle. The corresponding height noise is thus higher but the phase is easier to unwrap. The second coverage acquired with a larger baseline, has typically a lower height of ambiguity of about 30 to 35 m/cycle (thus approximately 0.7 times smaller than the first one) to reach the imposed relative height accuracy by combination of both data sets. The two global mappings are ideally separated by one year to avoid seasonal changes. Furthermore, second coverage acquisition beams are shifted by half a beam width compared to first coverage acquisitions. The mosaicked dataset exhibits then a more homogeneous signal-to-noise ratio (SNR) pattern (Bachmann et al., 2013). Table 4.1 summarises the main parameters, which constrain the design of the multi-baseline PU algorithm for the TanDEM-X mission.

Nonetheless, this acquisition plan, especially the shifted beams, implies several difficulties for the PU algorithm. First, every scene of the second mission phase is covered by two half scenes from the first coverage [4]. Second, overlapping data have different SNRs thus interferometric quality may vary dramatically. Last, there is a high temporal decorrelation between the SAR images of both acquisitions and possibly terrain changes due to the one year time span.

[3] Appendix A gives a complete description of the TanDEM-X mission. In particular, appendix A.3 reports the exact acquisition plan and appendix A.7 details the interferometric performance monitoring.

[4] The necessary special handling of the shifted acquisitions is described in appendix B.4

Typical number of acquisitions	2
First coverage acquisition HoA	$\sim 45 - 50$ m/cycle
Second coverage acquisition HoA	$\sim 30 - 35$ m/cycle
HoA ratio ($\frac{\text{second coverage}}{\text{first coverage}}$)	~ 0.7
Acquisition type	bistatic
Time span between acquisitions	~ 1 year
Spatial repartition	whole world
Amount of data	∼300,000 InSAR pairs

Table 4.1. Planned key parameters constraining the design of the dual-baseline phase unwrapping algorithm.

4.1.2 Adapted acquisition plan

Acquired interferograms suffered from strong volume decorrelation over dense forested areas especially when the tree height was in the order of the height of ambiguity (De Zan et al., 2013). Accordingly, the acquisition plan has been adjusted. Figures 4.1 and 4.2 depict on a global map, respectively the HoAs and coherences for the different mission phases i.e. for the first and second global coverages and for the additional acquisitions over dense forested and difficult terrain. Each dot represents one scene and corresponds to the average value of the HoA or the coherence over the whole scene.

The first global mapping has been performed with HoAs between 40 and up to 60-80 m/cycle depending on terrain and vegetation types. In this way, interferometric quality has been improved so that a better and more robust phase unwrapping is ensured. Besides, these latter regions as well as strongly varying forests and some difficult terrain have dedicated additional acquisitions with even higher HoAs (Martone et al., 2012). The range differences of the HoAs between the first global coverage and the additional acquisitions can be clearly observed in Figs. 4.1a and 4.1b as well as the resulting improved coherences in Figs. 4.2a and 4.2b. Finally, the second global coverage has also been adapted so that these identified difficult regions have a higher HoA (see Fig. 4.1c).

This thesis is focussed on the multi-baseline PU of the second global coverage data. The motivation is twofold: 1) this is the most challenging coverage and 2) it has to be processed operationally by default with multi-baseline PU (see appendix B). In this context, acquisitions of the first global mapping and the additional ones over dense forested and difficult terrain support the unwrapping of the second coverage. These interferometric data constitute the different channels for the multi-baseline PU. More specifically, data from the second coverage are called *master* data (typically of lower HoAs) and are indicated by the superscript m. The supporting data are referred as *slave* [5] and identified by the superscript s.

4.1.3 Impact on the key parameters

The different modifications of the acquisition plan lead the initially planned parameters listed in Table 4.1 to be dramatically affected (Lachaise et al., 2013). Among them, the HoA ratio and the time span between the interferograms are the most important parameters that are influenced.

[5] This designation has been chosen by analogy to InSAR processing where the slave SAR image has to be coregistered and resampled to the master one to build an interferogram. Here, the *slave* or supporting interferogram has to be coregistered to the *master* data (i.e. second coverage) so that they can be jointly used further on (see appendix B.4 for the procedure).

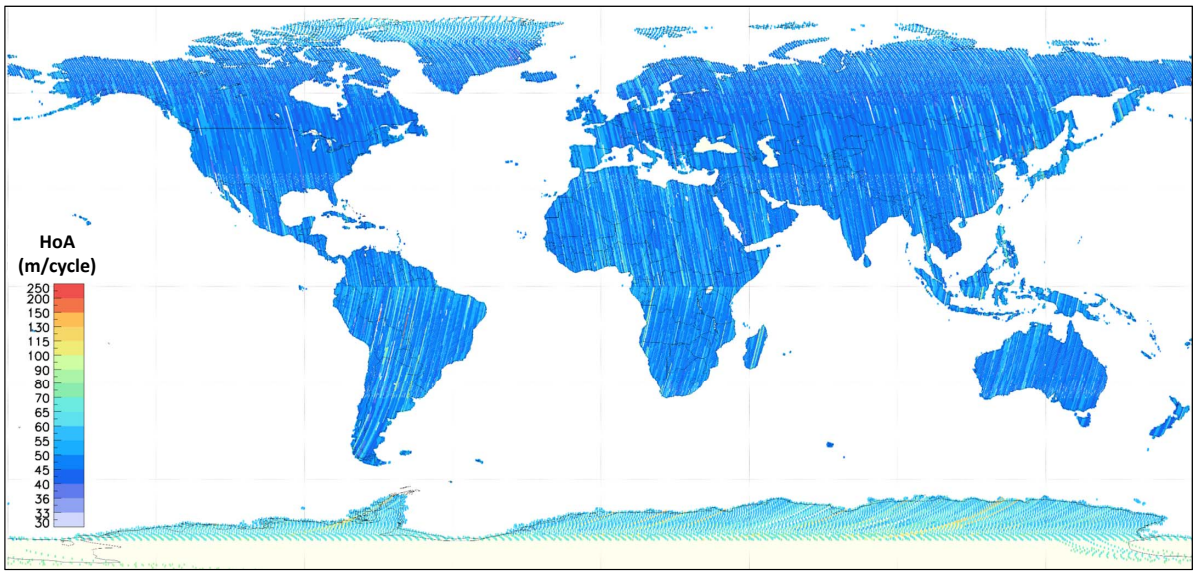

(a) First global coverage acquisitions (131,698 scenes acquired from end of December 2010 to March 2012)

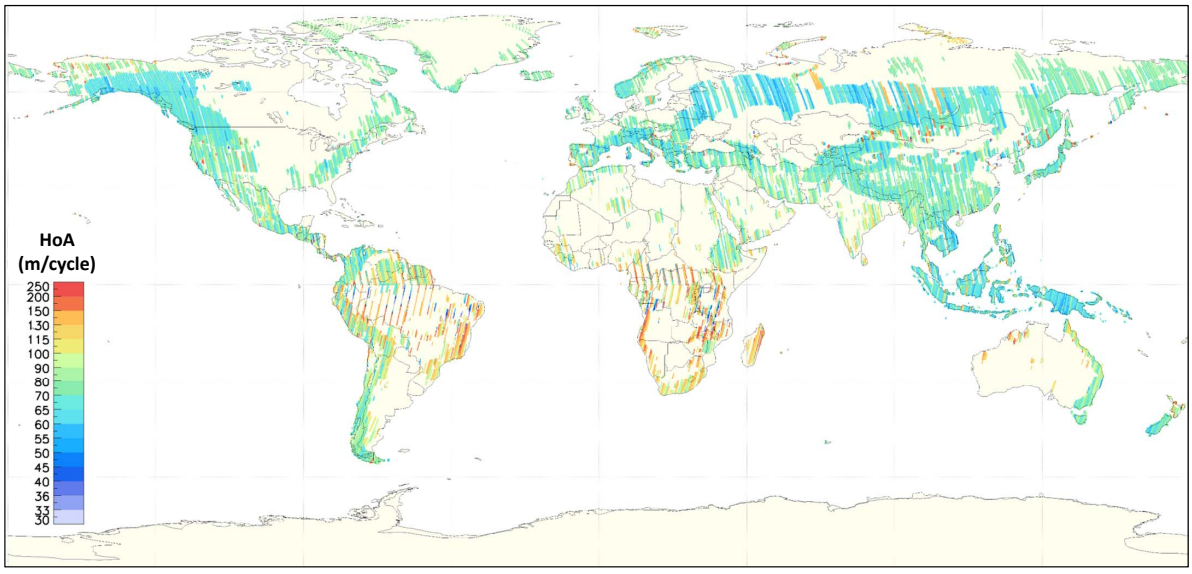

(b) Additional acquisitions over dense forested and difficult terrain (57,768 scenes acquired from April 2011 to March 2012)

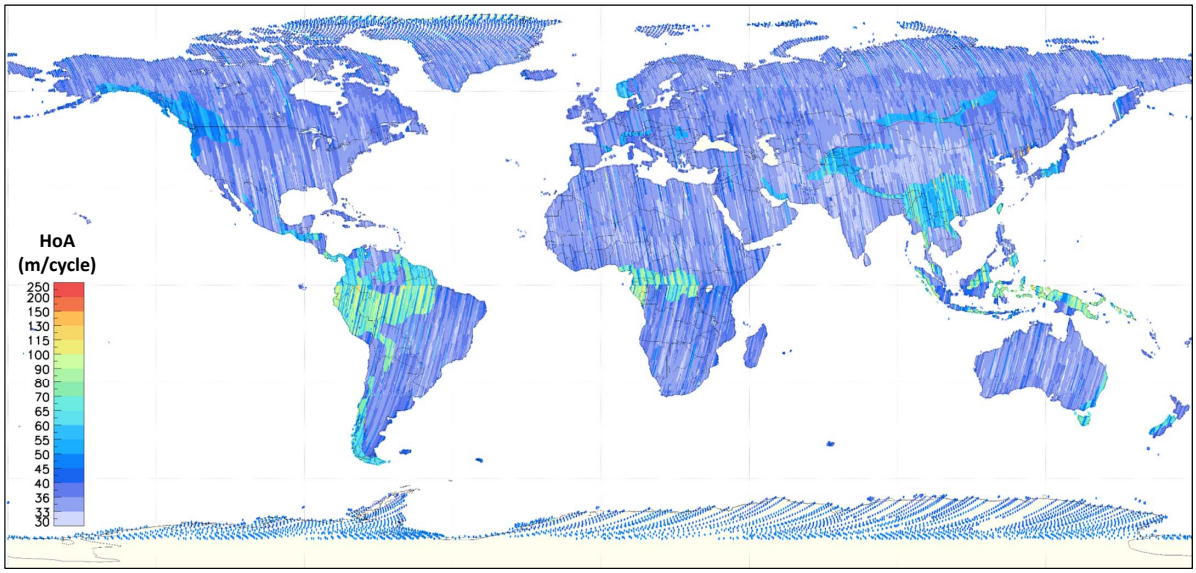

(c) Second global coverage acquisitions (142,716 scenes acquired from March 2012 to March 2013)

Fig. 4.1. Global maps of the heights of ambiguity (HoAs) for the different TanDEM-X coverages (data processed till 12/01/15). Each dot represents the average HoA over one scene.

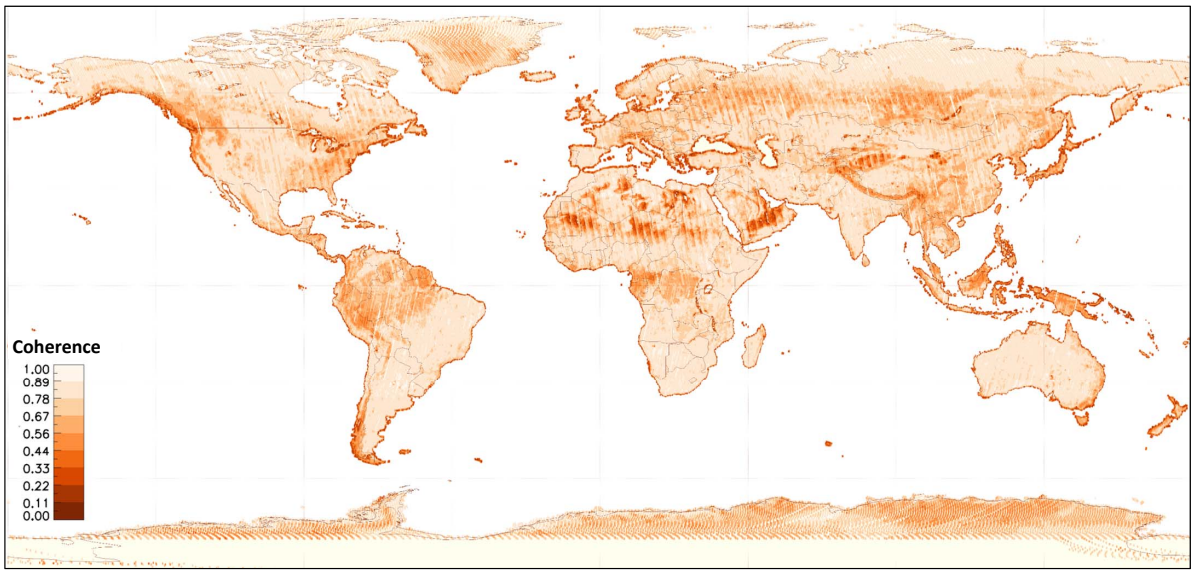

(a) First global coverage acquisitions (131,698 scenes acquired from end of December 2010 to March 2012)

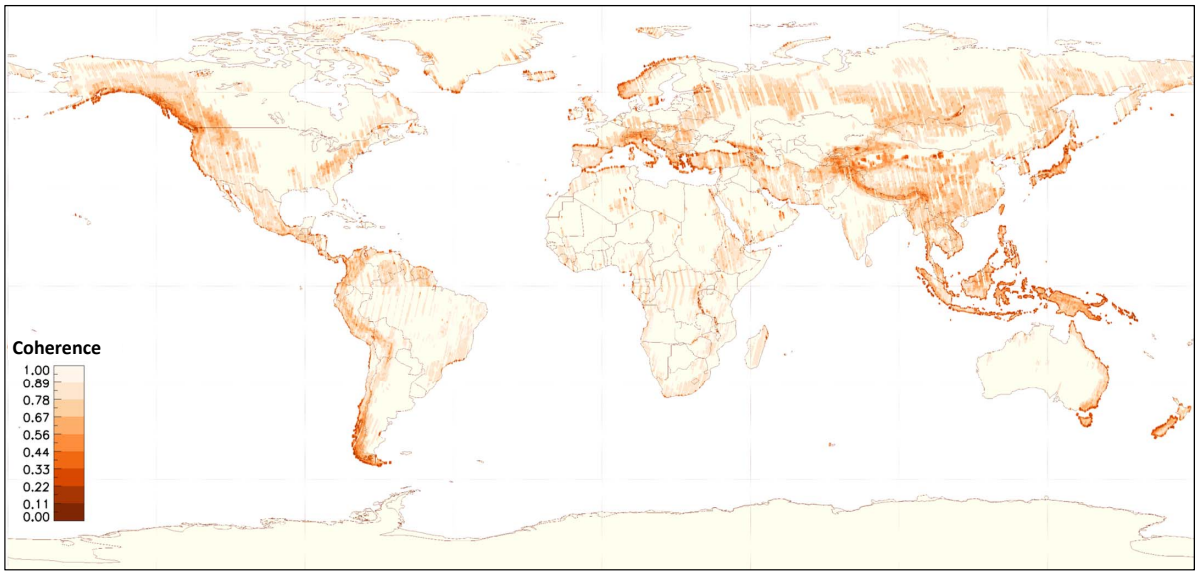

(b) Additional acquisitions over dense forested and difficult terrain (57,768 scenes acquired from April 2011 to March 2012)

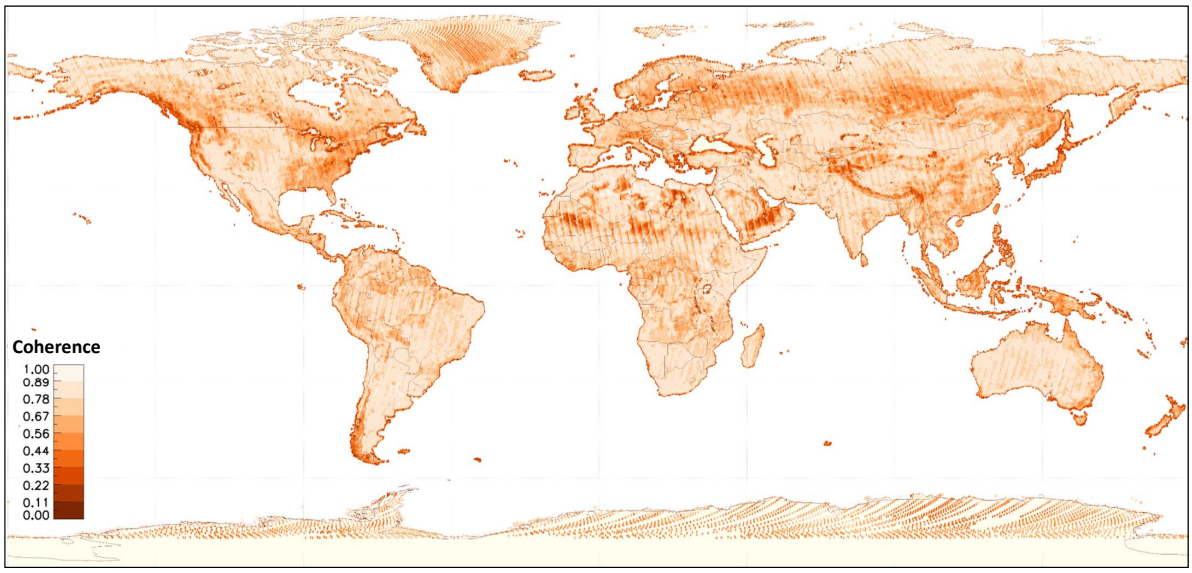

(c) Second global coverage acquisitions (142,716 scenes acquired from March 2012 to March 2013)

Fig. 4.2. Global maps of the coherence for the different TanDEM-X acquisition phases (data processed till 12/01/15). Each dot represents the average coherence over one scene.

4.1.3.1 Height of ambiguity (HoA)

The first consequence is that the range of heights of ambiguity (HoAs) is much wider than initially foreseen.

Figures 4.3a to 4.3c present the distributions of the HoAs ($h_{2\pi}$ given by eq. (2.7)) of the first, additional and second acquisitions. Most interferograms have a HoA lying within the initially planned ranges of about 45 to 50 m/cycle and 30 to 35 m/cycle for the first and the second coverages, respectively. Nevertheless, the histograms show a significant amount of scenes with HoAs higher than 50 m/cycle. Moreover, additional acquisitions have a completely different range (Fig. 4.3b). Figures 4.3d to 4.3f depict the joint distributions of HoAs and coherence for the three considered mission phases. They underline how both parameters are directly related and how coherence improves as the HoA increases (motivation of the acquisition plan adaptation).

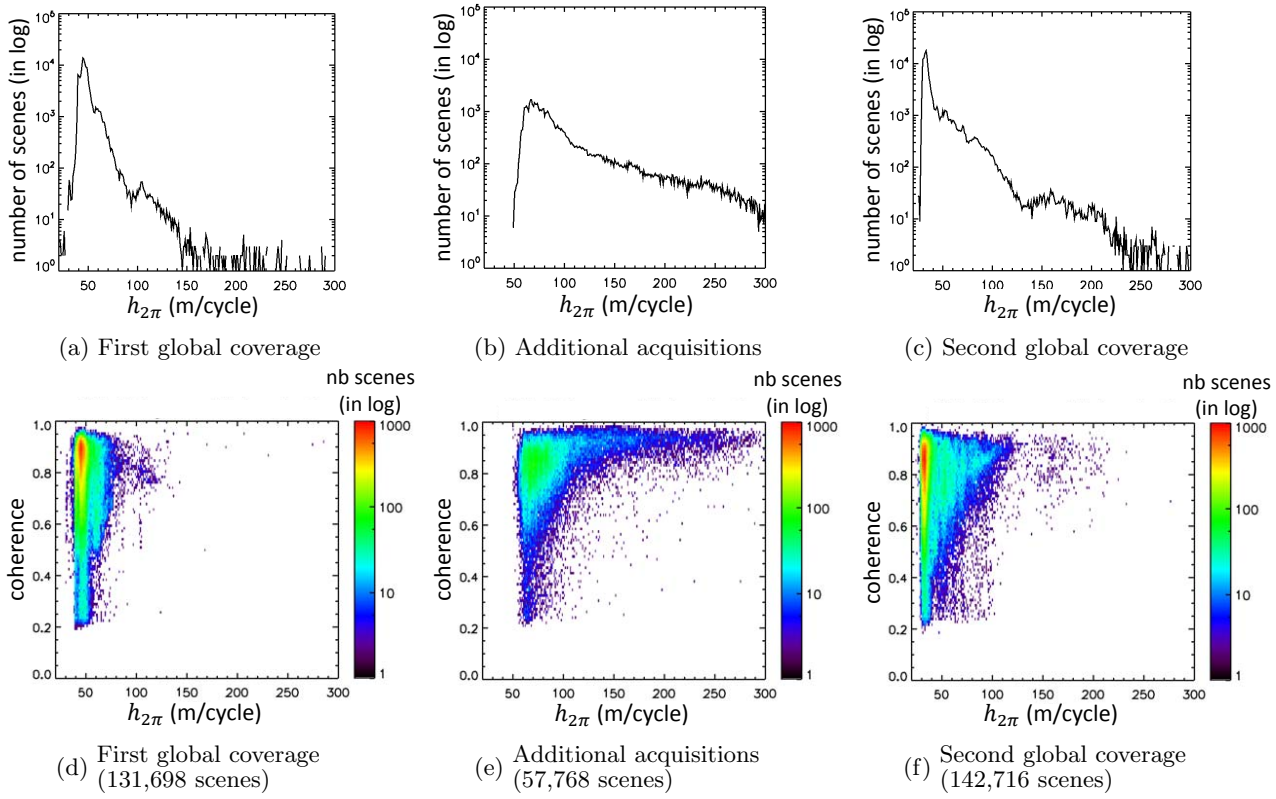

(a) First global coverage (b) Additional acquisitions (c) Second global coverage

(d) First global coverage (131,698 scenes) (e) Additional acquisitions (57,768 scenes) (f) Second global coverage (142,716 scenes)

Fig. 4.3. Distributions of the heights of ambiguity (HoAs) of the three acquisition phases of the TanDEM-X mission (top) and their joint distribution with the coherence (bottom). A significant amount of scenes have a HoA greater than 50 m/cycle. Moreover, the coherence improves as the HoA increases.

4.1.3.2 Height of ambiguity ratio (HoA) ratio

The HoA ratio μ is a crucial parameter for the multi-baseline PU. The latter is defined as the ratio of the *master* HoA $h^m_{2\pi}$ to the *slave* one $h^s_{2\pi}$ as follows:

$$\mu = \frac{h^m_{2\pi}}{h^s_{2\pi}} \tag{4.1}$$

The second year with lower HoAs being the reference, μ should be lower than 1. However, since the actual HoAs may take larger values, the HoA ratio may ultimately take every possible value (instead of being more or less a constant around 0.7).

Figure 4.4 displays the joint distributions of the *master* HoAs with respect to the supporting acquisitions HoAs (first row) and the resulting HoA ratios (second row). The supporting ac-

quisitions are the scenes acquired during the first coverage plus the additional ones. This figure proves that, even if the majority of data is well centred on the initially planned HoAs and μ, the diversity of combinations is non-negligible and is mainly due to the additional acquisitions.

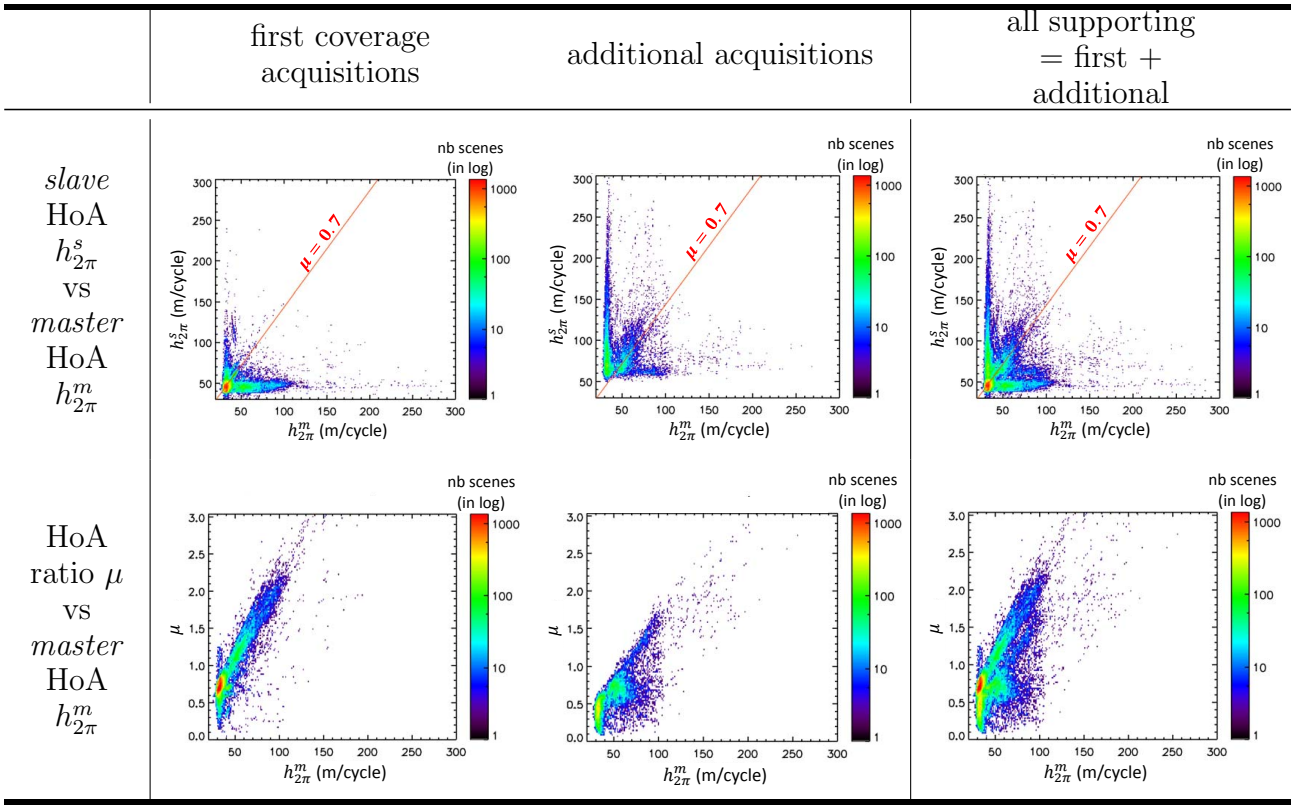

Fig. 4.4. Joint distributions of the *master* HoAs and (first row) *slave* HoAs and (second row) HoA ratios: from left to right, supporting scenes coming from the first coverage, additional acquisitions and both together. The straight line depicts $\mu = 0.7$. μ exhibits a large variation due to the higher HoAs and especially these of the additional acquisitions.

4.1.3.3 Time span between acquisitions

The season is an important factor for repeated acquisitions. Indeed, after one year, there is temporal decorrelation between the SAR images of the *master* and *slave* acquisitions but the interferograms should entail the same information if no topographic change occurred. If acquisitions took place at different seasons, natural changes (snow, ice, tree leaves, etc...) implying different penetration or height of the scattering centre, may affect not only the coherence but also the scene content. In this case, multi-baseline processing is not usable. Figure 4.5 displays the acquisition seasons on the global map for the different mission phases. Regions in the tropics do not suffer from seasonal changes so that acquisitions at different seasons are unproblematic (see for example the northern part of South America). On the other side, mountains, Siberia, Patagonia or the north west coast of North America are very likely to present seasonal changes.

4.2 Data from the ITP available for the dual-/multi-baseline PU

4.2.1 Overview

During the operational interferometric processing of the TanDEM-X images by the ITP (see appendix B), valuable information is provided. This may be helpful inputs for the multi-baseline phase unwrapping algorithm. Illustrated in Fig. 4.6, the different inputs are:

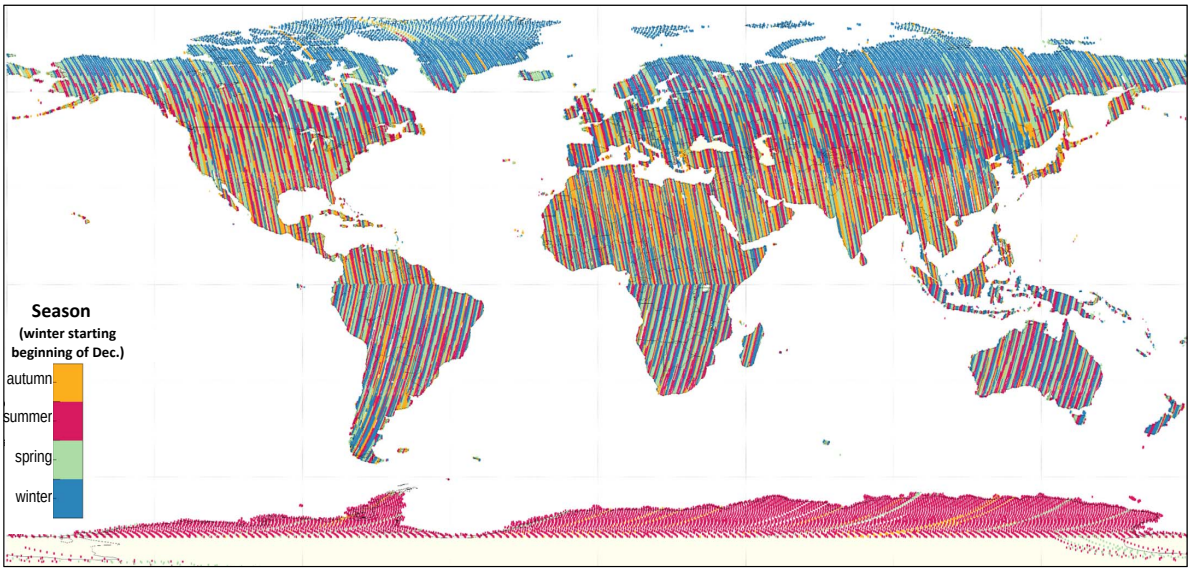

(a) First global coverage acquisitions (131,698 scenes acquired from end of December 2010 to March 2012)

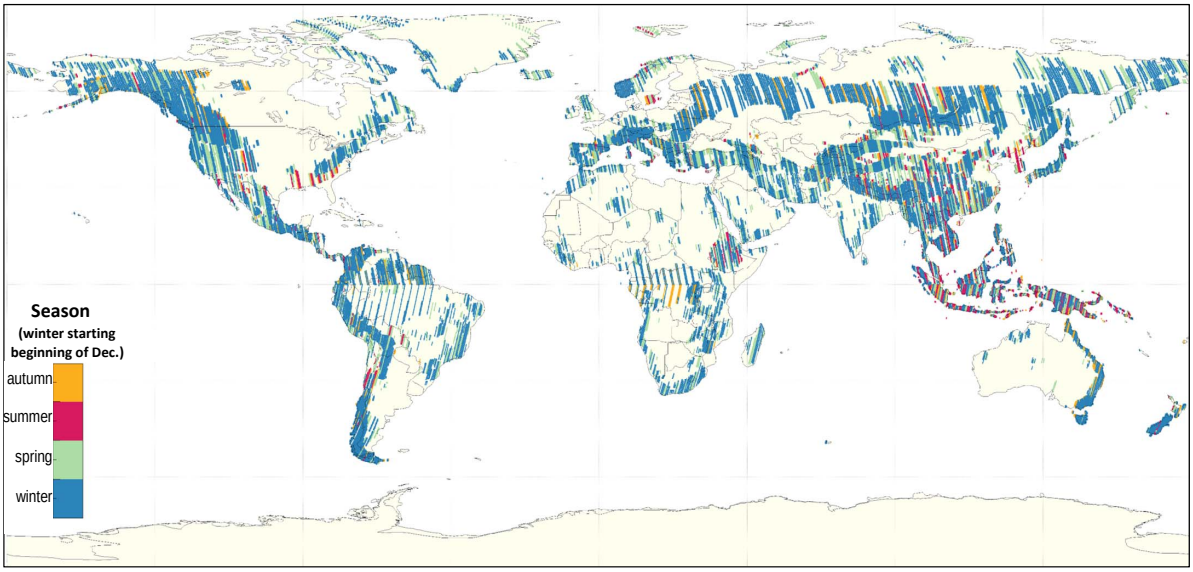

(b) Additional acquisitions over dense forested and difficult terrain (57,768 scenes acquired from April 2011 to March 2012)

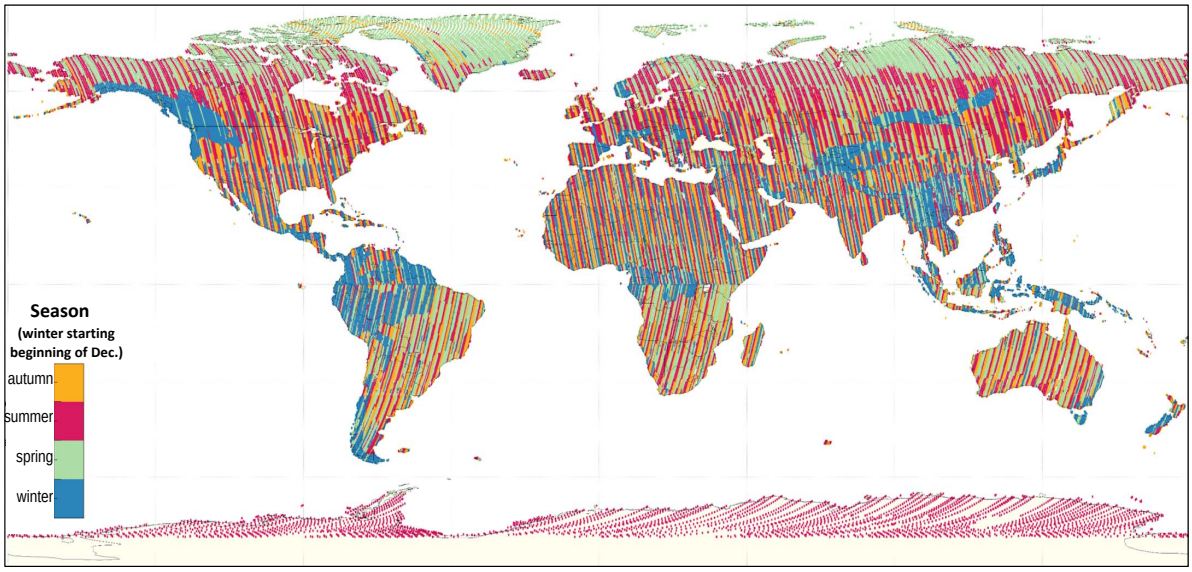

(c) Second global coverage acquisitions (142,716 scenes acquired from March 2012 to March 2013)

Fig. 4.5. Global maps of the acquisition season of the different TanDEM-X mission phases, seasons are given with reference to the Northern hemisphere and winter is considered starting beginning of December (data processed till 12/01/15).

- several interferograms, one *master* interferogram v^m and at least two partially overlapping *slave* interferograms v^s (shifted by half a swath width); their wrapped phases are denoted by ψ^m and ψ^s and their estimated unwrapped phases by $\hat{\phi}^m$ and $\hat{\phi}^s$,
- their coherences γ^m and γ^s,
- their heights of ambiguity (HoAs) $h^m_{2\pi}$ and $h^s_{2\pi}$,
- the so-called *stereo-radargrammetric phases* ϕ^m_{rdgr} and ϕ^s_{rdgr}, these are absolute measurements but have a coarse spatial resolution (about 13×13 down to 21×21 coarser, see section 4.2.2 and Table B.1).

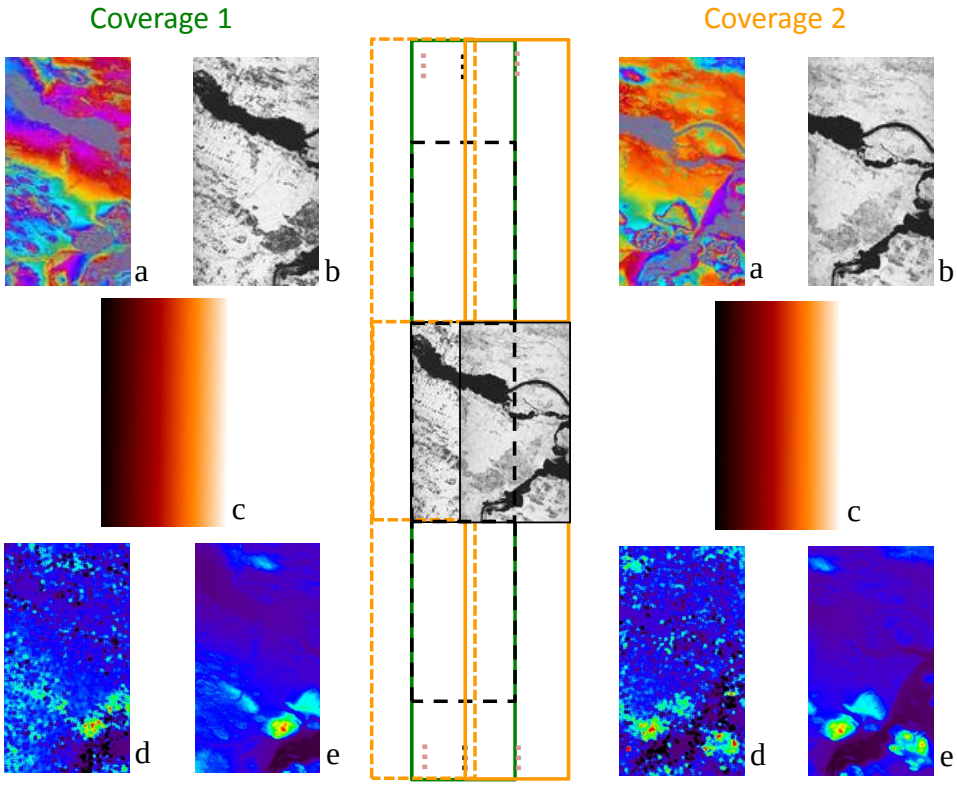

Fig. 4.6. Data from the Integrated TanDEM-X Processor (ITP) available for the dual-/multi-baseline phase unwrapping (PU): for every coverage, (a) the interferometric phase, (b) the coherence, (c) the HoA map, (d) the stereo-radargrammetric phase and (e) the simulated absolute phase from a reference DEM (SRTM or GLOBE) as a visual help.

4.2.2 Stereo-radargrammetric phase and PU quality ratio

The content of the two Synthetic Aperture Radar (SAR) images is locally shifted in the slant range direction from one image to the other as explained in section 3.2.1.2. This is the parallax due to the different viewing geometries. These shifts are proportional to the time delay between both acquisitions and consequently to the local height. Hence, they provide a coarsely sampled but absolute radargrametric DEM. The coregistration shifts are called *radargrammetric shifts* in this thesis and the phase derived from them, the *stereo-radargrammetric phase*.

The ITP coregistration reaches an accuracy sufficient to use the coregistration shifts to retrieve absolute phase offsets (see section 3.2.1.2) but also to evaluate phase unwrapping outcomes (refer to appendix B.3.5). Indeed, it is capable to segment the portion of the unwrapped phase that is not affected by errors. Additionally, it provides a convenient indicator namely the percentage of correctly unwrapped pixels (in the coarse shift matrices grid), the *phase unwrapping quality ratio* q_{ratio}. In this way, it enables quality control in a fully automatic way for the entire globe. Figure 4.8 illustrates on the global map the results of the single-baseline phase unwrapping (1B-PU) by way of the *PU quality ratio* for the different mission phases. The ITP considers that the 1B-PU is successful if $q_{\text{ratio}} > 0.97$. The scenes considered as correct according to this

threshold are depicted in green on the different maps. Other colours indicate scenes that are potentially subject to PU errors. However, since the radargrammetric phase is of lower resolution and noisy, small PU errors or the finer boundaries of a PU error are not detectable.

Shifts are estimated by means of the coherent cross-correlation. Incoherent cross-correlation is a fall-back solution when the first estimate is not reliable or the coherence is too low (see appendix B.3.2). Their accuracies $\sigma_{\Delta\chi_{cc}}$ and $\sigma_{\Delta\chi_{ic}}$ are given respectively by eq. (3.14) from Bamler and Eineder (2005) and eq. (3.15) from De Zan (2014). $\sigma_{\Delta\chi_{cc}}$ is the CRLB and depends only on the coherence and the size of the estimation window N_c. Figure 4.7 depicts the shift estimation errors for the ITP configuration i.e. $N_c = 1,024$ and $osf = f_{\mathrm{RS}}/W_R = 1.1$. Following eq. (3.17), an accuracy of the coregistration shifts better than 1/300 of a pixel is required to have $3\sigma_{\Delta\chi}$ and 1/100 for only one sigma (Rossi et al., 2012). These are obtained respectively for a coherence greater than 0.95 and 0.8 for coherent cross-correlation and only for coherences close to 1.0 for speckle tracking. For lower coherences, PU errors cannot be detected for an individual patch. Furthermore, the CRLB, given by eq. (3.14), is valid for uniform patches i.e. for flat terrain. It implies that the topographic phase has to be removed perfectly from the data. Residual artefacts or non-Gaussian scatterers degrade the accuracy. To determine the absolute phase offset, several thousands of patches are averaged allowing to reach a sufficient accuracy (see Fig. B.4b). If PU errors happen, several local phase offsets appear. Their accuracy is lower because of the reduced number of patches to average. The phase unwrapping check and a possible a fortiori correction is not possible pixel-wise. However, the coarse PU error detection is reliable for scene exhibiting a good coherence.

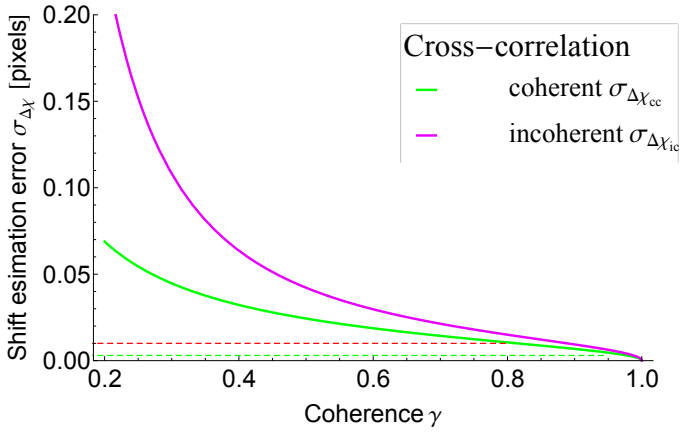

Fig. 4.7. Error of the shift estimation of one patch in pixels using coherent $\sigma_{\Delta\chi_{cc}}$ (green) and incoherent $\sigma_{\Delta\chi_{ic}}$ (purple) cross-correlation for $N_c = 1,024$ pixels and $osf = 1.1$.

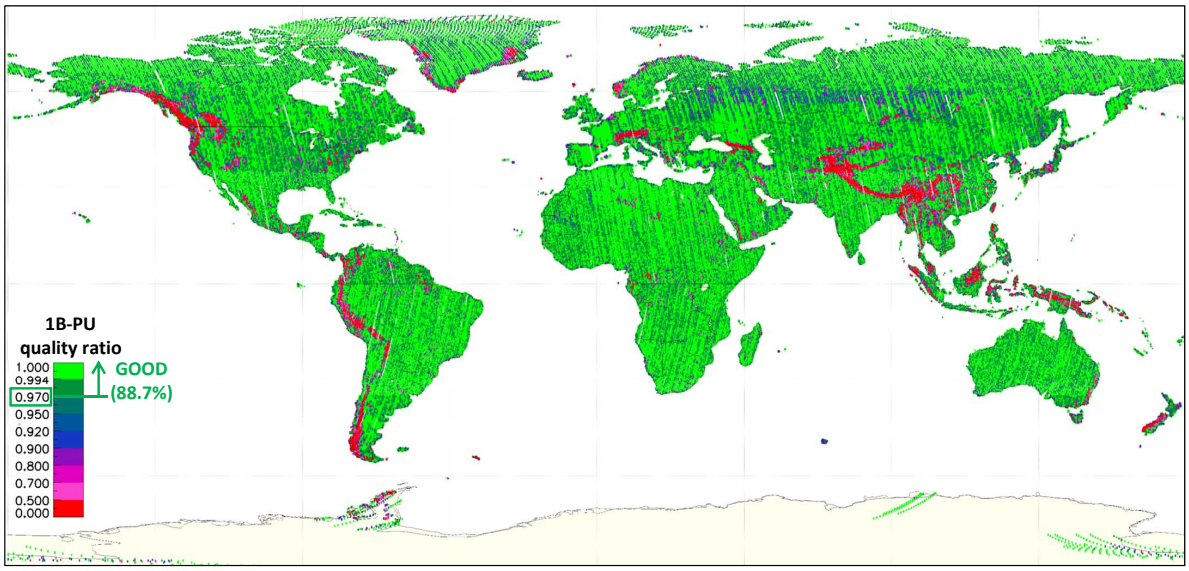

(a) First global coverage acquisitions (131,698 scenes acquired from end of December 2010 to March 2012)

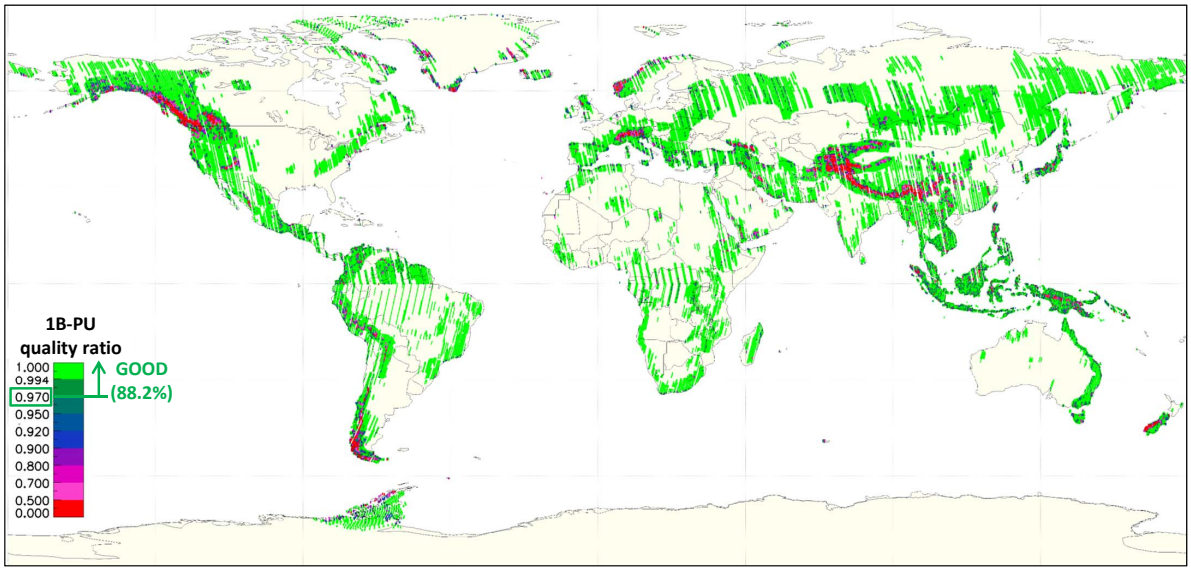

(b) Additional acquisitions over dense forested and difficult terrain (57,768 scenes acquired from April 2011 to March 2012)

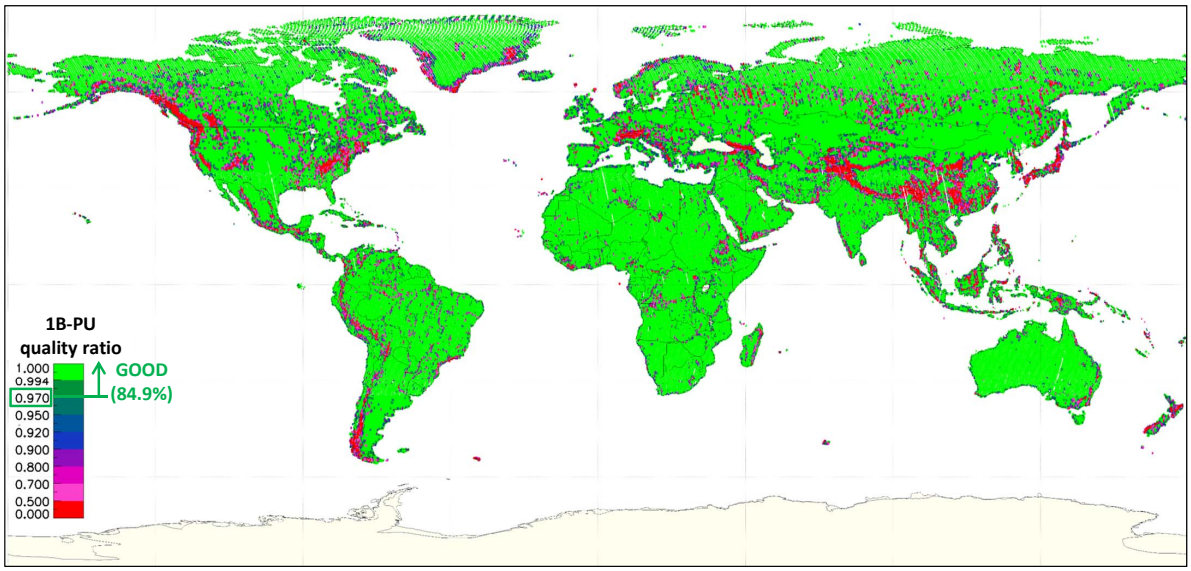

(c) Second global coverage acquisitions (142,716 scenes acquired from March 2012 to March 2013)

Fig. 4.8. Global maps of single-baseline phase unwrapping (1B-PU) quality ratios (after unwrapping with MCF algorithm) of the different mission phases. The Integrated TanDEM-X Processor (ITP) considers that a ratio greater than 0.97 means success of the phase unwrapping. Other colours indicate scenes exhibiting potentially PU errors.

4.3 Performance of PU algorithms on TanDEM-X data

Three typical difficulties for phase unwrapping are addressed in this section: large waterbodies, high plain borders and mountainous terrain. They represent the noise, surface discontinuities and geometrical distortions issues. Different PU algorithms from the literature are applied to TanDEM-X interferometric data exhibiting these problems.

4.3.1 Investigated PU algorithms and assessment methodology

Since 1B-PU methods have well-known limits (see section 2.2.2), only results obtained by means of the MCF algorithm (Costantini, 1998) will be shown hereafter. It is a widely accepted algorithm, which Eineder et al.'s (1998) version was used for the SRTM mission and has been adopted in the operational ITP (see section 2.2.2.1 and appendix B.3.4). The other widespread algorithm, SNAPHU (Statistical-cost, Network-flow Algorithm for Phase Unwrapping from Chen and Zebker (2001)) used in the InSAR processors NEST and Doris [6], gives similar outcomes. The unwrapped phase is not absolute so that a global phase offset has to be retrieved in a second step.

Regarding multi-baseline methods, the pixel-wise MLE and the Maximum A Posteriori (MAP) approach using neighbourhood information proposed by Ferraioli et al. (2009) are investigated (see section 3.1.3). The assessed version of the MLE is the one proposed by Eineder and Adam (2005) that was transformed in order to work in slant range domain for the purpose of this thesis (Lachaise et al., 2007). The second algorithm uses neighbourhood information by means of the Total Variation and solves the MAP with graph-cuts (denoted Graph-Cuts Total Variation (GC-TV) in the following). The reconstructed unwrapped phases are absolute, hence a global offset hints inconsistencies (such as uncompensated offsets between interferograms arising from miscalibration). Likelihood functions need to be computed for all possible height values appearing within the scene. However, the height interval has to remain smaller than the unambiguous height stemming from the interferograms combination (approximated by the least common multiple of the rounded [7] HoAs). A compromise is to centre the search area around a reference DEM to restrain this interval. Although the results presented thereafter have been obtained on search intervals restricted through prior information coming from a reference DEM, the pixel-wise results will still be designated as estimated by the MLE.

Results are assessed qualitatively and statistically with respect to the SRTM DEM based on ambiguity discrepancies to reduce the impact of the resolution differences. The unwrapped phases recovered with the different algorithms are represented in slant range height along with the Absolute Ambiguity Deviation (AAD) map where the Ambiguity Deviation is defined as:

$$\mathrm{AD} = \left\lfloor \frac{\left(\phi_{\mathrm{Ref}} - \hat{\phi}^m\right) - \mathrm{median}\left(W\left(\phi_{\mathrm{Ref}} - \hat{\phi}^m\right)\right)}{2\pi} \right\rceil \tag{4.2}$$

where $\lfloor . \rceil$ is the round function to the nearest integer, $W(.)$ the wrapping operator, ϕ_{Ref} the SRTM DEM-derived unambiguous reference phase and $\hat{\phi}^m$ the estimated unwrapped phase of the *master* interferogram. $W\left(\phi_{\mathrm{Ref}} - \hat{\phi}^m\right)$ gives the fractional part of the offset.

The median AD is removed from MCF outputs to compensate the absolute phase offset. A systematic statistical analysis is provided based on

- the percentage of correctly unwrapped pixels $\%_{(\mathrm{AD}=0)}$,

[6] NEST is the Next ESA SAR Toolbox and Doris, the Delft object-oriented radar interferometric software

[7] A round number is a number that is the product of a considerable number of comparatively small factors. A positive integer n is sometimes said to be round if it has no prime factors greater than $\sqrt{n}$ (definition from WolframMathWorld).

- the mean $\overline{\mathrm{AD}}$,
- the standard deviation σ_{AD},
- the median m_{AD},
- the Normalised Median Absolute Deviation (NMAD).

The NMAD (Höhle and Höhle, 2009) is a robust estimate of the standard deviation and is defined by:

$$\mathrm{NMAD} = 1.4826 \times \mathrm{median}\left(|\mathrm{AD} - m_{\mathrm{AD}}|\right) \tag{4.3}$$

The following test sites are portions of TanDEM-X scenes chosen in the middle (in range direction) of the *master* interferogram where the supporting *slave* interferograms overlap to have three data sets. Performance evaluation is restricted to the pixels exhibiting a coherence higher than 0.25. Low coherence pixels are masked out in the different pictures.

4.3.2 Challenging case 1: large waterbodies

Large water surfaces and more generally, incoherent regions may cause parts of a scene to be isolated and to form *islands*. In this case, gradient-integration based algorithms are unable to unwrap the phase correctly since no path exists from one *island* to the other.

The selected scene is over the fjord near the Preikestolen, south-west of Norway. Figure 4.9 depicts its relief map and the reference slant range height from SRTM. The relief varying between 41 and 750 m, is smooth and not problematic (apart from the Preikestolen itself). The *master* scene is an additional acquisition with a high HoA of 113 m/cycle. The three wrapped phases and their respective coherence are represented in Fig. 4.10. The scene is split into three parts because of the water.

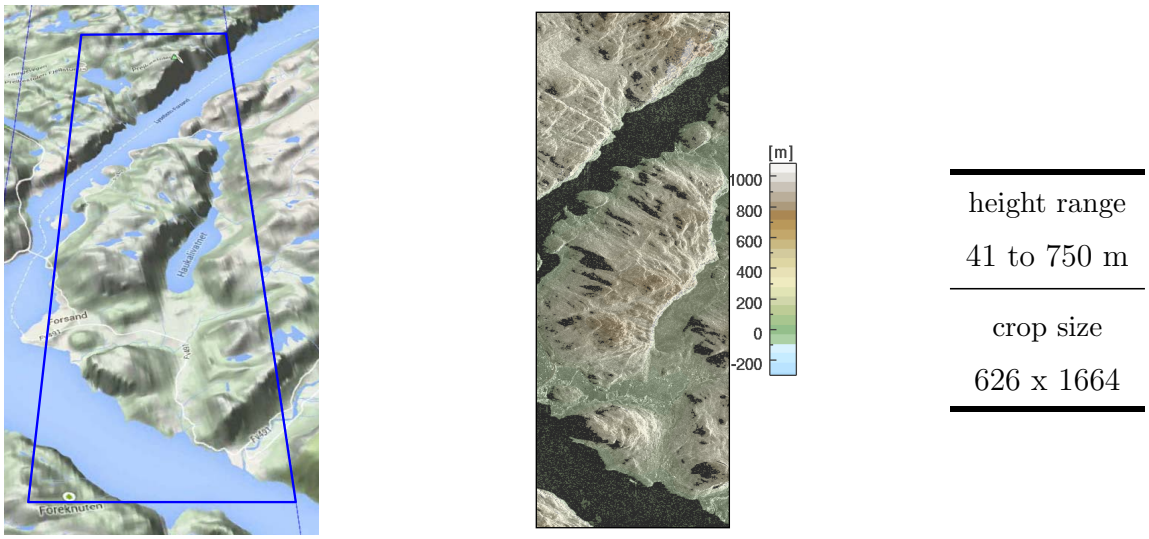

(a) Relief map (Google Maps) (b) Reference slant range height (SRTM)

Fig. 4.9. Relief map, reference height and height range for the test site of the Preikestolen region.

The MCF is the first investigated algorithm and its outcome is shown in Fig. 4.11. As expected, the water prevents it from performing properly ($\%_{(\mathrm{AD}=0)} \approx 69\%$ and NMAD=1.23).

To analyse the MLE and the GC-TV, it is necessary to determine the search interval. The height variation within the scene is 709 m $\approx 6 \times h_{2\pi}^{m}$ whereas the total unambiguous height is 13.2 km $\approx 117 \times h_{2\pi}^{m}$. The latter is not a constraint so that the search interval is fixed to 7 cycles i.e. $\pm$ 3 cycles around the reference height. Figure 4.12 presents the results of the two multi-baseline algorithms. The top of each image shows the results where only one supporting scene

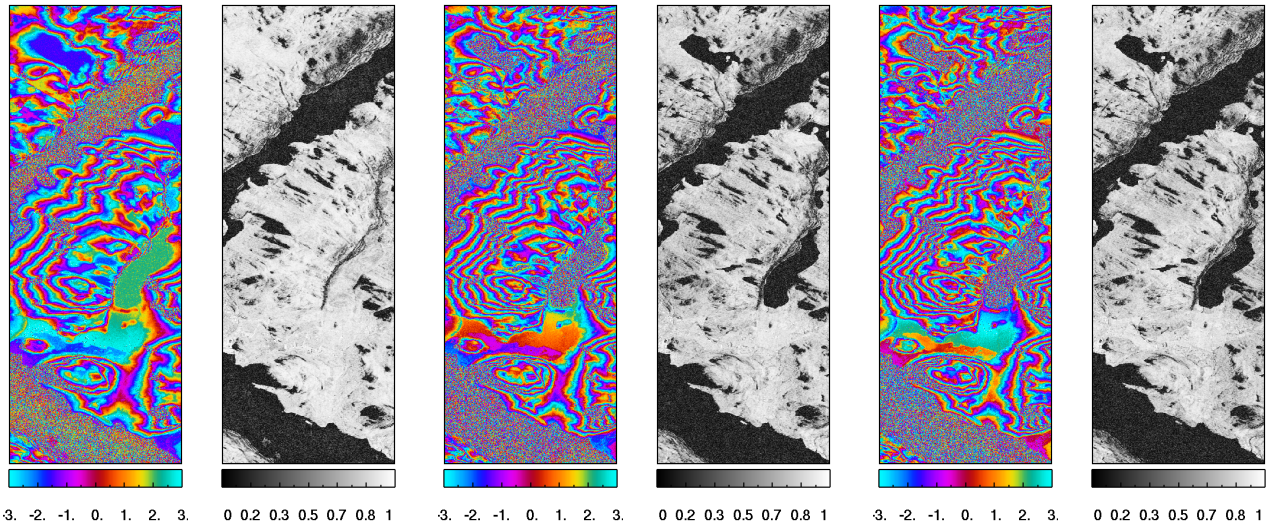

(a) ψ^m (b) γ^m (c) ψ^{s_1} (d) γ^{s_1} (e) ψ^{s_2} (f) γ^{s_2}

Fig. 4.10. Wrapped phases and coherences of the *master* and the two *slave* interferograms for the Preikestolen region. The respective HoAs are $h_{2\pi}^{m} = -113$ m/cycle, $h_{2\pi}^{s_1} = 81$ m/cycle and $h_{2\pi}^{s_2} = 76$ m/cycle. Average coherences (for $\gamma > 0.25$) are $\overline{\gamma^m} = 0.80$ (81% of the pixels), $\overline{\gamma^{s_1}} = 0.74$ (75% of the pixels) and $\overline{\gamma^{s_2}} = 0.73$ (75% of the pixels).

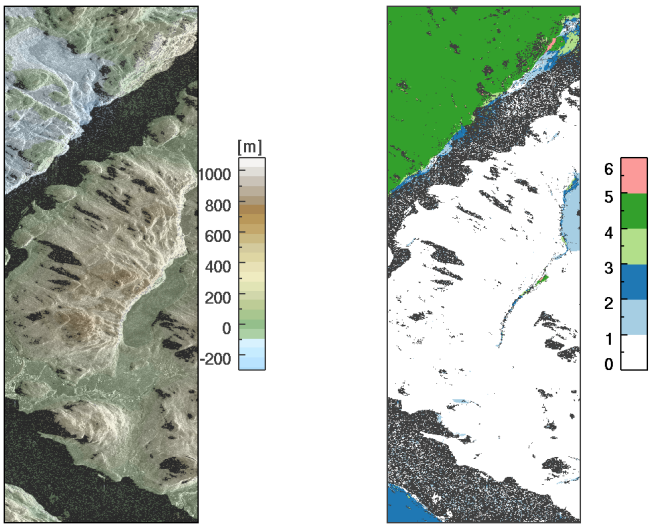

(a) Reconstructed slant range height (b) AAD map

$\%_{(\mathrm{AD}=0)}$	$\overline{\mathrm{AD}}$	σ_{AD}	m_{AD}	NMAD
69.65%	-0.96	1.73	-0.03	1.23

(c) Error measures (for $\gamma > 0.25$)

Fig. 4.11. MCF results for the Preikestolen region: (a) estimated *master* unwrapped phase converted to slant range height, (b) Absolute Ambiguity Deviation (AAD) map with respect to the reference DEM and (c) statistical assessment.

was used whereas the bottom depicts the outcomes with 2 supporting Coregistered Single-look Slant-range Complexes (CoSSCs) i.e. 3 scenes. The common case for the TanDEM-X mission (TDM) is to have only two interferograms. Table 4.2 summarises the different error measures.

The height has been estimated only every 9 metres (equivalent to 0.5 rad for the *master* interferogram) because of the size of the graph to optimise in the GC-TV (already 24 GB). Figures 4.12a and 4.12b have been estimated with the MLE on uncalibrated wrapped phases. The reconstructed absolute height exhibits an offset of several cycles and a slope over range due to the HoA variation (the GC-TV estimate, which is smoother, is not shown here). The offset depicted here ($m_{\mathrm{AD}} \approx -1$) is restricted by the limited search interval.

Figures 4.12c to 4.12f show the outputs of the MLE and the GC-TV when the different offsets have been compensated successfully. The unwrapped phases are offset free ($m_{\mathrm{AD}} \approx 0$). Only about 70% pixels ($\%_{(\mathrm{AD}=0)}$) have been successfully recovered with 2 scenes, which is comparable to the MCF results. However, no major PU error is visible, this poor result is due to the extremely noisy solution. With 2 supporting CoSSCs, more than 89% of the points agree with

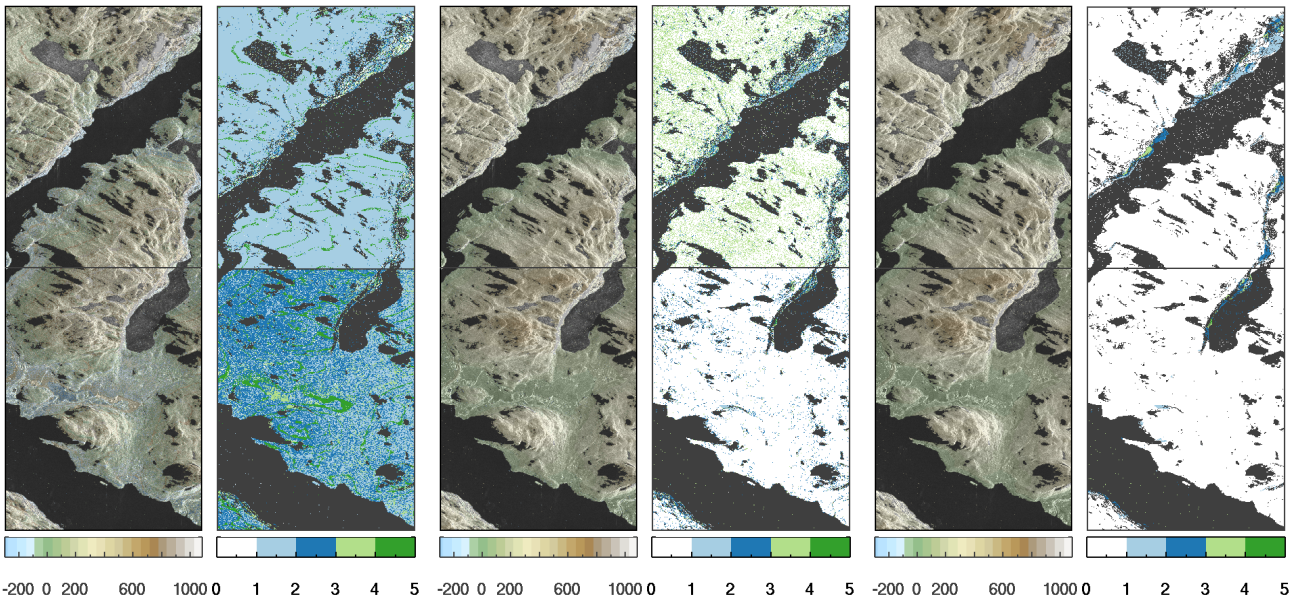

(a) MLE height (uncalibrated) (b) MLE AAD (uncalibrated) (c) MLE height (calibrated) (d) MLE AAD (calibrated) (e) GC-TV height (calibrated) (f) GC-TV AAD (calibrated)

Fig. 4.12. MLE and GC-TV results for the Preikestolen region with (top) two and (bottom) three scenes: pixel-wise estimation for (a-b) uncalibrated and (c-d) calibrated wrapped phases and (e-f) estimation using neighbourhood information for the calibrated wrapped phases. (a,c,e) reconstructed slant range height; (b,d,f) Absolute Ambiguity Deviation (AAD) map with respect to the reference DEM (search interval of ±3 cycles around the reference height, height increment is 9 m and $\lambda = 2.8$).

		MLE					GC-TV				
		$\%_{(AD=0)}$	$\overline{AD}$	σ_{AD}	m_{AD}	NMAD	$\%_{(AD=0)}$	$\overline{AD}$	σ_{AD}	m_{AD}	NMAD
1 CoSSC	Uncalibrated	1.46%	-0.48	1.28	-0.99	0.11	-	-	-	-	-
	Calibrated	70.46%	0.05	1.37	0.04	0.012	96.58%	0.018	0.29	0.005	0.07
2 CoSSCs	Uncalibrated	2.46%	-0.63	2.00	-1.08	1.36	0.40%	-1.62	0.72	-1.90	0.17
	Calibrated	89.36%	0.013	0.71	0.01	0.077	96.89%	0.069	0.35	0.02	0.07

Table 4.2. Summary of the performance of the MLE and GC-TV in terms of ambiguity deviation for the Preikestolen region with one and two supporting Coregistered Single-look Slant-range Complexes (CoSSCs) (search interval of ±3 cycles around the reference height, height increment of 9 m and $\lambda = 2.8$, $\gamma > 0.25$).

the reference ($\%_{(AD=0)}$). The estimated height with the GC-TV algorithm is less noisy (about $\%_{(AD=0)} = 97\%$). The good performance with the three scenes is mainly due to the large HoAs, their optimal ratio (about 0.7) and to the high coherence of the different scenes.

4.3.3 Challenging case 2: surface discontinuity

A high plain is characterised by a relatively flat surface which is elevated above nearby land and which is separated by steep slopes. Consequently, the addressed issue is the surface discontinuity. Depending on the acquisition parameters, significant layover and shadow regions may fractionate the scene.

The following example is located in the Ubajara National Park in Brazil. Figure 4.13 depicts its relief map and the reference slant range height from SRTM. The relief varying between 146 and 919 m, is smooth apart from the highland border. The *master* scene is a standard acquisition from the second global coverage with an average HoA of 40 m/cycle. Figure 4.14 depicts the wrapped phases and their respective coherence. The scene is divided into two parts because of the 400 m high cliff and its shadow.

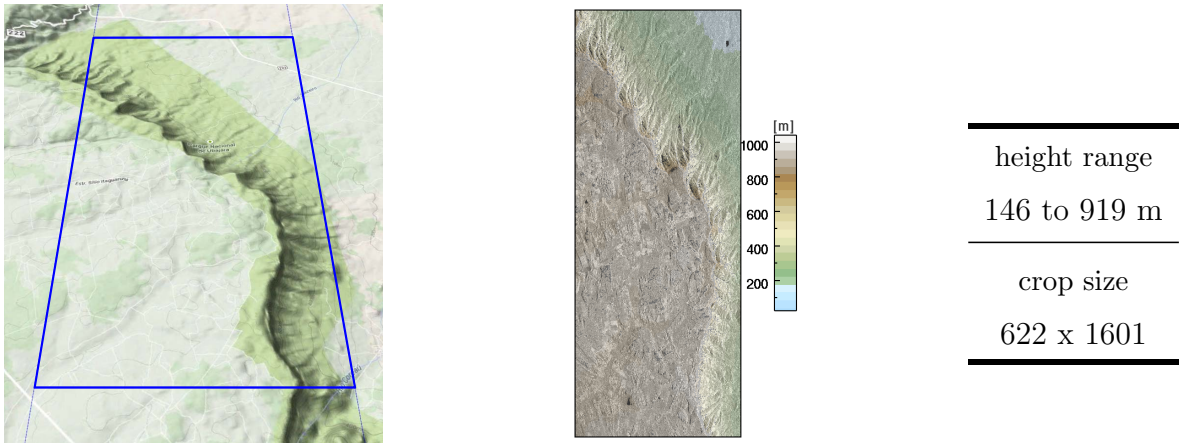

(a) Relief map (Google Maps) (b) Reference slant range height (SRTM)

Fig. 4.13. Relief map, reference height and height range for the test site of the Ubajara National Park area.

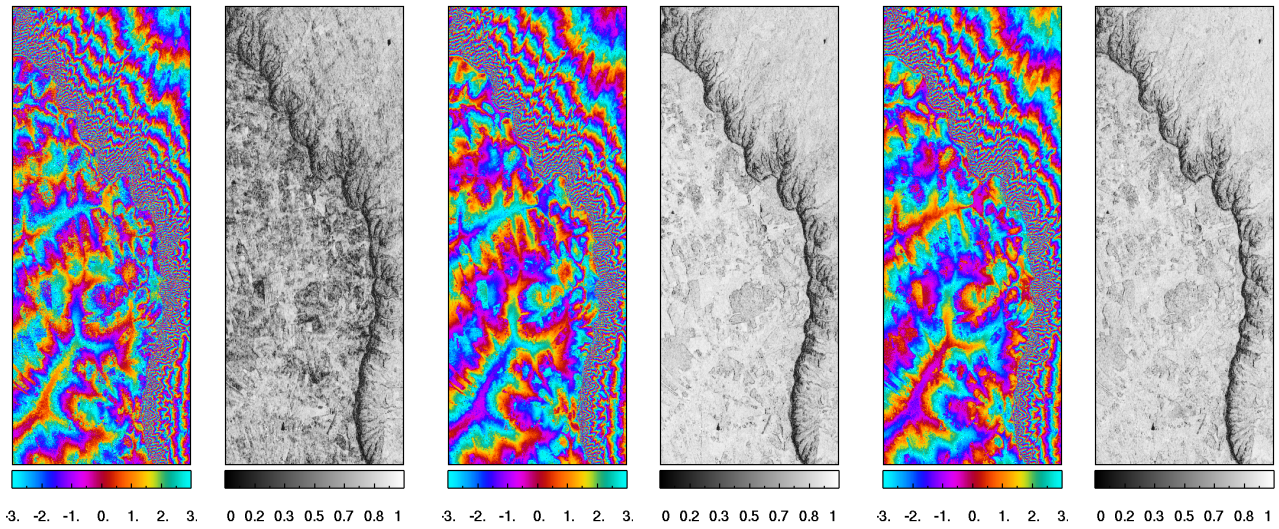

(a) ψ^m (b) γ^m (c) ψ^{s_1} (d) γ^{s_1} (e) ψ^{s_2} (f) γ^{s_2}

Fig. 4.14. Wrapped phases and coherences of the *master* and the two *slave* interferograms for the Ubajara National Park area. The respective HoAs are $h_{2\pi}^m = 41$ m/cycle, $h_{2\pi}^{s_1} = -48$ m/cycle and $h_{2\pi}^{s_2} = 50$ m/cycle. Average coherences (for $\gamma > 0.25$) are $\overline{\gamma^m} = 0.65$ (95% of the pixels), $\overline{\gamma^{s_1}} = 0.79$ (98% of the pixels) and $\overline{\gamma^{s_2}} = 0.79$ (98% of the pixels).

The MCF is uncapable to restore the plateau ($\%_{(\mathrm{AD}=0)} \approx 58\%$ and see Fig. 4.15). The height variation within the scene is 773 m $\approx 19 \times h_{2\pi}^m$ so that the search interval for the MLE and GC-TV should be greater than 19 cycles. Nevertheless, the resulting unambiguous height is about 1,200 m $\approx 40 \times h_{2\pi}^m$ but only about 200 m $\approx 5 \times h_{2\pi}^m$ considering $h_{2\pi}^{s_1} \approx h_{2\pi}^{s_2}$ (equivalent to considering a higher noise). Different search intervals of $\pm$ 4, 7 and 12 cycles (equivalent to $\pm$ 180, 300 and 500 m) around the reference height have been considered and results are shown in Fig. 4.16. The top of every picture shows the outcome of the GC-TV and the bottom, the ones of the MLE.

Table 4.3 summarises the different error criteria. The noise significantly increases from $\pm$ 4 to $\pm$ 7 cycles for the MLE ($\sigma_{\mathrm{AD}} = 0.81$ and $\sigma_{\mathrm{AD}} = 1.95$ respectively) but a higher number of cycles does not deteriorate more the performances ($\sigma_{\mathrm{AD}} = 2.06$). The GC-TV delivers comparable results independently of the search interval. Nonetheless, the size of the graph triples from 13 GB for $\pm$ 4 cycles to 36 GB for $\pm$ 12 cycles and the computation time increases from 12 min to 91 min (refer to Table 4.3). If the reference is trustworthy, the interval could be thus reduced to decrease the memory consumption.

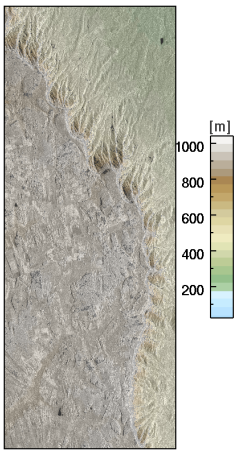

(a) Reconstructed slant range height

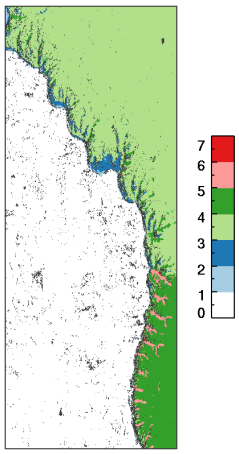

(b) AAD map

$\%_{(AD=0)}$	$\overline{AD}$	σ_{AD}	m_{AD}	NMAD
57.75%	-1.35	1.62	-0.12	0.34

(c) Error measures (for $\gamma > 0.25$)

Fig. 4.15. MCF results for the Ubajara National Park area: (a) *master* unwrapped phase converted to slant range height, (b) Absolute Ambiguity Deviation (AAD) map with respect to the reference DEM and (c) statistical assessment.

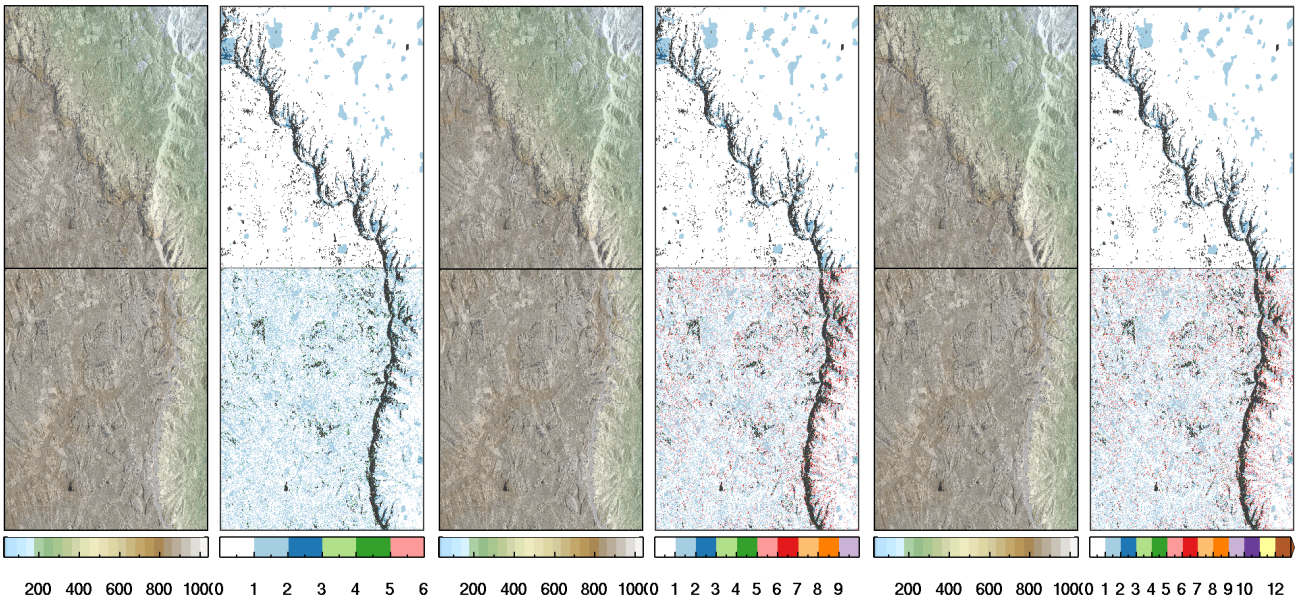

(a) ± 4 cycles i.e. ±180 m (b) ± 4 cycles i.e. ±180 m (c) ± 7 cycles i.e. ±300 m (d) ± 7 cycles i.e. ±300 m (e) ± 12 cycles i.e. ±500 m (f) ± 12 cycles i.e. ±500 m

Fig. 4.16. MLE and GC-TV results for the Ubajara National Park area for search intervals of (a-b) ±4 cycles or ±180 m, (c-d) ±7 cycles or ±300 m and (e-f) ±12 cycles or ±500 m around the reference height: (a,c,e) reconstructed slant range height, (b,d,f) Absolute Ambiguity Deviation (AAD) map with respect to the reference DEM. The top part of the figures depicts the results of the GC-TV whereas the bottom shows the MLE outcomes.

	MLE					GC-TV						
	$\%_{(AD=0)}$	$\overline{AD}$	σ_{AD}	m_{AD}	NMAD	$\%_{(AD=0)}$	$\overline{AD}$	σ_{AD}	m_{AD}	NMAD	size	time
± 4 cycles	63.46%	0.28	0.81	0.025	0.26	92.63%	0,052	0.31	0.005	0.12	13	12
± 7 cycles	57.98%	-0.21	1.95	-0.007	0.29	92.62%	0.053	0.31	0.005	0.12	22	38
± 12 cycles	57.98%	-0.22	2.06	-0.007	0.29	92.62%	0.053	0.31	0.005	0.12	36	91

Table 4.3. Summary of the performance of the MLE and GC-TV in terms of ambiguity deviation for the Ubajara National Park area for different search intervals (for $\gamma > 0.25$). For the GC-TV algorithm the size of the graph in GB and the execution time in minutes are indicated. The values are given for the estimation of half the scene.

Notwithstanding, if the reference DEM is wrong, the true height can hardly be recovered. Mount Roraima in eastern Venezuela (see Fig. 4.17) is a plateau located at a height around 2,350 m in SRTM but its real (local) height is about 2,810 m [8]. Another difficulty is that the huge abrupt height difference causes a large shadow in the SAR images (see the *master* coherence in Fig. 4.18). The HoAs configuration is the same as the preceding one. The true height of the plateau is thus about 11 to 12 cycles away than the reference height. The MLE requires a search interval of at least ± 12 cycles around the reference height but still it is unable to reconstruct the absolute phase (Fig. 4.19).

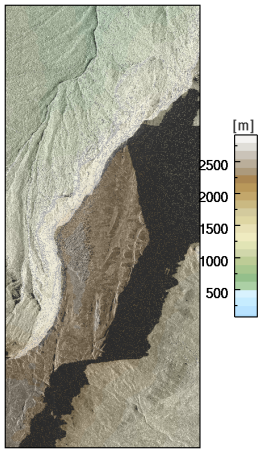

(a) Reference slant range height

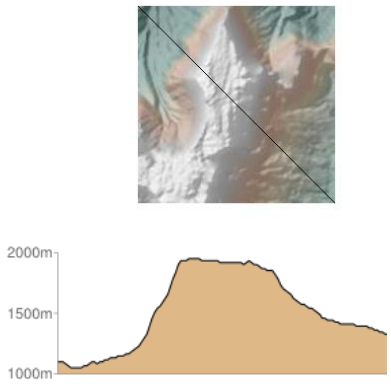

(b) Reference height profile

height range (SRTM)
577 to 2,354 m
real height
up to 2,810 m
crop size
694 x 1567

Fig. 4.17. Reference slant range height from SRTM, reference height profile and height range for the test site of the Mount Roraima example.

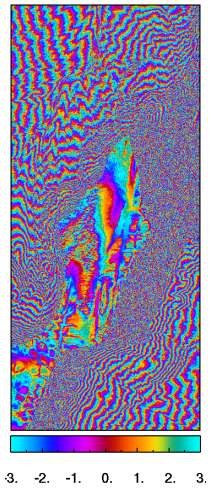

(a) ψ^m

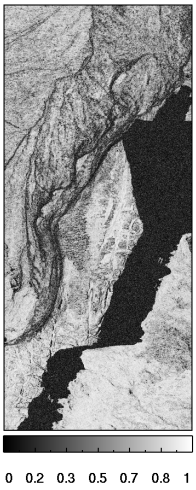

(b) γ^m

Fig. 4.18: Wrapped phase and coherence of the *master* interferogram for the Mount Roraima example. The HoA is $h^m_{2\pi} = 39$ m/cycle and the average coherence (for $\gamma > 0.25$) is $\overline{\gamma^m} = 0.68$ (80% of the points).

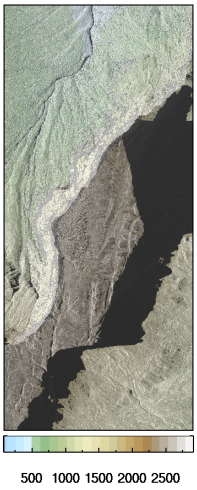

(a) ± 12 cycles

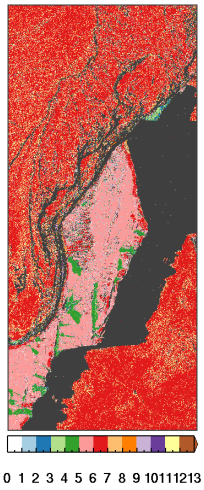

(b) ± 12 cycles

Fig. 4.19: MLE reconstructed slant range height of the Mount Roraima for a search intervals of ±12 cycles around the reference height.

4.3.4 Challenging case 3: mountainous terrain

Mountainous terrain is the last issue depicted in this chapter. The scene is located around the Isolation Peak in the Rocky Mountains in the USA. It is a usual test site for PU algorithms (Ghiglia and Wahl, 1994). Figure 4.20 depicts its relief map and the reference slant range height from SRTM. The relief varies between 2,976 and 4,065 m and is challenging. The *master* scene

[8] http://www.peakbagger.com/peak.aspx?pid=8684

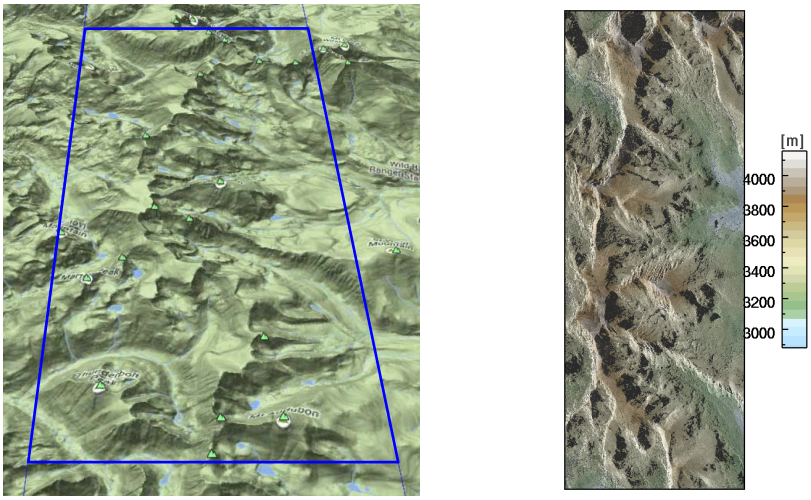

(a) Relief map (Google Maps) (b) Reference slant range height (SRTM)

Fig. 4.20. Relief map, reference height and height range for the test site of the Isolation Peak area.

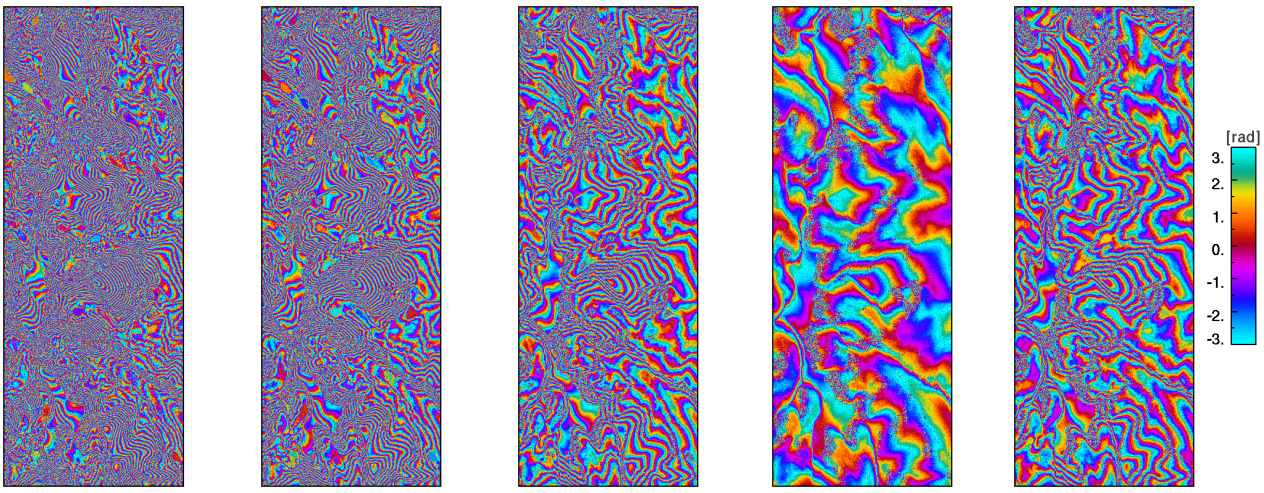

(a) ψ^m (b) ψ^{s_1} (c) ψ^{s_2} (d) ψ^{s_3} (e) ψ^{s_4}

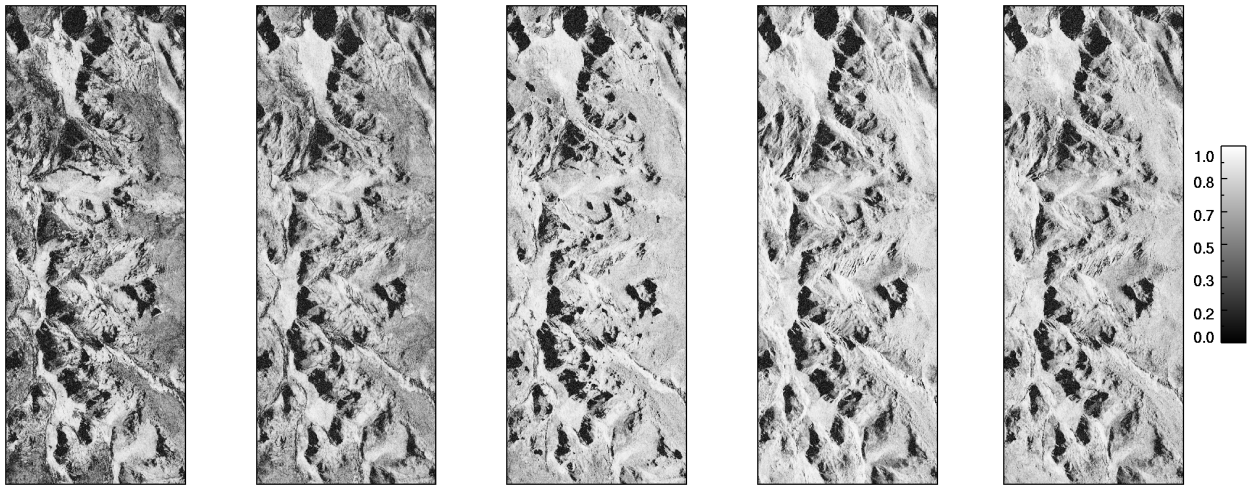

(f) γ^m (g) γ^{s_1} (h) γ^{s_2} (i) γ^{s_3} (j) γ^{s_4}

Fig. 4.21. Wrapped phases and coherences of the *master* and *slave* interferograms for the Isolation Peak region. The respective HoAs are $h_{2\pi}^{m} = 32$ m/cycle, $h_{2\pi}^{s_1} = -42$ m/cycle, $h_{2\pi}^{s_2} = 79$ m/cycle, $h_{2\pi}^{s_3} = 296$ m/cycle and $h_{2\pi}^{s_4} = -106$ m/cycle. Average coherences (for $\gamma > 0.25$) are $\overline{\gamma^m} = 0.64$ (83% of the pixels), $\overline{\gamma^{s_1}} = 0.67$ (87% of the pixels), $\overline{\gamma^{s_2}} = 0.77$ (88% of the pixels), $\overline{\gamma^{s_3}} = 0.76$ (89% of the pixels) and $\overline{\gamma^{s_4}} = 0.74$ (89% of the pixels).

has a HoA of 32 m/cycle. As a consequence, it is impossible for the MCF to unwrap successfully the phase (see Fig. 4.22).

For this area, additional acquisitions have been acquired so that 4 supporting CoSSCs are available (Fig. 4.21). The total height variation within the scene is 1,089 m $\approx 34 \times h_{2\pi}^m$ but the unambiguous height is only about 240 m $\approx 7.5 \times h_{2\pi}^m$ with the 2 first CoSSCs and up to 1,200 m $\approx 37.5 \times h_{2\pi}^m$ considering the 4 *slave* scenes.

MLE results shown in Fig. 4.23 have been processed with 2 and 4 supporting CoSSCs for the search intervals of ± 4, 7 and 12 cycles (i.e. ±144m, ± 240 m and ± 400 m) around the reference height. The GC-TV has not been used because of the huge graph size and processing time required. Table 4.4 summarises the different quality statistics. When only 2 supporting CoSSCs are used, the reconstruction fails and the result is not absolute even for the smallest search interval (± 4 cycles) ($\overline{\text{AD}} \neq 0$ and $m_{\text{AD}} \neq 0$ and see Figs. 4.23a to 4.23d). With 4 supporting slaves, the reconstruction is successful as long as the search interval is not too large. Nonetheless, one of the additional interferogram has a HoA of 296 m/cycle and is thus not ambiguous inside the search interval of ± 4 cycles (equivalent to ± 144 m) and only once for ± 7 cycles (± 240 m). Regardless, the noise has already increased significantly ($\sigma_{\text{AD}} = 0.59$ for ± 4 cycles and $\sigma_{\text{AD}} = 1.62$ for ± 7 cycles).

		$\%_{(\text{AD}=0)}$	$\overline{\text{AD}}$	σ_{AD}	m_{AD}	NMAD
2 CoSSCs	± 4 cycles (± 144 m)	1.87%	-1.67	1.26	-1.95	0.35
	± 7 cycles (± 240 m)	1.31%	-2.55	2.52	-2.07	0.52
4 CoSSCs	± 4 cycles	83.02%	-0.05	0.59	-0.02	0.30
	± 7 cycles	79.95%	-0.33	1.62	-0.04	0.32
	± 12 cycles (± 400 m)	5.10%	6.41	5.04	9.88	0.90

Table 4.4. Summary of the performance of the MLE in terms of ambiguity deviation for the Isolation Peak region for different search intervals (for $\gamma > 0.25$) and different number of supporting interferograms.

4.3.5 Discussion

In this section, the three main issues for PU algorithms have been presented: incoherent areas, surface discontinuities and mountainous terrain.

The MCF, and more generally 1B-PU algorithms, are unable to perform correctly when the Itoh condition is not met. Indeed, as it can be seen from all the test sites, as soon as the scene is split because of some incoherent regions or if the HoA is small (causing undersampling), they are not able to recover a correct unwrapped phase.

For this reason, multi-baseline methods have to be employed to take advantage of the baseline diversity. In this section, the MLE and the GC-TV have been studied. These are methods based on phases and require that the latter are calibrated. Uncompensated phase offsets would ruin the absolute slant range height recovery. Such offsets come from the non perfect synchronisation, possible SAR processing errors, atmospheric effects, baselines estimation errors. In the TDM, a π-ambiguity coming from the synchronisation link cannot be estimated properly. This is thus an important matter. Ferraioli et al. (2008) proposed an approach based on the MLE using the Expectation Minimisation to retrieve the different offsets, which is however not applicable due to the high load processing constraints.

Investigating the results estimated by means of the MLE, reconstructed slant range heights reveal outliers. As mentioned in section 3.1.3.1, the estimated unwrapped phase may lie in a different ambiguity band from one pixel to the other so that a large number of interferograms is required to restore the solution. This is confirmed by Fig. 4.12 where the outcomes of the MLE with only 1 supporting CoSSC is useless and Fig. 4.23 where 4 CoSSCs are required

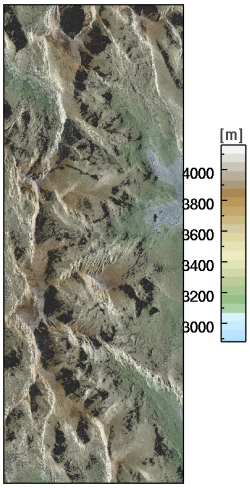

(a) Reconstructed slant range height

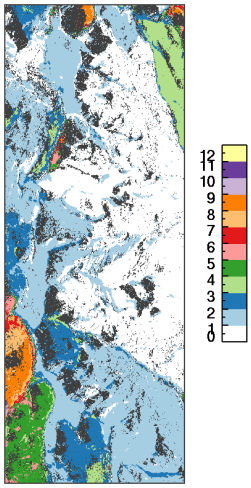

(b) AAD map

$\%_{(AD=0)}$	$\overline{AD}$	σ_{AD}	m_{AD}	NMAD
40.32%	-0.69	1.79	-0.38	0.92

(c) Error measures (for $\gamma > 0.25$)

Fig. 4.22. MCF results for the Isolation Peak region for the *master* phase: (a) unwrapped phase converted to slant range height, (b) Absolute Ambiguity Deviation (AAD) map with respect to the reference DEM and (c) statistical assessment.

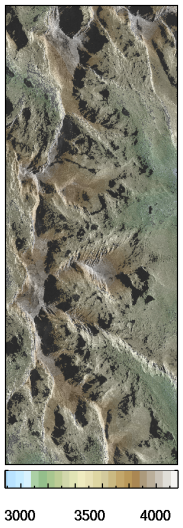

(a) ± 4 cycles

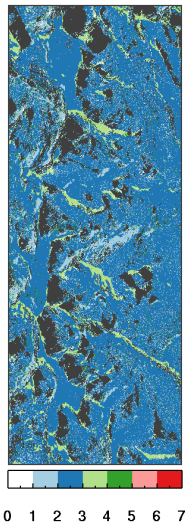

(b) ± 4 cycles

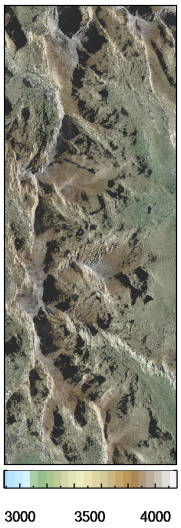

(c) ± 7 cycles

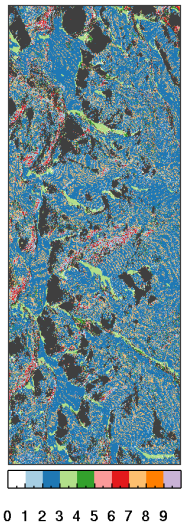

(d) ± 7 cycles

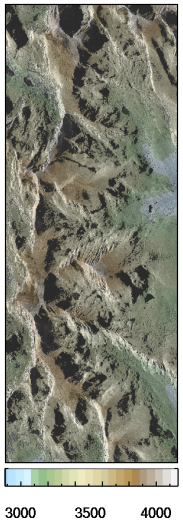

(e) ± 4 cycles

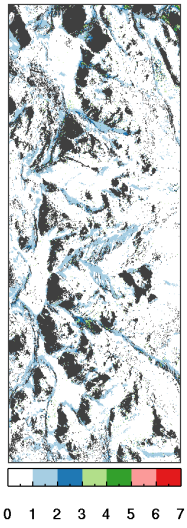

(f) ± 4 cycles

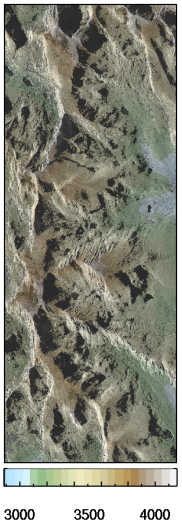

(g) ± 7 cycles

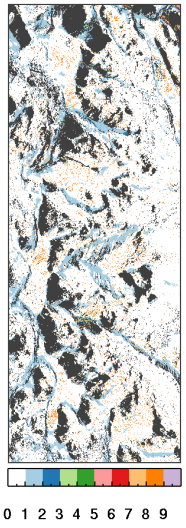

(h) ± 7 cycles

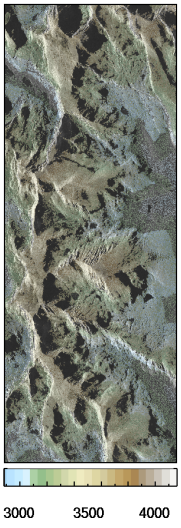

(i) ± 12 cycles

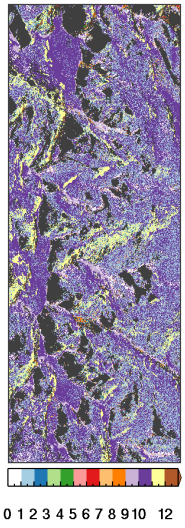

(j) ± 12 cycles

Fig. 4.23. MLE results processed with 2 (a-d) and 4 supporting CoSSCs (e-j) for the Isolation Peak region for search intervals of ±4 cycles (a-b, e-f), ±7 cycles (c-d,g-h) and ±12 cycles (i-j) around the reference phase: (a,c,e,g,i) reconstructed slant range height, (b,d,f,h,j) Absolute Ambiguity Deviation (AAD) map with respect to the reference DEM.

to retrieve a satisfactory solution (but sill under the condition of a relatively narrow search interval). As a result, the estimated height is meaningless when the terrain is mountainous, the input interferograms exhibit lower and/or different coherences or the HoAs constellation is unfavourable. Note that for TDM, the standard case is to have only 2 interferograms acquired with shifted beams so that the coherence may differ in the both available half scenes.

The GC-TV algorithm delivers reliable results and prevents from outliers (see Fig. 4.12 and 4.16). Yet, it necessitates huge memory resources and becomes heavy computationally as the size of the images and the height interval increase (consult Table 4.3). Consequently, it is impractical for large images.

A reference DEM may be used as a prior to restrict search intervals as proceeded in all the previous examples. Nonetheless, if this DEM presents large height errors, the proper solution cannot be retrieved (see Fig. 4.19).

As a conclusion, none of the tested algorithms is suitable to fulfil the TDM mission requirements as illustrated by the various presented examples. Indeed, even under the initially planned acquisition conditions described in section 4.1.1, their performances are not sufficient. As such, a global mapping requires a robust and versatile PU algorithm as the one proposed in the chapter 5. It is able to deal with the variety of data quality and baseline configurations.

5 Dual-Baseline Phase Unwrapping Correction (DB-PUC)

Multi-baseline phase unwrapping methods based on statistical signal processing are not suitable in cases where only two or three interferograms are available. Under these conditions, pixel-wise algorithms like the Maximum Likelihood Estimator (MLE) (Eineder and Adam, 2005) provide noisy unwrapped phases because different ambiguity bands may be chosen from pixel to pixel. On the other hand, algorithms considering the neighbourhood deliver satisfactory solutions at a cost of a long processing time (Ferraiuolo et al., 2004) and possibly of huge memory resources (like the Graph-Cuts Total Variation (GC-TV) from Ferraioli et al. (2009)). All in all, they are not compatible with a systematic and operational processing of world-wide data as required for the TanDEM-X mission.

In this chapter, a more reliable and more practicable approach is introduced. It is capable to deal with dual-baseline bistatic data of different quality and acquired with a long time separation. This is the major contribution of this thesis. The new proposed framework aims to correct phase unwrapping (PU) errors by modifying the ambiguity band region-wise with the help of the so-called *differential interferogram* (Lachaise et al., 2012b,a). It allows thus to reduce the impact of noise and terrain changes, which may have occurred between the two acquisitions.

This chapter is structured as follows. In the first section, the overall concept of the Dual-Baseline Phase Unwrapping Correction (DB-PUC) framework is presented after a short literature review on PU error detection and correction. Then, the next sections set forth the different stages of the DB-PUC approach: namely, the phase unwrapping consistency check, the use of the *differential interferogram* and the stereo-radargrammetry and finally the unwrapped phase correction itself. Concurrently, the constraints and requirements on the interferometric data for a successful detection or correction of the PU errors are precisely studied.

5.1 Overview of the DB-PUC framework

5.1.1 Brief literature review on PU error detection and correction

The means to detect or correct (single-baseline) PU errors can be classified into two categories:

(1) the segmentation map: in Hubig et al. (2000), it is obtained by a thresholding on the residue density. It is well adapted to branch-cut methods but is very sensitive to the threshold value. Galli (2001) assigns quality measures (coherence) to the integration paths from a reference point to each image pixel. The resulting map shows how well each pixel is connected to the reference one. A low value indicates the location of potential PU errors. In both approaches, tie points may be used in a second step to correct large-scale errors.

(2) an external Digital Elevation Model (DEM): it helps to localise PU errors via the difference image of the unwrapped phase and a simulated phase from the DEM (Suchandt and Eineder, 2003). This was used for the SRTM mission. A (possibly correct) reference DEM, which has a sufficient resolution is required. For the TanDEM-X mission (TDM), it should also be global (which does not exist).

These techniques are mainly meant as a preprocessing to facilitate an operator decision. Note that PU reliability is also discussed in the context of region growing algorithms (Chen and Zebker, 2002; Lachaise et al., 2008) although their goal is to avoid error propagation during the unwrapping stage.

In the Integrated TanDEM-X Processor (ITP), the *stereo-radargrammetric phase* is used to analyse the quality of the unwrapping outputs (Rossi et al. (2012), appendix B.3.5). This phase

stems from the coregistration shifts between the two interferometric channels. Since they are calculated patch-wise, the stereo-radargrammetric phase has a coarser resolution than the interferometric one. Moreover, its accuracy depends strongly on the coherence and the backscatter so that it is not suitable to correct pixel-wise PU errors of a standard TDM unwrapped phase (see section 4.2.2 for an analysis of the accuracy of the stereo-radargrammetric phase).

To our knowledge, no algorithm exists to correct PU errors with multi-baseline InSAR data.

5.1.2 Summary of the proposed approach

The DB-PUC is designed to be independent of the number of interferograms. It could be seen as a multi-baseline method but the different steps presented thereafter are performed sequentially on pairs of interferograms, hence referred to as dual-baseline. Figure 5.1 presents the flowchart of the proposed framework and its different levels of complexity. The unwrapped phase to be corrected and its relative interferometric data pair are called *master* data (the acquisitions of the second global TanDEM-X coverage with typically lower heights of ambiguity (HoAs)). They are denoted with the superscript m. The supporting data pair is referred to as *slave* and denoted with the superscript s.

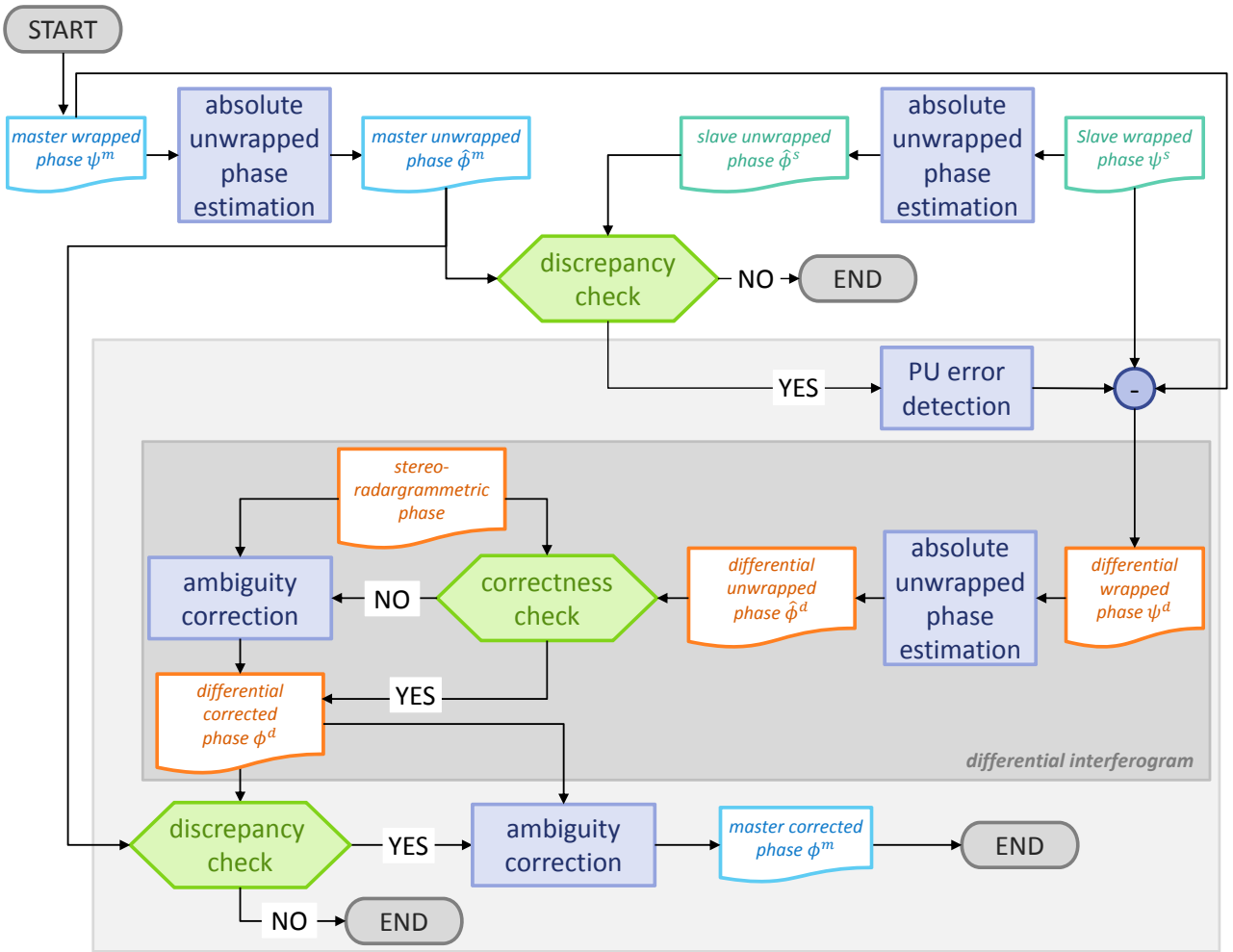

Fig. 5.1. Flowchart of the Dual-Baseline Phase Unwrapping Correction (DB-PUC) framework: the basic idea is to estimate the absolute unwrapped *master* (in cyan) and *slave* (in turquoise) phases separately and to compare them in slant range height domain. In this way, regions where the absolute unwrapped phases differ significantly can be detected. These local discrepancies are then corrected for an integer multiple of 2π determined from the (corrected) unwrapped *differential interferogram* phase (in orange). In the diagram, the green symbols indicate a decision and the purple boxes, algorithmic steps. The *absolute unwrapped phase estimation* consists of the phase unwrapping by means of the MCF algorithm and the absolute phase offset estimation.

The *master* and *slave* phases are unwrapped independently with the Minimum Cost Flow (MCF) algorithm (Costantini, 1998; Eineder et al., 1998) where the costs depend on the coherences (appendix B.3.4). Absolute phase offsets are determined afterwards using the stereo-radargrammetry (see section 3.2.1 and appendix B.3.5). The two estimated absolute unwrapped phases can be compared once they have been converted to (slant range) heights. If both unwrappings are successful, both heights agree. On the contrary, they differ significantly in the presence of PU errors. This is the topic of section 5.2. At this stage, it is impossible to clearly state which phase exhibits problems. Errors might be present in both unwrapped phases but, some might also not be detected. As a matter of fact, no correction is feasible and a third reliable information is necessary. This one will play the same role as the interferogram with the smallest baseline in Xu et al. (1994); Jakowatz et al. (1996); Robertson (1998). For this purpose, the *master* interferogram is demodulated with the *slave* one (Xu et al., 1994; Massonnet et al., 1996) to build a third interferogram, which has a smaller equivalent baseline. It is the *differential interferogram*, the central point of the DB-PUC. Due to its higher HoA, the *differential interferogram* is easier to unwrap. Yet, unwrapping errors may still arise and must be corrected. Wrongly unwrapped regions are detected and eliminated with the help of the coarse absolute height information given by the interferometric stereo-radargrammetry. This step is the most delicate one because of the resolution differences and the limited accuracy of the stereo-radargrammetry. This is detailed in section 5.3. Finally, discrepant regions are corrected in the *master* unwrapped phase. Only the ambiguity band is altered to reduce the impact of the different perturbations and keep the solution congruent (section 5.4).

The following sections will be illustrated by one representative example. Further results and assessments will be given in chapter 6. The chosen scene is the Marble Canyon, upstream of the Grand Canyon in the USA.

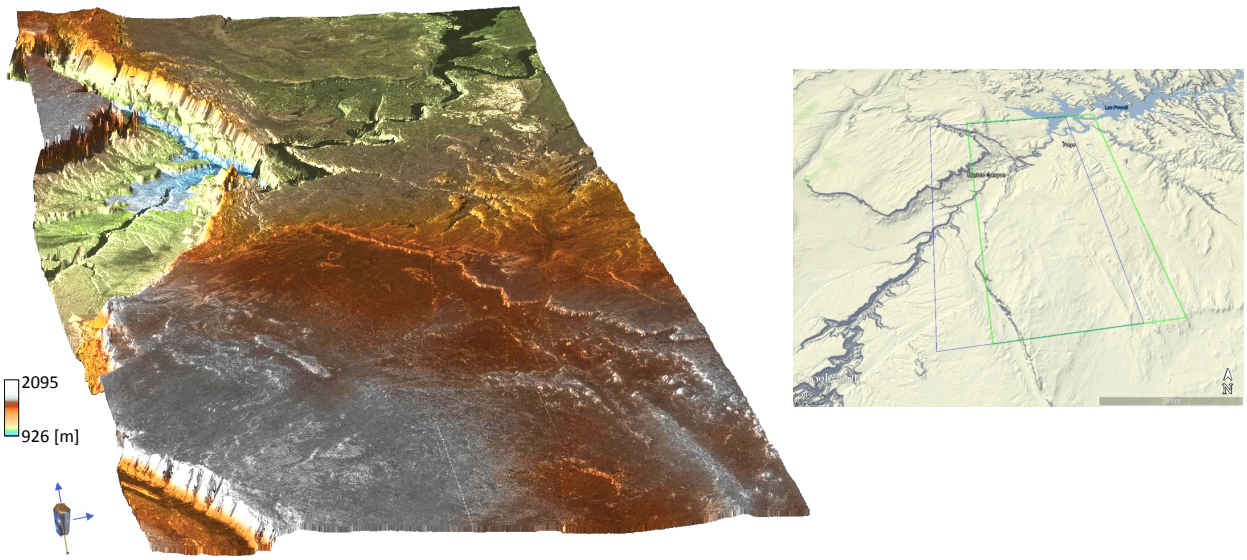

(a) 3-D view of the SAR image amplitude colour-coded with the terrain height

(b) Relief map (from Google Maps)

Fig. 5.2. Marble Canyon (USA) example: 3-D view and relief map overlaid by the *master* (green) and *slave* (blue) scene frames.

The *master* scene is a typical acquisition of the second global coverage with a HoA of 33.8 m/cycle . The supporting *slave* is characterised by a HoA of 50.1 m/cycle and was acquired about one year earlier. The HoA ratio μ equal to 0.68 is optimal. The region is arid so that both coherences are good. The difficulties of this scene are the Paria river, which cuts the scene into two parts and the canyon itself, which causes shadow and layover.

5.2 PU discrepancy check and error detection

The first stage of the DB-PUC is to check if both estimated unwrapped phases are consistent and to detect the PU errors otherwise. To begin with, this section describes the principle of the discrepancy check. Then, it addresses the issue of residual global offsets. Finally, it reveals how the inconsistencies are identified.

5.2.1 Phase unwrapping discrepancy check: principle

After the unwrapping and the absolute offset determination, the *master* and *slave* estimated phase values $\hat{\phi}^m$ and $\hat{\phi}^s$ can be written as (eqs. (2.8) and (2.17)):

$$\hat{\phi}^m = \psi^m + 2\hat{k}^m_{\mathrm{PU}}\pi + \hat{k}^m_{\mathrm{off}}\pi = \frac{2\pi}{h^m_{2\pi}}\hat{h}^m \qquad \text{and} \qquad \hat{\phi}^s = \psi^s + 2\hat{k}^s_{\mathrm{PU}}\pi + \hat{k}^s_{\mathrm{off}}\pi = \frac{2\pi}{h^s_{2\pi}}\hat{h}^s \tag{5.1}$$

where $\hat{h}^m$ and $\hat{h}^s$ are the estimates of the actual terrain height h and $\hat{k}^m_{\mathrm{PU}}, \hat{k}^s_{\mathrm{PU}}$ and $\hat{k}^m_{\mathrm{off}}, \hat{k}^s_{\mathrm{off}} \in \mathbb{Z}$ are the ambiguity bands estimated during the unwrapping procedure and the (integer) absolute phase offset retrieval, respectively. $\hat{k}^m_{\mathrm{PU}}$ and $\hat{k}^s_{\mathrm{PU}}$ vary pixel-wise whereas $\hat{k}^m_{\mathrm{off}}$ and $\hat{k}^s_{\mathrm{off}}$ are constant over the whole phase images. In the TDM framework, the integer absolute phase offsets include the 2π-ambiguity from the absolute phase offset and the π-ambiguity from the synchronisation link (see appendices A.5 and B.2). The case where $h^m = h^s = h$ i.e. the nominal case of no terrain changes (or only small scales variations, which are treated as noise) is considered here. The absolute unwrapped phases are congruent to their respective wrapped phases ψ^m and ψ^s. $\hat{\phi}^m$ and $\hat{\phi}^s$ may deviate from their true phase ϕ^m and ϕ^s because of possible estimation errors.

Since the two interferograms have different HoAs, possible estimation errors are detectable by computing the difference of the *master* and *slave* height estimates:

$$\begin{aligned}\Delta\hat{h} &= \hat{h}^m - \hat{h}^s \\ \Delta\hat{h} &= \frac{h^m_{2\pi}}{2\pi}\left(\psi^m + 2\hat{k}^m_{\mathrm{PU}}\pi + \hat{k}^m_{\mathrm{off}}\pi\right) - \frac{h^s_{2\pi}}{2\pi}\left(\psi^s + 2\hat{k}^s_{\mathrm{PU}}\pi + \hat{k}^s_{\mathrm{off}}\pi\right)\end{aligned} \tag{5.2}$$

Introducing k^m_{PU}, k^s_{PU} and k^m_{off}, k^s_{off} as the true ambiguity bands and offsets allowing to retrieve the true phases ϕ^m and ϕ^s and the integers $\varepsilon_{k^m_{\mathrm{PU}}}$, $\varepsilon_{k^s_{\mathrm{PU}}}$ and $\varepsilon_{k^m_{\mathrm{off}}}$, $\varepsilon_{k^s_{\mathrm{off}}}$ representing the errors that could occur either during the PU or the absolute phase offset estimation, $\Delta\hat{h}$ is rewritten as:

$$\begin{aligned}\Delta\hat{h} = &\frac{h^m_{2\pi}}{2\pi}\left(\psi^m + 2\left(k^m_{\mathrm{PU}} + \varepsilon_{k^m_{\mathrm{PU}}}\right)\pi + \left(k^m_{\mathrm{off}} + \varepsilon_{k^m_{\mathrm{off}}}\right)\pi\right) - \\ &\frac{h^s_{2\pi}}{2\pi}\left(\psi^s + 2\left(k^s_{\mathrm{PU}} + \varepsilon_{k^s_{\mathrm{PU}}}\right)\pi + \left(k^s_{\mathrm{off}} + \varepsilon_{k^s_{\mathrm{off}}}\right)\pi\right)\end{aligned} \tag{5.3}$$

$\varepsilon_{k^m_{\mathrm{off}}}$ and $\varepsilon_{k^s_{\mathrm{off}}}$ are constant over the image whereas $\varepsilon_{k^m_{\mathrm{PU}}}$ and $\varepsilon_{k^s_{\mathrm{PU}}}$ change pixel-wise. If both the absolute phase offset estimation and the unwrapping procedure are correct ($\varepsilon_{k^m_{\mathrm{off}}} = \varepsilon_{k^s_{\mathrm{off}}} = \varepsilon_{k^m_{\mathrm{PU}}} = \varepsilon_{k^s_{\mathrm{PU}}} = 0$), the *master* and *slave* height maps are equal to the noise-free terrain height plus some noise: $h = \hat{h}^m - h^m_N = \hat{h}^s - h^s_N$. In other words, $\Delta\hat{h}$ is equal to:

$$\Delta\hat{h} = \frac{h^m_{2\pi}}{2\pi}\left(\psi^m + 2k^m_{\mathrm{PU}}\pi + k^m_{\mathrm{off}}\pi\right) - \frac{h^s_{2\pi}}{2\pi}\left(\psi^s + 2k^s_{\mathrm{PU}}\pi + k^s_{\mathrm{off}}\pi\right) = h^m_N - h^s_N = \Delta h_N \tag{5.4}$$

The histogram of the height differences exhibits in this case only one peak. Both *master* and *slave* unwrapped phases are consistent and no correction is needed.

5.2.2 Residual global offset compensation

Residual baselines errors, various differential tropospheric delays (Krieger et al., 2012) but also wrongly determined absolute phase offsets imply a residual offset to the true absolute phase. The first effects are quite small due to the extensive TanDEM-X system calibration (see appendix A.5). They are visible only in the fractional part of the absolute phase offset. As a consequence, the main component of a residual phase offset arises from a wrong estimation of the integer absolute phase offsets particularly of the π-ambiguity (i.e. $\hat{k}^m_{\text{off}}\pi$ and $\hat{k}^s_{\text{off}}\pi$). Under the assumption that both unwrappings are error free ($\varepsilon_{k^m_{\text{PU}}} = \varepsilon_{k^s_{\text{PU}}} = 0$), eq. (5.3) becomes:

$$\begin{aligned}
\Delta\hat{h}_{\text{off}} &= \frac{h^m_{2\pi}}{2\pi}\left(\psi^m + 2k^m_{\text{PU}}\pi + \left(k^m_{\text{off}} + \varepsilon_{k^m_{\text{off}}}\right)\pi\right) - \frac{h^s_{2\pi}}{2\pi}\left(\psi^s + 2k^s_{\text{PU}}\pi + \left(k^s_{\text{off}} + \varepsilon_{k^s_{\text{off}}}\right)\pi\right) \\
\Delta\hat{h}_{\text{off}} &= \underbrace{\frac{h^m_{2\pi}}{2\pi}\left(\psi^m + 2k^m_{\text{PU}}\pi + k^m_{\text{off}}\pi\right) - \frac{h^s_{2\pi}}{2\pi}\left(\psi^s + 2k^s_{\text{PU}}\pi + k^s_{\text{off}}\right)\pi}_{=\Delta h_N \text{ according to eq. (5.4)}} + \frac{h^m_{2\pi}}{2}\varepsilon_{k^m_{\text{off}}} - \frac{h^s_{2\pi}}{2}\varepsilon_{k^s_{\text{off}}} \\
\Delta\hat{h}_{\text{off}} &= \frac{h^m_{2\pi}}{2}\varepsilon_{k^m_{\text{off}}} - \frac{h^s_{2\pi}}{2}\varepsilon_{k^s_{\text{off}}} + \Delta h_N
\end{aligned} \tag{5.5}$$

If a residual offset is present, $\Delta\hat{h}_{\text{off}}$ is not only a height offset but it manifests itself also as a tilt over range because of the HoA variation. For the relatively narrow TDM beams, this dependency with range can be approximated by linear regression lines of slope $a_{h^m_{2\pi}}$ and $a_{h^s_{2\pi}}$. Due to the formation configuration, they are latitude dependent and vary from $\pm 2\%$ to $\pm 10\%$ around the HoA from higher to lower (absolute) latitudes (see appendix C). The equation of the *master* HoA ramp is (the *slave* one is similar):

$$f_{h^m_{2\pi}}(r) = 2a_{h^m_{2\pi}} h^m_{2\pi} \frac{r}{N^m_r - 1} + (1 - a_{h^m_{2\pi}}) h^m_{2\pi} \tag{5.6}$$

where N^m_r is the interferogram width and $h^m_{2\pi} = \overline{h^m_{2\pi}} \approx h^m_{2\pi(r=(N^m_r-1)/2)}$, the HoA at mid-range. As a consequence, the height difference $\Delta\hat{h}_{\text{off}}$ is tilted over range when $\varepsilon_{k^m_{\text{off}}} \neq 0$ or $\varepsilon_{k^s_{\text{off}}} \neq 0$. Replacing $h^m_{2\pi}$ and $h^s_{2\pi}$ by their equations $f_{h^m_{2\pi}}(r)$ and $f_{h^s_{2\pi}}(r)$ in eq. (5.5), the variation of the height differences over range is:

$$\Delta\hat{h}_{\text{off}}(r) = \underbrace{\left(\frac{a_{h^m_{2\pi}} h^m_{2\pi}\varepsilon_{k^m_{\text{off}}}}{N^m_r - 1} - \frac{a_{h^s_{2\pi}} h^s_{2\pi}\varepsilon_{k^s_{\text{off}}}}{N^s_r - 1}\right)}_{\text{tilt}} r + \underbrace{\frac{1}{2}\left((1 - a_{h^m_{2\pi}}) h^m_{2\pi}\varepsilon_{k^m_{\text{off}}} - (1 - a_{h^s_{2\pi}}) h^s_{2\pi}\varepsilon_{k^s_{\text{off}}}\right)}_{\text{offset}} \tag{5.7}$$

Figure 5.3 illustrates the influence of wrongly estimated phase offsets in the *master* and/or the *slave* absolute phases. The HoAs variation are taken from real TDM acquisitions, thus they are representative for the real phenomena even if the phase is simplified for illustration purpose. Figure 5.3a presents two possible estimated *master* absolute phases: the solid line is a correct estimation ($\hat{\phi}^m = \phi^m$) whereas the dotted line represents the case of $\varepsilon_{k^m_{\text{off}}} = 1$. In Fig. 5.3b, three estimated *slave* absolute phases are depicted: $\hat{\phi}^s = \phi^s$, $\hat{\phi}^s = \phi^s + 2\pi$ i.e. $\varepsilon_{k^s_{\text{off}}} = 1$ and $\hat{\phi}^s = \phi^s - 2\pi$ (i.e. $\varepsilon_{k^s_{\text{off}}} = -1$). Figure 5.3c emphasises the resulting $\Delta\hat{h}_{\text{off}}(r)$. The slope increases together with $\varepsilon_{k^m_{\text{off}}}$ and $\varepsilon_{k^s_{\text{off}}}$.

Since the true k^m_{off} and k^s_{off} are unknowns, the trend due to the possible residual global offsets must be estimated to enable the PU errors detection. To this end, the median gradient of the low-pass filtered height difference map is calculated. However, the presence of a multitude of PU errors (e.g. in mountains) or low coherence areas complicates considerably a correct trend estimation. In these cases, only an offset is taken into consideration. The residual offset compensation permits the DB-PUC to cope with unknown π-ambiguities. The perfect knowledge

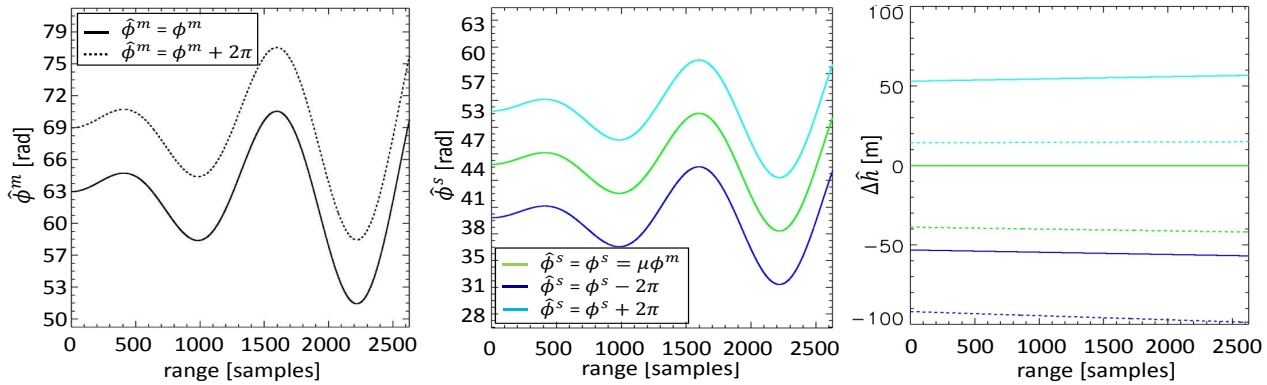

(a) $\hat{\phi}^m$ (b) $\hat{\phi}^s$ (c) $\Delta\hat{h}_{\text{off}}$

Fig. 5.3. Influence of wrongly estimated absolute phase offsets: (a) estimated *master* absolute phase: correctly $\hat{\phi}^m = \phi^m$ (solid line) and wrongly $\hat{\phi}^m = \phi^m + 2\pi$ (dotted line), (b) estimated *slave* absolute phases: $\hat{\phi}^s = \phi^s = \mu\phi^m$ (green), $\hat{\phi}^s = \phi^s + 2\pi$ (light blue) and $\hat{\phi}^s = \phi^s - 2\pi$ (dark blue) and (c) the resulting $\Delta\hat{h}_{\text{off}}(r)$ for the 2×3 cases.

of the absolute offsets is usually a pre-requirement (and a heavy constraint) for any other multi-baseline PU algorithms.

5.2.3 Height discrepancies determination

Once the trend is compensated, errors relative to a wrong absolute phase offset estimation are assumed to be eliminated: $\varepsilon_{k^m_{\text{off}}} = \varepsilon_{k^s_{\text{off}}} = 0$. Equation (5.3) becomes then:

$$\Delta\hat{h} = h^m_{2\pi}\varepsilon_{k^m_{\text{PU}}} - h^s_{2\pi}\varepsilon_{k^s_{\text{PU}}} + \Delta h_N \tag{5.8}$$

Height discrepancies appear as soon as one of the PU procedures fails. In this case, the height difference deviates locally from Δh_N. A height discrepancy is considered as a PU error if $\Delta\hat{h}$ is greater than the difference of a linear combination of both HoAs:

$$\left|\Delta\hat{h}\right| > nh^m_{2\pi} - mh^s_{2\pi} \tag{5.9}$$

with $n, m \in \mathbb{N}$ and $nh^m_{2\pi} > mh^s_{2\pi}$. For the standard TDM acquisitions (section 4.1.1), $m = n = 1$ because both HoAs are relatively close. Like $\Delta\hat{h}_{\text{off}}$, $\Delta\hat{h}$ varies also with r. Nonetheless, the variation is well below this threshold (a HoA ramp with a slope of 6% corresponds to a height variation of 6 m over the scene width for a HoA of 50 m/cycle).

Height differences are calculated and their histogram is computed. When phases are unwrapped successfully, both heights have a constant offset (after correct trend compensation) so that the distribution is unimodal. In this case, both PU outputs are consistent and no further correction is needed. On the contrary, as soon as the histogram presents several peaks, the two unwrapped phases are not consistent anymore. The histogram of the height differences $\Delta\hat{h}$ presents ideally one extra peak per PU error. The main peak is considered as representing the region where both unwrapped phases are compatible. All the other secondary peaks indicate height discrepancies of which a mask is generated. It may still happen that some PU errors are not detected.

Figure 5.4 presents the *master* and *slave* Absolute Ambiguity Deviation (AAD) maps calculated with respect to the reference phases simulated from SRTM DEM (from eq. (4.2)) for the Marble Canyon example. They give the reader hints to comprehend the different errors which arose during the unwrapping procedures with the MCF algorithm.

Figure 5.6 presents the height differences histogram. For the Marble Canyon example, the threshold to detect an unwrapping error is $h^m_{2\pi} - h^s_{2\pi} = 16.3$ metres. It is emphasised by the

striped area on the plot. Only local maxima outside these limits can be detected. These are the regions depicted in Fig. 5.5 in green in case $\hat{h}^m > \hat{h}^s$ or in red for $\hat{h}^m < \hat{h}^s$. The oval designates a region where the PU errors could not be detected. Indeed, with the help of Fig. 5.4, the height in the *master* scene is found to be 3×33.8 m and 2×50.1 m in the *slave* one. As a result, the height difference there is close to 0 m.

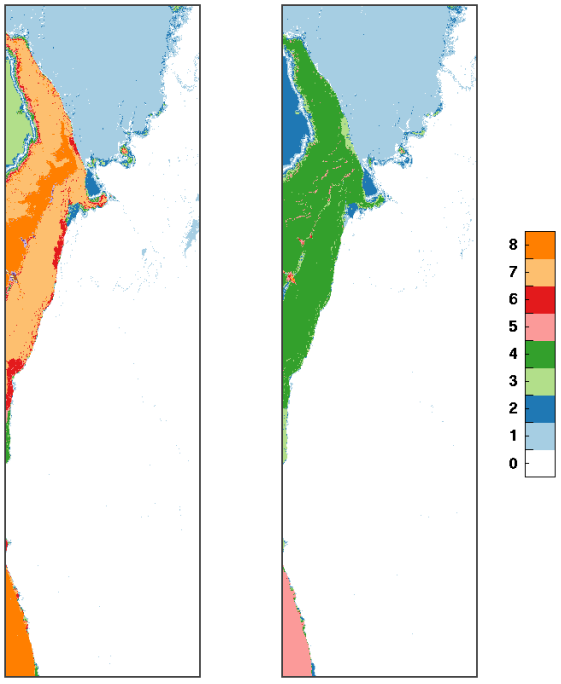

(a) *master* AAD map (b) *slave* AAD map

Fig. 5.4: Absolute Ambiguity Deviation (AAD) maps with respect to the reference height from SRTM for the Marble Canyon example: (a) *master* and (b) *slave* maps.

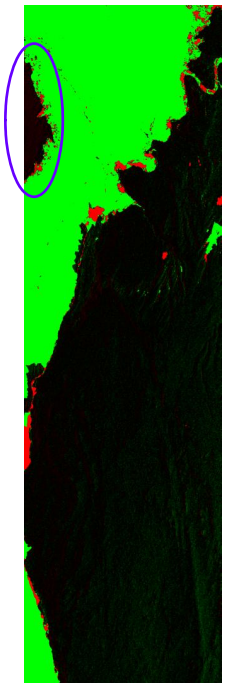

Fig. 5.5: Height discrepancies: regions in green indicate that $\hat{h}^m > \hat{h}^s$ and in red the contrary. The black part represents the main peak of the histogram where both estimated heights are consistent.

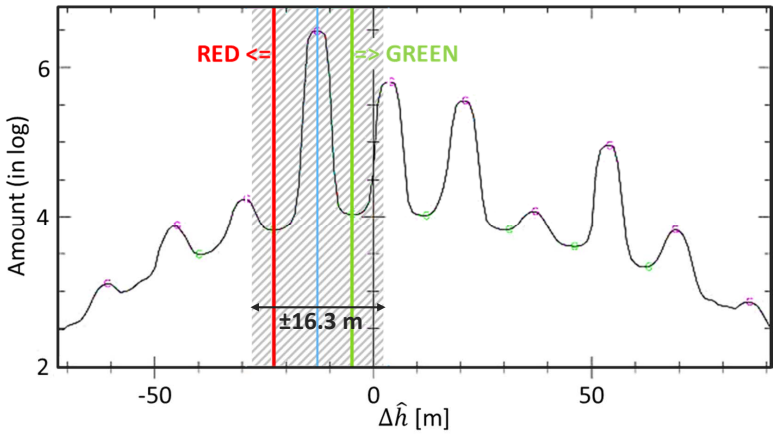

Fig. 5.6. Histogram of the estimated height difference $\Delta\hat{h}$. The main peak indicates the *consistent area* and the other peaks, the height discrepancies i.e. the PU errors. The strips on the histogram indicate the part below the minimum height threshold to detect a PU error.

5.2.4 Constraints and requirements on the data

If both unwrappings are correct, then $\varepsilon^m_{k_{\mathrm{PU}}} = \varepsilon^s_{k_{\mathrm{PU}}} = 0$ and $\Delta\hat{h} = \Delta h_N$. The height difference estimate depends then only on the noise present in both height maps. Accordingly, the detection of a PU error following eq. (5.9) can be successful only if the height threshold given by eq. (5.9) is higher than the level of noise. Figure 5.7 displays the maximum height noise which still allows the detection of PU errors depending on the HoAs configuration. The smaller this value, the

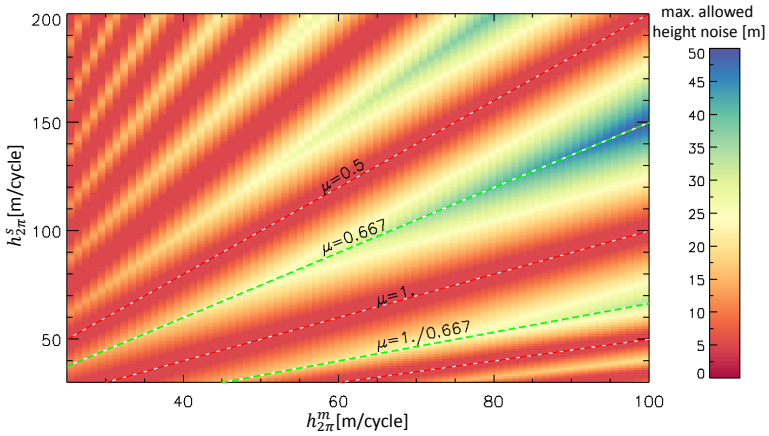

Fig. 5.7. Maximum allowed height noise ($h^m_{2\pi} - h^s_{2\pi}$) to detect a PU error represented as a function of $h^m_{2\pi}$ and $h^s_{2\pi}$. Significant values of the HoA ratio μ are plotted as lines.

more sensitive the detection is with respect to perturbations. A high value means that a clear PU error detection is possible. In this way, the worst cases are when the HoA ratio is equal to 1, 0.5, 2, etc. i.e. when one height of ambiguity is an integer multiple of the other. On the contrary, the best configurations are for $\mu \approx 2/3$ or $\mu \approx 3/2$ for example.

The minimum $\Delta\hat{h}$ which can be identified is thus the maximum value that the noise may take. The goal is to find out the minimum necessary *master* and *slave* coherences, γ^m and γ^s. For simplification, Gaussian distributions are assumed for both height maps. Consequently, the height noise standard deviation is:

$$\sigma_{\Delta h} = \sqrt{{\sigma_{h^m}}^2 + {\sigma_{h^s}}^2} = \sqrt{\left(\frac{h^m_{2\pi}}{2\pi}\sigma_{\psi^m}\right)^2 + \left(\frac{h^s_{2\pi}}{2\pi}\sigma_{\psi^s}\right)^2} \tag{5.10}$$

or as a function of $h^m_{2\pi}$ and μ:

$$\sigma_{\Delta h} = \frac{h^m_{2\pi}}{2\pi}\sqrt{\sigma^2_{\psi^m} + \left(\frac{\sigma_{\psi^s}}{\mu}\right)^2} \tag{5.11}$$

where σ_{ψ^m} and σ_{ψ^s} are the *master* and *slave* phase errors (see Fig. 2.4a).

σ_{ψ^m} and σ_{ψ^s} depend only on γ^m and γ^s and on the multi-looking factor. Presuming that $\gamma^m = \gamma^s$, γ^m has to be found so that $3\sigma_{\Delta h} < h^m_{2\pi} - h^s_{2\pi}$ (i.e. 99.7% of the pixels are below the threshold). The minimum necessary coherence decreases as the number of looks increases. Figure 5.8 depicts the minimum coherence required to detect a height discrepancy depending on both HoAs assuming 25 looks. Several key values for μ are overplotted. When the required coherence approaches 0, it means that a height discrepancy can be detected without limitations. For 25 looks, a minimum coherence of 0.29 is required in the best case and 0.95 in the worst case.

To summarise, a HoA ratio of about 2/3 (or 3/2) offers the best configuration to detect PU errors with a limiting coherence of 0.29. In contrast, for ratios close to 0.5, 1 or 2, the interferometric quality has to be unrealistically high ($\gamma^m > 0.95$) to enable a detection. It is assumed than no significant temporal changes happened between the two acquisitions.

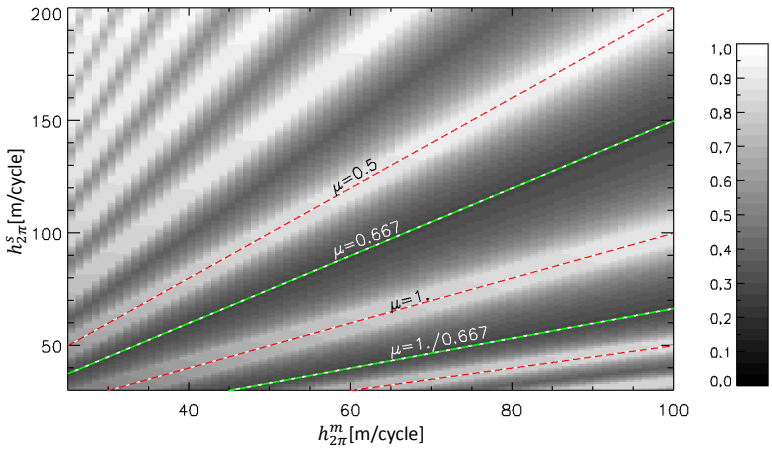

Fig. 5.8. Minimum coherence necessary to detect a PU error with respect to $h^m_{2\pi}$ and $h^s_{2\pi}$ considering 25 looks (it is assumed that both interferograms have the same coherence). Significant values of the HoA ratio μ are plotted as lines.

5.3 Differential interferogram

With two interferograms acquired with similar baselines, only the detection of (some) PU errors is possible. A third (correctly unwrapped) information is required to enable the correction: this is the *differential interferogram*. It has typically a higher HoA and is thus less prone to unwrapping problems.

5.3.1 Characterisation and requirements on the HoA ratio

5.3.1.1 Definition and height of ambiguity

The *differential interferogram* is obtained by demodulating both *master* and *slave* interferograms with respect to each other. All the data related to it are denoted here with the superscript d. By analogy with eq. (2.2), the complex *differential interferogram* v^d is defined by:

$$v^d = v^m v^{s*} = |u_1^m||u_2^m|e^{j\phi^m}|u_1^s||u_2^s|e^{-j\phi^s} \tag{5.12}$$

Therefore, its true phase is the difference of both interferometric phases:

$$\phi^d = \phi^m - \phi^s \tag{5.13}$$

Considering that $\phi = \frac{2\pi}{h_{2\pi}}h$, its HoA $h^d_{2\pi}$ is deduced to be:

$$\frac{1}{h^d_{2\pi}} = \frac{1}{h^m_{2\pi}} - \frac{1}{h^s_{2\pi}} \Leftrightarrow h^d_{2\pi} = \frac{h^m_{2\pi}h^s_{2\pi}}{h^s_{2\pi} - h^m_{2\pi}} \tag{5.14}$$

The *differential interferogram* [9] can exist only if the *master* and *slave* HoAs are not equal. Figure 5.9 depicts the behaviour of $h^d_{2\pi}$ with respect to $h^m_{2\pi}$ and $h^s_{2\pi}$. $h^d_{2\pi}$ tends to infinity when $h^s_{2\pi}$ approaches $h^m_{2\pi}$. Since the aim of the *differential interferogram* is to have a phase which is easy to unwrap, the HoA $h^d_{2\pi}$ has to be greater than $h^m_{2\pi}$ and $h^s_{2\pi}$. Hence, the following constraints must be satisfied:

(1) $h^m_{2\pi} \neq h^s_{2\pi}$
(2) $\left|h^d_{2\pi}\right| > h^m_{2\pi}$ and $\left|h^d_{2\pi}\right| > h^s_{2\pi}$

[9] In this thesis, the *differential interferogram* has thus a different meaning than the one used in D-InSAR e.g. in Permanent Scatterers Interferometry (PSI), where it is the complex interferogram from which a terrain simulated phase is subtracted (Hanssen, 2001).

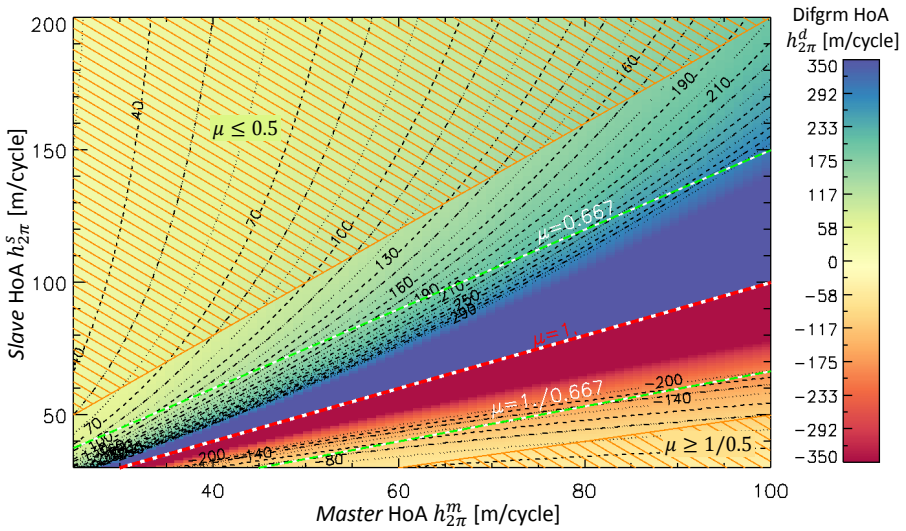

Fig. 5.9. Height of ambiguity (HoA) of the *differential interferogram* $h^d_{2\pi}$ with respect to the *master* and *slave* HoAs. $h^d_{2\pi}$ is positive if $h^s_{2\pi} > h^m_{2\pi}$ (greenish to purple) and negative otherwise (yellow to red). Its limit as $h^m_{2\pi}$ approaches $h^s_{2\pi}$ is $\pm\infty$ (the abrupt change from purple to red).

Figure 5.10 represents the *master* and *slave* wrapped phases of the Marble Canyon example together with the *differential* phase resulting from the interferograms demodulation. The latter has a higher HoA and accordingly less fringes, which eases the PU procedure.

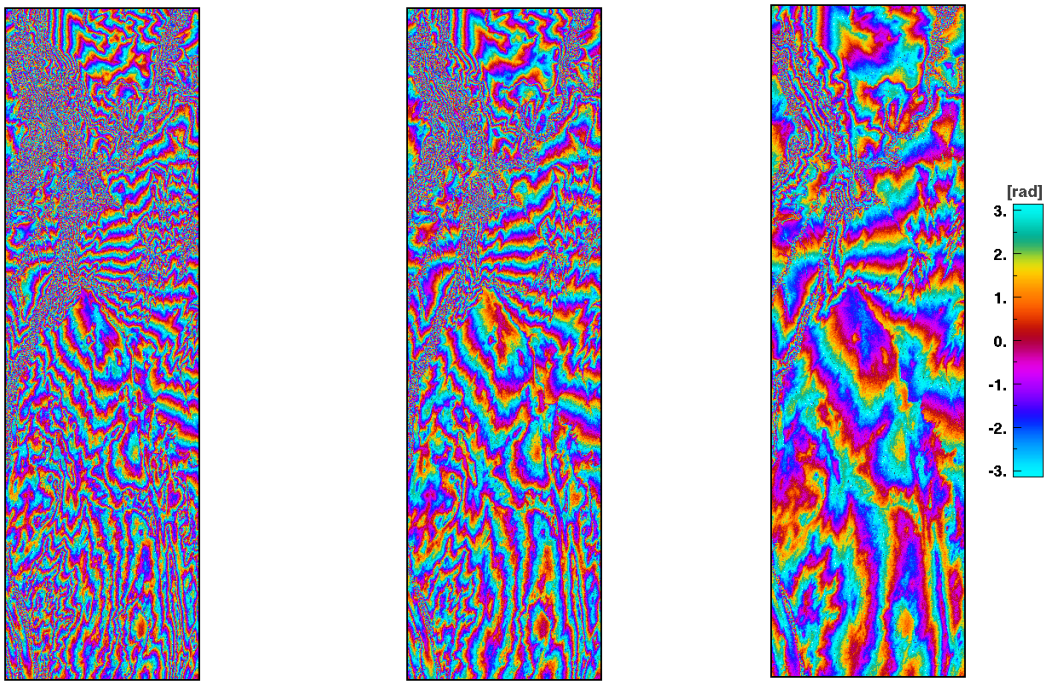

(a) ψ^m, $h^m_{2\pi} = 33.8$ m/cycle (b) ψ^s, $h^s_{2\pi} = 50.1$ m/cycle (c) ψ^d, $h^d_{2\pi} = 102.9$ m/cycle

Fig. 5.10. Wrapped phases of the (a) *master*, (b) *slave* and (c) *differential* interferograms for the Marble Canyon example. The *differential* phase exhibits less fringes than both the *master* and *slave* wrapped phases and is consequently easier to unwrap.

5.3.1.2 Requirements on the HoA ratio μ

By inserting the HoA ratio μ given by eq. (4.1) in eq. (5.14), the following relationships are deduced:

$$h^d_{2\pi} = \frac{h^m_{2\pi}}{1-\mu} \qquad \text{and} \qquad h^d_{2\pi} = \frac{\mu h^s_{2\pi}}{1-\mu} \tag{5.15}$$

Constraint (1) stated in section 5.3.1 is also obvious with these two new equations: μ is not allowed to be equal to 1. Let us analyse the effect of constraint (2) on μ:

$$\left|h_{2\pi}^{d}\right| > h_{2\pi}^{m} \Leftrightarrow \frac{1}{|1-\mu|} > 1 \Rightarrow \begin{cases} \mu > 0 & \text{when } 1-\mu > 0 \Leftrightarrow 0 < \mu < 1 \\ \mu < 2 & \text{when } 1-\mu < 0 \Leftrightarrow 1 < \mu < 2 \end{cases}$$

$$\left|h_{2\pi}^{d}\right| > h_{2\pi}^{s} \Leftrightarrow \left|\frac{\mu}{1-\mu}\right| > 1 \Rightarrow \begin{cases} \mu > 0.5 & \text{when } 1-\mu > 0 \Leftrightarrow 0.5 < \mu < 1 \\ \text{always} & \text{when } 1-\mu < 0 \Leftrightarrow \mu < 1 \end{cases}$$

As a result, a *differential interferogram* able to support the PU correction of the master unwrapped phase is obtained only if:

$$0.5 < \mu < 1 \qquad \text{or} \qquad 1 < \mu < 2 \tag{5.16}$$

When μ approaches 0.5, $h_{2\pi}^{d}$ gets close to $h_{2\pi}^{s}$. Similarly when μ gets near to 2, $h_{2\pi}^{d}$ approaches $h_{2\pi}^{m}$. In both cases, the advantage of the *differential interferogram* is dramatically reduced. Besides, if μ approaches 1, $h_{2\pi}^{d}$ tends to infinity and so does the resulting height noise. Therefore, a suitable range for μ must be found.

5.3.2 Differential interferogram phase statistics

The statistics of the *differential interferogram* phase are derived under the assumption that the SAR images of the *master* interferogram are uncorrelated with these of the *slave* one. In this way, both interferograms are independent. This is a classical simplification in multichannel interferometry (see section 3.1). In the special case of TDM, the two acquisitions are two bistatic independent measurements separated in time (and space) so that the two interferograms can be treated as uncorrelated. Consequently, the probability density function (*pdf*) of the true *differential* phase $p(\phi^d;\gamma^m,\gamma^s)$ is the convolution (Urkowitz, 1983) of the two *master* and *slave* interferometric phase *pdfs* $p(\phi^m;\gamma^m)$ and $p(\phi^s;\gamma^s)$ given by eq. (2.11):

$$p(\phi^d;\gamma^m,\gamma^s) = p(\phi^m;\gamma^m) * p(-\phi^s;\gamma^s) \tag{5.17}$$

$p(\phi^d;\gamma^m,\gamma^s)$ is centred in $\phi_0^d = \phi_0^m - \phi_0^s$. The *differential* phase *pdf* is comparable to the gradient *pdf* (Bamler et al., 1998) but with phase values taken from different interferograms. Table 5.1 gathers shapes that $p(\phi^d;\gamma^m,\gamma^s)$ may take for various values of the coherences γ^m and γ^s. Since the true *differential* phase is bounded within $[\phi_0^d - 2\pi; \phi_0^d + 2\pi[$, every value lying out of the $[\phi_0^d - \pi; \phi_0^d + \pi[$ interval will be wrapped inside $[-\pi;\pi[$ when the wrapped *differential* phase is computing. It results in an increase of the noise. Consequently, the *differential interferogram* has to be computed with the *multi-looked* phases. In this case, its *pdf* is:

$$p(\phi^d;\gamma^m,\gamma^s,L) = p(\phi^m;\gamma^m,L) * p(-\phi^s;\gamma^s,L) \tag{5.18}$$

where $p(\phi^m;\gamma^m,L)$ and $p(\phi^s;\gamma^s,L)$ are the multi-looked *master* and *slave* phase *pdfs* given by eq. (2.12). Table 5.2 depicts the shapes that $p(\phi^d;\gamma^m,\gamma^s,L)$ has with 25 looks for the coherences of the previous table. With a sufficient number of looks, the *master* and *slave* phase *pdfs* are well inside an interval $[-\pi/2;\pi/2[$ centred in their respective expected phases even for low coherences. Thus the resulting *differential pdf* is well bounded within $[\phi_0^d - \pi; \phi_0^d + \pi[$ and no additional noise appears.

Based on simulations, the behaviour of the standard deviation of the *differential* phase σ_{ϕ^d} depending on γ^m and γ^s can be studied in more detail. Figure 5.11 displays σ_{ϕ^d} as a function of γ^m and γ^s. The standard deviation of the *differential* phase has the same limit as the

Coherences	Interferometric phase *pdf*	*Differential* phase *pdf*
$\gamma^m = 0.3$ $\gamma^s = 0.3$	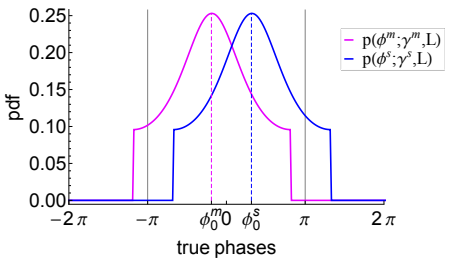	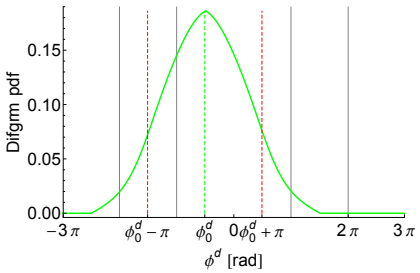
$\gamma^m = 0.5$ $\gamma^s = 0.75$	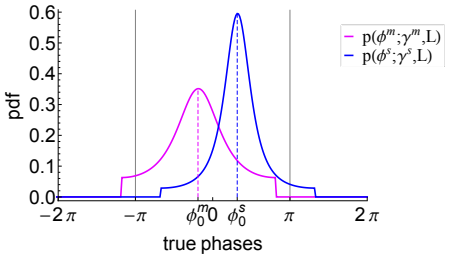	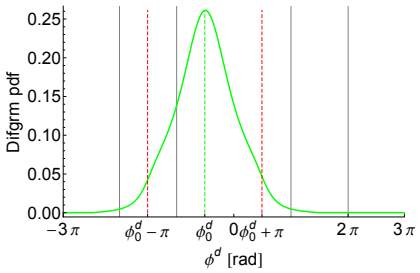

Table 5.1. Single-look *pdfs* of the true *differential* phase: (left side) the two true interferometric phase *pdfs* $p(\phi^m;\gamma^m)$ and $p(\phi^s;\gamma^s)$ and (right side) the resulting *differential* phase *pdf* $p(\phi^d;\gamma^m,\gamma^s)$ for γ^m and γ^s: $\gamma^m = \gamma^s = 0.3$ and for $\gamma^m = 0.5$ and $\gamma^s = 0.75$.

Coherences	Interferometric phase *pdf*	*Differential* phase *pdf*
$\gamma^m = 0.3$ $\gamma^s = 0.3$	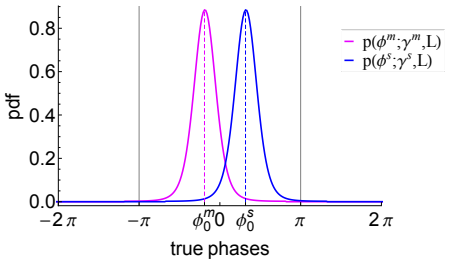	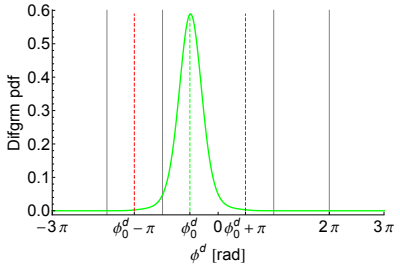
$\gamma^m = 0.5$ $\gamma^s = 0.75$	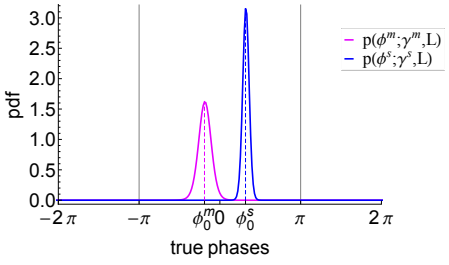	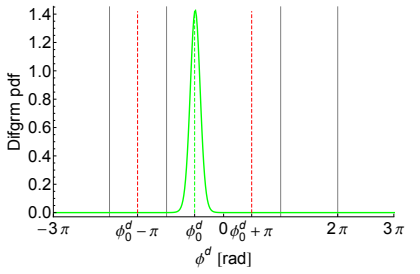

Table 5.2. Multi-looked *pdfs* of the true *differential* phase assuming 25 looks: (left side) the two true interferometric phase *pdfs* $p(\phi^m;\gamma^m,25)$ and $p(\phi^s;\gamma^s,25)$ and (right side) the resulting *differential* phase *pdf* $p(\phi^d;\gamma^m,\gamma^s,25)$ for $\gamma^m = \gamma^s = 0.3$ and for $\gamma^m = 0.5$ and $\gamma^s = 0.75$.

interferometric phase standard deviation when both coherences approach 0. Otherwise, σ_{ϕ^d} is obviously always higher than σ_{ϕ^m} or σ_{ϕ^s}.

Figure 5.12 presents two profiles of σ_{ϕ^d} as a function of γ^m: one for $\gamma^s = \gamma^m$ and the other for $\gamma^s = 0.4$ for different number of looks. Comparing Fig. 5.12a to Fig. 2.4a that showed the phase standard deviation, a very similar behaviour is noticeable. Indeed, the relationship $\sigma^2_{\phi^d} = \sigma^2_{\phi^m} + \sigma^2_{\phi^s}$ (i.e. presuming Gaussian distributions to derive the *differential* phase standard deviation) is true for medium to high coherences and number of looks. In case $\gamma^m \neq \gamma^s$, σ_{ϕ^d}

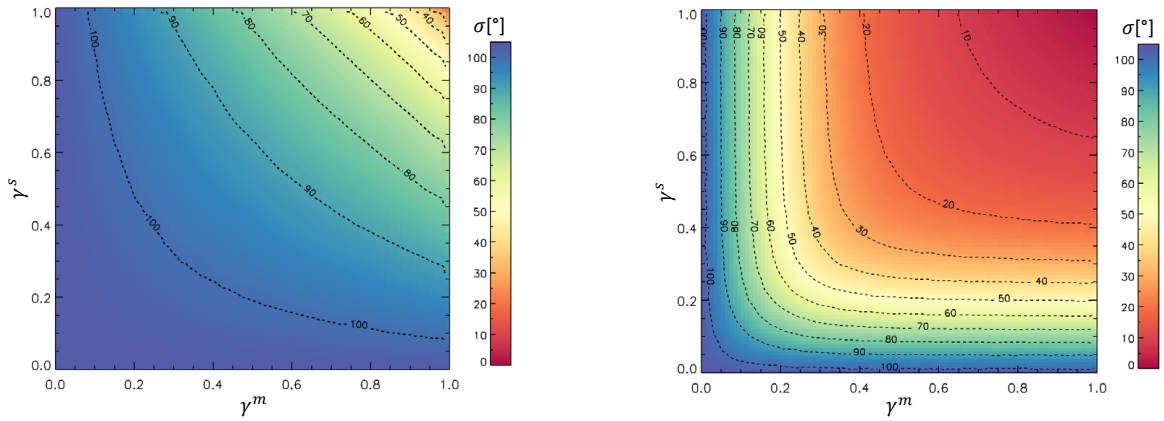

(a) σ_{ϕ^d} for L=1 (b) σ_{ϕ^d} for L=25

Fig. 5.11. *Differential* phase standard deviation σ_{ϕ^d} as a function of γ^m and γ^s for (a) 1 look and (b) 25 looks.

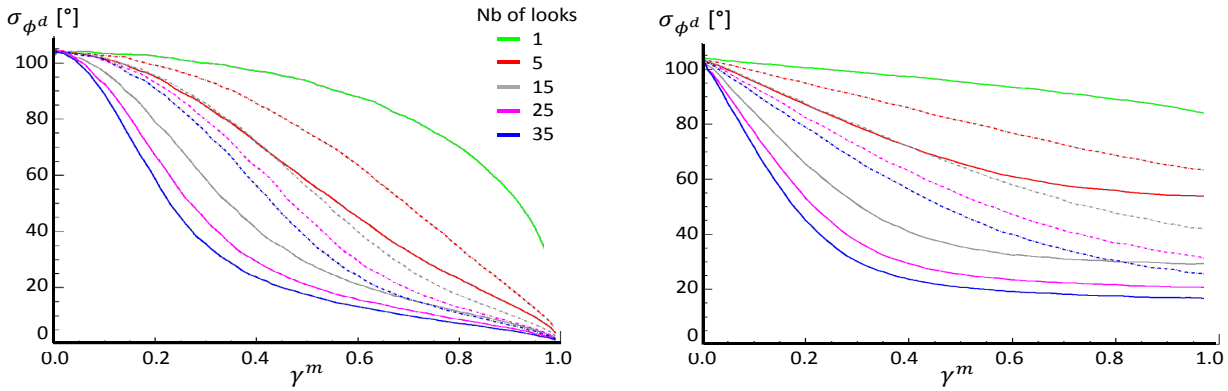

(a) $\gamma^s = \gamma^m$ (b) $\gamma^s = 0.4$

Fig. 5.12. *Differential* phase standard deviation σ_{ϕ^d} as a function of γ^m for (a) $\gamma^s = \gamma^m$ and (b) $\gamma^s = 0.4$ for different number of looks. The solid lines show the *differential* phase standard deviation when the *master* and *slave* interferograms are multi-looked before the *differential interferogram* computation whereas the dash-dotted lines depict σ_{ϕ^d} when the multi-looking is applied after the formation of the *differential interferogram*.

cannot be better than the standard deviation of the lower coherence (see Fig. 5.12b). The standard deviation has been calculated for the cases the multi-looking has been done after the formation of the *differential interferogram* (dash-dotted lines in Fig. 5.12) or prior to its computation (solid lines). The noise reduction due to a multi-looking carried out in a first step increases with the number of looks.

To conclude, σ_{ϕ^d} is always equal or greater than σ_{ϕ^m} and σ_{ϕ^s}. In addition, because of its higher HoA, the height map obtained by means of the *differential interferogram* is more sensitive to noise and has to be handled carefully. Finally, it is mandatory to perform a multi-looking on the *master* and *slave* interferograms before the calculation of the *differential interferogram* to avoid additional noise and enhance the phase quality.

5.3.3 Differential coherence and compatibility

Similarly to the coherence coefficient for an interferogram, measures to evaluate the *differential interferogram* quality are required. The *differential* phase is assessed by the *differential coherence* and the *compatibility* gives an impression on how the *master* and *slave* interferograms agree.

5.3.3.1 Differential coherence

In InSAR, the complex interferometric coherence is defined as the normalised complex correlation between the two SAR images. It is a local measure of the interferogram quality. The intention is here to define an alike criterion for the *differential interferogram*: the *differential coherence*. The latter cannot be the complex correlation coefficient of the two interferograms considering it is equal to the product of the cross-interferogram coherences (see the demonstration in appendix D). Indeed, the complex correlation would be equal (or close) to 0 due to the large temporal separation between the interferograms (the SAR images of one interferograms are considered as uncorrelated with those of the second).

By analogy with the interferometric coherence, the *differential coherence* γ^d is defined in this thesis as:

$$\gamma^d = \frac{\mathrm{E}\left[v^m v^{s*}\right]}{\sqrt{\mathrm{E}\left[|v^m|^2\right]\mathrm{E}\left[|v^s|^2\right]}} \tag{5.19}$$

In comparison to the complex correlation coefficient, the mean values are not subtracted before the computation of the expected values. After similar calculations as those of appendix D, an expression of γ^d is obtained:

$$\gamma^d = \frac{\gamma^m\gamma^{s*} + \gamma_1\gamma_2^*}{\sqrt{\left(1+|\gamma^m|^2\right)\left(1+|\gamma^s|^2\right)}} \approx \frac{\gamma^m\gamma^{s*}}{\sqrt{\left(1+|\gamma^m|^2\right)\left(1+|\gamma^s|^2\right)}} \tag{5.20}$$

where γ_1 and γ_2 are the coherences of the cross-interferograms defined by eq. (D.8) thus approaching 0. In this case, the *differential coherence* cannot be greater than 0.5.

Its estimate is computed as follows (assuming ergodicity):

$$\left|\hat{\gamma}^d\right| = \frac{\left|\sum_{l=1}^{L} v^m[l]\exp^{-j\phi_T^m} v^{s*}[l]\exp^{j\phi_T^s}\right|}{\sqrt{\sum_{l=1}^{L}|v^m[l]|^2\sum_{l=1}^{L}|v^s[l]|^2}} \tag{5.21}$$

where v^m and v^s have already been multi-looked as suggested in section 5.3.2. Figure 5.13 depicts $\hat{\gamma}^d$ as a function of γ^m respectively for $\gamma^s = \gamma^m$ and $\gamma^s = 0.4$. In a same way as the interferometric coherence estimate, $\hat{\gamma}^d$ is overestimated. The bias is reduced with higher number of looks. For low values of γ^m and γ^s, $\hat{\gamma}^d$ converges to comparable values to the interferometric coherences.

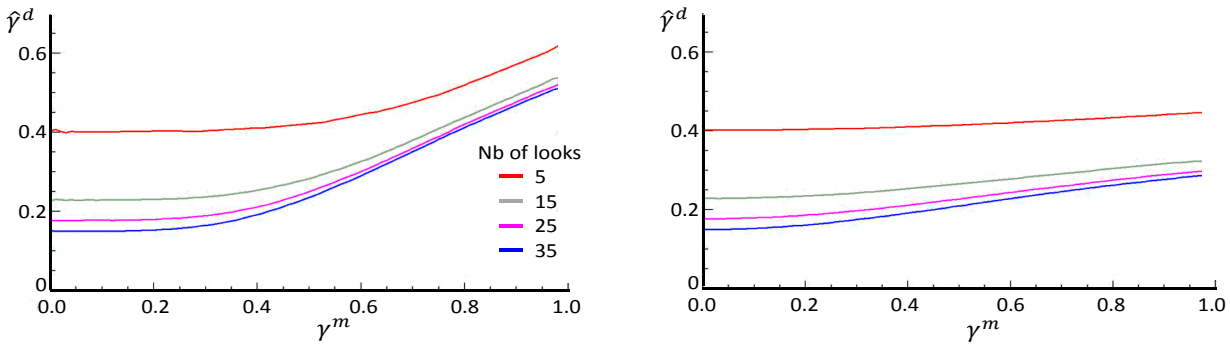

(a) $\gamma^s = \gamma^m$ (b) $\gamma^s = 0.4$

Fig. 5.13. Estimated *differential coherence* as a function of γ^m for (a) $\gamma^s = \gamma^m$ and (b) $\gamma^s = 0.4$ for different number of looks.

5.3.3.2 Interferograms' compatibility

It is also necessary to know how well the *master* and the *slave* interferograms agree or how *compatible* they are. The motivation is simple: the correction can be achieved only if the two interferograms are *compatible* i.e. if they have the same scene content (i.e. no terrain or extreme surface properties changes).

This new quality parameter, called *compatibility*, has the following characteristics:

- when one of the *master* and *slave* interferograms is incoherent, the *compatibility* is low,
- the *compatibility* may be low although both interferograms are coherent: the terrain may have changed between the two acquisitions; therefore, it depends also on the *differential coherence* γ^d,
- persistent areas are highly compatible.

The harmonic mean, which allows to average ratios, is chosen. Both *master* and *slave* coherences are first averaged, then their harmonic mean is averaged with γ^d. As a result, γ^m and γ^s have a bigger influence on the *compatibility* ξ (which varies between 0 and 1):

$$\xi = \frac{2}{\frac{1}{\gamma^d} + \frac{\frac{1}{\gamma^m}+\frac{1}{\gamma^s}}{2}} = \frac{4\gamma^m\gamma^s\gamma^d}{2\gamma^m\gamma^s + \gamma^m\gamma^d + \gamma^s\gamma^d} \tag{5.22}$$

This definition allows to get a *compatibility* map which is richer in contrast than the one proposed in Lachaise et al. (2012b).

The *differential interferogram* values are then divided into three classes by means of ξ:

- *compatible* areas: both *master* and *slave* interferograms agree, they can be corrected if necessary
- *incompatible* areas: the *master* and *slave* interferograms disagree or one of them has locally a very low coherence; such regions are for example, in shadow or layover, temporary flooded areas, melting glaciers, etc. They are excluded from a potential correction because the available information does not match.
- *low compatible* areas: they are those which cannot be clearly determined to belong to one or the other category. These regions are corrected depending on their neighbourhood.

Figure 5.14 depicts the compatibility mask together with the *master* and *slave* coherences. The distribution of ξ can be seen in Fig. 5.14d. An adaptive thresholding permits to segment the *incompatible* and *low compatible* pixels. In the presented example of the Marble Canyon, *incompatible* areas (in black in Fig. 5.14c) are due to the radar shadow and the Paria river.

5.3.4 Unwrapping of the differential phase and correctness check

The *differential interferogram* exhibits a higher noise so that an extra fringe-direction adaptive filtering (which is computationally efficient) is applied on its phase after the multi-looking. Interferometric phase filtering is studied extensively in different contexts but is not the matter of this thesis and will not be further discussed.

The filtered *differential* phase is unwrapped with the MCF algorithm. In most cases, its unwrapping is straightforward due to its high HoA. However, in very steep terrain, in presence of high noise level or when the baselines configuration is not optimal ($\mu \to 0.5$, $\mu \to 1$ or $\mu \to 2$), errors may arise. Similarly to eqs. (5.1) and (5.3), the estimated absolute unwrapped phase of the *differential interferogram* can be written as:

$$\hat{\phi}^d = \psi^d + 2\hat{k}^d_{\mathrm{PU}}\pi + \hat{k}^d_{\mathrm{off}}\pi = \psi^d + 2\left(k^d_{\mathrm{PU}} + \varepsilon_{k^d_{\mathrm{PU}}}\right)\pi + \hat{k}^d_{\mathrm{off}}\pi \tag{5.23}$$

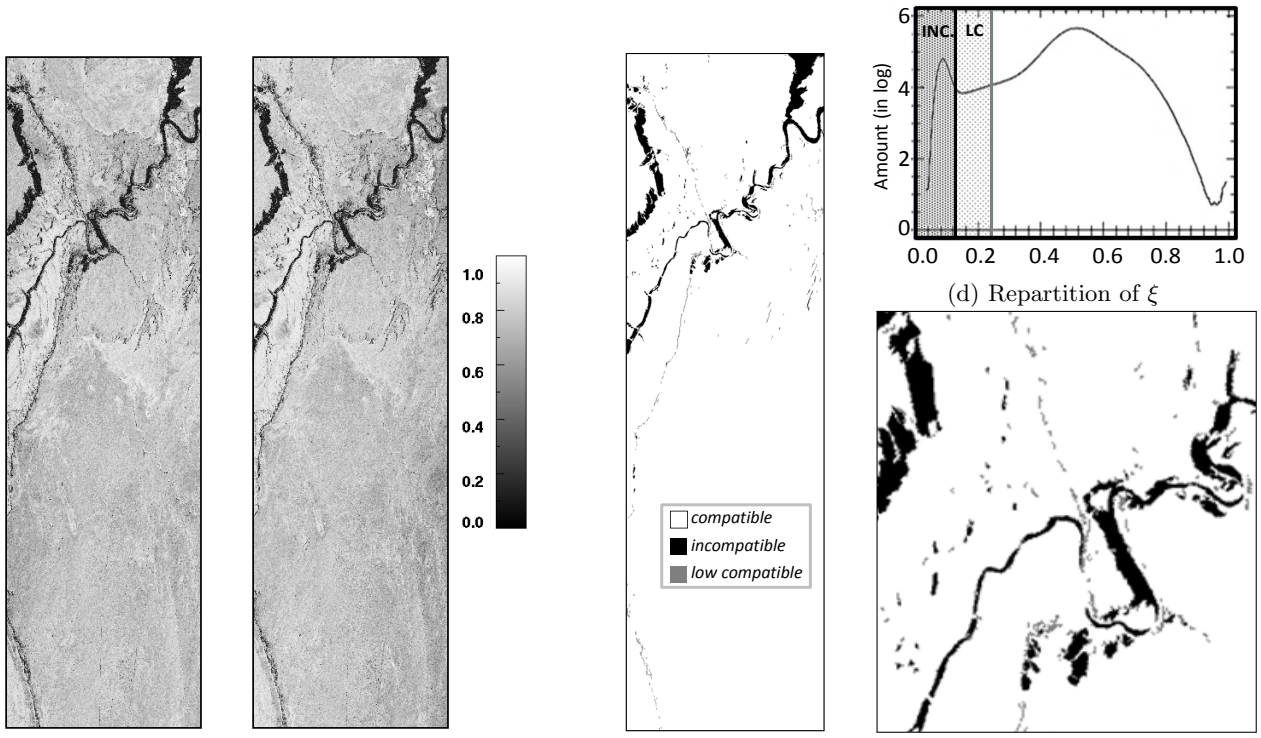

(a) γ^m (b) γ^s (c) mask from ξ (d) Repartition of ξ (e) zoom of in ξ mask

Fig. 5.14. Coherences of the *master* and the *slave* interferograms (a-b) and mask of the compatibility (c) for the Marble Canyon example. The *incompatible* (in black) and *low compatible* (in gray) regions are found by means of an adaptive thresholding on the compatibility distribution in (d). (e) is a zoom to distinguish the *low compatible* pixels.

where $\varepsilon_{k^d_{\mathrm{PU}}}$ reflects a possible misestimated ambiguity band $\hat{k}^d_{\mathrm{PU}}$, thus a potential PU error. The absolute phase offset estimation ($\hat{k}^d_{\mathrm{off}}\pi$) is performed together with the evaluation of the unwrapping results.

In the ITP, the assessment of the estimated unwrapped phase of an interferogram is performed using the stereo-radargrammetric phase derived from the coregistration shifts. The goal here is to follow the same approach. Nonetheless, no coregistration shifts, i.e. no stereo-radargrammetric phase, exist for the *differential interferogram*. Therefore, a substitute is adopted.

The shifts come from the parallaxes between the satellites. The phase stemming from them is absolute and reflects the interferometric geometrical configuration (section 3.2.1). Consequently, an equivalent stereo-radargrammetric phase ϕ^d_{rdgr} can be deduced from ϕ^m_{rdgr} and ϕ^s_{rdgr}. By converting these two phases into height, two equivalent height maps are obtained (characterised by different level of noise). These maps are averaged in order to reduce the noise and enhance the quality and accuracy. Finally, an equivalent of ϕ^d_{rdgr} is generated by converting the resulting height to the *differential interferogram* geometry by means of $h^d_{2\pi}$. Altogether, ϕ^d_{rdgr} is obtained as follows:

$$\phi^d_{\mathrm{rdgr}} = \frac{1}{h^d_{2\pi}} \left(\frac{\phi^m_{\mathrm{rdgr}} h^m_{2\pi} + \phi^s_{\mathrm{rdgr}} h^s_{2\pi}}{2} \right) \tag{5.24}$$

The correctness check can now be performed with the ITP algorithm described in Rossi et al. (2012) and section B.3.5.2. A downsampled version of the estimated unwrapped phase $\hat{\phi}^d$ is compared to ϕ^d_{rdgr}, which is approximately equal to (eq. (3.16)):

$$\phi^d_{\mathrm{rdgr}} \approx \psi^d + 2k_{\mathrm{PU}}\pi + \hat{k}^d_{\mathrm{off}}\pi \tag{5.25}$$

Referring to $\hat{\phi}^d_{\text{DoSa}}$ as the downsampled version of $\hat{\phi}^d$, the phase difference is approximately equal to:

$$\phi^d_{\text{rdgr}} - \hat{\phi}^d_{\text{DoSa}} \approx 2\varepsilon_{k^d_{\text{PU}}}\pi + \hat{k}^d_{\text{off}}\pi \tag{5.26}$$

The absolute offset and the possible errors in the estimation of the ambiguity band during the unwrapping procedure remain unchanged in the downsampled version of $\hat{\phi}^d$.

The main peak of the distribution of the phase differences defines the absolute phase offset $\hat{k}^d_{\text{off}}\pi$. If the distribution is unimodal, no correction of the *differential* ambiguity band is required and the next step is to correct the master unwrapped phase. On the contrary, if both phases diverge, the distribution is multimodal. Inasmuch as the stereo-radargrammetric phase is absolute, local maxima correspond directly to the unwrapping errors in the (low resolution) estimated *differential* unwrapped phase. However, the coarser resolution forbids from mitigating errors pixel-wise.

Figure 5.15 presents the unwrapping results of the *differential* phase and its assessment for the Marble Canyon example. The AAD map in Fig. 5.15b allows to get a visual impression of the PU errors localisation of the unwrapped phase depicted in Fig. 5.15a. The outputs of the correctness check with the stereo-radargrammetric phase are provided by Figs. 5.15c and 5.15d. The histogram of the phase differences $\phi^d_{\text{rdgr}} - \hat{\phi}^d_{\text{DoSa}}$ presents several peaks pointing out (automatically) the existence of PU errors. The estimated absolute phase offset is given by the ambiguity band where the main peak is located. The three secondary peaks are in compliance with the three distinct regions observable in Fig. 5.15b.

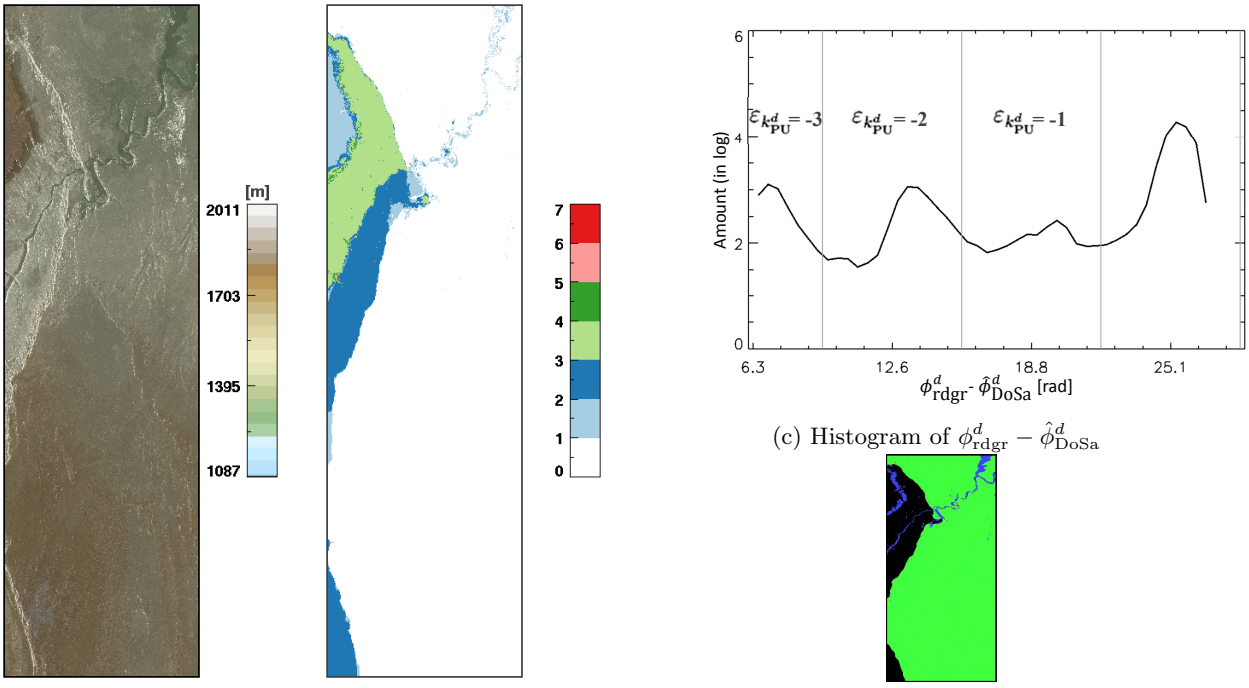

(a) Slant range height (b) AAD map (c) Histogram of $\phi^d_{\text{rdgr}} - \hat{\phi}^d_{\text{DoSa}}$ (d) Radargrammetry

Fig. 5.15. *Differential interferogram* unwrapping results and assessment for the Marble Canyon example: (a) *differential* phase unwrapped with the MCF algorithm converted to slant range height, (b) Absolute Ambiguity Deviation (AAD) with respect to SRTM (visual check); and automatic correctness check by means of the stereo-radargrammetry: (c) histogram of the phases differences and (d) correctness mask: green means agreement between the unwrapped and the stereo-radargrammetric phases (representing the main peak of the distribution depicted in (c)) and black the presence of probable PU errors (the resolution of the stereo-radargrammetric phase is about 13×21 coarser than the interferometric one).

5.3.5 Differential interferogram unwrapped phase correction by means of the stereo-radargrammetry

Contrary to a single interferogram (refer to section 4.2.2), the correction of the *differential interferogram* with the stereo-radargrammetric phase is possible. This phase is obtained by averaging ϕ^m_{rdgr} and ϕ^s_{rdgr}, therefore it has a better accuracy. In addition, the higher HoA of the *differential interferogram* (about 100 m/cycle) makes it less subject to PU errors. The correction must still be carried out carefully due to the coarser resolution of the stereo-radargrammetric absolute measurements.

5.3.5.1 Principle

The correction of the unwrapped phase of the *differential interferogram* is a critical point in the whole DB-PUC framework. Indeed, this phase and the stereo-radargrammetric one differ in resolution and quality. Not only the correction cannot be performed pixel-wise but also regions must be big enough to counter the limited accuracy of the stereo-radargrammetry.

Every secondary peak of the distribution of the phase differences presented in section 5.3.4, represents a part of the unwrapped phase which has been wrongly estimated by a certain integer $\varepsilon_{k^d_{\text{PU}}}$. The correction to apply on the ambiguity band (this one is thereby not estimated again) equal to $-\varepsilon_{k^d_{\text{PU}}}$ is retrieved as follows:

$$-\varepsilon_{k^d_{\text{PU}}} = -\left\lfloor \frac{\phi^d_{\text{rdgr}} - \hat{\phi}^d_{\text{DoSa}} - \hat{k}^d_{\text{off}}\pi}{2\pi} \right\rceil \tag{5.27}$$

where $\lfloor . \rceil$ is the round function to the nearest integer. In other words, the difference in cycles between the main and a secondary peak corresponds to the correction to apply (see Fig. 5.15c). However, to be able to correct the *differential* unwrapped phase, it is necessary to go back to the full interferogram resolution. As a consequence, regions detected as erroneous in the coarser difference map have to be identified in the original unwrapped phase. The critical step is to find the exact boundaries of these regions. After that, the correction is performed and the *master* unwrapped phase can be analysed.

The edges are composed of the borderlines of the discrepancies found by comparing the *master* and the *differential* height maps, of the incompatible regions, and of the residues and branch-cuts. The discrepancy map and the incompatible regions provide a first idea of the borderlines position, which is enhanced by examining the residues and the branch-cuts. Indeed, the former are an indicator of phase gradient exceeding π and consequently, of possible sources of PU errors. As for branch-cuts, they may be wrongly placed by the MCF algorithm, hence are possible lines of demarcation for incorrect regions. The regions are then clearly delimited. A region growing allows to find the corresponding area to each low resolution region. The ambiguity bands to correct are finally applied to the recovered areas. Figure 5.16 illustrates the results of the edge detection as well as the correction achieved for the *differential interferogram* for the Marble Canyon example.

5.3.5.2 Theoretical feasibility and limits of the correction

Given the errors $\sigma_{\Delta\chi^m}$ and $\sigma_{\Delta\chi^s}$ of the shifts estimated either by coherent or incoherent cross-correlation (see section 3.2.1 and Bamler and Eineder (2005); De Zan (2014)), the standard deviations of the stereo-radargrammetric phases ϕ^m_{rdgr} and ϕ^s_{rdgr} are:

$$\sigma_{\phi^m_{\text{rdgr}}} = \sigma_{\Delta\chi^m}\frac{2\pi f_0}{f_{\text{RS}}} \qquad \text{and} \qquad \sigma_{\phi^s_{\text{rdgr}}} = \sigma_{\Delta\chi^s}\frac{2\pi f_0}{f_{\text{RS}}} \tag{5.28}$$

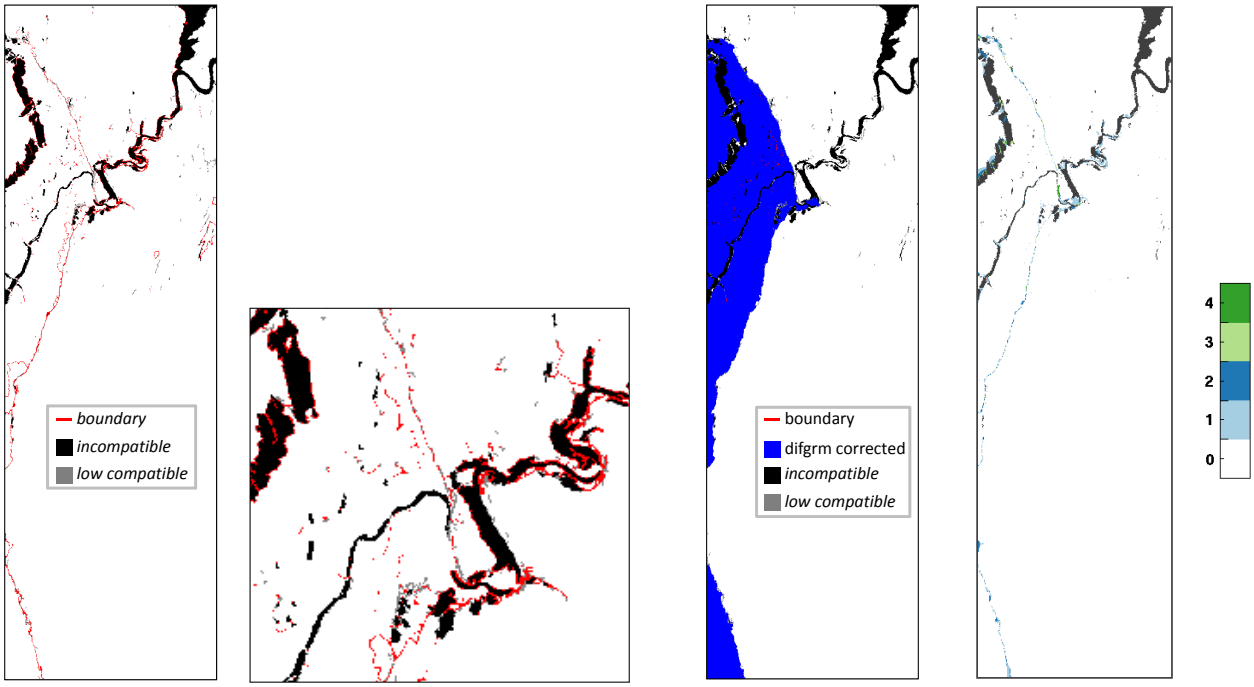

(a) Boundary mask (b) zoom of boundary mask (c) Areas detected for the correction (d) AAD map after correction with respect to SRTM

Fig. 5.16. Correction of the unwrapped *differential* interferogram: (a) edges which delimit the potential regions to correct, (b) zoom of the edge mask (c) the detected regions to rectify and (d) resulting Absolute Ambiguity Deviation (AAD) map with respect to SRTM where the incompatible regions have been masked out (the remaining discrepant pixels are due to the resolution differences with SRTM).

Assuming Gaussian distributions of the shifts, $\sigma_{\phi^d_{\text{rdgr}}}$ is derived as follows:

$$\sigma_{\phi^d_{\text{rdgr}}} = \frac{1}{2}\left|\frac{h^m_{2\pi}}{h^d_{2\pi}}\right|\sqrt{\sigma^2_{\phi^m_{\text{rdgr}}} + \left(\frac{h^s_{2\pi}}{h^m_{2\pi}}\right)^2 \sigma^2_{\phi^s_{\text{rdgr}}}} \tag{5.29}$$

or, as a function of the HoA ratio μ:

$$\sigma_{\phi^d_{\text{rdgr}}} = \frac{|1-\mu|}{2}\sqrt{\sigma^2_{\phi^m_{\text{rdgr}}} + \frac{\sigma^2_{\phi^s_{\text{rdgr}}}}{\mu^2}} \tag{5.30}$$

Accordingly, the *master* and *slave* stereo-radargrammetric phase accuracies influence differently $\sigma_{\phi^d_{\text{rdgr}}}$ since $\sigma_{\phi^s_{\text{rdgr}}}$ is divided by μ.

The coregistration shifts are estimated by means of the coherent cross-correlation (when possible). $\sigma_{\phi^d_{\text{rdgr}}}$ is then equal to:

$$\sigma_{\phi^d_{\text{rdgr}}} = |1-\mu|\sqrt{\frac{3}{2N_c}}osf^{3/2}\frac{f_0}{f_{\text{RS}}}\sqrt{\frac{1-\gamma^{m2}}{\gamma^{m2}} + \frac{1-\gamma^{s2}}{\mu^2\gamma^{s2}}} \tag{5.31}$$

Incoherent correlation is used for low coherent patches. In this case, the *differential coherence* and the *compatibility* are also low so that the concerned areas are *incompatible* and are not considered in the correction process. For this reason, the case of the incoherent shifts is not addressed.

If $\sigma_{\phi^m_{\text{rdgr}}}$ is assumed to be equal to $\sigma_{\phi^s_{\text{rdgr}}}$ i.e. that $\gamma^m = \gamma^s$, the ratio between $\sigma_{\phi^d_{\text{rdgr}}}$ and $\sigma_{\phi^m_{\text{rdgr}}}$

can be derived from eq. (5.30):

$$\frac{\sigma_{\phi^m_{\text{rdgr}}}}{\sigma_{\phi^d_{\text{rdgr}}}} = \frac{2\mu}{|1-\mu^2|} \tag{5.32}$$

The behaviour of this ratio is depicted on Fig. 5.17. For the typical HoA ratio $\mu = 0.7$, $\sigma_{\phi^d_{\text{rdgr}}}$ is about 3 times smaller than $\sigma_{\phi^m_{\text{rdgr}}}$. Thus, possible phase unwrapping errors are detectable in the unwrapped phase of the *differential interferogram* with these settings.

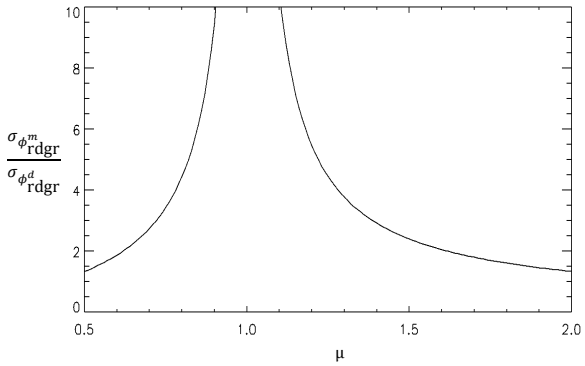

Fig. 5.17. Ratio of the standard deviations of the *master* and *differential* stereo-radargrammetric phases versus the HoA ratio μ (eq. (5.32)).

To derive the correct ambiguity band, $\sigma_{\phi^d_{\text{rdgr}}}$ must be smaller than 1/3 of a cycle thus:

$$\sigma_{\phi^d_{\text{rdgr}}} \leq \frac{2\pi}{3} \text{ [rad]} \qquad \text{or} \qquad \sigma_{\phi^d_{\text{rdgr}}} \leq 120 \text{ [°]} \tag{5.33}$$

Equation (5.31) is depicted on Fig. 5.18 for different μ lower than 1 (the behaviours are inverted for $1 < \mu < 2$). It can be noticed that the error gets lower as μ approaches 1. For optimal HoA ratio $\mu = 0.7$, $\sigma_{\phi^d_{\text{rdgr}}}$ is lower than 120° only for higher coherences. Consequently, the PU error cannot be determined patch-wise but only region-wise i.e. for several patches (since the resulting error is improved by the square root of the number of averaged patches N_{patches}). Finally, the minimum amount of patches necessary to achieve the required accuracy (eq. (5.33)) is:

$$N_{\text{patches}} \geq \left(\frac{3\sigma_{\phi^d_{\text{rdgr}}}}{2\pi}\right)^2 \qquad \text{or} \qquad N_{\text{patches}} \geq \left(\frac{\sigma_{\phi^d_{\text{rdgr}}}}{120}\right)^2 \tag{5.34}$$

This holds only for uniform patches i.e. flat terrain. It implies a perfect removal of the terrain phase. Any residual artefacts or non-Gaussian scatterers degrade the accuracy. In practice, N_{patches} must be higher.

5.3.6 Summary

In this section, the *differential interferogram* has been presented. It is obtained by demodulating the *master* and the *slave* interferograms with respect to each other.

Its aim is to support the correction of the *master* unwrapped phase. For this reason, its HoA must be greater than the two other. Consequently, it can be helpful only if $0.5 < \mu < 1 < \mu < 2$. As μ approaches 1, the height noise tends to infinity so that no correction of the *master* unwrapped phase is conceivable. By contrast, if it gets close to 0.5 or 2, its HoA has the same order of magnitude than $h^m_{2\pi}$ and $h^s_{2\pi}$. A compromise on μ is thus when $\mu \in [0.65, 0.85]$ or $[1/0.85, 1/0.65]$.

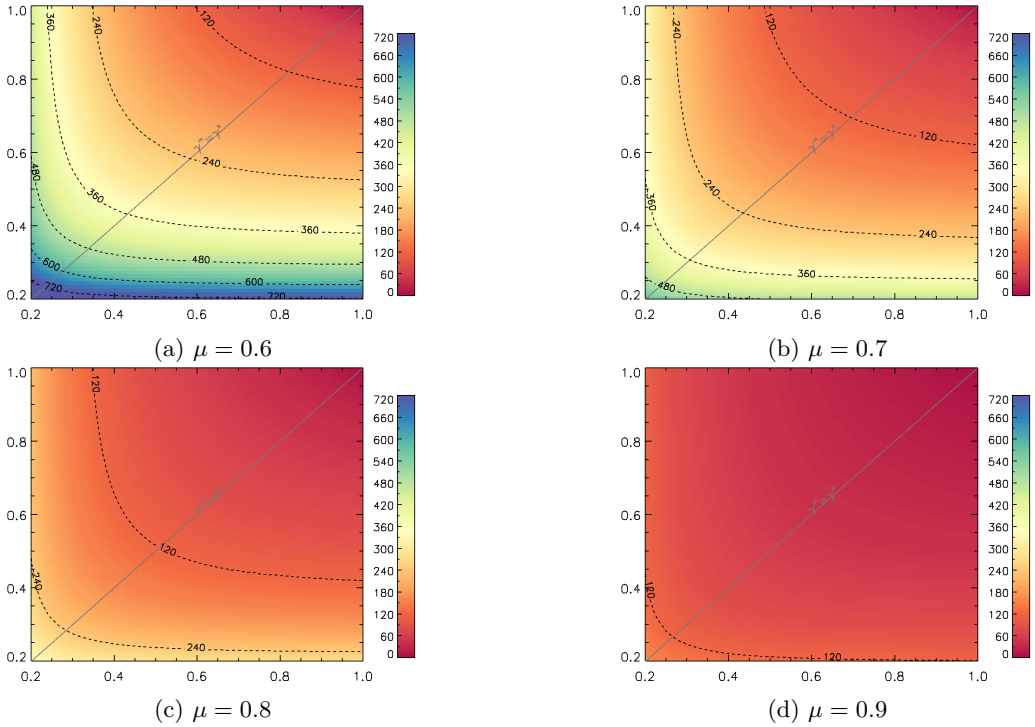

(a) $\mu = 0.6$ (b) $\mu = 0.7$

(c) $\mu = 0.8$ (d) $\mu = 0.9$

Fig. 5.18. Standard deviation of the stereo-radargrammetric phase $\sigma_{\phi^d_{\text{rdgr}}}$ as a function of the *master* and *slave* coherences γ^m and γ^s for different HoA ratios: (a) $\mu = 0.6$, (b) $\mu = 0.7$, (c) $\mu = 0.8$ and (d) $\mu = 0.9$. The contour lines emphasise the multiples of the required accuracy i.e. 120°. The number of patches to average to reach 120° can be then deduced directly from the contour lines following eq. (5.34): e.g. for $\sigma_{\phi^d_{\text{rdgr}}} = 360°$, at least $\left(\sigma_{\phi^d_{\text{rdgr}}}/120\right)^2 = 9$ patches are mandatory (theoretically).

A second requirement to enable a correction is that the absolute estimated unwrapped phase of the *differential interferogram* is correct. The assessment and the error mitigation is achieved by means of the stereo-radargrammetry. Contrary to the correction of a TDM interferogram (cf. section 4.2.2), the rectification of the misestimated ambiguity band is feasible because of the enhanced accuracy of the derived stereo-radargrammetric phase (average of the *master* and *slave* measurements) and because the *differential interferogram* is less subject to numerous (and small size) PU errors. Nevertheless, the mitigation is only possible region-wise. The theoretical minimum number of stereo-radargrammetric patches depends on the HoA ratio and both *master* and *slave* coherences. This number decreases as μ or the coherences increase. Practically, it should not be lower than 50 patches meaning that the minimum size for a PU error that can be corrected in the *differential interferogram* is about 110×110 pixels.

5.4 *Master* unwrapped phase correction

The correction of the *master* unwrapped phase is the ultimate aim of the DB-PUC framework. This section recalls briefly the discrepancy check, this time, applied to the absolute *master* and *differential* unwrapped phases and the correction process. An analysis of the feasibility and the requirements is proposed afterwards.

5.4.1 Final PU error detection and correction

The discrepancy check and the PU error detection follow the same idea as the one exposed in section 5.2. The *master* and the *differential* estimated unwrapped phases $\hat{\phi}^m$ (given by eq. (5.1))

and $\hat{\phi}^d$ (provided by eq. (5.27)) are compared in the slant range height domain:

$$\begin{aligned}\Delta\hat{h} = &\frac{h^m_{2\pi}}{2\pi}\left(\psi^m + 2\left(k^m_{\mathrm{PU}} + \varepsilon_{k^m_{\mathrm{PU}}}\right)\pi + \left(k^m_{\mathrm{off}} + \varepsilon_{k^m_{\mathrm{off}}}\right)\pi\right) - \\ &\frac{h^d_{2\pi}}{2\pi}\left(\psi^d + 2\left(k^d_{\mathrm{PU}} + \varepsilon_{k^d_{\mathrm{PU}}}\right)\pi + \left(k^d_{\mathrm{off}} + \varepsilon_{k^d_{\mathrm{off}}}\right)\pi\right)\end{aligned} \tag{5.35}$$

The *differential interferogram* is supposed to be correctly unwrapped after the steps described in section 5.3, thus $\varepsilon_{k^d_{\mathrm{PU}}} = 0$. Furthermore, the trend due to possible residual global offsets is compensated as introduced in section 5.2.2 ($\varepsilon_{k^m_{\mathrm{off}}} = \varepsilon_{k^d_{\mathrm{off}}} = 0$). As a result, eq. (5.35) can be rewritten as:

$$\Delta\hat{h} = \frac{h^m_{2\pi}}{2\pi}\left(\psi^m + 2\left(k^m_{\mathrm{PU}} + \varepsilon_{k^m_{\mathrm{PU}}}\right)\pi + k^m_{\mathrm{off}}\pi\right) - \frac{h^d_{2\pi}}{2\pi}\left(\psi^d + 2k^d_{\mathrm{PU}}\pi + k^d_{\mathrm{off}}\pi\right) \tag{5.36}$$

Since

$$\Delta\hat{h} = \frac{h^m_{2\pi}}{2\pi}\left(\psi^m + 2k^m_{\mathrm{PU}}\pi + k^m_{\mathrm{off}}\pi\right) - \frac{h^d_{2\pi}}{2\pi}\left(\psi^d + 2k^d_{\mathrm{PU}}\pi + k^d_{\mathrm{off}}\pi\right) = h^m_N - h^d_N = \Delta h_N \tag{5.37}$$

the observed height difference $\Delta\hat{h}$ is equal to:

$$\Delta\hat{h} = h^m_{2\pi}\varepsilon_{k^m_{\mathrm{PU}}} + \Delta h_N \tag{5.38}$$

The height discrepancy is considered as a PU error when $\left|\Delta\hat{h}_{\mathrm{PU}}\right| > h^m_{2\pi}/2$. Considering that the *differential interferogram* is (supposed to be) correctly unwrapped, the detection is straightforward.

Finally, the correction to apply on the ambiguity band (equal to $-\varepsilon_{k^m_{\mathrm{PU}}}$) is easily derived from eq. (5.38):

$$-\varepsilon_{k^m_{\mathrm{PU}}} = \left\lfloor \frac{\Delta\hat{h} + \Delta h_N}{h^m_{2\pi}} \right\rceil \tag{5.39}$$

Only the ambiguity band of the unwrapped phase is modified. Accordingly, the algorithm is congruent.

The correction is performed on the previously detected *regions* to avoid the creation of outliers, a typical issue of pixel-wise approaches. The *incompatible* areas remain unaltered if they are not adjacent to a region to correct. Otherwise, they are masked out (and set to a simulated phase value to avoid artefacts during the geocoding).

Figure 5.19b presents the (absolute) rectified ambiguity band for the *master* scene of the Marble Canyon example. The *incompatible* regions are masked out from the corrected unwrapped phase. The corrections are in compliance with the AAD map obtained by comparing the estimated unwrapped phase with respect to SRTM after the MCF algorithm (Fig. 5.19c). Figure 5.19a illustrates where and in which phase (*differential*, *master* or both) a correction was required.

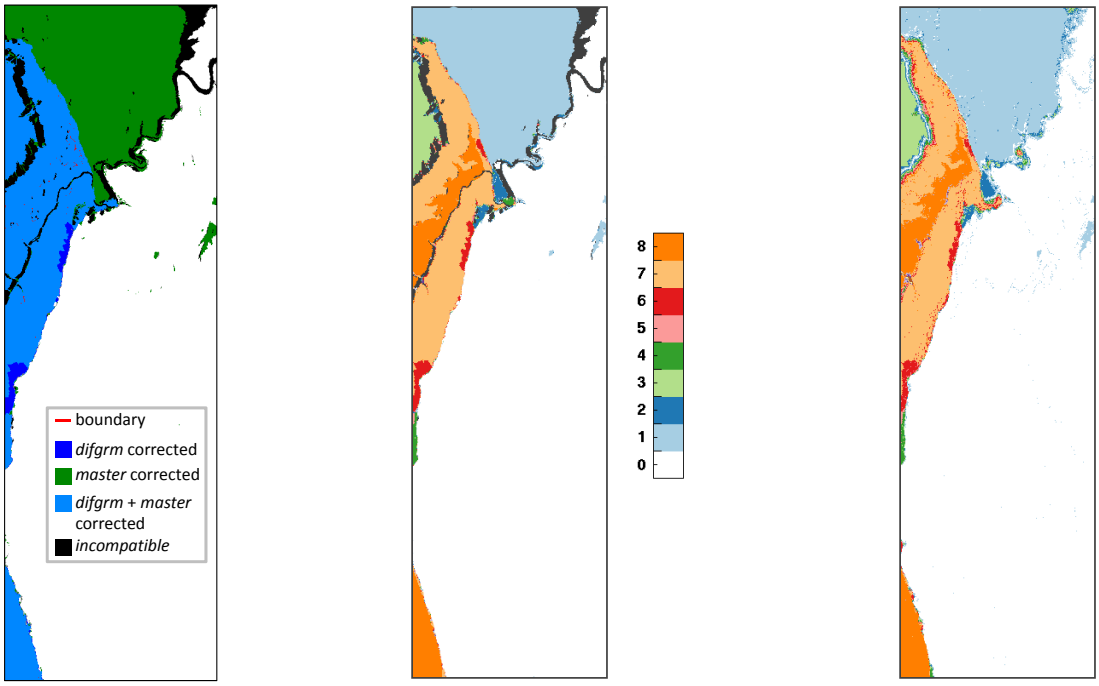

(a) Corrected regions (b) Corrected (absolute) ambiguity band (c) Initial AAD map w.r.t. SRTM

Fig. 5.19. *Master* unwrapped phase correction of the Marble Canyon example: (a) mask of the corrected regions (b) map of the corrected ambiguity band in the *master* unwrapped phase with the help of the *differential interferogram*, (c) recall of the Absolute Ambiguity Deviation (AAD) map of the unwrapped phase with respect to SRTM for visual comparison.

5.4.2 Constraints and requirements on the data

Similarly to section 5.2.4, the conditions required for a successful correction, especially those on the *master* and *slave* coherences, are investigated. The height noise standard deviation is:

$$\sigma_{\Delta h} = \sqrt{{\sigma_{h^m}}^2 + {\sigma_{h^d}}^2} = \sqrt{\left(\frac{h^m_{2\pi}}{2\pi}\sigma_{\phi^m}\right)^2 + \left(\frac{h^d_{2\pi}}{2\pi}\sigma_{\phi^d}\right)^2} \tag{5.40}$$

where σ_{ϕ^d} is approximated by (see section 5.3.2):

$$\sigma_{\phi^d} = \sqrt{\sigma^2_{\phi^m} + \sigma^2_{\phi^s}} \tag{5.41}$$

thus

$$\sigma_{\Delta h} = \frac{h^m_{2\pi}}{2\pi}\sqrt{\sigma^2_{\phi^m} + \left(\frac{h^s_{2\pi}}{h^s_{2\pi} - h^m_{2\pi}}\right)^2\left(\sigma^2_{\phi^m} + \sigma^2_{\phi^s}\right)} \tag{5.42}$$

or as a function of $h^m_{2\pi}$ and μ:

$$\sigma_{\Delta h} = \frac{h^m_{2\pi}}{2\pi}\sqrt{\sigma^2_{\phi^m} + \frac{\sigma^2_{\phi^m} + \sigma^2_{\phi^s}}{(1-\mu)^2}} \tag{5.43}$$

Figure 5.20 depicts the minimum coherence required to correct an ambiguity error in the *master* unwrapped phase. Because $h^d_{2\pi}$ tends to infinity when $h^s_{2\pi}$ approaches $h^m_{2\pi}$, the height noise tends to infinity too, thus the correction is impossible (minimum required coherences tend to 1.). The minimum required coherence is the lowest when μ approaches 0.5 or 2 since $h^d_{2\pi} \to h^m_{2\pi}$ or $h^s_{2\pi}$, but as already mentioned, the *differential interferogram* is not helpful in these configurations. Finally, $\mu = 2/3$ or $\mu = 3/2$ turns out to be again the best compromise between

the coherence and the suitability of the *differential interferogram*. Under these conditions, a minimum coherence of only 0.37 is required.

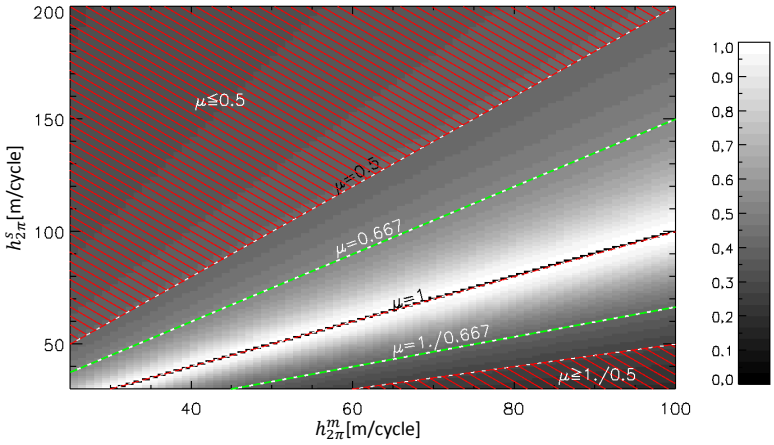

Fig. 5.20. Minimum coherence necessary to correct a PU error with respect to $h^m_{2\pi}$ and $h^s_{2\pi}$ assuming 25 looks (and that both interferograms have the same coherence). Significant values of the HoA ratio μ are plotted as lines. The red strips emphasise where it is not worthy to compute the *differential interferogram* (because of the resulting HoA, which is lower than the data to correct).

5.5 Summary

In this chapter, the Dual-Baseline Phase Unwrapping Correction (DB-PUC) framework has been presented. Briefly, its aim is to correct wrongly unwrapped phases by altering the misestimated ambiguity bands by means of the (corrected) unwrapped phase of the *differential interferogram* (Fig. 5.21).

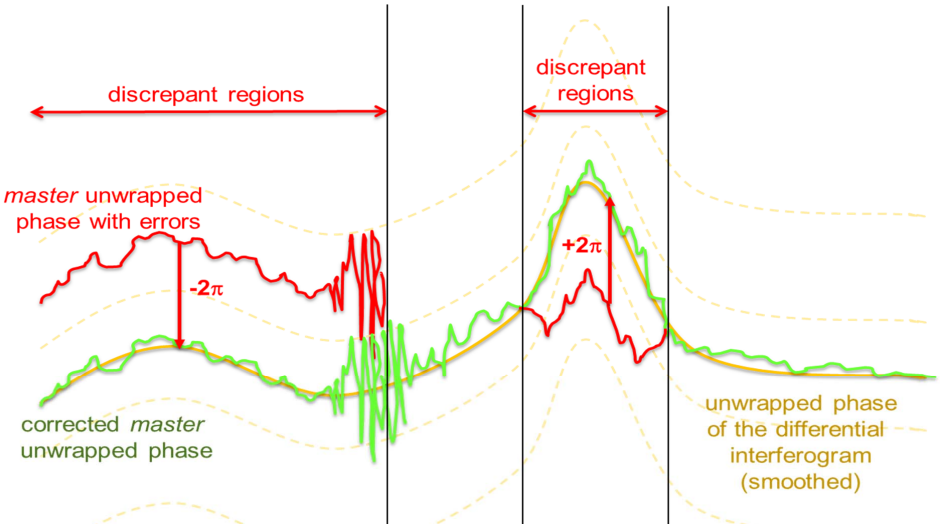

Fig. 5.21. *Master* unwrapped phase correction principle.

The *differential interferogram* is obtained by demodulating the two interferograms with respect to each other. Its higher height of ambiguity makes it easier to unwrap. The stereo-radargrammetry, which is an absolute measurement resulting from the parallaxes between the satellites, is used to correct the possible PU errors of the *differential interferogram* unwrapped phase region-wise.

The DB-PUC has been designed and developed to cope with the constraints of the TanDEM-X mission. Hence, through this chapter, the different requirements on the data for a successful use of the workflow have been verified. They are:

- the *master* and the *slave* HoAs must be sufficiently different ($h_{2\pi}^m \neq h_{2\pi}^s$) (see sections 5.2.4 and 5.3.1);
- all in all, the HoA ratio should optimally be $\mu \approx 2/3$ or $\mu \approx 3/2$ (refer to sections 5.2.4, 5.3.2 and 5.4.2);
- with this optimal HoA ratio, coherences have to be better than (only) 0.36, otherwise, the requested minimum coherences are higher (see sections 5.2.4 and 5.4.2);
- large-scale terrain changes should not be present in the data, the possible affected regions have to be masked out (*incompatible* regions from section 5.3.3.2);
- the stereo-radargrammetry allows to correct PU errors in the *differential interferogram*, which are bigger than about 110×110 pixels (consult section 5.3.5).

These requirements conform to the initially planned acquisitions (summarised in section 4.1.1) of the TanDEM-X mission where $h_{2\pi}^m$ and $h_{2\pi}^s$ have the same order of magnitude with a ratio $\mu \approx 0.7$.

The proposed method has the following advantages:

- it is independent of the amount of interferometric pairs available (starting from two);
- the algorithm is independent of any external reference such as a DEM
- phases do not have to be perfectly calibrated (i.e. absolute), especially a wrongly estimated π-ambiguity coming from the synchronisation link is not problematic (if the data are sufficiently coherent for the offset determination);
- small to medium scale terrain changes are not dramatic, they can be handled as noise inside the ambiguity bands (it depends however on the baseline configurations and its resulting sensitivity to noise, see section 5.2.4);
- it is computationally efficient so that it can process more than 400 scenes per day;
- since the approach is to correct unwrapping errors, it is flexible and independent of the phase unwrapping algorithm itself, another one could be used if required (as long as its solution is congruent).

This framework is the core of the Integrated TanDEM-X Processor (ITP) when it comes to the treatment of dual-baseline data. It is used operationally for the processing of all acquisitions from the second global coverage but also for the correction of wrongly unwrapped data from the first coverage (see appendix A.3). It has already processed more than 100,000 scenes. Complete results and assessments are proposed in chapter 6.

6 Results and assessment

This chapter demonstrates the ability of the Dual-Baseline Phase Unwrapping Correction (DB-PUC) framework to address the demanding requirements of the TanDEM-X mission (TDM). It also clarifies how this approach manages to deal with interferometric data of various quality and with the different acquisition configurations presented in chapter 4. This thesis is focussed on the multi-baseline processing of the second global coverage data. Only results related to it are shown hereafter.

Due to the huge amount of data to process (cf. Table 4.1), one important concern is the time efficiency. For this reason, the DB-PUC is applied by default only to scenes where single-baseline phase unwrapping (1B-PU) may fail. The criteria for a successful 1B-PU are stringent: 1) the quality ratio must be $q_{\text{ratio}} > 0.994$ i.e. more than 99.4% of the scene (in the coarse resolution) has to agree with the stereo-radargrammetric phase (scenes not fulfilling this criterion are depicted in Fig. 6.1a) and 2) the average coherence must be higher than 0.65 to ensure the above-mentioned assessment to be trustworthy (acquisitions violating this limit are identified in Fig. 6.1b). All in all, 36% of the second global coverage data are processed with the DB-PUC framework. It may be needed at any place in the world and may map all possible kind of terrain under disparate conditions.

In the first section, the results obtained with the DB-PUC for the test sites presented in section 4.3 are illustrated. Then, the influence of the modifications of the acquisition plan on the outcomes are investigated (Lachaise et al., 2014a,b). Finally, a global assessment of the DB-PUC results for the second global coverage is provided as well as an overview of the resulting absolute height accuracy of the final TDM DEM.

6.1 Demonstration of the DB-PUC framework

In section 4.3, examples for three typical issues for phase unwrapping (PU) have been depicted: these are (large) incoherent regions, surface discontinuities and mountainous terrain. It has been proven that none of the evaluated algorithms is able to deliver correctly reconstructed absolute phases under the constraints of a global mapping as compulsory for the TanDEM-X mission. The outputs of the proposed framework are depicted hereafter. Results for other test sites have been already published in Lachaise et al. (2012a, 2013).

The various results are provided for the complete overlap of the *master* with one *slave* image. The PU quality ratio q_{ratio} obtained by comparing the unwrapped and the stereo-radargrammetric phases is the only quality control parameter delivered automatically by the Integrated TanDEM-X Processor (ITP) (refer to section 4.2.2). The other statistical quality indicators used for the systematic assessment were introduced in section 4.3.1. Similarly as in section 4.3, the statistical analysis of the three initially estimated (1B) unwrapped phases $\hat{\phi}^m$, $\hat{\phi}^s$ and $\hat{\phi}^d$ is performed only for pixels having a coherence greater than 0.25. The analysis of the two corrected unwrapped phases is done only for *compatible* pixels. Note that the whole *master* phase is unwrapped in one go to be assessed prior to the DB-PUC. The smaller parts, which were selected for the evaluations in section 4.3, are emphasised by a brown rectangle on the *master* Absolute Ambiguity Deviation (AAD) map of the 1B-PU outputs. Since the size of the (*master*) wrapped phases are different, outcomes of the Minimum Cost Flow (MCF) algorithm may differ from those presented there.

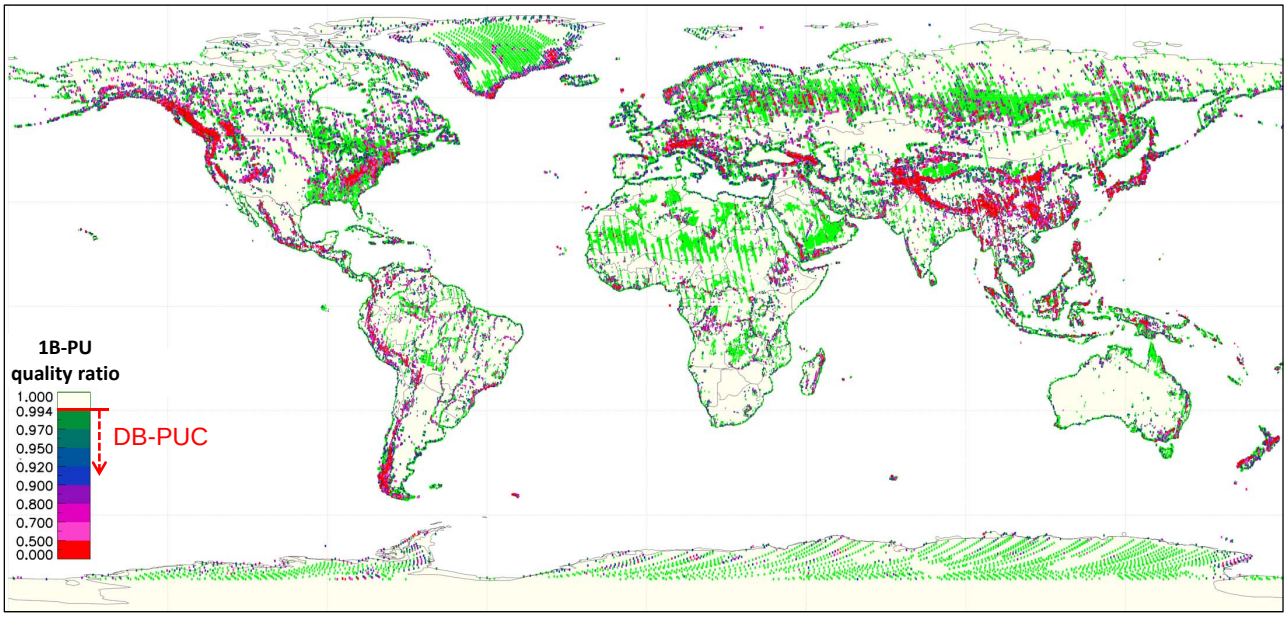

(a) Scenes exhibiting a single-baseline phase unwrapping (1B-PU) quality ratio lower than 0.994 (28,242 scenes)

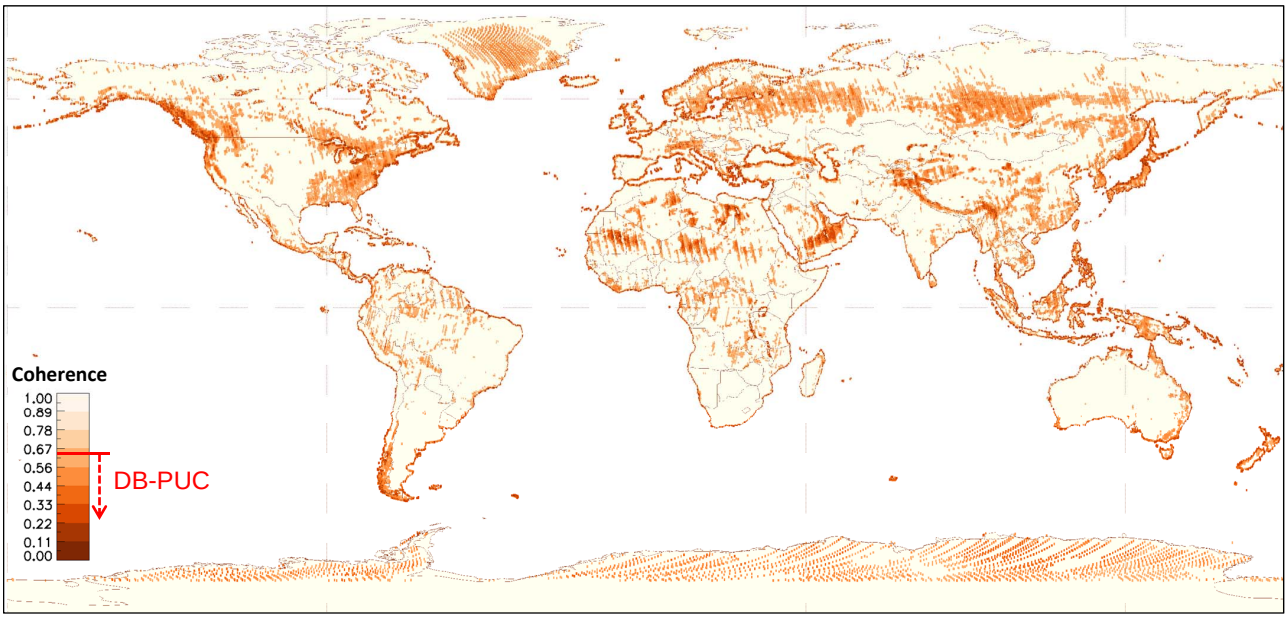

(b) Scenes with an average coherence lower than 0.65 (36,008 scenes)

Fig. 6.1. Maps of the TanDEM-X acquisitions of the second global coverage which violate (a) the (single-baseline) phase unwrapping (PU) quality ratio and/or (b) the coherence thresholds. The union of both maps give all the candidates to the Dual-Baseline Phase Unwrapping Correction (DB-PUC) (representing 51,279 scenes i.e. 35.93% of the second global coverage acquisitions, data processed till 12/01/15)).

6.1.1 Challenging case 1: large waterbodies

The first studied challenging case was that of large waterbodies and more generally, incoherent regions. It has been illustrated by a scene surrounding the Preikestolen in Norway.

Figure 6.2 depicts the different steps of the DB-PUC workflow for this test site. The same colour scheme as in Fig. 5.1 is adopted to distinguish the *master* (cyan), *slave* (turquoise) and *differential* (orange) data and the different steps of the framework (darker gray for the *differential interferogram* processing and light gray for the *master* unwrapped phase correction). The *master* and *slave* interferograms have a height of ambiguity (HoA) of -113 m/cycle and 76 m/cycle respectively (see Figs. 4.10a and 4.10e), and are characterised by a HoA ratio of 1.49=1/0.67 that is optimal.

First, the wrapped phases ψ^m and ψ^s are unwrapped separately with the MCF algorithm.

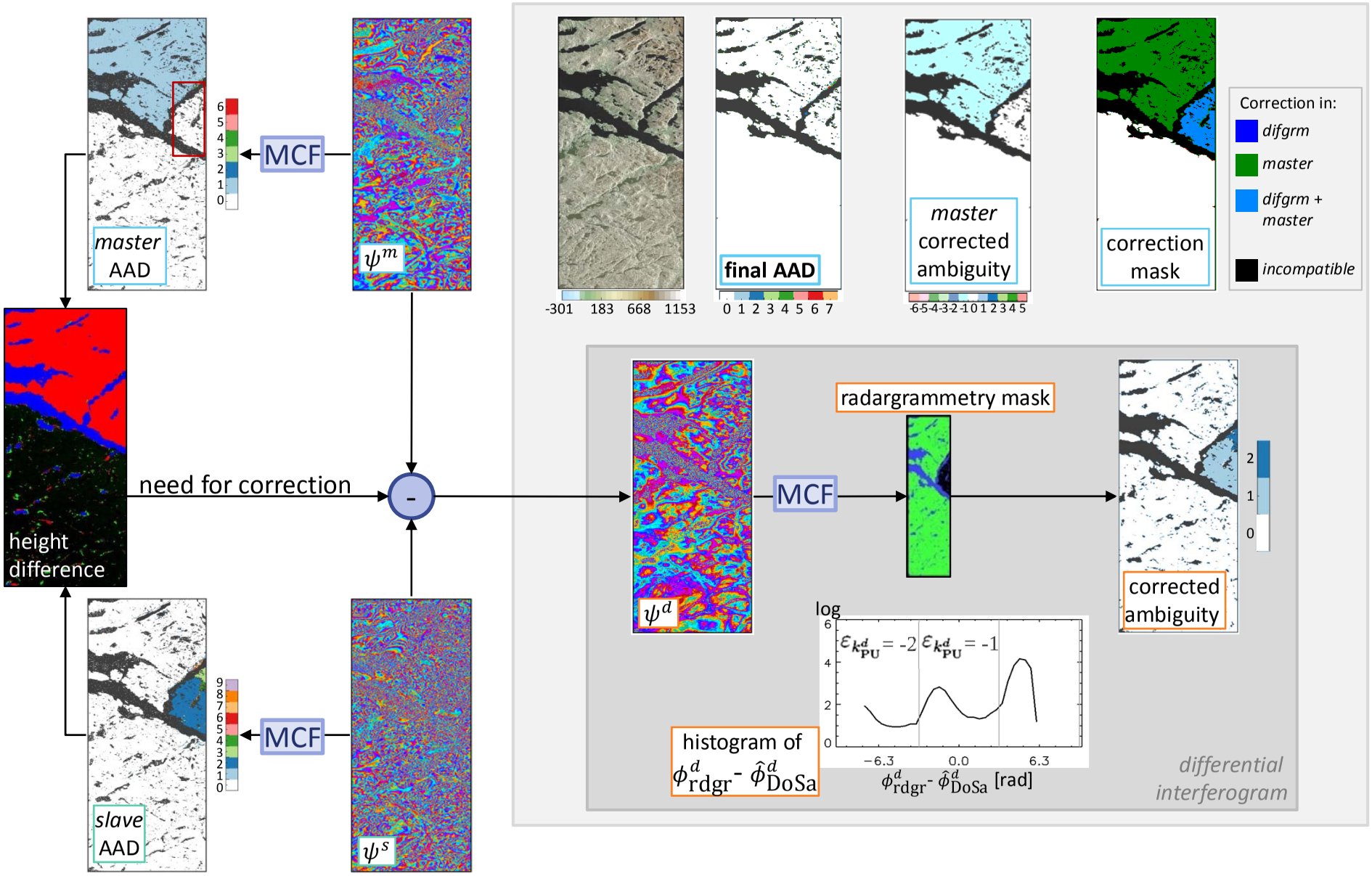

Fig. 6.2: Illustration of the different steps and intermediate results of the Dual-Baseline Phase Unwrapping Correction (DB-PUC) framework for the Preikestolen region. On the left side, outputs of the MCF algorithm for the *master* and *slave* phases are displayed with their resulting height difference. The dark gray insert presents the unwrapping result and the necessary ambiguity band correction of the *differential interferogram*. The corrected *master* absolute unwrapped phase i.e. the output of the DB-PUC is presented on the upper side of the light gray rectangle with the final AAD map, the corrected ambiguity map and the correction mask (*difgrm* stands for *differential interferogram*). Only the *incompatible* regions adjacent to areas to be corrected are kept in the final correction mask.

The corresponding AAD maps of the estimated absolute phases calculated with respect to a simulated phase from SRTM DEM are shown on the left side of Fig. 6.2. These maps only allow to assess qualitatively and visually the unwrapping results and are not used in the operational processing. The brown rectangle on the *master* AAD indicates the smaller region depicted in section 4.3.2. Since the distribution of the height difference is not unimodal, the *differential interferogram* is computed, unwrapped and its estimated absolute phase $\hat{\phi}^d$ is checked with its equivalent stereo-radargrammetric phase. It can be observed that its unwrapped phase includes PU errors at different positions than in the *master* one. The upper right part illuminates the mask of the areas which necessitated a correction in the *differential* and/or in the *master* unwrapped phases and the applied ambiguity band correction. Finally, the corrected *master* unwrapped phase converted to slant range height and its corresponding AAD map are provided. The only remaining discrepancies are located close to the Preikestolen cliff, which is inaccurate in SRTM DEM and subject to layover. Figure 6.3 presents the 3-D view of the *master* SAR amplitude image colour-coded with the corrected terrain height.

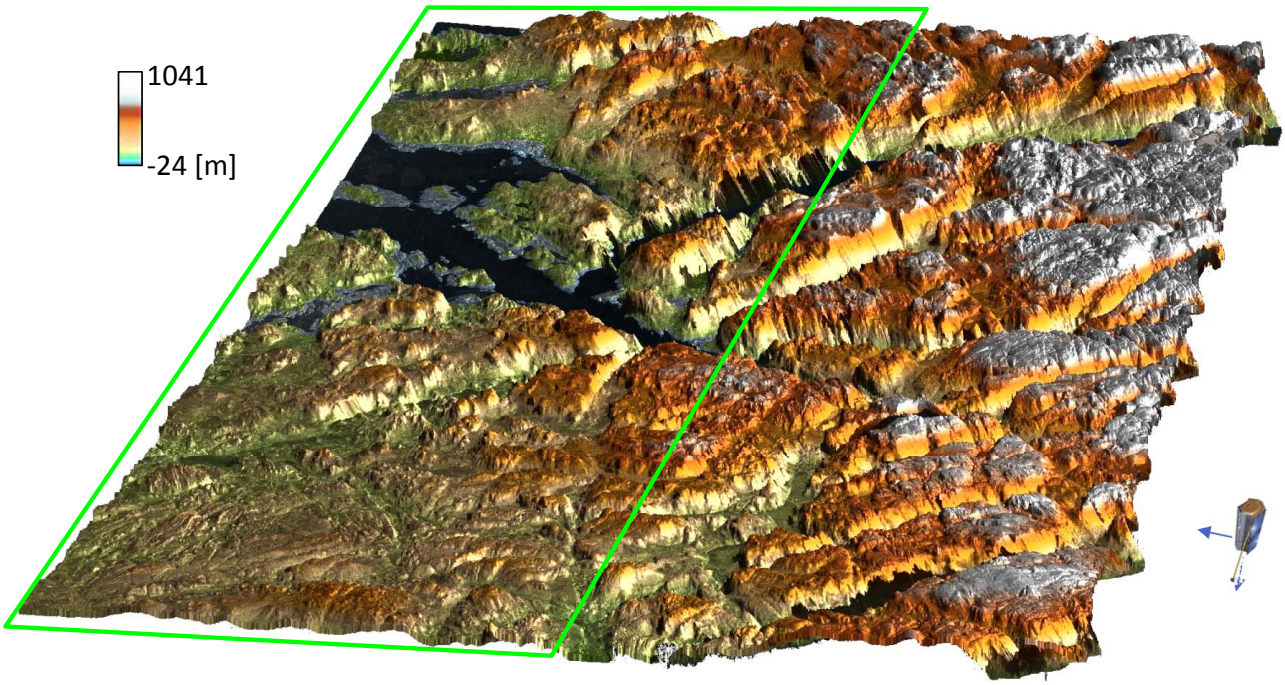

Fig. 6.3. 3-D view of the *master* SAR image of the Preikestolen test site colour-coded with the corrected terrain height The green lines delimit the half of which the correction process is illustrated in Fig. 6.2.

Table 6.1 summarises the statistical assessments for the initial estimated phases $\hat{\phi}^m$, $\hat{\phi}^s$ and $\hat{\phi}^d$ unwrapped with the MCF (1B-PU) and the final *differential* and *master* unwrapped phases corrected during the DB-PUC process. The PU quality ratios q_{ratio} obtained using the stereo-

	q_{ratio}	$\%_{(\text{AD}=0)}$	$\overline{\text{AD}}$	σ_{AD}	m_{AD}	NMAD	% coherent / *compatible* pixels
initial $\hat{\phi}^m$ (1B-PU)	0.802*	67.77%	-0.31	0.50	0.077	0.144	90.45%
initial $\hat{\phi}^s$ (1B-PU)	0.941	93.48%	-0.13	0.57	0.056	0.082	81.92%
initial $\hat{\phi}^d$ (1B-PU)	0.841	94.14%	-0.06	0.28	0.021	0.031	94.72%
corrected $\hat{\phi}^d$ (DB-PUC)	0.998	99.19%	-0.006	0.12	0.020	0.029	84.07%
corrected $\hat{\phi}^m$ (DB-PUC)	**1.000***	**99.07%**	-0.006	0.20	0.038	0.056	86.76%

Table 6.1. Summary of the performances of the DB-PUC framework for the Preikestolen region (see section 4.3.1 for the explanation of the statistical quality indicators used for the assessment). The results of the *master*, *slave* and *differential* phases unwrapped with the MCF algorithm, respectively $\hat{\phi}^m$, $\hat{\phi}^s$ and $\hat{\phi}^d$, and the DB-PUC outputs are assessed (*the *master* q_{ratio} are given for the whole scene). Only coherent ($\gamma > 0.25$) or *compatible* pixels are taken into account for the statistics, their percentage is indicated in the last column.

radargrammetry are given. For the *master* phases, the specified ratios are obtained for the whole scene whereas for the other phases, they are only available for the overlap. These ratios are the main drivers to initiate and to enable the DB-PUC but also to verify that the estimated absolute *differential* phase is suitable for the correction of the *master* unwrapped phase. The different q_{ratio} agree with the percentage of correctly unwrapped pixels with respect to the simulated phase from SRTM DEM ($\%_{(\text{AD}=0)}$, two first columns of Table 6.1). In this test site, the HoAs are high and the coherences good ($\gamma^m = 0.80$ and $\gamma^s = 0.73$). Moreover, the water clearly delimits the area to correct in the *differential interferogram*. The correction of the *differential interferogram* was successful ($q_{\text{ratio}} = 0.998$). Hence, it can be used to correct the *master* unwrapped phase. The final correction worked well so that the final q_{ratio} is 1.

6.1.2 Challenging case 2: surface discontinuity

Surface discontinuity occurs for example at the border of high plains. In section 4.3.3, two scenes have been analysed: one in the Ubajara National Park in Brazil and the other around the Mount Roraima in eastern Venezuela. The latter example emphasises more especially the need of being independent of any reference since SRTM DEM is wrong by about 420 m there.

The results of the scene in the Ubajara National Park are summarised in Fig. 6.4 and 6.5 and Table 6.2. The *master* interferogram has a HoA of 41 m/cycle with an average coherence of 0.76 and the selected *slave*, a HoA of 50 m/cycle and $\gamma^s = 0.88$ (see Figs. 4.14a and 4.14e). The HoA ratio is thus $\mu = 0.82$.

Due to the layover caused by the steep and high border of the plateau, the scene is split into two parts and 1B-PU of all three phases fail ($q_{\text{ratio}} = 0.546$ for the (full) *master* and $q_{\text{ratio}} \approx 0.62$ for the *slave* and *differential* single-baseline unwrapped phases and $\%_{(\text{AD}=0)} \approx 60\%$). The *mas-*

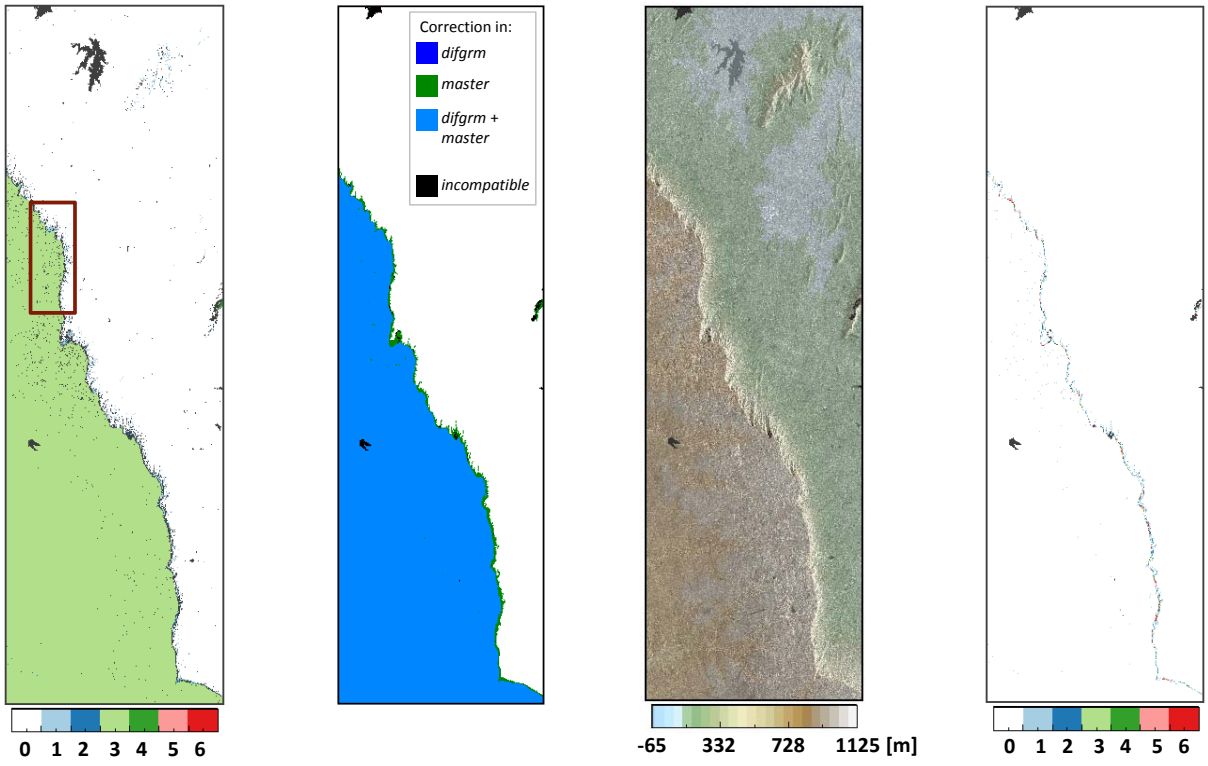

(a) Initial AAD map (incoherent pixels masked out)

(b) Correction map

(c) Final slant range height

(d) Final AAD map (*incompatible* pixels masked out)

Fig. 6.4. Dual-Baseline Phase Unwrapping Correction (DB-PUC) results for the scene in the Ubajara National Park: (a) Absolute Ambiguity Deviation (AAD) map of the initial *master* unwrapped phase (1B-PU, the rectangle delimits the part illustrated in section 4.3.3), (b) correction map applied to the *differential* (*difgrm*) and/or *master* unwrapped phases, (c) final reconstructed slant range height and (d) final AAD map of the corrected *master* unwrapped phase.

ter unwrapped phase is incorrect there by 3 cycles (Fig. 6.4a). Notwithstanding, the *differential interferogram* can be easily corrected because the plateau to recover has a clear border marked by the incoherent pixels of the layover (Fig. 6.4b). The proposed approach based on correcting the ambiguity band region-wise allows to avoid or at least to strongly reduce the noise due to ambiguity changes from one pixel to the next ($\sigma_{\text{AD}} = 0.264$ and NMAD=0.077 for the corrected *master* phase whereas $\sigma_{\text{AD}} = 0.31$ and NMAD=0.12 for the Graph-Cuts Total Variation (GC-TV) in Table 4.3 and as it can be noticed by comparing Fig. 6.4d and Fig. 4.16). 98.66% of the pixels agree in ambiguity with SRTM ($\%_{(\text{AD}=0)}$). The discrepancies, located on the surface discontinuity (Fig. 6.4d) come from the incoherent pixels and the resolution differences between SRTM and TDM DEMs.

	q_{ratio}	$\%_{(\text{AD}=0)}$	$\overline{\text{AD}}$	σ_{AD}	m_{AD}	NMAD	% coherent / *compatible* pixels
initial $\hat{\phi}^m$ (1B-PU)	0.546*	59.48%	1.17	1.48	0.18	0.26	98.21%
initial $\hat{\phi}^s$ (1B-PU)	0.622	59.63%	1.19	1.49	0.16	0.23	97.98%
initial $\hat{\phi}^d$ (1B-PU)	0.621	60.16%	0.40	0.50	0.055	0.082	99.39%
corrected $\hat{\phi}^d$ (DB-PUC)	0.994	99.73%	0.002	0.062	0.017	0.026	99.39%
corrected $\hat{\phi}^m$ (DB-PUC)	**1.000***	**98.66%**	-0.0002	0.264	0.052	0.077	99.77%

Table 6.2. Summary of the performances of the DB-PUC for the test site in the Ubajara National Park (see section 4.3.1 for the explanation of the statistical quality indicators used for the assessment). The results of the *master*, *slave* and *differential* phases unwrapped with the MCF algorithm, respectively $\hat{\phi}^m$, $\hat{\phi}^s$ and $\hat{\phi}^d$, and the DB-PUC outputs are assessed (*the *master* q_{ratio} are given for the whole scene). Only coherent ($\gamma > 0.25$) or *compatible* pixels are taken into account for the statistics, their percentage is indicated in the last column.

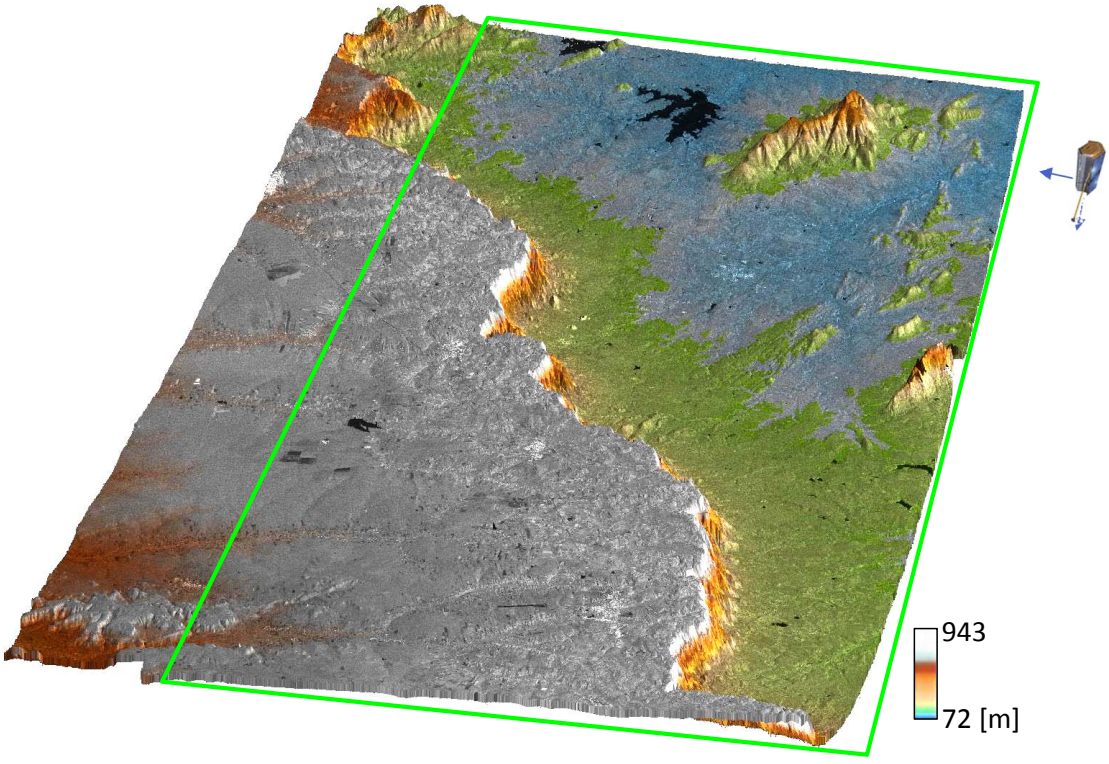

Fig. 6.5. 3-D view of the *master* SAR image for the Ubajara National Park area colour-coded with the corrected terrain height. The green lines delimit the half of interest in Fig. 6.4.

The second provided example is the Mount Roraima. The results are presented in Fig. 6.6 and 6.7 and Table 6.3. The *master* interferogram has a HoA of 39 m/cycle and an average coherence $\gamma^m = 0.66$ and the selected *slave*, a HoA of -48 m/cycle with $\gamma^s = 0.71$ (see Fig. 4.18). The HoA ratio is thus $\mu = 0.81$. The difficulties of this scene are the plateaus, which are also wrong in the reference DEM from SRTM. The *master* phase $\hat{\phi}^m$ has been successfully corrected: the q_{ratio} is 1 (refer to Table 6.3). The final AAD over the Mount Roraima (bottom left) is 11 to

12 ambiguity bands corresponding to about 420 m to 460 m (see Fig. 6.6d). This is in agreement with the height difference found between the highest point in the SRTM DEM (2,354 m) in this region and the known highest point of the Mount Roraima (2,810 m [10]). Therefore, it may be assumed that the DB-PUC performed correctly in this case.

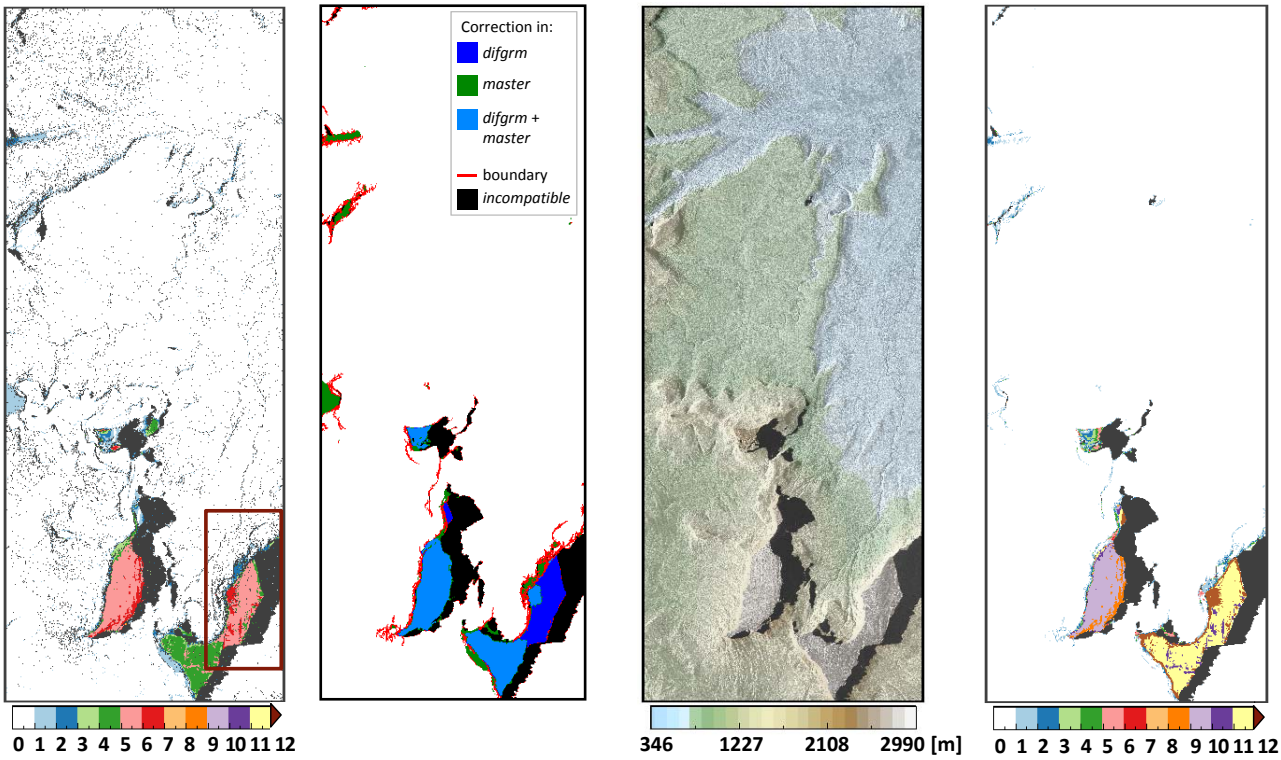

(a) Initial AAD map (incoherent pixels masked out) (b) Correction map (c) Slant range height (d) Final AAD map (*incompatible* pixels masked out)

Fig. 6.6. Dual-Baseline Phase Unwrapping Correction (DB-PUC) results for the Mount Roraima example: (a) Absolute Ambiguity Deviation (AAD) map of the *master* unwrapped phase (1B-PU, the rectangle delimits the part illustrated in section 4.3.3), (b) correction map applied to the *differential interferogram* (*difgrm*) and/or *master* unwrapped phases, (c) reconstructed slant range height and (d) AAD map of the corrected *master* unwrapped phase (the residual apparent errors are consequences of a wrong SRTM DEM).

	q_{ratio}	$\%_{(\text{AD}=0)}$	$\overline{\text{AD}}$	σ_{AD}	m_{AD}	NMAD	% coherent / *compatible* pixels
initial $\hat{\phi}^m$ (1B-PU)	0.955*	93.14%	0.19	0.95	0.089	0.13	92.60%
initial $\hat{\phi}^s$ (1B-PU)	0.919	95.71%	0.04	0.22	0.024	0.036	95.98%
initial $\hat{\phi}^d$ (1B-PU)	0.957	91.81%	-0.21	0.87	0.084	0.12	91.22%
corrected $\hat{\phi}^d$ (DB-PUC)	0.966	95.60%	-0.07	0.39	0.024	0.036	95.98%
corrected $\hat{\phi}^m$ (DB-PUC)	**1.000***	93.15%	-0.38	2.04	0.09	0.13	96.15%

Table 6.3. Summary of the performances of the DB-PUC for the Mount Roraima example (see section 4.3.1 for the explanation of the statistical quality indicators used for the assessment). The results of the *master*, *slave* and *differential* phases unwrapped with the MCF algorithm, respectively $\hat{\phi}^m$, $\hat{\phi}^s$ and $\hat{\phi}^d$, and the DB-PUC outputs are assessed (*the *master* q_{ratio} are given for the whole scene). Only coherent ($\gamma > 0.25$) or *compatible* pixels are taken into account for the statistics, their percentage is indicated in the last column.

6.1.3 Challenging case 3: mountainous terrain

Mountainous terrain is a more complicated case than the previous ones. PU errors are numerous, of variable size and their delimitations are unclear. The chosen example is an acquisition

[10] http://www.peakbagger.com/peak.aspx?pid=8684

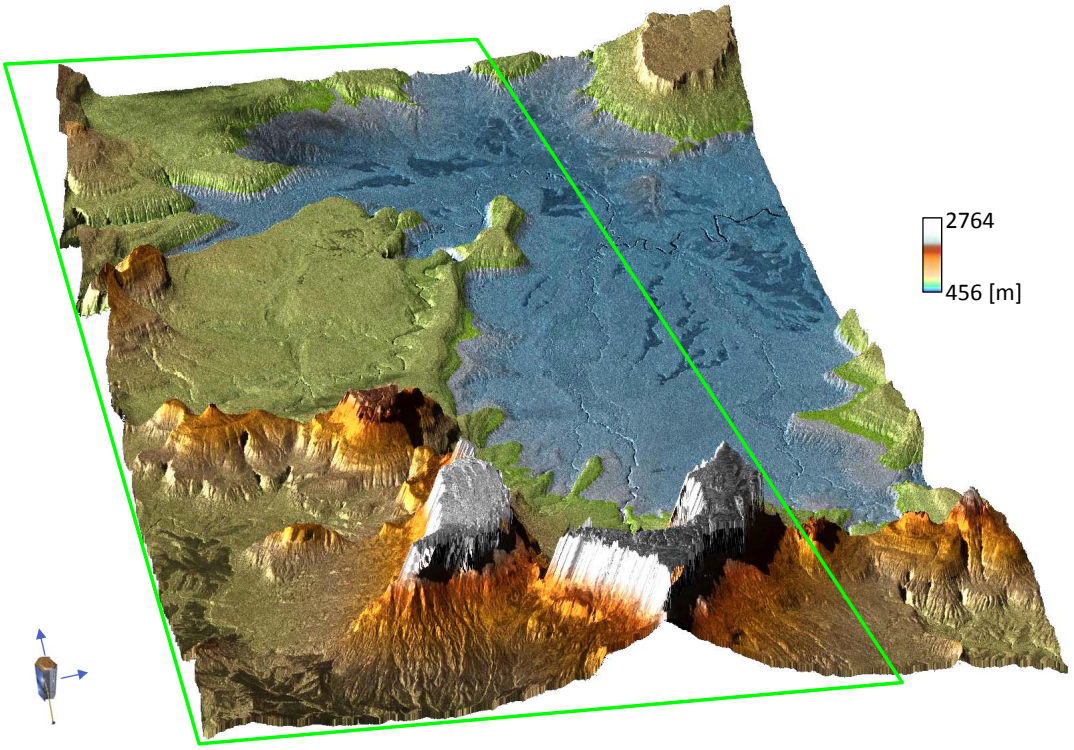

Fig. 6.7. 3-D view of the *master* SAR image for the Mount Roraima example colour-coded with final corrected terrain height. The green lines delimit the half of interest in Fig. 6.6.

surrounding the Isolation Peak in the Rocky Mountains, USA.

The results of the DB-PUC for this test site are shown in Fig. 6.8 and 6.9 and Table 6.4. The *master* interferogram has a small HoA of 32 m/cycle and moderately low coherence ($\gamma^m = 0.57$). The selected *slave* interferogram has a HoA -42 m/cycle with $\gamma^s = 0.62$ (see Figs. 4.21a and 4.21b). As a result, the HoA ratio is $\mu = 0.76$. The 1B-PU of the *master* and *slave* phases were unsuccessful (the percentage of correctly unwrapped pixels is respectively $\%^m_{(\mathrm{AD}=0)} = 5.40\%$ with a median value of $m_{\mathrm{AD}} = 2.69$ and $\%^s_{(\mathrm{AD}=0)} = 79.03\%$, see Table 6.4). In this example, the two q_{ratio} are not in compliance with the two $\%_{(\mathrm{AD}=0)}$ because the coherences are quite low and the PU errors so numerous that it is not possible to distinguish the different local maxima of the distributions of the stereo-radargrammetric and downsampled unwrapped phase differences (see appendix B.3.5). As for the *differential interferogram*, its phase has been properly unwrapped ($q_{\mathrm{ratio}} = 1.0$ and $\%_{(\mathrm{AD}=0)} = 99.07\%$), thus only the *master* unwrapped phase had to be corrected (see the correction map which is only green in Fig. 6.8b). The final AAD map (Fig. 6.8d) reveals isolated discrepancies with respect to SRTM DEM. This is due to the resolution differences as perceptible from Fig. 6.8e, which depicts the difference between the corrected *master* unwrapped

	q_{ratio}	$\%_{(\mathrm{AD}=0)}$	$\overline{\mathrm{AD}}$	σ_{AD}	m_{AD}	NMAD	% coherent / *compatible* pixels
initial $\hat{\phi}^m$ (1B-PU)	0.563*	5.40%	0.16	2.62	2.69	3.99	83.69%
initial $\hat{\phi}^s$ (1B-PU)	0.992	79.03%	-0.15	0.57	0.19	0.28	92.25%
initial $\hat{\phi}^d$ (1B-PU)	1.000	99.07%	0.0034	0.14	0.052	0.077	84.37%
corrected $\hat{\phi}^d$ *(DB-PUC)*	1.000	99.07%	0.0034	0.14	0.052	0.077	84.37%
corrected $\hat{\phi}^m$ (DB-PUC)	**1.000**	85.52%	0.062	0.53	0.19	0.29	80.30%

Table 6.4. Summary of the performances of the DB-PUC for the Isolation peak example (see section 4.3.1 for the explanation of the statistical quality indicators used for the assessment). The results of the *master*, *slave* and *differential* phases unwrapped with the MCF algorithm, respectively $\hat{\phi}^m$, $\hat{\phi}^s$ and $\hat{\phi}^d$, and the DB-PUC outputs are assessed (*the *master* q_{ratio} are given for the whole scene). Only coherent ($\gamma > 0.25$) or *compatible* pixels are taken into account for the statistics, their percentage is indicated in the last column.

phase and the simulated phase from SRTM DEM. The smooth transitions indicate the inability of SRTM DEM to represent correctly the steep slopes on small scales.

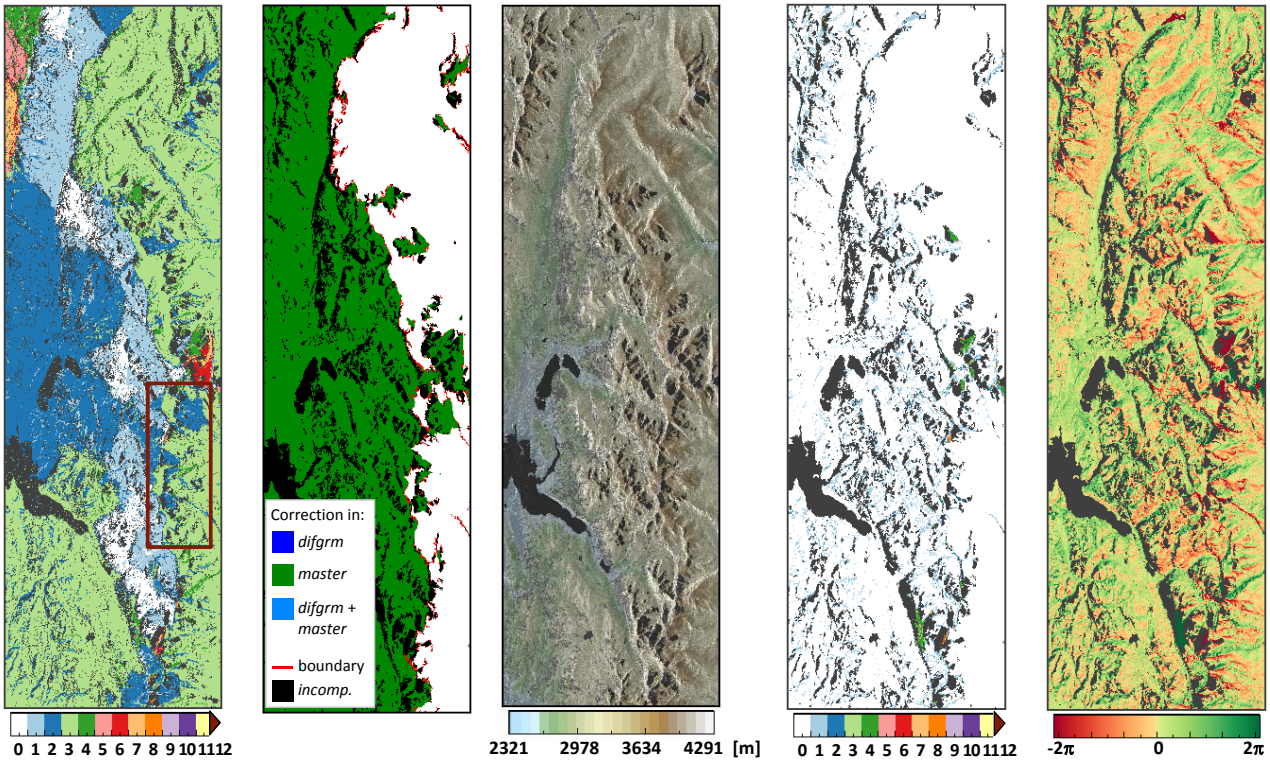

(a) Initial AAD map (b) Correction map (c) Slant range height (d) Final AAD map (e) Phase difference

Fig. 6.8. Dual-Baseline Phase Unwrapping Correction (DB-PUC) results for the Isolation peak example: (a) Absolute Ambiguity Deviation (AAD) map of the *master* unwrapped phase (1B-PU, the rectangle delimits the part illustrated in section 4.3.4), (b) correction map applied to the *differential interferogram* (*difgrm*) and/or *master* unwrapped phases, (c) the reconstructed slant range height, (d) the AAD map of the corrected *master* unwrapped phase and (e) difference with the simulated phase from SRTM DEM.

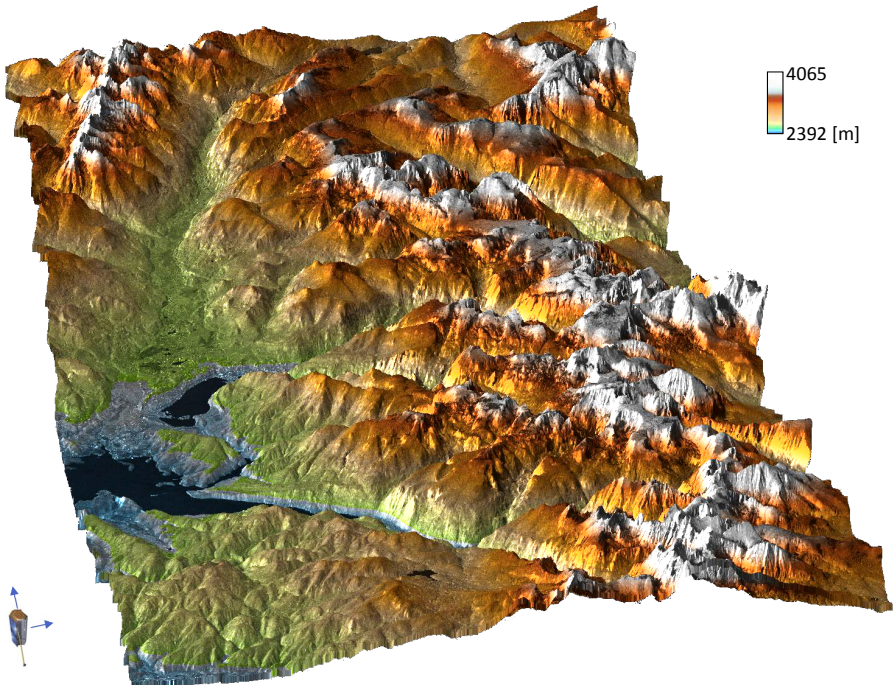

Fig. 6.9. 3-D view of the *master* SAR image for the Isolation peak example colour-coded with final corrected terrain height. This is only the half presented in Fig. 6.8.

6.1.4 Summary

In this section, the results of the proposed DB-PUC framework for the examples introduced in section 4.3 have been given. For the two first challenging cases of large waterbodies and surface discontinuities, PU problems arose in the three single-baseline unwrapped phases (*master*, *slave* and *differential*). Nonetheless, the borders of the wrongly unwrapped regions are clearly delimited by the incoherent/incompatible areas due to the water and layover/shadow and the correction is straightforward. In contrast, in mountainous terrain, shadow and layover lead to more problems. Errors are numerous and might be of small scale (and thus could not be mitigated through the stereo-radagrammetry). In the presented example, the *differential interferogram* was correctly unwrapped enabling a successful final correction. Especially for mountainous terrain, the higher HoA of the *differential interferogram* is helpful. Often, this one does not need to be unwrapped. These four test sites exhibited all sufficiently good characteristics (μ and γ) to enable a correct DB-PUC.

The approach developed in this thesis, the Dual-Baseline Phase Unwrapping Correction (DB-PUC) framework, outperforms the evaluated algorithms: the Minimum Cost Flow (MCF) (Costantini, 1998), the Maximum Likelihood Estimate (MLE) (estimation in slant range adapted from Eineder and Adam (2005)) and the Graph-Cuts Total Variation (GC-TV) (Ferraioli et al., 2009). It corrected successfully all *master* unwrapped phases. Its multi-level approach makes it flexible, computationally efficient and well adapted to the various PU error scenarios. Last but not least, the region-wise error determination and correction in terms of ambiguity bands allow it to be less sensitive to noise and to potential terrain changes.

6.2 Challenges ensued from the adapted acquisition plan

As explained in sections 4.1.2 and 4.1.3, interferometric data had to be acquired differently as originally planned because of the unexpectedly high volume decorrelation over dense forested regions. This affected the HoAs and HoA ratios. Additionally, the time span between the acquisitions may vary extremely. This section describes the encountered difficulties, the consequences for the operational DB-PUC process and how this framework is still able to deal with them (Lachaise et al., 2014a,b).

6.2.1 Height of ambiguity and HoA ratio

Typical HoAs are 40 to 50 m/cycle for the first global coverage and 30 to 35 m/cycle for the second coverage acquisitions so that the HoA ratio μ is about 0.7 (Table 4.1). Nevertheless, a significant amount of HoAs are out of these narrow ranges (refer to section 4.1.3.1). For this reason, μ may not be anymore optimal for the DB-PUC framework (see section 4.1.3.2). Undeniably, the resulting large range of HoA ratios influences dramatically the correction process and more especially the processing of the *differential interferogram*. Since the whole correction procedure relies on the assumption of having a trustworthy absolute *differential* phase, this is of major importance. The worst cases are (detailed in section 5.3):

- both HoAs are exactly equal ($\mu = 1$): it is not possible to compute the *differential interferogram*,
- both HoAs are similar (μ approaches 1.0): the resulting HoA of the *differential interferogram* gets very large and the PU error correction in the *master* phase is compromised,
- μ is smaller than 0.5 or greater than 2: the HoA of the *differential interferogram* is smaller than the ones of two interferograms; moreover, PU errors in the *master* estimated phase are usually not detectable (explained in section 5.2.4).

In these cases, the *differential interferogram* is not helpful. Figure 6.10 illustrates on a global map the HoA ratios μ between the *master* scenes from the second coverage and each of their *slave* supporting scenes coming either from the first global coverage (Fig. 6.10a) or the additional acquisitions over dense forested and difficult terrain (Fig. 6.10b). The dark red ($\mu \approx 1$) and dark blue ($\mu \leq 0.5$ or $\mu \geq 2.0$) dots represent HoA ratios for which the *differential interferogram* cannot be computed or is not useful. The orange and lighter blue marks denote suboptimal ratios for which the *differential interferogram* is still used. Finally, the green dots are for the ratio which are considered as optimal. For example, for the west coast of North America, the second coverage acquisitions have an unsuitable HoA ratio with those of the first global coverage but they have a favourable possible combination by means of the additional acquisitions.

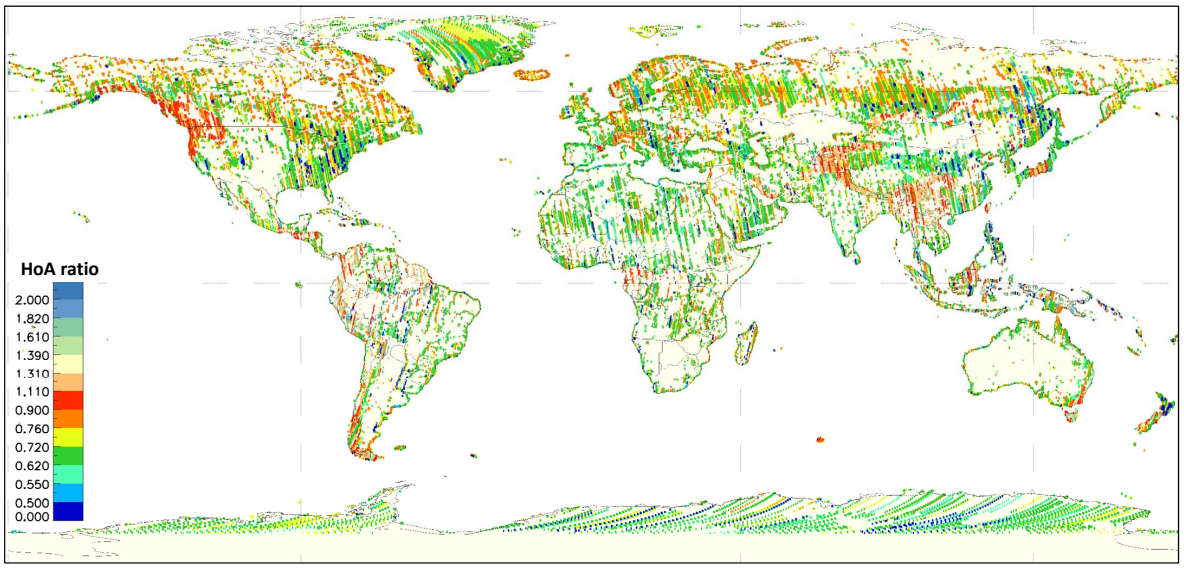

(a) Acquisitions from the first global coverage used as *slave*

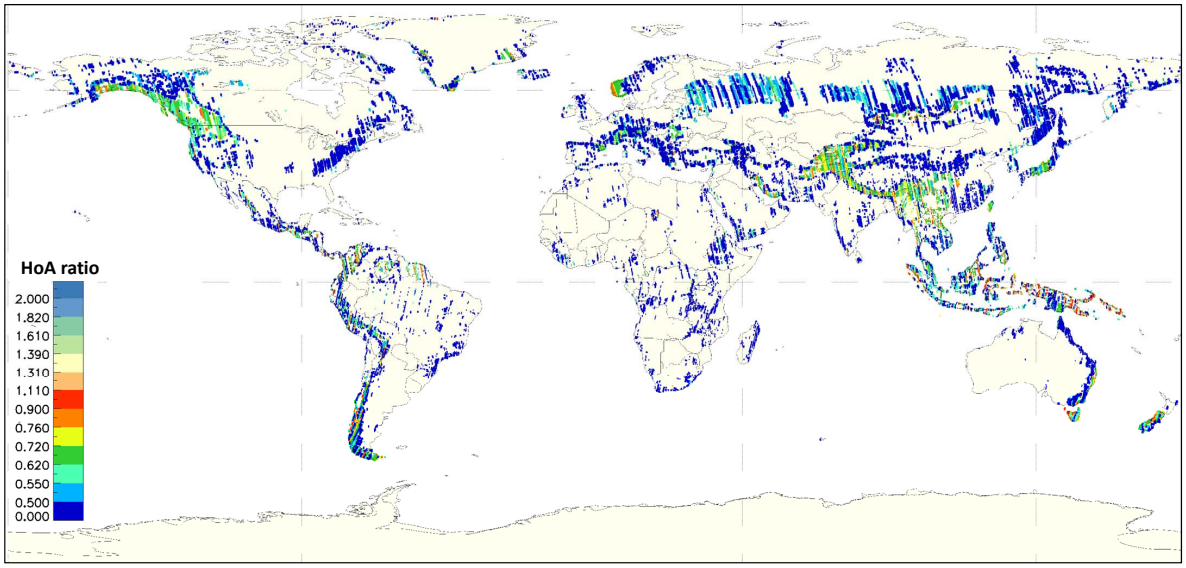

(b) Additional acquisitions used as *slave*

Fig. 6.10. Global maps of the height of ambiguity (HoA) ratios of the scenes of the second global coverage processed with the Dual-Baseline Phase Unwrapping Correction (DB-PUC) framework. The *master* is the acquisition of the second coverage (HoAs mapped in Fig. 4.1c) and the *slave* is either from (a) the first global coverage (HoAs mapped in Fig. 4.1a) or (b) the additonal acquisitions over forested and difficult terrain (HoAs mapped in Fig. 4.1b). For $\mu \approx 1$ (red) and $\mu \leq 0.5$ or $\mu \geq 2.0$ (dark blue), the *differential interferogram* cannot be computed. The orange and lighter blue marks denote suboptimal ratios for which the *differential interferogram* is used. Finally, the green dots are for the ratio which are considered as optimal.

The amount of inadequate scene combinations ($\mu \approx 1$, $\mu \leq 0.5$ or $\mu \geq 2.0$) is not negligible but also and especially they might be the only pairs available for the DB-PUC. As a consequence, the scenes with unfavourable HoAs have to be used as far as practicable. Yet, the only handy information is the *slave* interferogram. Its 1B-PU output can be assessed only by means of the stereo-radargrammetry. The 1B-PU is said successful if the q_{ratio} greater than 0.97. Under these circumstances, the q_{ratio} has to be trusted. This is a strong limiting factor but it enables the use of the DB-PUC workflow for most of the scene combinations.

Last but not least, the *differential interferogram* contains the noise of both interferograms. In consequence, in mountainous or forested terrain, a correct PU may not be achievable or the resulting corrected *master* unwrapped phase may be of low quality. The *differential* absolute phase is thus verified prior to the correction of the *master* estimated phase. Also in this case, the outcomes of the stereo-radargrammetric assessment have to be relied on.

Figure 6.11a recalls the joint distribution of the *master* and the *slave* HoAs. It shows all the scenes that fulfil the requirements for the DB-PUC. It displays also those that could eventually be used using the above-mentioned improvement (i.e. the use of *slave* interferograms for the correction if μ is unfavourable and their unwrapping is successful according to the stereo-radargrammetry) and depicted in red or dark blue in Fig. 6.10. Figures 6.11b and 6.11c illustrate the minimum coherences required to detect or to correct a PU error. These are the same figures as Fig. 5.8 and 5.20 with the difference that the combinations of *master* and *slave* HoAs which do not exist in TDM, are masked out. **Thresholds on μ to achieve the best performance in the DB-PUC are $\mu \geq 0.55$ and $\mu \leq 0.76$.** These limiting ratios have been determined for a threshold on the minimum coherence of 0.65 and 3σ assuming 25 looks. The limitation for the former is the ability to detect PU error (see Fig. 6.11b) whereas for the latter, it is the required

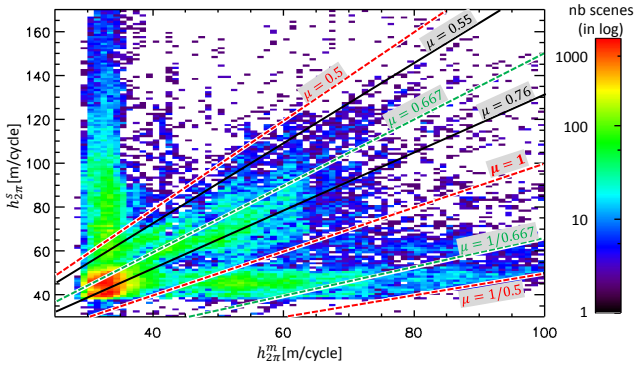

(a) Joint distribution of the *master* and *slave* HoAs (recall from Fig. 4.4)

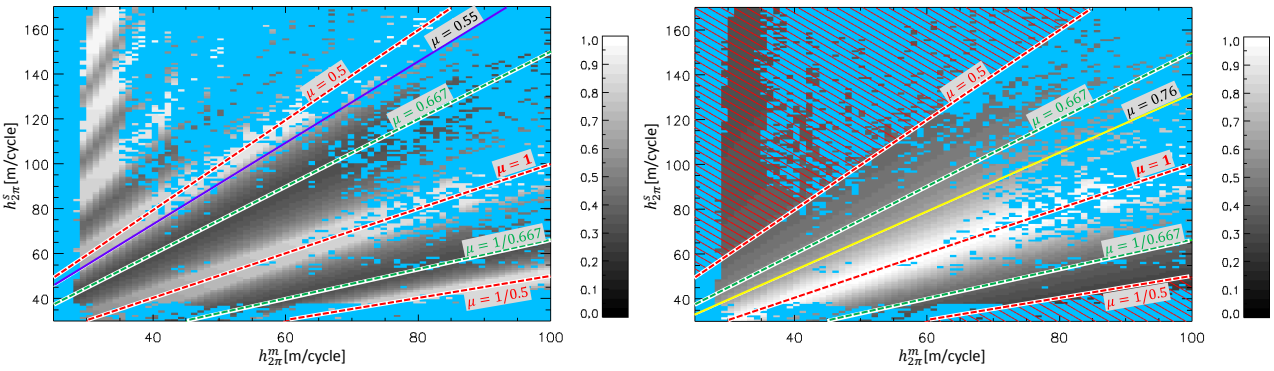

(b) Minimum coherence necessary to detect a PU error

(c) Minimum coherence necessary to correct a PU error

Fig. 6.11. Minimum coherences necessary to (b) detect and (c) correct a PU error for the joint distribution of the *master* and *slave* HoAs (a) assuming 25 looks (3σ and that both interferograms have the same coherence). Significant values of the HoA ratio μ are plotted as lines. In (b), $\mu = 0.55$ is the lower limit for the HoA ratio obtained for a maximum allowed minimum coherence of 0.65 to detect a PU error. In (c), $\mu = 0.76$ is the upper limit for a straightforward *master* estimated phase correction. The red strips emphasise where the *differential interferogram* is not helpful for the DB-PUC.

quality of the *differential interferogram* for a successful correction of the *master* unwrapped phase. The 3σ ensure that the detection and the correction of PU errors is successful for 99.7% of the pixels. These thresholds emphasise consequently the ideal conditions for the DB-PUC framework. 46% of the used configurations conform with these ideal requirements on the HoA ratio. If the number of looks is greater, the thresholds can be relaxed.

6.2.2 Time span between the acquisitions and temporal changes

A time span of several months or more separates the different acquisitions. Thus, temporal changes such as seasonal ones may take place. Figure 6.13 shows the difference in months between the acquisition dates of the *master* and the *slave* interferograms coming either from the first global coverage or the additional acquisitions over dense forested and difficult terrain (absolute value of the difference wrapped into ±6 months). One year difference between both acquisitions results into 0 month of difference whereas a difference of 10 months is represented like one of 2 months to emphasise the season differences. The vegetation may have different heights or, and it is not the least effect, snow or ice may be present in only one scene (see an example of frozen/non-frozen water in Fig. 6.12). This is very likely to happen for the additional acquisitions over Russia of the Alps (see Fig. 6.13b). This is an important issue because such height discrepancies that are not detected as *incompatible* regions may locally disturb the correction.

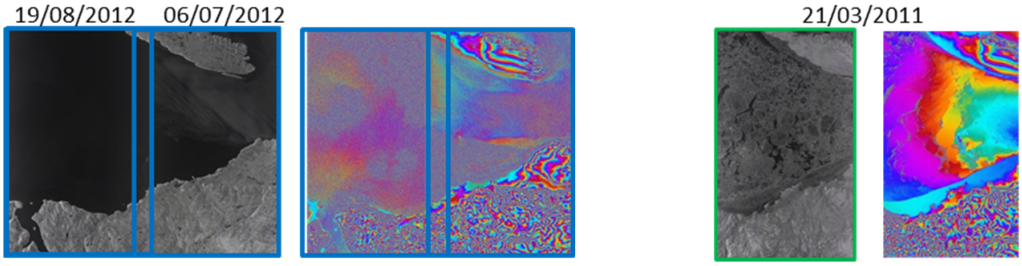

Fig. 6.12. Seasonal changes: the two acquisitions on the left (second coverage) were taken in summer thus the water is incoherent whereas the first coverage acquisition (on the right) is from early spring and the river is still frozen thus coherent.

Figure 6.14 depicts the influence of possible seasonal changes on the phases of the different interferograms. Both the different vegetation height and the presence of snow in only one of the scenes are studied. In late spring/summer (*slave* interferogram), the ground and trees are mapped at a certain height $h^s = h_{\text{summer}}$. In late autumn/winter (*master* interferogram, the one to correct), trees and ground may be covered with snow and thus have a different height (the penetration may also be different due to, e.g., the leaf loss). Without loss of generality, the height discrepancy denoted ε_h is considered in the *master* interferogram. The height is then $h^m = h_{\text{winter}} = h_{\text{summer}} + \varepsilon_h$. The corresponding phases are:

$$\phi^s = \frac{2\pi}{h^s_{2\pi}} h_{\text{summer}} \qquad \text{and} \qquad \phi^m = \frac{2\pi}{h^m_{2\pi}} (h_{\text{summer}} + \varepsilon_h) \tag{6.1}$$

The *differential* interferogram exhibits then a phase, which is neither the ground phase nor the *ground plus snow* nor the *ground plus trees* phases but an intermediate one:

$$\phi^d = \frac{2\pi}{h^d_{2\pi}} h_{\text{summer}} + \frac{2\pi}{h^m_{2\pi}} \varepsilon_h \tag{6.2}$$

Accordingly, the height corresponding to the *differential* phase is:

$$h^d = h_{\text{summer}} + \frac{h^d_{2\pi}}{h^m_{2\pi}} \varepsilon_h = h_{\text{summer}} + \varepsilon_h \frac{1}{1-\mu} \tag{6.3}$$

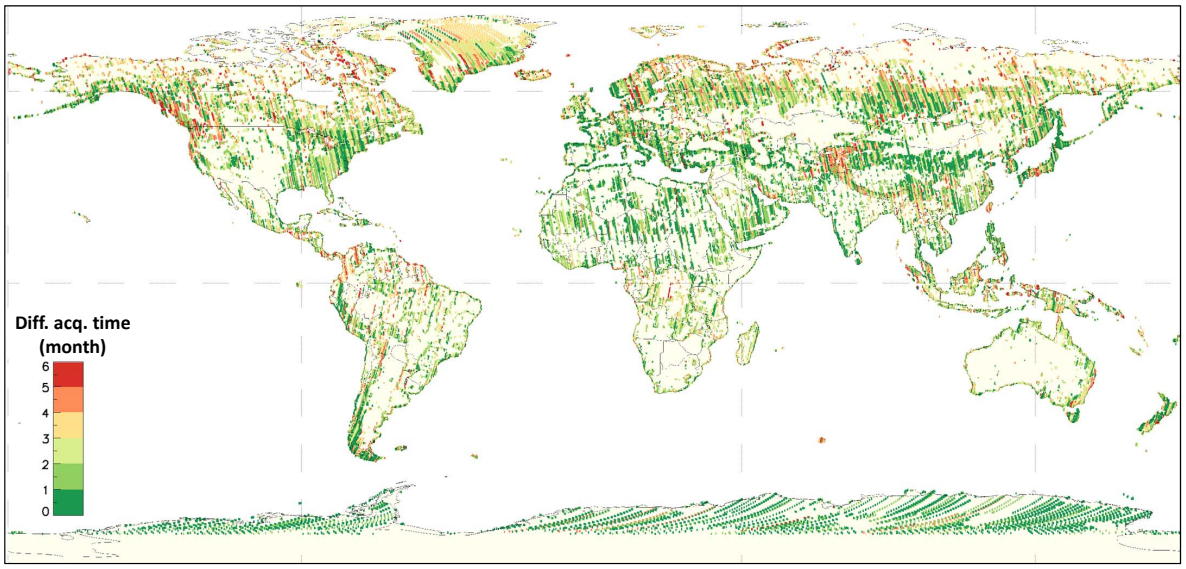

(a) Acquisitions from the first global coverage used as *slave*

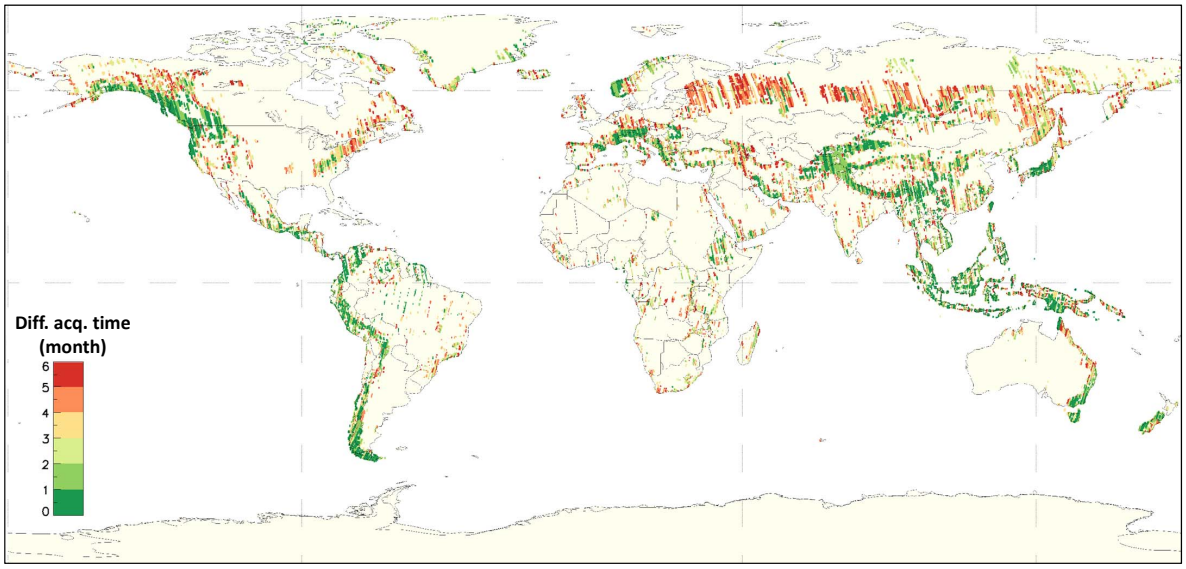

(b) Additional acquisitions used as *slave*

Fig. 6.13. Global maps of the difference in months (absolute value of the difference wrapped into ±6 months) of the acquisition times of the scenes of the second global coverage processed with the Dual-Baseline Phase Unwrapping Correction (DB-PUC) framework. The *master* is the acquisition of the second coverage and the *slave* is either from (a) the first global coverage or (b) the additonal acquisitions over forested and difficult terrain. One year difference between both acquisitions results into 0 month of difference whereas a difference of 10 months is represented as one of 2 months to emphasise the season differences.

In Fig. 6.14, $\varepsilon_h = -5\ m < 0$ over the forest, so that the resulting height is lower than the real ones. On the contrary, on the ground, $\varepsilon_h = 2\ m > 0$ because of the snow and the height coming from the *differential interferogram* is higher.

Figure 6.15a shows the maximum allowed height noise to detect a PU error (Fig. 5.7 where the combinations of *master* and *slave* HoAs which do not exist, are masked out). In section 5.2.1, the case of no terrain changes or small ones which are considered as noise has been studied. Consequently, this plot can equivalently be interpreted as representing the maximum height discrepancy allowed so that this one is not recognised as a PU error. Figure 6.15b shows for which configurations a height discrepancy of 5 m like the height difference over the forest in the example of Fig. 6.14 would be detected as a PU error (in dark red). For the illustrated configuration (marked by a blue star), the 5 m would still be considered as noise and would not disturb the correction. This specific height discrepancy is not problematic for any HoAs combinations for which $\mu \in [0.55, 0.76]$.

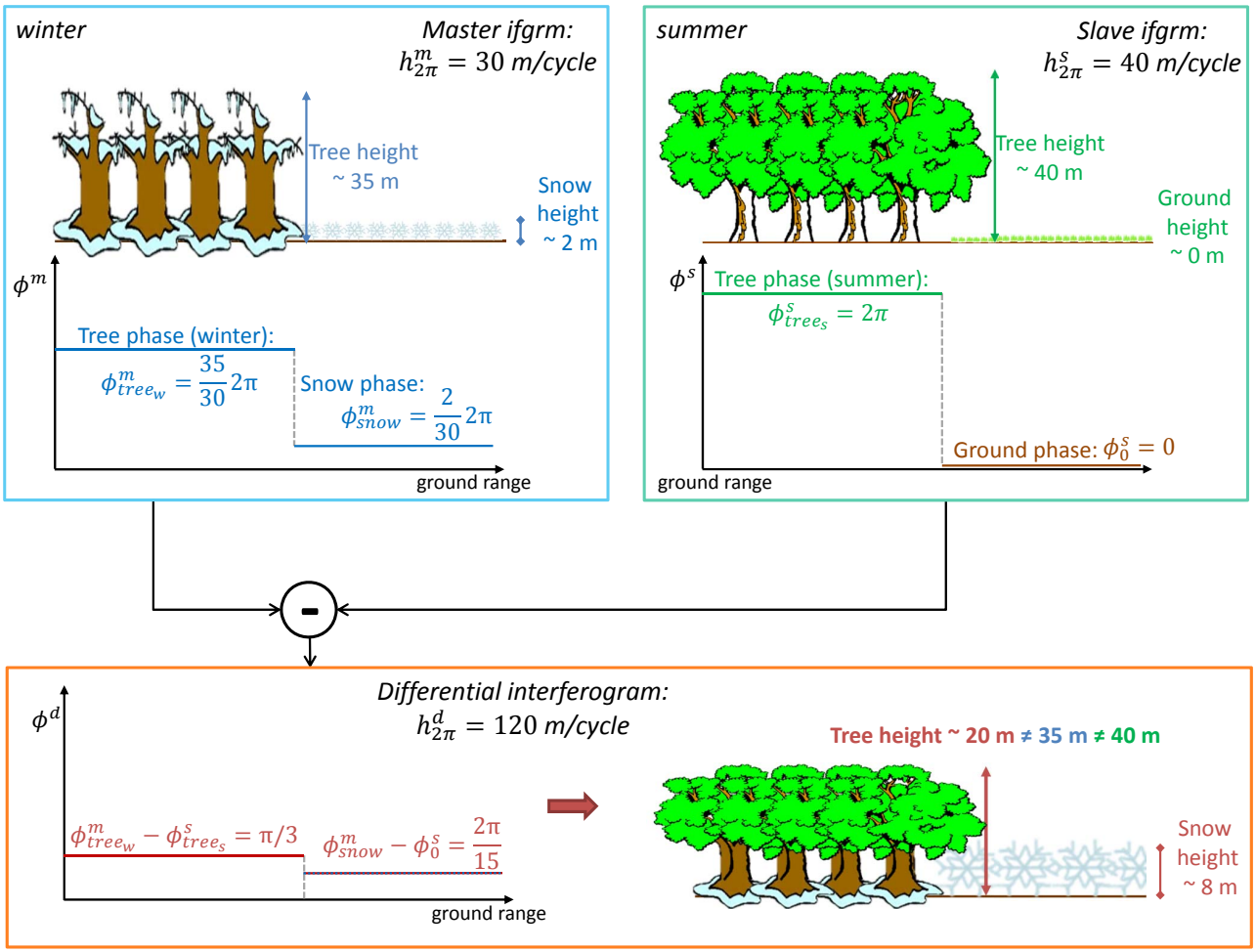

Fig. 6.14. Description of the effect of seasonal changes on the phase and height of the *differential interferogram*. The *master* scene was acquired in winter and is covered by snow whereas the *slave* was acquired in summer. The heights are different by 5 m in the forest and by 2 m on the ground. The corresponding heights in the *differential interferogram* are respectively 20 m and 8 m i.e. 4 times bigger than the height discrepancy (eq. (6.3)) and totally different from both real heights.

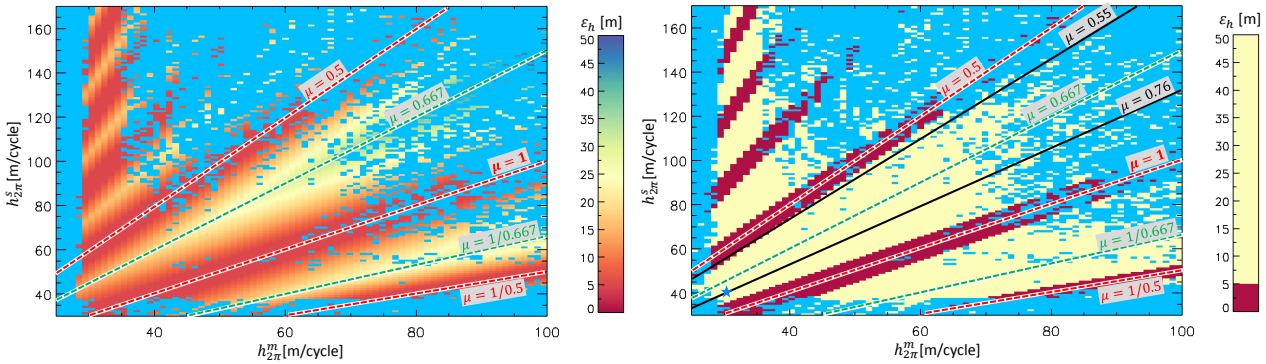

(a) Maximum allowed height discrepancy

(b) Configurations which detect ε_h =5 m as a PU error

Fig. 6.15. Maximum allowed height discrepancy ε_h which is seen as noise and not as a PU error represented as a function of $h^m_{2\pi}$ and $h^s_{2\pi}$. (b) emphasises the configurations which would consider $\varepsilon_h = 5$ m as a PU error (in dark red). The blue star is the configuration of Fig. 6.14. Significant values of the HoA ratio μ are plotted as lines.

In contrast, if the height discrepancy is detected as a PU error or if there is a PU error and a height discrepancy, the correction performed by means of the *differential interferogram* is misleading. If the unwrapped phase over the forest is misestimated in one of the interferograms of Fig. 6.14, the discrepancy would be detected, the *differential interferogram* computed, and the ambiguity band of the *master* unwrapped phase would be modified to be in agreement with a *differential* phase equivalent to a "height" of 20 m which does not represent the ground truth

of any acquisitions.

6.2.3 Joint analysis of the two effects and summary

In this section, the effects of the large ranges of heights of ambiguity (HoAs) and more especially, the influence of the HoA ratios on the DB-PUC framework were first analysed. The amount of acquired regions affected by an inappropriate ratio being not negligible, the DB-PUC has been adapted so that *master* scenes which have *slave* interferograms with an unsuitable HoA ratio can still be corrected. However, this is achievable only under the condition that the *slave* is correctly unwrapped according to the stereo-radargrammetry. Table 6.5 summarises the repartition of the *slave* scenes fulfilling (or not) the ideal requirements on the HoA ratio and those exhibiting a relatively good average coherence. 37% of the used *slave* scenes have the ideal conditions to perform a successful DB-PUC (depicted in green in Fig. 6.16a). These thresholds ($\mu \in [0.55, 0.76]$) were computed for 25 looks and an error of 3σ i.e. they ensure that 99.7% of the pixels can be corrected without uncertainty (considering a Gaussian distribution). However, the framework is robust enough to use data exhibiting conditions less ideal. Figure 6.16a depicts in green *master* scenes for which at least two *slave* with suitable HoA ratio are available. On the contrary, the red colour shows all *master* scenes which had to be processed with data exhibiting an unfavourable combination (μ and/or γ).

The second part of this section brought to the reader's attention the consequences of the combination of scenes acquired at different seasons (and per extension of any terrain height changes). It was shown that areas with wrong height may occur in deciduous forests or snow and ice covered regions if data from totally different seasons have to be combined. Notwithstanding, for typical HoAs and HoA ratios μ, temporal height discrepancies below 5 to 8 m do not affect the DB-PUC. 85% of the data have a difference of less than 4 months between their acquisitions time (absolute value of the wrapped difference into $\pm$ 6 months) and are depicted in red in Fig. 6.16b. Red points indicate that at least one of the *slave* scenes used for the DB-PUC was acquired at the opposite season (winter/summer) than the *master* scene.

Red dots in Fig. 6.16 indicate where the DB-PUC may encounter problems because the HoA ratio is not ideal and the coherence low and/or because the season is opposite in the considered acquisitions (summer vs winter). The worst possible case is when both the conditions on μ and on the (same) season are not fulfilled. However, the DB-PUC framework is robust and still performs good as it is shown in section 6.3.

	fulfil ideal conditions	do not fulfil ideal conditions
HoA ratio $\mu \in [0.55, 0.76]$	46.33%	53.67%
coherence $\gamma > 0.55$	82.82%	17.18%
$\mu \in [0.55, 0.76]$ and $\gamma > 0.55$	**37.18%**	**62.82%**
difference acquisition time ($\leq$ 4 months)	84.58%	15.42%

Table 6.5. Repartition of the *slave* scenes used during the Dual-Baseline Phase Unwrapping Correction (DB-PUC) with respect to the ideal requirements for a straightforward DB-PUC procedure ($\mu \in [0.55, 0.76]$ and $\gamma > 0.55$).

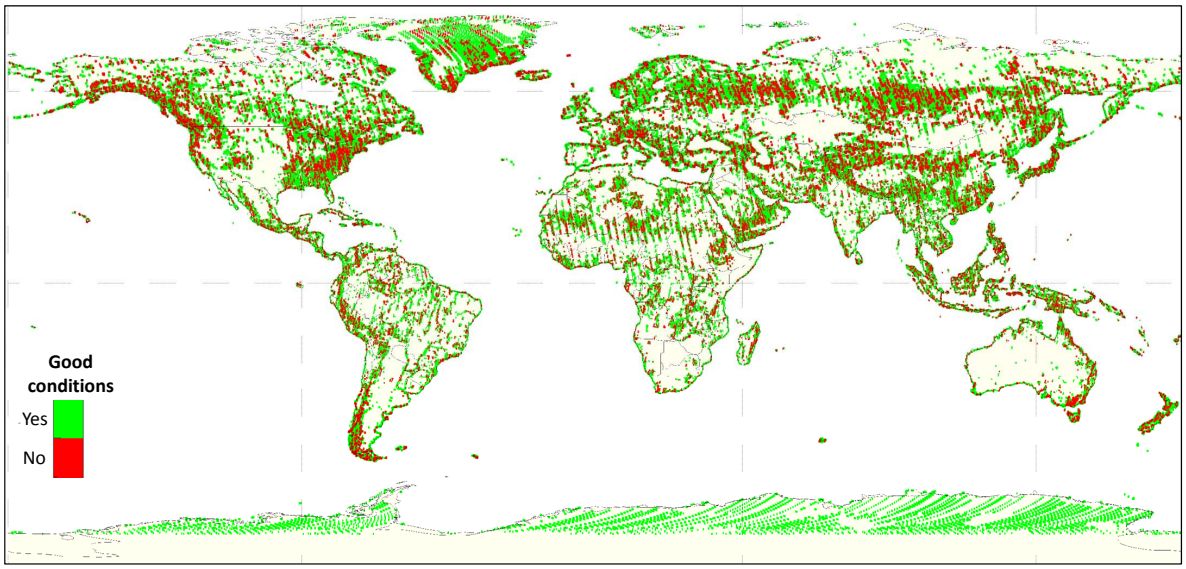

(a) Conditions for the DB-PUC: good (green) means that at least 2 *slave* scenes exist with ideal HoA ratios and coherences better than 0.55, red indicates that no or only one favourable combination is available.

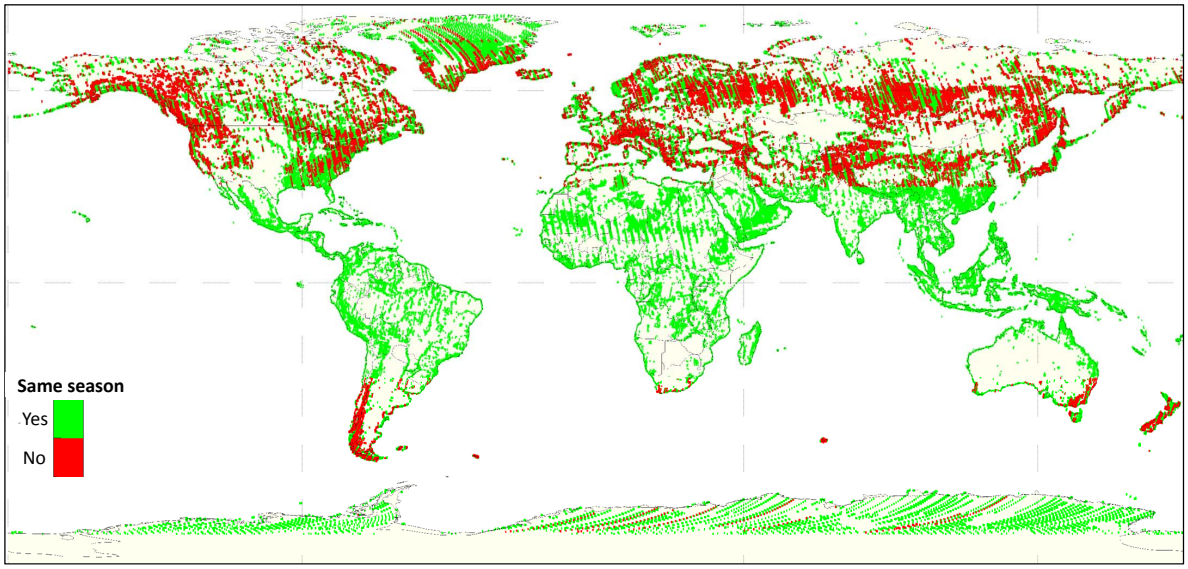

(b) Acquisition at the same season: green indicates that all *slave* have been acquired at the same season whereas red means that the difference between the acquisition times is greater than 4 months (absolute value of the wrapped difference into ± 6 months) for at least one *slave*. Scenes inside ±30° of latitudes are not shown because seasonal changes are not likely to happen.

Fig. 6.16. Location of scenes according to their (a) conditions in terms of HoA ratio and coherence for the Dual-Baseline Phase Unwrapping Correction (DB-PUC) and (b) relative acquisition seasons. Green means that either the condition on the HoA ratio and coherence or the season are ideal for the correction process. On the contrary, red emphasises where the scene combinations is not optimal and where problems could occur.

6.3 Results of the DB-PUC framework and vertical accuracy of the final TanDEM-X DEM

Figure 6.18 exhibits on a global map the 1B-PU quality ratio for the regions where the DB-PUC has been processed automatically. These regions are the union of scenes exhibiting a PU ratio lower than 0.994 and of those with an average coherence lower than 0.65 (see Fig. 6.1). Green means success and other colours possible failures. The other scenes were processed only using 1B-PU (data that exhibit errors which escaped that check are reprocessed in a second iteration using a forced DB-PUC approach). 36% of the second coverage data were processed with the DB-PUC. Figure 6.19 represents on a global map the PU quality ratio after the DB-

PUC procedure. Almost every scene has been corrected successfully: the overall success rate is 96.5% (see Table 6.6).

Number of scenes	142,716	
Number of scenes processed with DB-PUC	51,279	35.93%
Scenes successfully unwrapped and/or corrected ($q_{\mathbf{ratio}} > 0.97$)	**137,666**	**96.46%**

Table 6.6. Summary of the results of the phase unwrapping (PU) for the TanDEM-X second global coverage.

The absolute vertical accuracy of the final TanDEM-X DEM is displayed on a global map on Fig. 6.17. According to Wessel et al. (2013), *"the absolute vertical accuracy is the uncertainty in the height of a pixel with respect to its true height caused by random and uncorrected systematic errors. The value is expressed as a linear error at 90% confidence level.* The absolute height error is computed with respect to the ICESat points which were not used during the calibration process (see appendix A.6). This map shows the 90% error of every DEM tile with respect to the ICESat points lying in it. Consequently, it shows the discrepancy to ICESat points such as possible remaining PU errors but also different signal penetration. 99.8% of all ICESat points used for the assessment achieve the absolute height error required by the specification i.e. below 10 m. The mean offset over all ICESat validation points is 0.16 cm and the accumulated absolute height accuracy (90%) is 1.1 m thus significantly below the requirements (see Table 6.7).

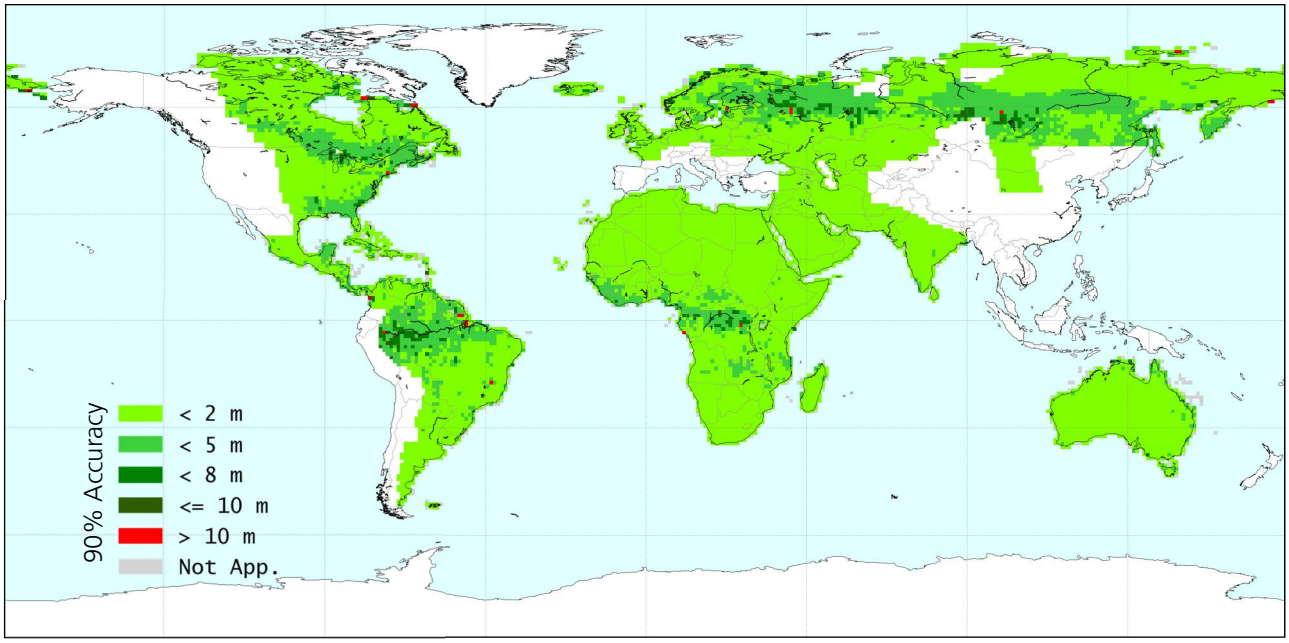

Fig. 6.17. Absolute vertical accuracy (9,691 DEM tiles, courtesy of TanDEM-X System Performance Working Group, final DEM processed till 22/04/2015).

Number of DEM tiles	9,691
Number of assessed points (w.r.t ICESat)	8,741,165
Linear Error for Absolute Height Accuracy (<10 m, 90% error)	**99.77%**
Mean height deviation	0.15 m
Accumulated absolute height accuracy (90% error)	1.07 m

Table 6.7. Summary of the vertical accuracy of the final TanDEM-X DEM (courtesy of TanDEM-X System Performance Working Group, final DEM processed till 22/04/2015).

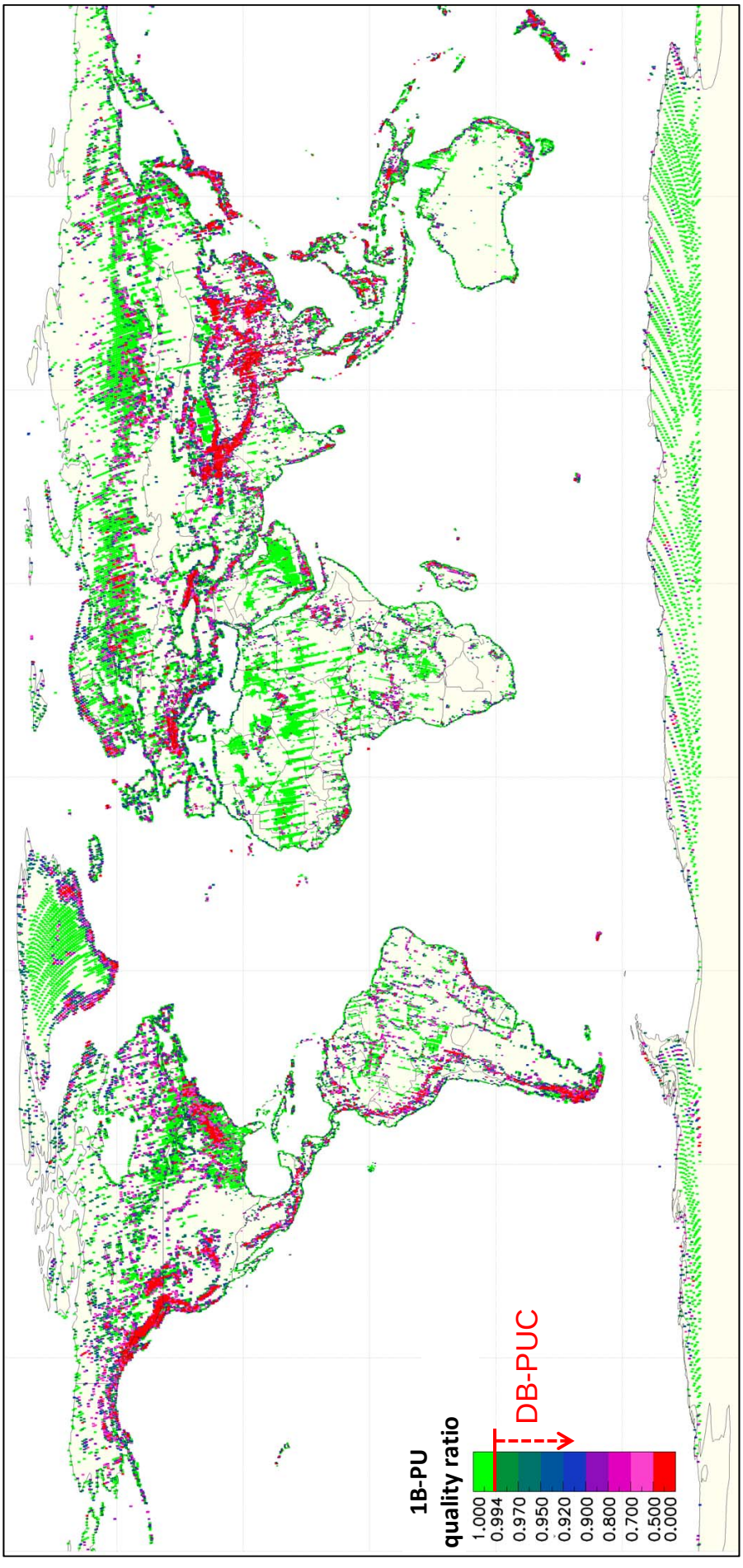

Fig. 6.18: Maps of the initial single-baseline phase unwrapping (1B-PU) quality ratio of the TanDEM-X second global coverage acquisitions which were then processed with the Dual-Baseline Phase Unwrapping Correction (DB-PUC) (representing 51,279 scenes i.e. 35.93% of the second global coverage acquisitions, data processed till 12/01/15).

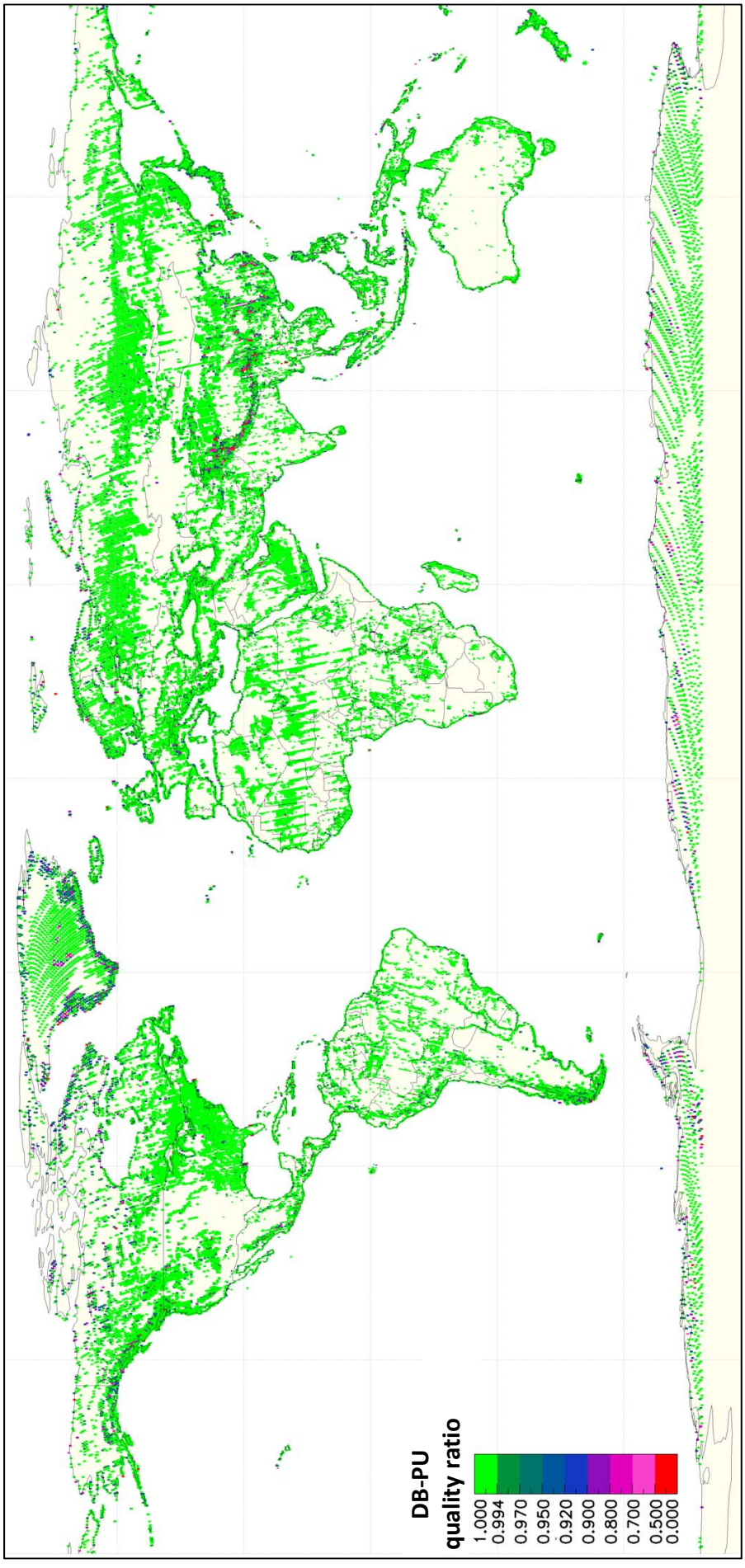

Fig. 6.19: Maps of the final phase unwrapping (PU) quality ratio of the TanDEM-X second global coverage acquisitions after the Dual-Baseline Phase Unwrapping Correction (DB-PUC) procedure (representing 51,279 scenes i.e. 35.93% of the second global coverage acquisitions, data processed till 12/01/15).

Figure 6.20 display two 3-D views of the first processed tile of the final TanDEM-X DEM which contains difficult terrain. It is over the Kamchatka peninsula in Russia. This contains scenes which required DB-PUC and scenes acquired from two different incidence angles to fill in shadow and layover regions.

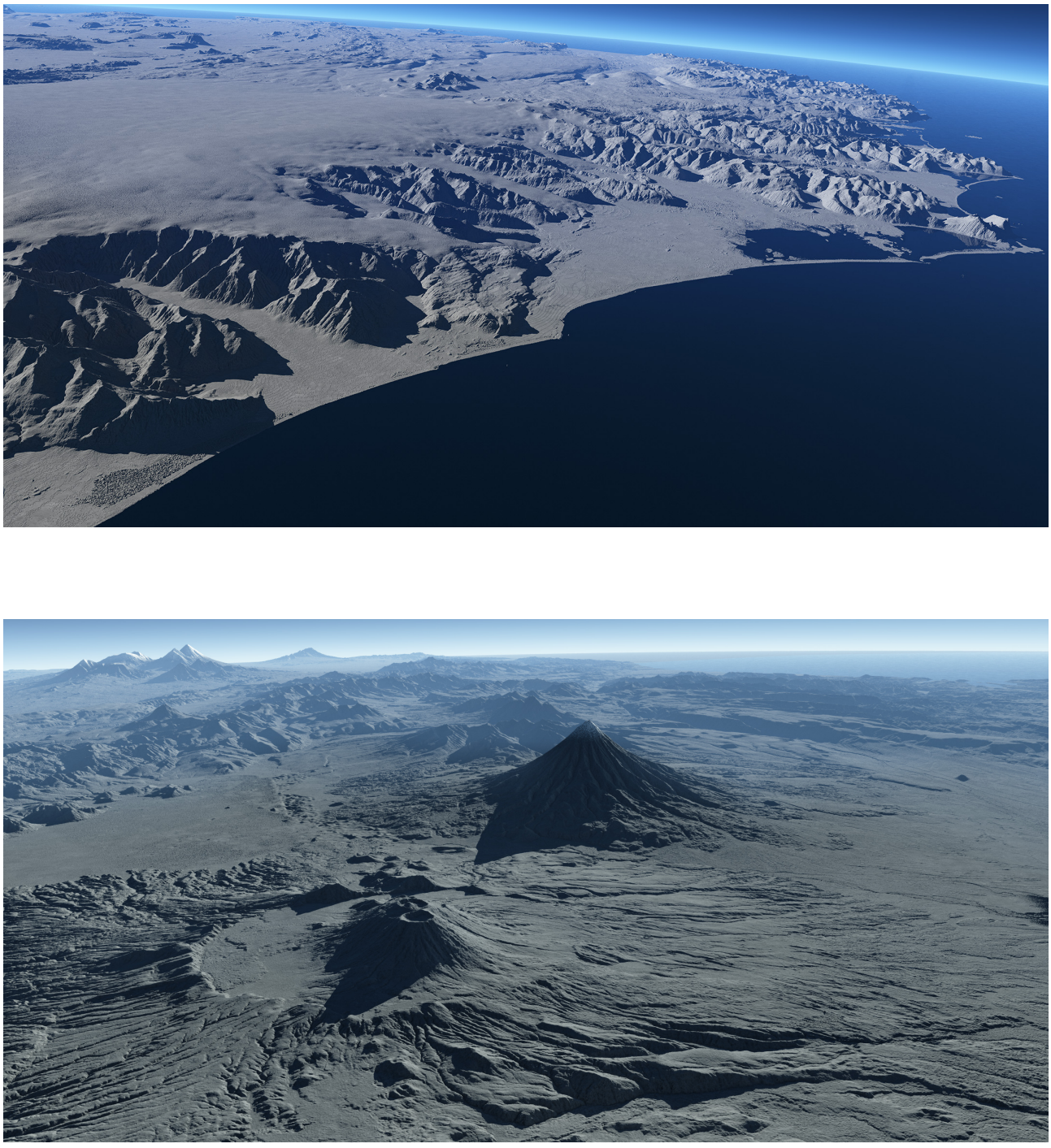

Fig. 6.20. 3-D views of the final TanDEM-X DEM over the Kamchatka peninsula in Russia (courtesy of Nils Sparwasser from the Science Communication and Visualisation Department of DLR-EOC).

The presented results showed that the proposed Dual-Baseline Phase Unwrapping Correction (DB-PUC) framework performed very well even under not ideal conditions. It is computationally efficient, flexible and robust. It has been successfully used for the processing of the second global coverage acquisitions. Finally, the vertical accuracy of the final TanDEM-X is well below the requirements.

7 Conclusion and outlook

7.1 Conclusion

The aim of this thesis was to combine multi-temporal bistatic high-resolution interferometric data in order to perform a correct and accurate phase unwrapping on a global scale. More particularly, it was to

"develop a robust and fast multi-channel phase unwrapping algorithm which is reliable, fully automatic and usable operationally for the TanDEM-X mission"

In order to achieve this goal, which was crucial for the success of the TanDEM-X mission, this work had four main phases reflected in the four main parts of this thesis. First of all, the fundamentals of elevation retrieval from InSAR data have been explained and a review of the existing methods have been carried out in chapters 2 and 3. Second, the peculiarities of the TanDEM-X bistatic interferometric data have been presented and three representative algorithms have been assessed in chapter 4. Third, the proposed approach, the *Dual-Baseline Phase Unwrapping Correction (DB-PUC)* framework, has been described and analysed in chapter 5. Finally, in chapter 6, an assessment of the developed method has been presented for selected examples followed by an analysis of the results of the operational processing.

The design of an adequate phase unwrapping (PU) method intended to an operational usage on a global scale was challenging. The following conclusions can be drawn based on the investigations carried out:

- A global mapping requires a robust, versatile and computationally efficient PU method, which is able to deal with data of heterogeneous quality and acquired with very different baseline configurations.
- Designing a totally new phase unwrapping algorithm is not always an appropriate solution. For example, elevation extraction based on statistical estimation with dual-baseline (or few multi-baseline) data acquired at different time periods does not allow to recover a satisfactory height map. A more suitable solution is to use an existing single-baseline phase unwrapping (1B-PU) algorithm of which the advantages and limits are well-known and then, to correct its outputs.
- Because temporal changes of the topography occur, a global mapping requires to be independent of external (possibly outdated or partially erroneous) reference.

As a result, a new PU approach, the Dual-Baseline Phase Unwrapping Correction (DB-PUC) framework, has been designed and developed considering the above-mentioned facts. Its key characteristics are to:

- perform the correction region-wise,
- *only* correct the misestimated ambiguity bands,
- take benefit of the *differential interferogram* as a third reliable information,
- use the absolute measurements stemming from the radargrammetric shifts,
- be independent of external reference data,
- be versatile, robust and computationally efficient.

The proposed DB-PUC framework follows a multi-stage approach. Its first step is to seek possible discrepancies between the *master* and *slave* height maps in the slant range geometry. Logically, the correction is made only in the presence of inconsistencies. The second step consists in the unwrapping of the phase of the *differential interferogram*, which has typically a higher height of ambiguity (HoA). The *differential* unwrapped phase is validated and potentially

corrected region-wise by means of the *stereo-radargrammetric phase*. Finally, the *master* unwrapped phase is corrected in terms of ambiguity bands with the help of the absolute *differential* phase. The region-wise correction of the ambiguity bands ensures that the correction process is less sensitive to external perturbation such as noise and, more important, temporal changes.

The DB-PUC framework was the default phase unwrapping method to process operationally the acquisitions of the second global coverage. The proposed approach has been also used to correct phase unwrapping errors, which arose during the single-baseline processing of the other acquisitions.

In the following, results of both the studies performed along this thesis and the operational processing of more than 100,000 bistatic scenes are summarised:

- The DB-PUC framework performs optimally for dual-baseline data exhibiting a HoA ratio μ within 0.55 and 0.76 (or within 1/0.76 and 1/0.55) and sufficient coherence ($\gamma \geq 0.55$). These thresholds on μ have been obtained for 25 looks. If more looks can be used, the thresholds can be relaxed.
- The *differential interferogram* is helpful, i.e. its HoA is higher than the *master* and *slave* ones, only if $\mu \in]0.5, 2[$ (but $\mu \neq 1$). Out of this range, the *slave* interferograms are used as a replacement for the *differential interferogram* under the condition of a correct phase unwrapping (consistent with the radargrammetry).
- Terrain changes for example due to seasonal changes (presence of snow or vegetation only in one of the two acquisitions) are not problematic for the ideal acquisition configurations ($\mu \in [0.55, 0.76]$) if they do not exceed 5 to 8 m.
- 36% of the data of the second global coverage required a correction of the 1B-PU outputs. The success rate of this correction is 96.5%. For the other 3.5%, available data are not of sufficient quality, have unfavourable HoA ratios and/or exhibit terrain changes due to different climatic conditions.

7.2 Outlook

In this thesis, a multi-level approach to correct PU errors in terms of ambiguity bands, the DB-PUC framework, has been developed and successfully applied within the TanDEM-X mission. In this section, recommendations for possible improvements are outlined and a recommendation for a future mission is formulated. Finally, further research and applications are suggested.

Three algorithmic improvements are conceivable:

- In case that $\mu \notin]0.5, 2[$, the *differential interferogram* is not useful. However, if the interferogram of longer baseline is multiplied by a small integer, the computation of a *differential interferogram* with a favourable HoA is enabled again (linear combinations of interferograms). Scenes or at least parts of them could be restored. This has however, a limited impact since it is only worth considering for scenes having a high coherence because the noise is also amplified.
- In the proposed approach, the correction of the *master* unwrapped phase by means of the *differential interferogram* phase is ensured to work satisfactory with an adequate HoA ratio and a sufficiently good coherence. However, the variety of possible baseline combinations and interferometric quality complicates dramatically the task. Until now, the wrongly estimated ambiguity band is the *master* unwrapped phase is corrected to the nearer ambiguity band suggested by the *differential interferogram*. A cluster analysis of the *master* and *differential* ambiguity bands distributions with respect to each other could improve the robustness in case of extreme configurations or very low SNR as suggested by

Yu et al. (2011); Liu et al. (2015). Furthermore, the *slave* interferogram is only used to compute the *differential interferogram*. The cluster analysis could be enhanced to work in 3-D to take the three unwrapped phases into account.

- Additional acquisitions might be acquired to fill the gaps in the final DEM in the on-going TanDEM-X mission. These new data would have up to four years difference with the actual ones. Moreover, a gap in the final DEM hints that available data are not suitable to retrieve a trustworthy height map. A robust change detection and possibly segmentation would then become important. It should be based on the complex interferogram values.

With the experience gained during the TanDEM-X mission, a recommendation for a future mission can be formulated. The bistatic mode allows to avoid temporal decorrelation within an interferogram but there is still decorrelation between the two interferograms used in the DB-PUC. Also terrain changes may occur between the acquisitions. In consequence, a *multi-static acquisition system* would allow several interferograms with various baselines and possibly different frequencies to be acquired simultaneously. The interferometric cartwheel configuration proposed by Massonnet (2001) seems to be a low cost but effective solution. He suggested to form a constellation of several passive micro-satellites in an orbit configuration forming a cartwheel and flying close to an active satellite. As a result, several bistatic interferograms can be acquired simultaneously.

Besides the algorithmic improvements, the extension of the DB-PUC method to *multi-geometry* and/or *repeat-pass* data is an appealing research topic. Likewise, its application to *higher resolution* data is a great challenge.

- Regarding repeat-pass data, the framework has been already applied successfully and operationally to pursuit-monostatic data i.e. to repeat-pass interferometric data with a very short time lag. By incorporating the necessary corrections such as atmospheric compensation, an extension of the method to repeat-pass data with higher time separation could be promising for further use.
- The proposed approach works in the slant range geometry. As such, it can use only data from the same acquisition geometry. An interesting research topic would be to adapt it to process data from different viewing geometries. In the TanDEM-X mission, a pair of interferograms acquired from the crossing orbit is available for difficult terrain. A first step could be to separately unwrap the two sets of dual-baseline data with the DB-PUC approach and then, to correct and fuse the resulting geocoded height maps with a similar correction concept but in the ground projected geometry. It is also conceivable to use a radargrammetric approach to obtain a coarse DEM fusing the two geometries. This one could support in a second step the accurate unwrapping of the interferometric pairs.
- The developed method is strongly related to the TanDEM-X mission. Nonetheless, it remains flexible and relatively independent of the 1B-PU method and the sampling of the input phases. Consequently, it can be applied to generate DEMs of higher resolution in height and space with TanDEM-X data. 1) To get a higher height accuracy, the HoA has to be smaller (e.g. about 20 m/cycle or less). It leads to potential difficulties in the unwrapping of the phase of the *differential interferogram*. As a result, the success of the DB-PUC is compromised. To overcome this problem, the simulated phase from the final TanDEM-X DEM could be removed to ease and speed-up the 1B-PU. The DB-PUC would be then applied on the unwrapped residual phases. 2) The method can also be applied on filtered phases with state-of-the-art techniques such as non-local ones. In that case, the noise is reduced while the details are preserved and DEMs of higher resolution and spacing can be derived.

A The TanDEM-X mission

The TanDEM-X (TerraSAR-X add-on for Digital Elevation Measurement) mission is the first free flying bistatic Synthetic Aperture Radar (SAR) space mission. A single-pass high resolution SAR interferometer (Fig. A.1) has been formed in June 2010 by adding a second (almost identical) TanDEM-X satellite (TDX) to the TerraSAR-X satellite (TSX), launched in June 2007.

The primary mission objective is the generation of a global consistent high resolution Digital Elevation Model (DEM). However, TDX and TSX also form a configurable platform allowing the demonstration of different SAR techniques and applications.

Both satellites fly in a close HELIX formation (Moreira et al., 2004b) and are typically separated by distances varying between 200 and 500 metres. In addition, baselines are adjustable in across- and along-track directions. Hence, acquisition of highly accurate cross- and along-track interferograms with almost no temporal decorrelation and atmospheric perturbations is made possible.

The TanDEM-X mission is, like the TerraSAR-X mission, a public-private partnership between the German Aerospace Center (DLR) and Airbus Defense and Space (former EADS Astrium). Airbus Defense and Space cares for the spacecraft itself and DLR for the mission planning and operation as well as the scientific use of the data. The Airbus Defence and Space German subsidiary company, Infoterra GmbH, is responsible for the commercial exploitation of the DEM data (the global DEM is sold under the name WorldDEM^{TM}).

Fig. A.1. The tandem formation TSX and TDX: the first single-pass radar interferometer in space employing two satellites.

A.1 Mission goals

The main goal is the generation of a world-wide, consistent, high-precision DEM. This DEM will be the basis for a broad range of scientific research, global positioning systems, and many geoscience and commercial applications (like hydrology, glaciology, oceanography, land environment (Moreira et al., 2004a)). Indeed, they all need precise and up-to-date information about

the Earth's topography. In 2003, when the TanDEM-X mission idea arose (Moreira, 2003), no global coverage was available at sufficiently high spatial resolution.

Having a global reliable map of the Earth's topography has always been of first matter. The very first global map has been compiled from heterogeneous data sources and with inhomogeneous resolution, accuracy and quality. In 2000, the Shuttle Radar Topographic Mission (SRTM) (Rabus et al., 2003; Farr et al., 2007) acquired in 10 days the first nearly complete and consistent DEM. It was the first global radar mission and brought spectacular progress (it is still the reference). The DEM generated at that time has a spatial resolution down to 30 metres and fulfils the DTED-2 (Digital Terrain Elevation Data Level 2) specification. Nevertheless, it was limited to latitudes between 56°S and 60°N due to the inclined orbit of the space shuttle and its mapping geometry. SAR data were acquired both by wide swath SIR-C (complete coverage) and X-SAR (only limited surfaces due to smaller swathes) sensors.

The TDX/TSX formation has been designed to provide a global DEM with an extended coverage and a significantly improved resolution and accuracy. Table A.1 compares both DTED-2 and TanDEM-X DEM specifications. As for Fig. A.2, it emphasises visually the resolution and accuracy differences between SRTM and TanDEM-X DEMs over a small mountainous region.

Requirement	**Specification**	**DTED-2**	**TanDEM-X**
Relative vertical accuracy	90% linear point-to-point error over a $1° \times 1°$ cell	12 m (slope $< 20\%$) 15 m (slope $> 20\%$)	2 m (slope $< 20\%$) 4 m (slope $> 20\%$)
Absolute vertical accuracy	90% linear error	18 m	< 10 m
Absolute horizontal accuracy	90% circular error	23 m	< 10 m
Spatial resolution	independent pixels	30 m (1 arc sec @ equator)	12 m (0,4 arc sec @ equator)

Table A.1. Specifications of DTED-2 standard and TanDEM-X DEM (Wessel et al., 2013).

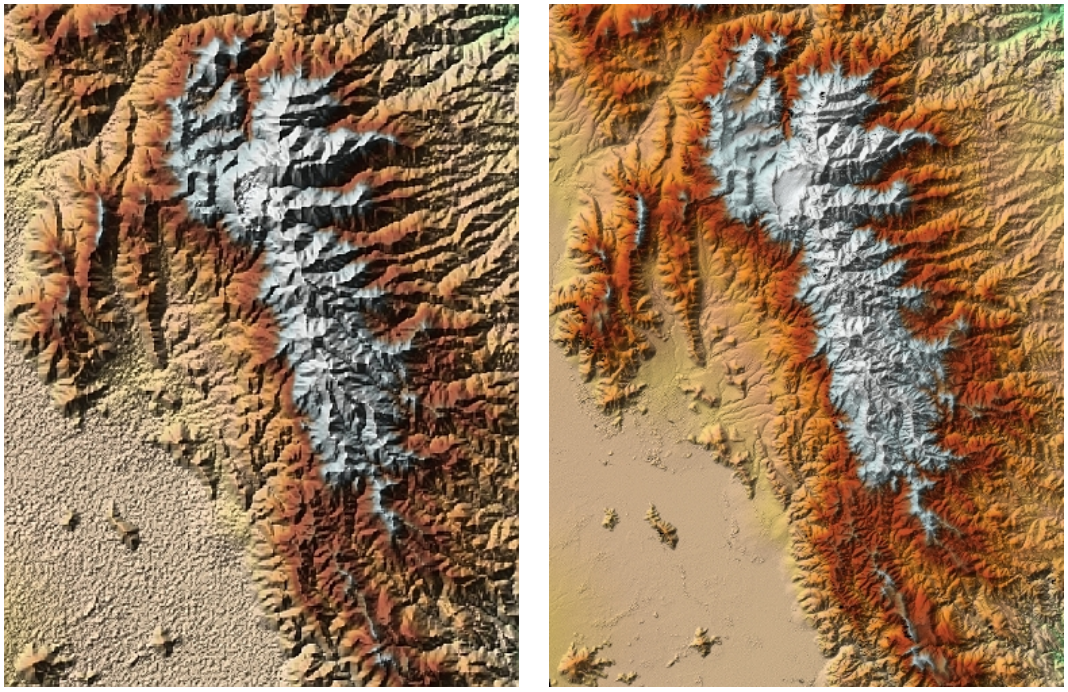

(a) SRTM DEM (b) TanDEM-X DEM

Fig. A.2. Comparison of SRTM and TanDEM-X DEMs over a small mountainous area.

Besides the global DEM, TanDEM-X data are also used to generate local DEMs of very high quality (e.g. for hydrology), for along-track interferometry (e.g. measurement of ocean currents or traffic monitoring), and to evaluate new bistatic applications (e.g. single-pass polarimetric

SAR interferometry). More precisely, further important goals are (list taken from TanDEM-X Science Website):

- development of close formation flying technology being a basis for many future missions;
- development of precise orbit and baseline determination techniques using dual-frequency GPS;
- achievement of a long term availability of X-band data for scientific and commercial users, ensuring a sustainable product development and data delivery;
- new applications based on velocity measurements with along-track interferometry: ocean currents, glacier movements, road traffic, etc.;
- demonstration of innovative SAR techniques in bistatic measurement configuration: digital beam-forming, super resolution, polarimetric SAR interferometry, etc.

A.2 Mission concept

The originally developed mission concept enables the acquisition and generation of a global DEM within three years. It includes multiple data takes with different baselines, different incidence and viewing angles to deal with difficult terrain like mountains or high vegetation.

A.2.1 Orbit configuration and flying formation

The TSX spacecraft keeps its original sun-synchronous dawn-dusk orbit and 11 days repeat cycle. Its trajectory is thus maintained for the entire mission in a 250 m tube around a predefined reference orbit (D'Amico et al., 2004). TDX flies a few hundred metres away in a precisely controlled formation: the so-called HELIX formation (Moreira et al., 2004a,b). As depicted in Fig. A.3, both orbits never cross each other. Collisions are accordingly avoided and a safe spacecraft operation is enabled without the necessity for autonomous control. Additionally, this formation ensures on one hand, a maximal horizontal cross-track orbital displacement at equator by small ascending node differences and on the other hand, a maximum vertical (radial) separation at poles by orbits with slightly different eccentricity. Exclusion zones have been defined in which one of the satellites is not allowed to transmit radar pulses in order to avoid mutual illumination (Krieger et al., 2013, sect. 13.2.3). Finally, since there is no crossing of the orbits, it is possible to shift arbitrarily the satellites along their orbits with cross- and along-track baselines ranging respectively from 200 m to 10 km and from 0 km to several 100 km, depending on the acquisition requirement (note that for cross-track interferometry, the along-track baseline has to be as small as possible). The fine tuning of the satellite position is possible using different specific components of the spacecrafts (see Miller (2008); Pitz and Miller (2010); Krieger et al. (2013, sect. 13.3 and 13.6) for more details).

The HELIX formation allows an interferometric mapping of the Earth with a controlled height of ambiguity (HoA) and very small along-track baselines. Specifically, a given orbit configuration allows the DEM generation only within certain latitudes. Another advantage of this flying formation is that southern and northern latitudes can be mapped with the same formation using ascending orbits (northern hemisphere, NH) and descending orbits (southern hemisphere, SH) as shown in Fig. A.3. The different HELIX equations and parameters can be found in Krieger et al. (2007).

A.2.2 Interferometric acquisition modes

The SAR instruments of TSX and TDX are fully compatible and both offer transmit and receive capabilities as well as polarimetry. Table A.2 summarises the main TanDEM-X parameters.

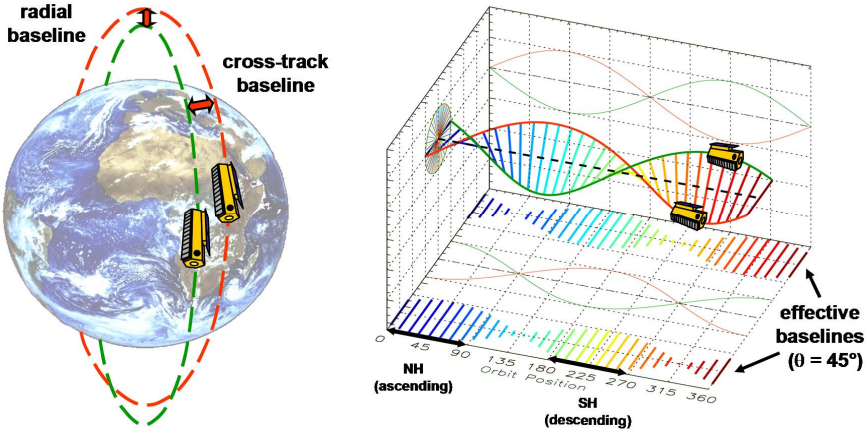

Fig. A.3. HELIX satellite formation for TanDEM-X. Left: orbit configuration with the vertical (radial) and horizontal (cross-track) baselines. Right: effective baseline with respect to the orbit position during one complete orbit cycle in northern (NH) and southern hemisphere (SH) (from Krieger et al. (2007, 2013)).

Parameter	Value
Satellite height (@equator)	514 km
Carrier frequency f_0	9,65 GHz
Chirp bandwidth W_R	100 MHz (up to 300 MHz)
Sampling Frequency f_{RS}	110 MHz and 165 MHz
Along-track baseline	< 1 km
Swath width	~ 30 km

Table A.2. TanDEM-X parameters (Krieger et al., 2007).

The TanDEM-X formation can acquire data in different operational modes like bistatic, pursuit monostatic, alternating bistatic as illustrated in Fig. A.4. In bistatic mode, one satellite (either TDX or TSX) emits and illuminates a radar footprint on the Earth's surface and both receive the scattered signal making efficient use of transmit power. It allows to avoid temporal decorrelation and possible atmospheric disturbances. The different requirements such as pulse repetition frequency synchronisation, an overlap of the Doppler spectra will not be further detailed here. Pursuit monostatic mode is comparable to a repeat-pass system with a small temporal baseline of few seconds. For this reason, temporal decorrelation is avoided for most terrain types (it was intended as a backup mode for DEM generation). Finally, alternating bistatic mode is similar to bistatic but the transmitter switches from pulse to pulse between the two satellites. As a result, this mode provides two baselines simultaneously. Operationally, the bistatic interferometric StripMap is used but other imaging modes like ScanSAR or (High Resolution) Spotlight are also available. More details and explanations can be found in Fritz et al. (2012).

A.2.3 Radar synchronisation

Independent oscillators are used for modulation and demodulation of the radar pulses during the bistatic data acquisition. Nonetheless, any deviation between the two oscillators causes a residual modulation of the recorded radar echoes and oscillator phase noise may cause significant errors in both SAR focusing and interferometric phase (Eineder, 2003b; Krieger and Younis, 2006). For this reason, both satellites exchange radar pulses establishing a synchronisation link (Krieger et al., 2013, section 13.3). For this, the nominal bistatic SAR data acquisition is interrupted for some transmit pulses, and the radar signal is redirected from the main SAR antenna to one of six dedicated synchronisation horns of the other satellite. The pulse is recorded afterwards by the other satellite, which in turn transmits a synchronisation pulse

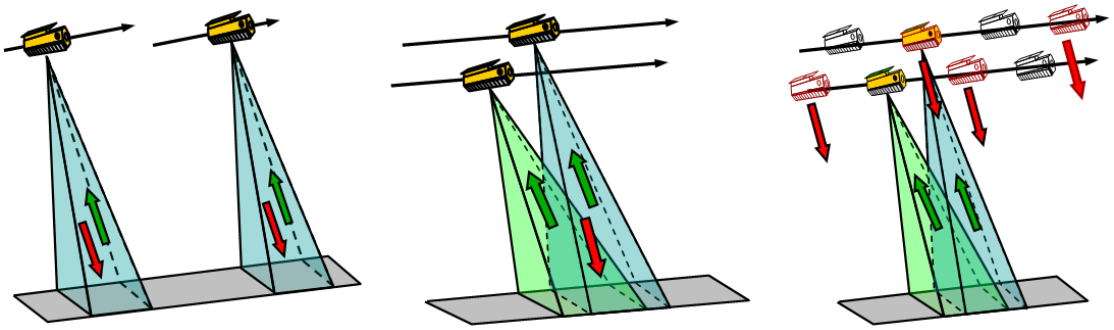

Fig. A.4. Interferometric acquisition modes. From left to right: (pursuit) monostatic mode, bistatic mode and alternating bistatic mode (from Krieger et al. (2007, 2013)).

(see Fig. A.5). This technique allows mutual phase referencing without exact knowledge of the distance between both satellites. A correction signal can be then derived during the processing on ground from the recorded synchronisation pulses to compensate the oscillator induced phase errors ensuring interferometric phase stability (Breit et al., 2011).

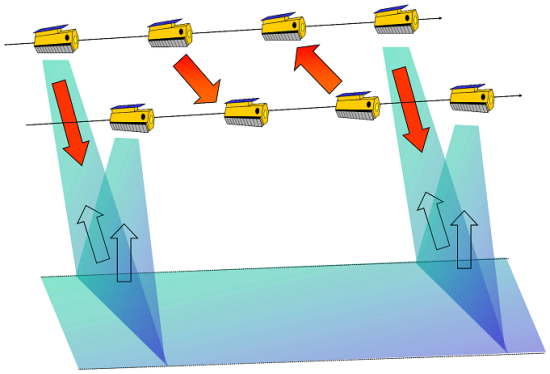

Fig. A.5. Synchronisation scheme of TSX and TDX satellites: exchange of radar pulses (from Krieger et al. (2007, 2013)).

A.3 Mission status and acquisition plan

TanDEM-X has an ambitious time schedule to reach the main mission goal. The TDX and TSX satellites have been designed for a nominal lifetime of five and a half years. Hence, a joint operation time of only three years could be guaranteed. The acquisition concept was thus based on such a short joint operation phase. However, this overlap is already over and predictions based on the current status of system resources indicate several more years of joint lifetime.

A.3.1 Initial acquisition plan

As explained in section 4.1.1, two coverages of the whole landmass were planned to be acquired within two years with different HoAs. The HoA ratio would be around 0.7 (second year over first one). A time span of ideally one year is planned between both acquisitions to avoid seasonal changes. Besides that, the second coverage is shifted by half a swath width (different beam angles) with respect to the first one. This forms the so-called clapboard pattern (Fig. A.6). In this way, the edges of the antenna pattern characterised by a lower gain overlap the high antenna gain in the centre of the main lobe of the other coverage. Performance is improved and more homogeneous over the whole range (Bachmann et al., 2013). All in all, the acquisition plan allowed to reach the high requirement on relative accuracy and to get a homogeneous global DEM. Fig. A.7 exhibits the predicted height accuracy as a function of ground range position for

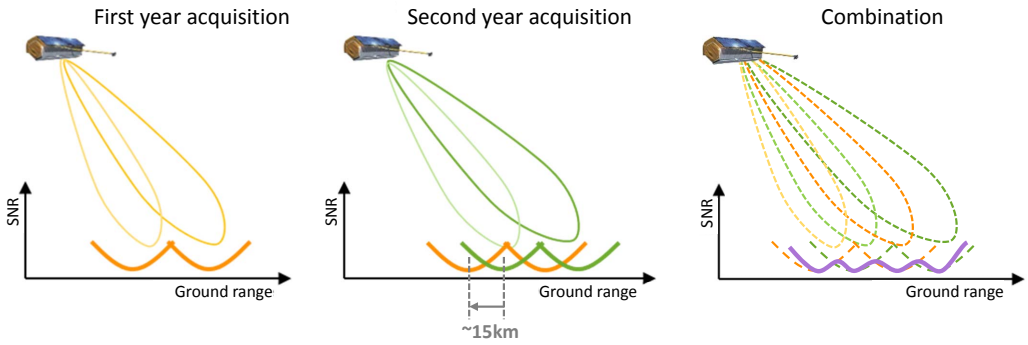

Fig. A.6. The so-called clapboard pattern: from left to right, first (orange) and shifted second (green) year acquisitions with their respective noise pattern and the lower and more homogeneous error (purple) ensured from their combination.

representative first and second acquisition HoAs as well as the resulting height accuracy (taken from Krieger et al. (2007)). The dashed green and dotted blue lines exhibit also the clapboard pattern obtained with the shifted beams. The red line depicts the resulting pretty flat height error distribution over the whole range, which is achievable only with (at least) two coverages.

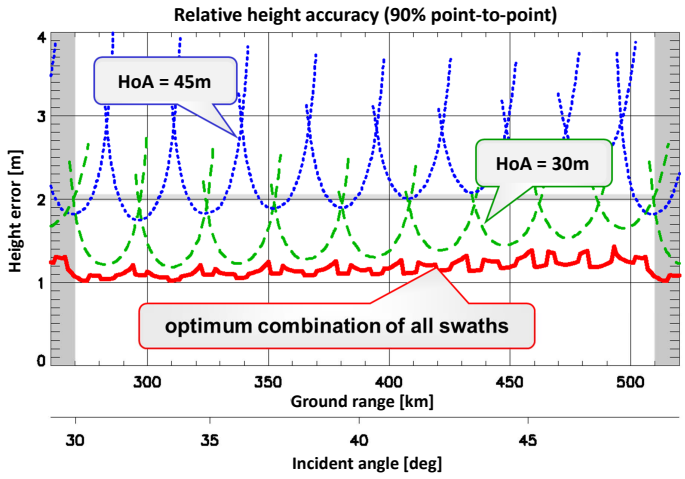

Fig. A.7. Theoretic performance (taken from Krieger et al. (2007)): curves are computed for HoAs of 45 m/cycle (dotted blue) and 30 m/cycle (dashed green); the solid red curve shows the final error, resulting from the combination of both swaths.

More acquisitions were planned to be acquired with different viewing geometries over difficult terrain. Mountainous areas, for example, need to be acquired with the opposite viewing geometry to solve shadow and layover effects.

More than 300,000 interferometric image pairs have to be acquired driven by the HoA (and thus the acquisition geometry). Therefore, the HELIX configuration has to be adjusted frequently so that an optimised global acquisition plan is required (Krieger et al., 2013, section 13.5). Considering TanDEM-X main parameters (Table A.2) and typical data take length of 1,000-1,500 km, nine adjacent swaths are needed to map the ground area at the equator with look angles from 28° to 44°. Further north or south, the number of adjacent swaths reduces since the ground distance between two orbits gets smaller. Furthermore, the acquisition plan has to take into account TerraSAR-X acquisitions and to deal with the limited on-board memory and downlink capacity, the power limitations and the thermal behaviour of the radar instruments. Acquisition planning is further detailed in Fiedler et al. (2008); Ortega-Miguez et al. (2012); Kraus et al. (2012); Weigt et al. (2012); Krieger et al. (2013, section 13.5).

A.3.2 Actual adapted acquisition plan and mission status

The acquisition plan had to be adjusted due to unexpectedly strong volume decorrelation over forests. Fig. A.8 exhibits the different mission phases and the actual various HoAs measured during interferometric processing. From end of December 2010 till March 2012 (Fig. 4.1a), a first global acquisition excluding Antarctica has been performed with HoAs between 40 m/cycle and up to 60-80 m/cycle depending on terrain type to ensure a better and more robust phase unwrapping (depicted in light blue in Fig. A.8). Thanks to InSAR quality monitoring (see appendix A.7), the minimum HoA to acquire with has been changed to 45 m/cycle in April 2011 for dense vegetated areas to reduce the strong volume decorrelation. The discontinuity of the HoAs is clearly visible in Fig. A.8. In addition, new acquisitions have taken place with HoAs larger than 60 m/cycle over strongly varying forests and some difficult terrain (in salmon pink in Fig. A.8 and see Fig. 4.1b for their location on a global map). During that time the formation was adjusted to reach the minimum allowed separation of 150 metres between both satellites. The second global acquisition with smaller HoAs between 35 and 45 m/cycle has been acquired from April 2012 to April 2013 (light green in Fig. A.8) together with missing acquisitions retake.

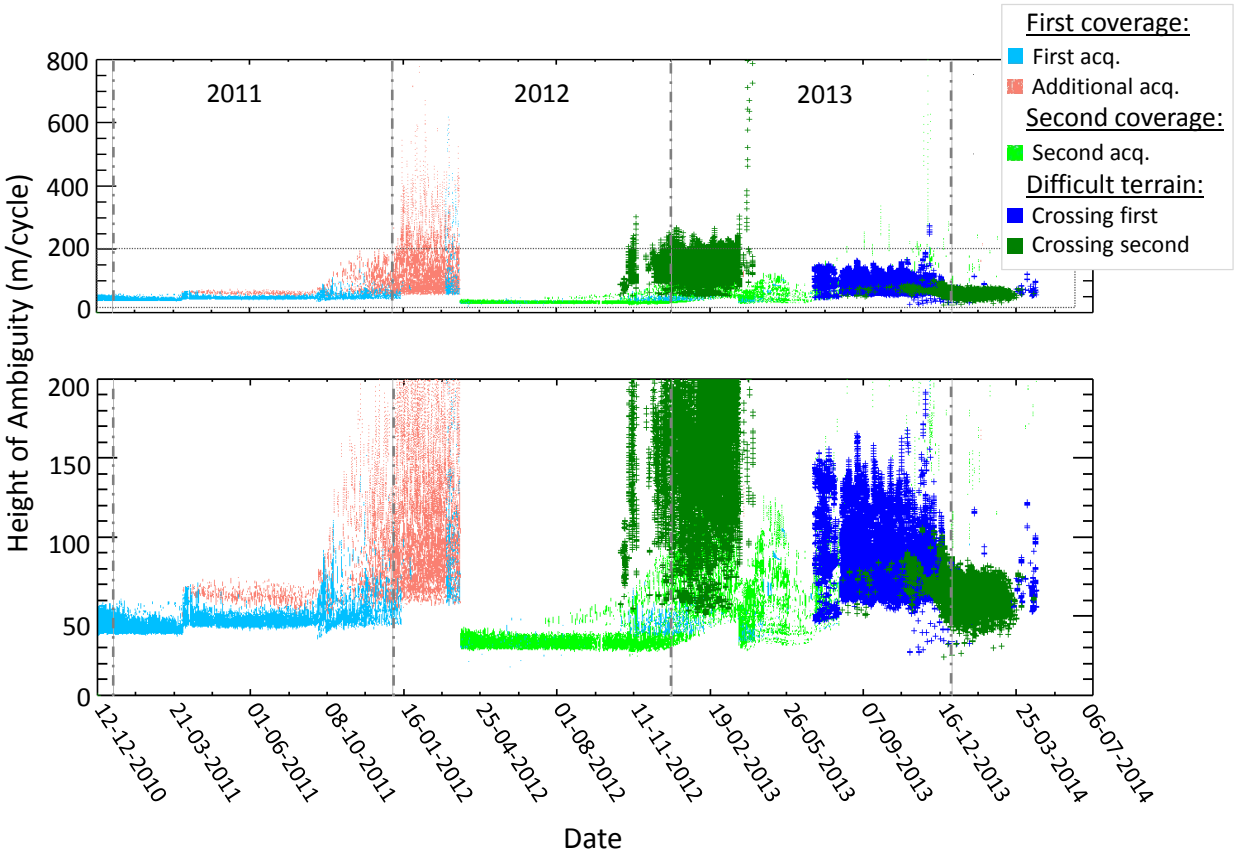

Fig. A.8. Acquisition timeline: heights of ambiguity over the different mission phases (status of May 2014). Bottom: zoom in the smaller HoAs.

Between April 2013 and July 2013, a dedicated phase took place to acquire Antarctica in local winter. Acquisitions took place partly in left-looking because standard configurations were not usable due to the inclination of the orbit (Borla Tridon et al., 2013). It was the first time that Antarctica was acquired with a space-borne X-band SAR. The acquisition plan elaboration required a special performance study to retrieve data of sufficient quality. Indeed, acquisitions are done with very large incidence angles (larger than 50° and 60°) so that they are subject to strong azimuth and range ambiguities (Borla Tridon et al., 2014).

After the first Antarctica coverage, the third year acquisitions dedicated to difficult terrain (mountainous regions and deserts) took place from August 2013 till April 2014 (dark blue in

Fig. A.8). The flying formation has been changed in early August 2013 so that the northern hemisphere can be acquired in descending and the southern one in ascending direction (opposite as before) with suitable HoAs. Deserts, especially sandy ones, were also acquired again because they suffered of very low backscatter leading to a high height error (Martone et al., 2012, 2014). There, acquisitions with steeper incidence angles were performed. Figure A.9 displays the difficult terrain, which has been acquired from an other viewing geometry (regions affected by shadow and layover in red and deserts in orange). Both have been reacquired twice with different heights of ambiguity to enable the Dual-Baseline Phase Unwrapping Correction (DB-PUC) processing. In April 2014, the HELIX formation has been reversed and a second coverage of the Antarctica could be acquired in April-June 2014 one year after the first one. Afterwards, some further gap filling were acquired. Data acquisition for the global DEM was finished in the second half of 2014 (Zink et al., 2014).

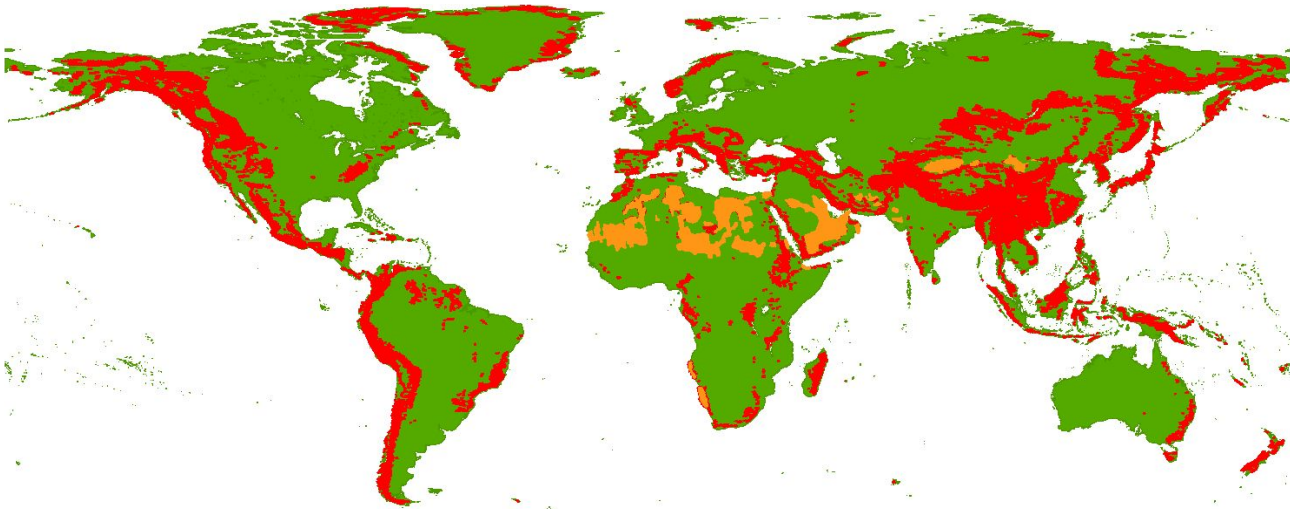

Fig. A.9. Map of the areas acquired from opposite viewing geometries: mountainous terrain exhibiting shadow and layover in red and deserts in orange.

Besides these acquisitions for the global DEM generation, acquisitions for the scientific community are performed. From October 2014, the mission will continue with a devoted science phase (Borla Tridon et al., 2014; Zink et al., 2014).

A.4 The ground segment

TerraSAR-X and TanDEM-X missions share both the same space and ground segments (Schättler et al., 2011). The ground segment was originally developed for TerraSAR-X (Buckreuss and Schättler, 2010) and has been extended for TanDEM-X. A key issue is that both missions have to be operated jointly. Since they have different goals, they also have different acquisition strategies: the TerraSAR-X mission requests are typically single scenes for individual scientific and commercial customers, whereas the global DEM requires a global mapping strategy depending on the current formation flying geometry (Mrowka et al., 2011).

The ground segment is divided into three main segments:

- the Mission Operations Segment (MOS),
- the Instrument Operations and Calibration Segment (IOCS),
- the Payload Ground Segment (PGS).

Fig. A.10 gives an overview of the different parts of the joint TerraSAR-X and TanDEM-X ground segment and summarises the different roles of each segment (the sub-segments in grey were already available for TerraSAR-X). The challenging mission concept required the introduction of several new and innovative elements in all three segments (in black in Fig. A.10).

Especially, the TanDEM-X acquisition planner including a systematic monitoring of the interferometric performance in IOCS (see appendix A.7) or an automated chain for the reception, archiving and processing of all TanDEM-X data in PGS have been created (Schättler et al., 2011).

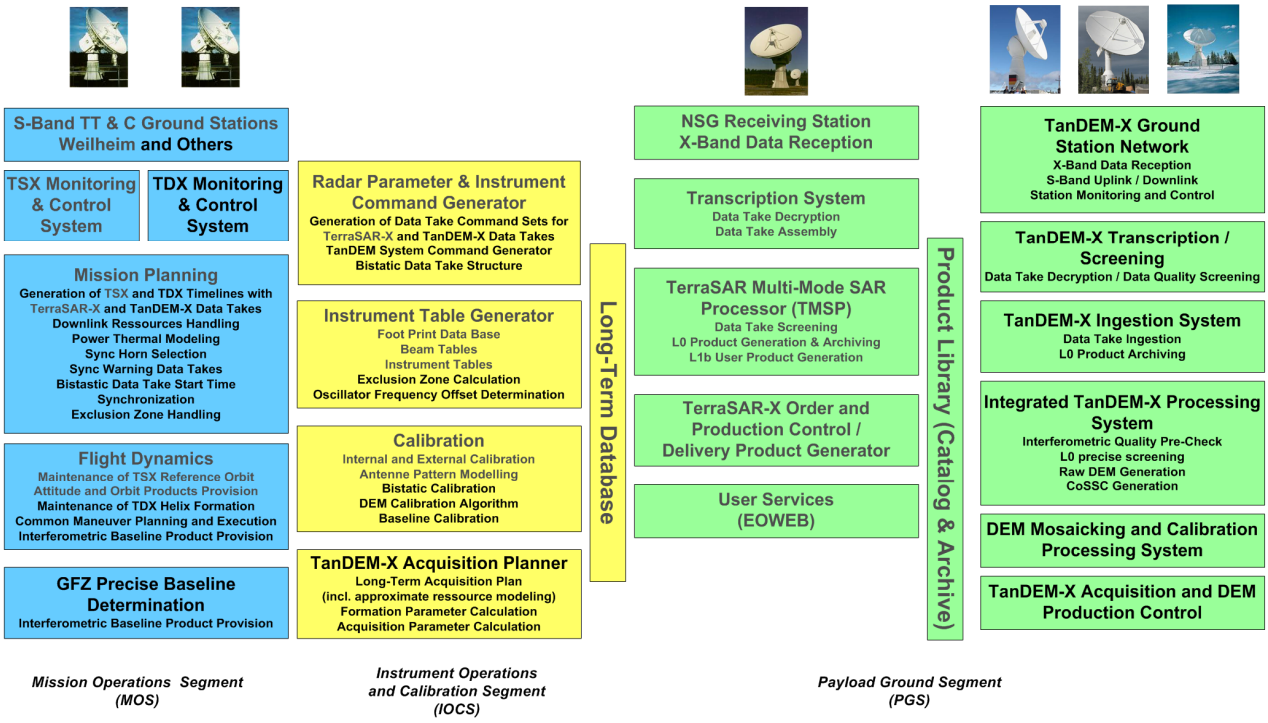

Fig. A.10. Sub-segments of the joint TerraSAR-X/TanDEM-X ground segment (from Schättler et al. (2011)).

A.4.1 Spatial baseline determination

A prerequisite to get a high resolution DEM is a precise knowledge of the spatial baseline. The latter is known at millimetre accuracies thanks to the on ground processing of the navigation information derived from double differential GPS carrier phase measurements between both satellites. The use of differential information allows to eliminate ionospheric errors and other typical GPS perturbations.

Three approaches have been implemented to operationally provide baseline products by two institutes: the German Research Centre for Geosciences (GFZ), which supplies the two baselines called GFZ and GFZ-B, and the German Space Operations Center (GSOC) at DLR, which provides the MOS baseline. These three baselines are based on three different softwares:

- Earth Parameter and Orbit determination System (EPOS-OC) (Zhu et al., 2004) producing the GFZ baseline;
- Bernese (Beutler et al., 2007) delivering the GFZ-B baseline;
- Filter for Relative Navigation of Spacecraft (FRNS) (Kroes, 2006) generating the MOS baseline.

The determined baselines have relative accuracies within millimetres. Nonetheless, offsets of a few millimetres may not be excluded from this approach. Therefore, they have been calibrated during the TanDEM-X pursuit monostatic commissioning phase and combined to provide a final baseline product with a precision in the order of 2 mm (Hueso González et al., 2012; Antony et al., 2013).

A.4.2 Payload ground segment

Both satellites downlink their huge amount of data (about 350 terabytes in total) to four ground stations: Kiruna in Sweden, Inuvik in Canada, O'Higgins in the Antarctic, and Chetumal in Mexico. Data are then quality checked directly at the receiving stations and sent to the processing facilities in DLR, Oberpfaffenhofen to the Integrated TanDEM-X Processor (ITP). It is a new TanDEM-X specific development. This processor major design drivers result from the multiple coverage acquisition strategy requiring the application of multi-baseline processing techniques based on supporting intermediate products. The ITP is further explained in appendix B. All interferometric data sets are processed into so-called single Raw DEMs, which are mosaicked and calibrated into a global, homogeneous DEM in a final step by the DEM Mosaicking and Calibration Processor (MCP) (appendix A.6).

A.5 Bistatic and interferometric system calibration

Calibration is a mandatory process to reach the best possible height accuracy for the InSAR DEM. Indeed, besides the noise-like contributions, accuracy depends also on systematic non-deterministic errors, which come mainly from inaccuracies in the baseline determination and drifts in the SAR instrument. These sources cause additional absolute height errors up to several metres, which have to be corrected.

A.5.1 DEM calibration workflow

Several Raw DEMs are processed with the precise (non-calibrated) baseline over dedicated areas. In this way, baseline biases perpendicular to flight direction can be monitored and determined by comparison to external reference DEMs to calibrate the baseline (Hueso González et al., 2012). Finally, the calibrated baseline is used for the instrument calibration and the generation of the precise Raw DEMs. During the final DEM calibration process in MCP (appendix A.6), the DEM acquisitions are calibrated relative to each other and against globally distributed ICESat reference points (ICESat (Ice, Cloud and land Elevation Satellite) is a spaceborne laser altimeter providing a very good global coverage (Zwally et al., 2002)) and subsequently mosaicked to ensure the 2 m relative height accuracy of the final TanDEM-X global DEM.

A.5.2 Calibration of instrument and external delays

The SAR instrument is mainly affected by temperature drifts due to the warming of the transmit/receive modules over an acquisition and by initial offsets due to small differences in the interferometic behaviour of the two (independent) satellites.

As explained in appendix B, the global remaining ambiguity of the interferometric phase is correctly resolved by the absolute stereo-radargrammetric phase. This absolute phase is derived from the travel times of the radar signals. Hence, it is very sensitive to differential instrument delays, which are caused by the following effects (Hueso González et al., 2012):

- unbalanced global internal delays of both satellites;
- internal delays either dependent on the chirp bandwidth or the synchronisation horn combination or coming from different receiver gain settings;
- relativistic effects on the time references dependent on the relative position of the satellites, which affect the processing of the synchronisation pulses (Krieger et al., 2012);
- differential tropospheric delays.

The dependencies were derived by statistical evaluations and dedicated analyses of the stereo-radargrammetric shifts delivered by the ITP during the Raw DEMs processing. All these contributions are compensated during the interferometric processing so that the ambiguity of the interferometric phase can be solved. After that, about 90% of the DEMs have an absolute height error better than ±10 m (Bachmann et al., 2012). Most outliers are due to a remaining π-ambiguity caused by the synchronisation link processing. In fact, it combines the sum of two synchronisation phases, one from each satellite, in a common average. This ambiguity is finally solved through a reprocessing, where the height offset is determined by comparison to reference ICESat points (appendix A.6).

Instruments and SAR performance of both spacecrafts as well as the baseline have been successfully verified and calibrated during the 11-month commissioning phase (Hueso González et al., 2010; Schwerdt et al., 2011).

A.6 DEM mosaicking and calibration

The Mosaicking and Calibration Processor (MCP) is in charge of calibrating and mosaicking all the Raw DEMs into the final global TanDEM-X DEM (Wessel et al., 2008).

In a first data-driven preparation step, the Raw DEMs generated by the ITP (appendix B) are processed. A water body detection mask and a list of calibration (tie) points are then produced. Some measures for height discrepancies and overall quality are also performed triggering a possible reprocessing (to solve the π-ambiguity and correct phase unwrapping errors).

The second step is the DEM calibration. It estimates for each data take its offset, tilt in range and slope in azimuth direction. This calibration is based on two key elements: relative height offset measurement on chips of 1 km^2 in overlapping parts of the different data takes and absolute height measurements based on ICESat data. ICESat points are carefully selected depending on their amount, the width of peaks in the waveforms (indicator for vegetation), their standard deviation. The received signal level and the chosen points are averaged thereafter (Huber et al., 2009, 2010). They are eventually compared to TanDEM-X data from which water, shadow, layover and height discrepancies have been masked out. DEM calibration is performed on blocks of larger connected DEM data takes (up to continental scale). A polynomial correction is estimated for each data take by means of a least-squares adjustment under the constraint that the heights in overlapping areas are identical (apart from noise) after application of the error function (Gruber et al., 2009; Wessel et al., 2009). This approach guarantees smooth height transitions at data take borders. The DEM calibration of larger blocks could start after the end of the first global acquisition once whole continents were available.

The final step is the DEM mosaicking, which merges different corrected DEM acquisitions. The calibrated corrections are applied to each Raw DEM and the different coverages are mosaicked through an average of the consistent elevation values weighted by their single height errors. The amplitude and Height Error Mask (HEM) are similarly fused and a Water Indication Mask (WAM) (Wendleder et al., 2013) is generated. The latter is not a global water mask but gives supplementary information to support the DEM editing process (for example of water surfaces, which appear noisy). Finally, the resulting DEM mosaic and additional product layers are tiled into one-by-one degree geocells and an interactive quality control is performed on them (Gruber et al., 2012; Huber et al., 2012). Figure A.11 is the first processed mosaic: it is over Iceland and contains only first year acquisitions.

At the time of writing (May 2014), all efforts are concentrated in producing the final DEM for regions where only first and second acquisitions are required. Until end of April 2014, most of Australia (see Fig. A.12), flat parts of Northern America and Russia have been finished while

South Africa and parts of South America are in production (Wessel et al., 2014; Zink et al., 2014).

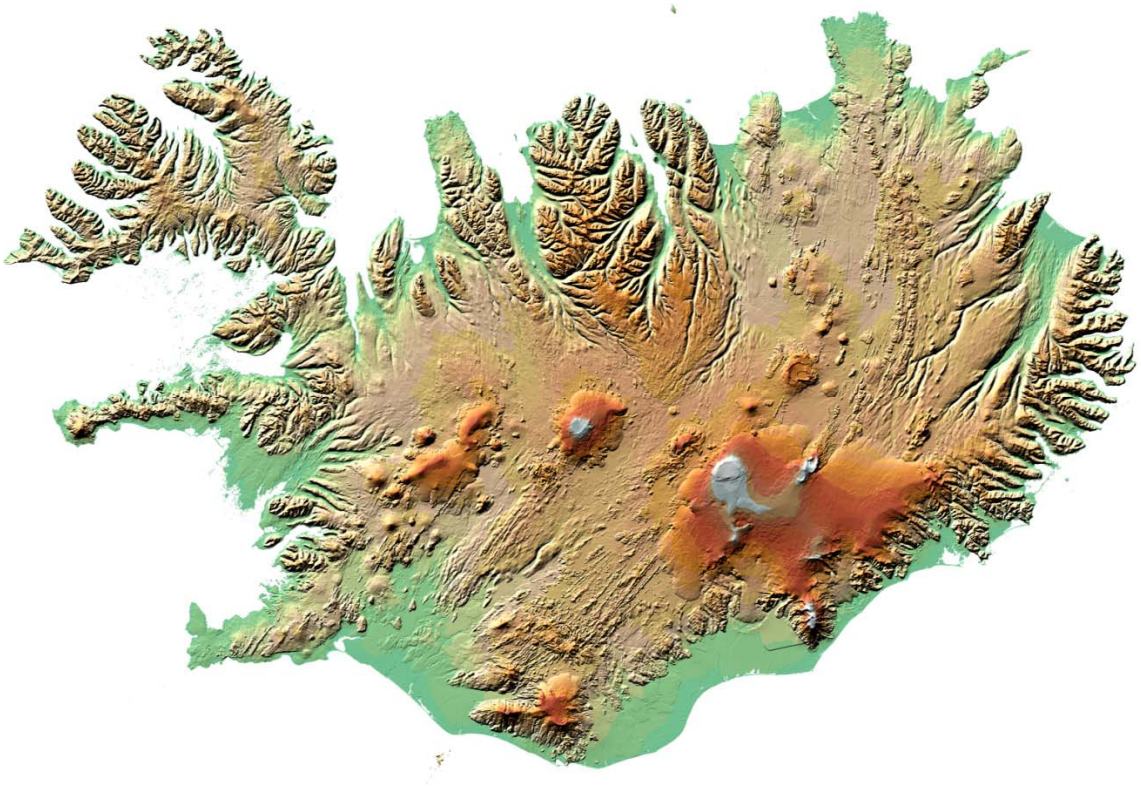

Fig. A.11. Mosaick of Iceland from the first year acquisitions only.

A.7 Interferometric and DEM quality monitoring of TanDEM-X

Interferometric capabilities and processed DEMs are meticulously monitored in order to be sure that the TanDEM-X requirements will be met. Key parameters such as the interferometric coherence, the phase unwrapping quality indicator delivered by the ITP, and the relative vertical height accuracy are considered. Note that the relative vertical accuracy is the requirement (Table A.1) the most difficult to meet. It is related to the relative vertical height error, which corresponds to the uncertainty due to white noise-like disturbance contributions and therefore cannot be removed by the final calibration and mosaicking process. This monitoring allowed the detection of different problems so that strategies could be defined to reacquire data to obtain better performance (Rizzoli et al., 2012a; Martone et al., 2012).

A.7.1 Interferometric performance analysis through the coherence

The coherence is the key parameter for the evaluation of the interferometric performance since it gives information about the amount of phase noise in the interferogram (see section 2.1.3.2), which in turns influences the height accuracy. Figure 4.2a depicts on a world map, the coherence of about 132,000 data sets from the first global acquisition phase in 2011. More than 90% of the landmass exhibits an average coherence greater than 0.6 and about 45% higher than 0.8. From the coherence, the mean height error per scene can be theoretically derived and is depicted in Fig. A.13. After the first acquisition year, about 25% of all single Raw DEMs already show a predicted relative height error better than 1.8 m (for example over Australia) i.e. already

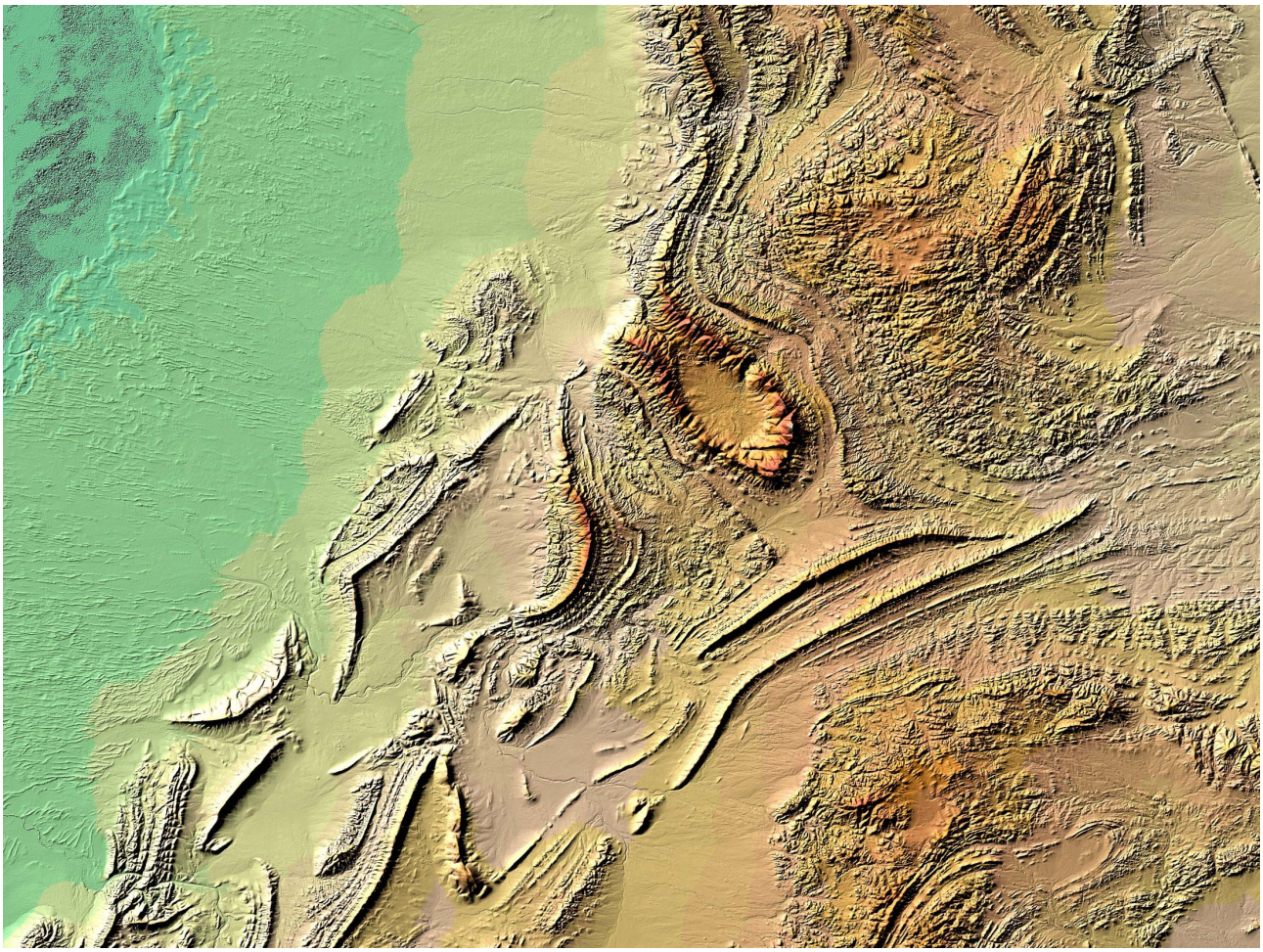

Fig. A.12. First tile of the final TanDEM-X DEM: Flinders Ranges in Australia.

fulfilling the TanDEM-X DEM requirements. Nevertheless, over vegetated areas like over rain forest (north of South America or Indonesia), coherence is much lower that the theoretical one derived from the signal-to-noise ratio (SNR) (Zebker and Villasenor, 1992). This is due to the unexpectedly high volume decorrelation (De Zan et al., 2013). Indeed, these areas have been acquired with typical HoAs around 40 m/cycle i.e. in the order of trees height increasing thus dramatically volume decorrelation. For this reason, the minimum HoA has been changed to 45 m/cycle for acquisitions over vegetated areas (appendix A.3.2) in order to ensure a better coherence and to enable a more reliable phase unwrapping (Martone et al., 2012).

As a result of the performance analysis, a mission phase with larger HoAs especially dedicated to the identified difficult areas has been introduced at the end of the first global coverage. These additional acquisitions complement the first global data set to form a robust basis to process the second coverage data. Figure 4.2b depicts their improved coherence.

Another problematic area, sand deserts, can be identified from very low coherence (dark areas in Fig. 4.2a) and consequently high height error (red regions in Fig. A.13). There, the backscattered signal is too weak (Martone et al., 2012, 2013, 2014). Consequently, additional acquisitions with steeper incidence angles have been planned and acquired during the third mission phase (see appendix A.3.2).

A.7.2 Global DEM quality monitoring and relative height error

Rizzoli et al. (2012b) calculated relative height errors for typical flat and mountainous terrain from the high-pass filtered DEM difference of two repeated acquisitions (of same geometry) to verify if they meet the relative height accuracy specifications (estimated 90% height error).

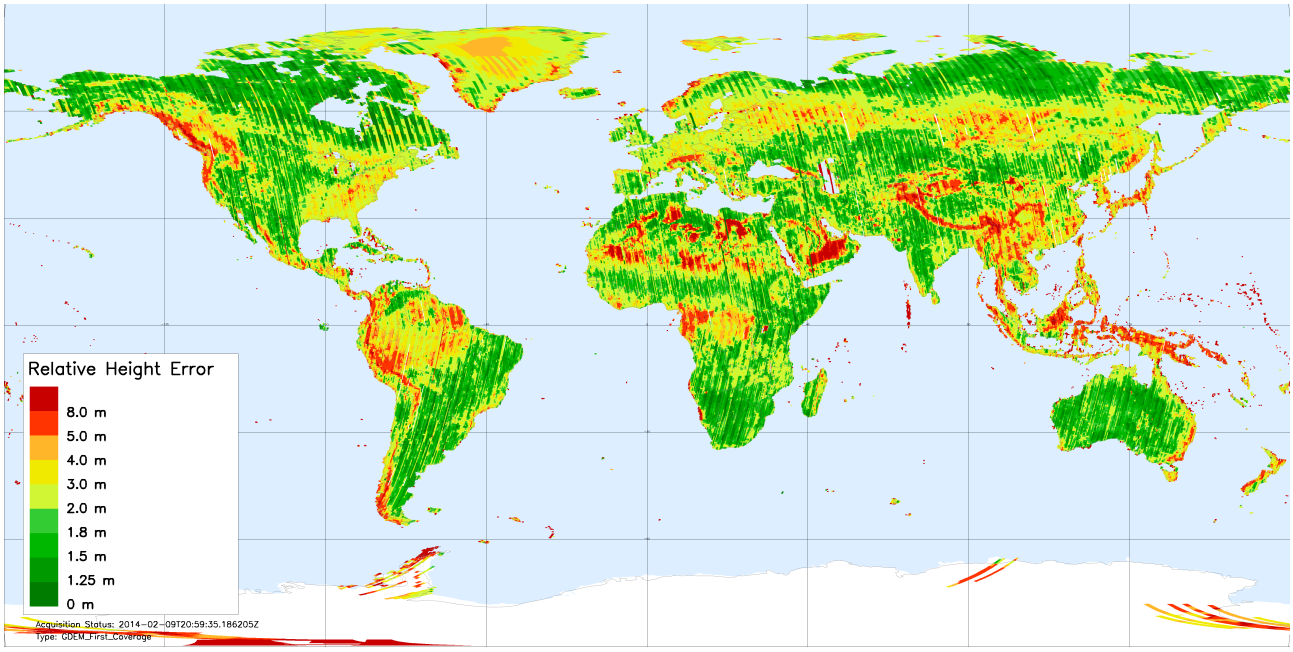

Fig. A.13. Height error map of the TanDEM-X first year acquisitions (December 2010 to January 2012, from (Rizzoli et al., 2012a; Martone et al., 2012, 2013)).

Figure A.14 shows the obtained results for 6 different scenes over soil and rock flat terrain. It shows very similar (or even better) behaviour to the predicted height error (cf. Fig. A.7) for ground areas characterised by stable backscatter. It also confirms that for several test sites acquired with HoA smaller than 40 m/cycle, one acquisition is already sufficient to achieve the required specification. The authors also analysed the relative height error for different land cover classes such as ice, agricultural areas or rain forest. There, DEM specifications are not fulfilled because volume decorrelation and seasonal changes have additional impacts. The combination of several acquisitions reduces the overall height error.

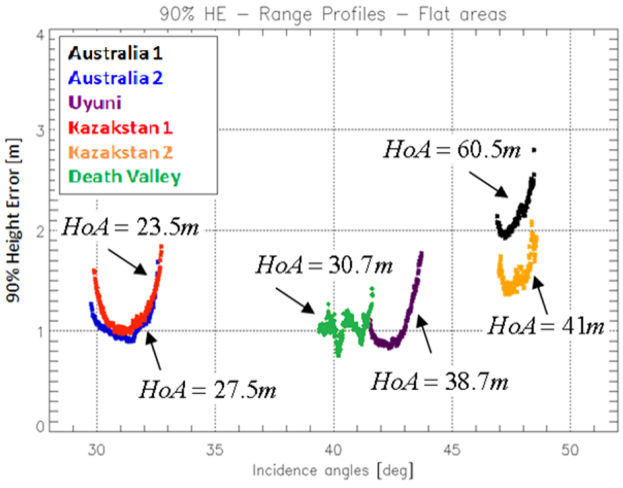

Fig. A.14. Height error (90%) range profiles with respect to incidence angles for six different test sites over flat soil and rocks terrain (taken from Rizzoli et al. (2012b)).

Analysis over the whole Earth's landmass is performed by means of the coherence quicklooks delivered by the ITP. The quicklooks are used to monitor and predict the final Raw DEM quality before the DEM mosaicking is achieved. Every pixel can be associated either to terrain with slopes lower then 20% or to mountainous terrain, where slopes exceed 20% as required by the specifications from Table A.1. Finally, the global relative height error (point-to-point) can be evaluated from the mean cumulative density function (Gonzalez et al., 2014). Rizzoli et al.

(2014) announce that the required accuracy is already reached for about 88% of the first coverage for rather flat terrain. The mosaicking of the several coverages increases significantly the confidence level (Table A.3).

Case	**Relative height error** < 2**m** (slope $< 20\%$)	**Relative height error** < 4**m** (slope $> 20\%$)
First global coverage	88.1%	91.0%
1^{st}, 2^{nd} and additional coverages	96.0%	97.0%

Table A.3. Confidence level for the global relative height error derived from quicklook mosaics (from Schulze et al. (2014)).

A.7.3 Final global DEM absolute height accuracy

The absolute height calibration has been presented in appendix A.5. The final height is validated by comparing the final DEM with ICESat tracks. In March 2014, 1,722 final DEM tiles were already checked: they exhibit an average offset of +0.26 m. Figure A.15 displays the height differences between TanDEM-X DEM and ICESat tracks over Australia. Some cross-checks have been also performed with GPS tracks (over restricted areas) and an average offset of −0.37 m has been measured (Zink, 2014).

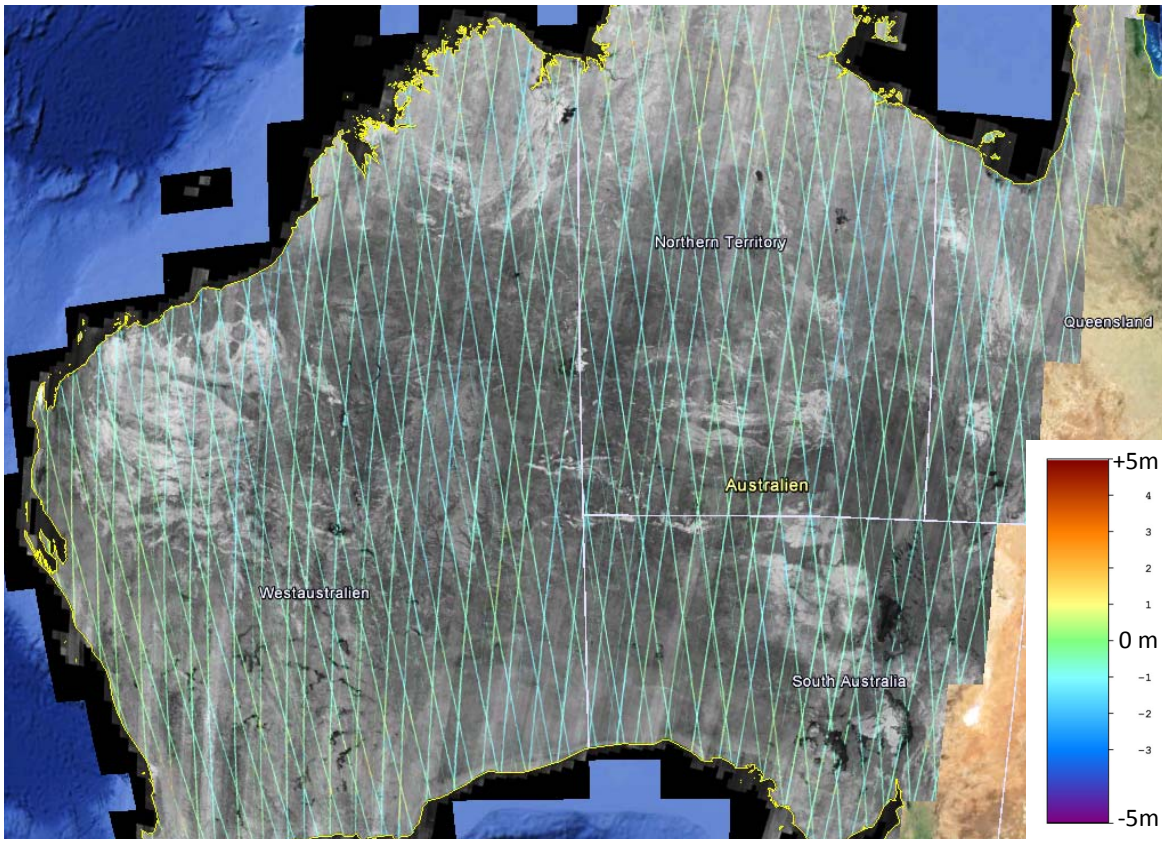

Fig. A.15. TanDEM-X amplitude mosaic of Australia over plotted by the height difference between the final DEM and ICESat tracks (taken from Zink (2014)).

B The Integrated TanDEM-X processor (ITP)

Synthetic Aperture Radar (SAR) data from the TanDEM-X mission are operationally processed by the Integrated TanDEM-X Processor (ITP) (Breit et al., 2010b, 2012; Fritz et al., 2011, 2012). It is a new and optimised processing chain even though it strongly benefits from the heritage of the TerraSAR Multimode SAR Processor (TMSP) (Breit et al., 2004) and DLR's InSAR processor of the SRTM mission.

This appendix presents an overview of the ITP and its different algorithms. At the end, a description of the dual-baseline chain is given.

B.1 Overview

The main task of the ITP is to process fully automatically bistatic data takes to Raw DEMs for the global Digital Elevation Model (DEM) generation. The processor has thus been designed to respond to the high throughput requirement to process in-line with the reception of the data at the processing facility (about 400 new acquired scenes/day). It is a strong constraint on operations and performance. Consequently, the SAR data workflow has a consistent systematic and data driven screening and processing approach. In addition, there is a need for fast feedback on instrument characteristics, data take quality and suitability for interferometric processing. This is quite challenging since acquisitions are downlinked as separated interferometric channels in segments of data take files at different receiving stations without having access to auxiliary data (like orbit products or calibrated baselines). As a result, the ITP is subdivided into three major steps:

1. screening of the downlinked data take segments at the receiving station,
2. quality check and assessment of screening results at the processing facility,
3. processing of the data take into several separated Raw DEMs when all necessary input data are available.

The quality check (Interferometric Quality Pre-Check (IQPC)) provides the necessary fast feedback on the success of the joint acquisition. A last constraint is that the operational Raw DEM processing chain has to deal with a systematic global acquisition in several coverages. These have to be combined later on to achieve the final product specifications. As a result, the processor requires archived intermediate products as additional inputs for processing. It has also to be able to reprocess scenes of insufficient quality. For example, Raw DEMs from the first coverage where single-baseline phase unwrapping (1B-PU) was unsuccessful have to reprocessed using the Dual-Baseline Phase Unwrapping Correction (DB-PUC) framework.

The main task of the ITP is to process acquisitions for the global DEM. As it is designed in a generic way, it can also process customised DEMs or experimental acquisitions for the scientific community without any external manual intervention. The long operational standard data takes are subdivided into slightly overlapping scenes of approximately 50 km azimuth extent. Moreover, there is a fix framing on ground in order to minimise the overhead for later reprocessing. These scenes are processed individually and in parallel. Nevertheless, an important functionality is a consistent processing parameter generation for the entire data take and both channels. Bistatic focussing parameters like geometric Doppler estimation, antenna pattern projection and geolocation grid generation are determined with the help of a reference DEM. Additionally, consistent calibration data and interferometric processing parameters (baselines, coregistration grids) are calculated over the entire data take time span. The processor consists thus of individual modules and is organised as sequences of single processing steps divided into two main blocks (from Breit et al. (2010b)):

(1) the bistatic SAR processing comprising:
- synchronisation pulse analysis and evaluation for timing and phase corrections (Eineder, 2003b; Krieger and Younis, 2006; Balss et al., 2010; Breit et al., 2011);
- generation of a bistatic focusing replica from calibration pulses of both channels;
- calculation of the time variant bistatic acquisition geometry and focusing parameters (Bamler et al., 2007);
- determination and analysis of common ground coverage and beam illumination overlap;
- mutual Doppler centroid deviation analysis;
- bistatic SAR data focusing (Breit et al., 2010a).

(2) the interferometric processing consisting of:
- filtering of both interferometric channels to common spectra (the master image is the one coming from the active sensor) (Yague-Martinez et al., 2010b);
- high resolution slave image co-registration (Yague-Martinez et al., 2010a) and resampling;
- single and dual-baseline phase unwrapping (Lachaise et al., 2007, 2012a,b, 2013, 2014b,a);
- generation of the Raw DEM and a set of geocoded quality maps (Rossi et al., 2010).

A schematic overview of the bistatic processing workflow for Raw DEM generation is illustrated in Fig. B.1. Besides the essential processing steps (in blue boxes), the diagram depicts the SAR data input and both main outputs: the Coregistered Single-look Slant-range Complexes (CoSSCs) and the Raw DEM. Additional inputs for the DB-PUC are represented with the dashed box. They are scenes acquired with a different baseline in an earlier phase of the mission, called *supporting CoSSCs*. SAR data acquired in new and experimental acquisition modes are all processed to CoSSCs (hence not unwrapped and geocoded) for the scientific community (see Fritz et al. (2012) for further details). The reprocessing starts directly from the CoSSCs with the interferogram generation. The operational implementation of the ITP on 20 processing nodes can produce more than 1,200 scenes/day (about one Raw DEM every minute) for single-baseline processing and more than 400 scenes/day for dual-baseline processing.

B.2 Bistatic SAR processing

In comparison to repeat-pass interferometry, requirements on instrument accuracy are much more demanding for bistatic operations. In particular, the oscillators of the two instruments are running independently and drift (Eineder, 2003b; Krieger and Younis, 2006). Thus, an extended bistatic system calibration phase of half a year took place to analyse and compensate all instruments and physical effects of the bistatic system (see appendix A.5). These include, for example, differential electronic delay variations from instrument gain settings, relativistic effects, ambiguities in the synchronisation link phases but also differential tropospheric signal propagation due to the slightly different viewing geometries of both instruments. As a consequence, the ITP bistatic SAR processing comprises two major blocks. First, the SAR data are corrected for instrument related effects. Second, the corrected SAR data of both channels are focussed following the bistatic acquisition geometry.

B.2.1 Timing and phase synchronisation

As explained in appendix A.2.3, the two satellites exchange directly interleaved synchronisation pulse signals in order to quantify the differential phase. The active satellite is used as reference and the timing of the passive satellite is evaluated relative to it. The frequencies of both USOs (Ultra Stable Oscillators) slightly differ and drift independently within a data take. Accordingly, USO derived instrument timing parameters such as the radar frequency f_0, the pulse repetition frequency or the range sampling frequency differ. Another effect is an ambiguity of π of the synchronisation link phase due to the combination of two 2π ambiguous signals from the two

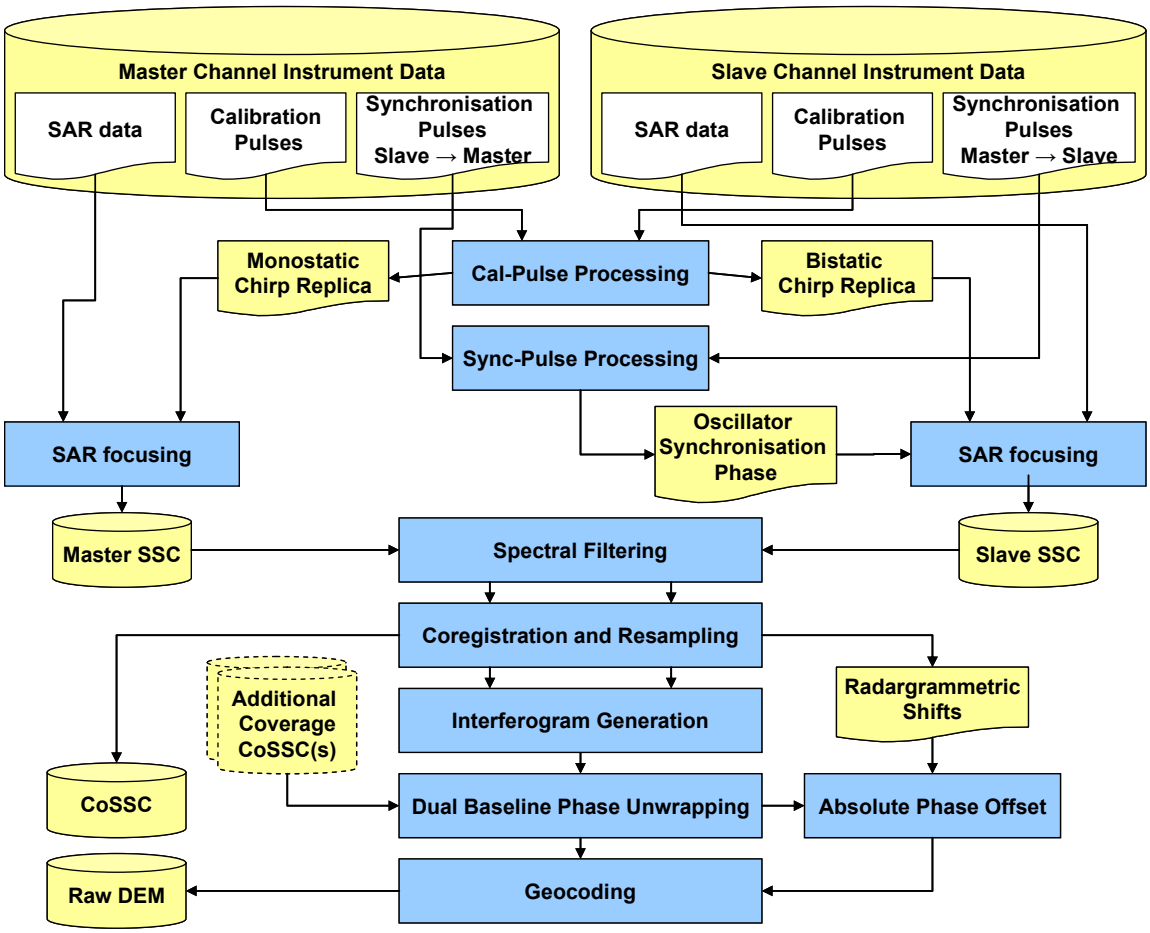

Fig. B.1. Processing workflow of the Integrated TanDEM-X Processor (combined from (Breit et al., 2012) and (Fritz et al., 2011).

instruments. Also, phases resulting from the relative motion and the limited speed of light during pulse exchange for example yield several degrees in phase offsets (Krieger and De Zan, 2012).

Both SAR channels are first individually corrected to compensate instrument characteristics like antenna phase patterns, electronic delays, and calibration networks effects already known from the TerraSAR-X mission. Then, the passive bistatic channel must be additionally corrected for:

- a pulse-by-pulse phase and range time values compensating the frequency deviation and phase drifts of the oscillators (both up to 2 cm),
- a range time offset due to the data take start time difference (several metres),
- differential range time offsets dependent of Rx-gain settings (up to 2 cm),
- synchronisation horn delays (up to 2 cm).

Centimetre level offsets are not detectable in a single image but dependent range time offsets become noticeable as radargrammetric height estimates. Therefore, the bistatic interferometric calibration required iterative processing of thousands of individual Raw DEMs and the exploitation of processing parameter coming from the ITP especially the coregistration shifts (see appendix B.3.2). Besides the above mentioned effects, statistical analysis exhibited trends and offsets depending on instrument modes and settings as well as on the master-slave role of the satellites. After on-ground analysis and processing, differential phase variations and frequency offsets of both instruments oscillators have been determined. Details on the synchronisation concept are given in Breit et al. (2011, 2012).

The synchronisation and calibration of differential bistatic range measurements are successful

down to millimetres. Together with the exploitation of the high geometric precision of the instruments and the SAR processor (Cong et al., 2012; Balss et al., 2012), radargrammetric height estimates allowed to maximise the accuracy of the final product and to acquire a truly independent measurement of the absolute topographic heights.

B.2.2 Focussing

The moderate bistatic acquisition geometry of TanDEM-X allows to use the TerraSAR-X chirp scaling focussing algorithm extended by a bistatic computation of an equivalent monostatic range history (Bamler et al., 2007). The true bistatic range history for a given target on ground is determined by the distance of the target to the active satellite at the time of transmit and the distance to the passive satellite at the time of receive. The true range history is computed iteratively interpolating precise orbits. Finally, the monostatic equivalent range is fitted to the true range to derive the azimuth focussing parameters but also the along- and across-track shifts caused by the bistatic geometry. The along-track shift of the bistatic channel is compensated during the azimuth focussing step to facilitate the interferometric image coregistration.

B.3 Interferometric processing

B.3.1 Spectral shift filtering

The interferometric processing begins with the spectral shift filtering. Due to the different viewing geometry of TerraSAR-X satellite (TSX) and TanDEM-X satellite (TDX), master and slave received spectra are composed of a coherent and a non-coherent bands both in range and azimuth. The non-coherent bands yield geometrical decorrelation in range (Gatelli et al., 1994) implying a loss of coherence of about 3 to 5% for TanDEM-X. For this reason, they are eliminated to increase the coherence. The common band in azimuth is determined with the help of Doppler estimates and azimuth processing bandwidth. In range, the spectral displacement is determined based on a simulation of a phase corresponding to flat terrain at the scene average height. Implementation details can be found in Yague-Martinez et al. (2010b).

B.3.2 Coregistration and coregistration shifts

SAR image coregistration consists in estimating and correcting the grid of the slave image with respect to the master grid in order to obtain a precise match of the two images. Both rasters differ because of the parallax effect due to the different viewing geometries. An imprecise coregistration implies again coherence losses in the interferogram resulting in a lower relative height accuracy. The high resolution of TanDEM-X causes a severe impact of the topography on the mutual shift between the slave and the master samples. Consequently, mutual shifts estimation is more demanding.

The coarse coregistration in along-track direction of the passive bistatic (slave) SAR image is already performed during focussing (appendix B.2.2). However, this coregistration has to be refined according to the local topography to ensure optimal coherence. The precise estimation of the mutual shifts consists in two steps (Yague-Martinez et al., 2010a). First, a geometrical estimation on a regular grid (every 64 pixels) of the range and azimuth shifts is performed (similarly to Sansosti et al. (2006)). An external DEM and precise orbit information of both satellites are used as input information. Secondly, the two SAR signals are directly used in order to refine the geometric estimation through the cross-correlation (performed on patches of typically 32×32 pixels). The a-priori estimates coming from the geometrical coregistration are used to extract patches in the slave scene to maximise the overlap with the patches of

the master image. Coherent cross-correlation is first performed. If the correlation coefficient is too low, incoherent cross-correlation is applied afterwards (see section 3.2.1.2 for theoretical explanations and Bamler (2000); De Zan (2014)). Finally, outliers are eliminated and replaced by shifts interpolated bilinearly.

The coregistration procedure has an accuracy better than a hundredth of a pixel for a coherence of 0.8 (Cramér-Rao Lower Bound (CRLB) given by eq. (3.14) for a patch size of 32×32 and an oversampling factor of 1.1, see Fig. B.4a). The correlation patch size has been selected as a trade-off between achieved accuracy and computation time.

The coregistration shifts are the core of the ITP for the calibration (see appendices A.5 and B.2) but also to assess the unwrapping quality of the interferometric phases. Indeed, since they come from the geometric parallaxes between both satellites, they allow to get a coarsely sampled but absolute radargrametric DEM (operationally about 13×13 to 21×21 times smaller than the interferogram, see appendix B.3.5, section 3.2.1.2, and section 4.2.2). For this reason, the coregistration shifts are called *radargrammetric shifts* in this thesis. In the dual-baseline phase unwrapping chain, the phase derived from the coregistration shifts, the so-called *stereo-radargrammetric phase*, even supports the correction of unwrapping errors.

B.3.3 Interferogram formation

After the coregistration, the slave image is resampled to the master grid using the shifts matrices. The outputs of the operational processing so far are two co-registered complex images (the so-called CoSSCs). For experimental products not acquired for DEM generation, the processing is finished here (a full-resolution interferogram is also generated). The other data acquired for the global DEM are processed further to Raw DEMs.

The interferogram is generated by performing the complex conjugate multiplication of the two CoSSCs. It is multilooked and downsampled to achieve the approximate required ground resolution. A coherence estimate, which is not corrected for the topographic phase, is also obtained. Table B.1 presents the typical possible size of CoSSCs, interferograms and radargrammetric shifts. The number of looks gives the size of the averaging window to compute wrapped phase estimates. A standard boxcar filtering is applied here because the overall processing time has to remain low (less than 20 minutes). Eventually, a new coherence is estimated on a 11×11 window, where the terrain is compensated through a phase simulated from a reference DEM (SRTM when available, GLOBE[11] otherwise). Figure B.2 exhibits an example of a part of a wrapped phase and coherences respectively not corrected and corrected for the topography.

B.3.4 Single-baseline phase unwrapping (1B-PU)

Phase unwrapping is a complicated task in this accuracy class. The (single-baseline) Minimum Cost Flow (MCF) phase unwrapping (PU) algorithm (see section 2.2.2.1) is used for the first coverage. It is an optimised version for large interferograms of Costantini (1998)'s algorithm (Eineder et al., 1998). It has been successfully applied for the unwrapping of SRTM data (Suchandt and Eineder, 2003). The costs functions have been defined thanks to the experience gained from the SRTM mission. They have been fixed to the square of the terrain corrected coherence. The use of the amplitude is not appropriate for TanDEM-X due to the relatively low backscatter. On the contrary, the coherence gives good results and the square of it allows to gain contrast. Beside the unwrapped phase, the optimised MCF algorithm delivers also a control file depicting the residues (positive in green and negative in red) and the branch-cuts (single in blue and multiple in pink) overlaid on the wrapped interferometric phase (gray level, see Fig. B.3).

[11] Global Land One-km Base Elevation Project

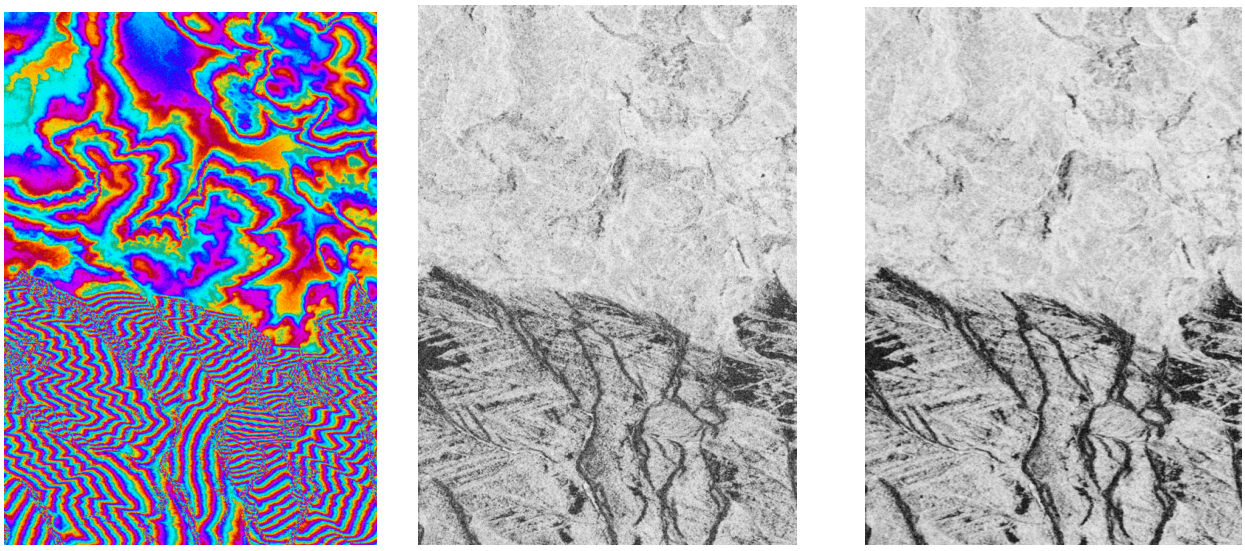

(a) Wrapped phase (b) Coherence estimate (c) Terrain corrected coherence estimate

Fig. B.2. Example of an interferometric wrapped phase and coherences (crop of $700 \times 1,000$ pixels, Grand Canyon, USA), the terrain corrected coherence is a less biased estimate.

Width of a CoSSC	13,000 to 23,000 samples
Height of a CoSSC	20,000 to 31,000 lines
Subsampling in range	3 to 7
Subsampling in azimuth	3 to 5
Looks in range and azimuth	subsampling + 2
Width of radargrammetric shifts	200 to 360 samples
Height of radargrammetric shifts	310 to 490 lines
Width of an interferogram	3,000 to 6,000 samples
Height of an interferogram	4,000 to 10,000 lines

Table B.1. Typical size of CoSSCs, radargrammetric shifts and interferograms.

For the more sensitive second coverage and to correct PU errors in the first one, the more sophisticated DB-PUC framework is used (see appendix B.4).

B.3.5 Absolute phase offset determination and PU check

B.3.5.1 Absolute phase offset

After unwrapping, the phase image has still a global 2π-ambiguity plus a π-ambiguity due to the synchronisation link phases. The extensive calibration phase (appendices A.5 and B.2) ensured the consistency between the unambiguous coarse radargrammetric (coregistration) shifts and the accurate, but ambiguous, interferometric phase. As a consequence, the absolute phase derived from the radargrammetric shifts, the so-called *stereo-radargrammetric phase*, can be used for absolute phase offset determination as described in section 3.2.1.2. The main steps of the algorithm are (Rossi et al., 2012):

- computation of the phase differences of the stereo-radargrammetric phase and a downsampled version of the interferometric unwrapped phase;
- noise reduction through median filtering;

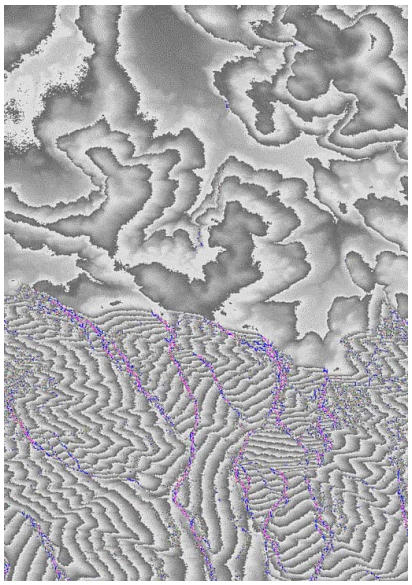

Fig. B.3. Control image of MCF algorithm exhibiting single (blue) and multiple (pink) branch-cuts.

- peak(s) detection of the phases differences histogram;
- the absolute phase offset is the main peak of the histogram.

The integer part (modulo 2π) of this offset is used to ensure that the Raw DEMs of a same data take are correctly connected. To put it simply, height discrepancies and discontinuities between the Raw DEMs can be avoided in this way (Rossi et al., 2012). This procedure is also capable to derive the absolute π-ambiguity phase offset for averagely coherent data. A by-product is an accurate fractional offset for the scene, which is an input for absolute calibration.

B.3.5.2 Phase unwrapping quality check

Coregistration or radargrammetric shifts also serve as independent coarse measurements to detect and assess errors in the unwrapped phase. Taking into account the high amount of data, it is an important advantage of the ITP. Indeed, it enables quality and production control in a fully automatic way for the entire globe. For this matter, the so-called *phase unwrapping quality ratio* q_{ratio} gives an idea of the success of the interferometric processing. It is the ratio or percentage of correctly unwrapped pixels with respect to all pixels (in the coarse shift matrices size, Table B.1).

During the absolute offset determination, a map of possible phase unwrapping problems is also generated for quality control. This map is obtained with the help of the computed histogram of the phase differences. This main lobe represents the principal region inside the scene (depicted in green in Fig. B.6a). If a phase unwrapping error occurred, at least one more lobe would appear in the histogram and the corresponding pixels would be masked out in this map (black in Fig. B.6a) (Rossi et al., 2012). This approach also ensures that absolute phase offsets are not biased by PU errors. However, since the radargrammetric phase is of lower resolution and noisy, small PU errors or the finer boundaries of a PU error are not detectable as exhibited in Fig. B.6.

B.3.5.3 Accuracy of the absolute phase offset

The accuracy of the absolute phase offset is proportional to the accuracy of the cross-correlation shifts (see section 3.2.1.2 for theoretical explanations). Shifts are estimated by means of the coherent cross-correlation. Incoherent cross-correlation is a fall-back solution when the first estimate is not reliable or the coherence is too low (see appendix B.3.2). Their accuracies $\sigma_{\Delta\chi_{cc}}$ and $\sigma_{\Delta\chi_{ic}}$ are given respectively by eq. (3.14) from Bamler and Eineder (2005) and eq. (3.15)

from De Zan (2014). $\sigma_{\Delta\chi_{cc}}$ is the CRLB and depends only on the coherence and the size of the estimation window N_c. Figure B.4a depicts the shift estimation errors for the ITP configuration i.e. $N_c = 1,024$ and $osf = f_{\mathrm{RS}}/W_R = 1.1$.

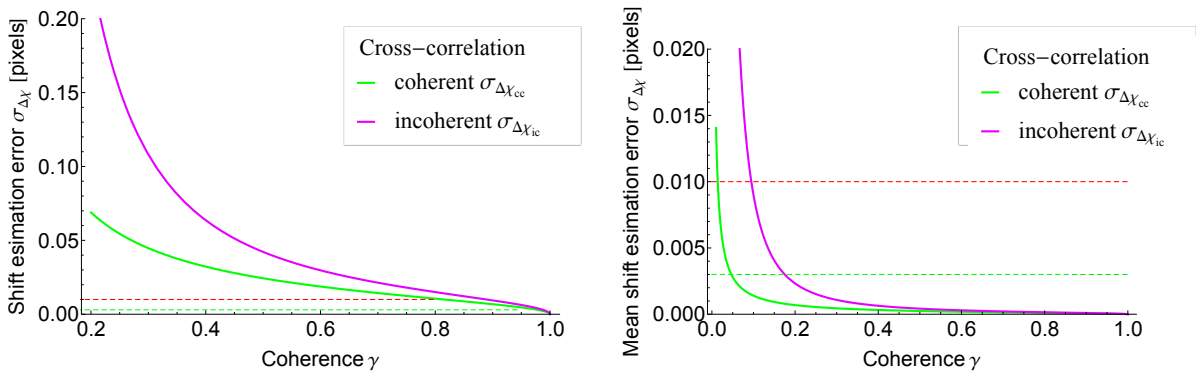

(a) Errors of one patch

(b) Mean error over 10,000 patches

Fig. B.4. Error of the shifts estimation using coherent $\sigma_{\Delta\chi_{cc}}$ (green) and incoherent $\sigma_{\Delta\chi_{ic}}$ (purple) cross-correlation for $N_c = 1,024$ and $osf = 1.1$.

Following eq. (3.17), an accuracy of the coregistration shifts better than 1/300 of a pixel is required to have $3\sigma_{\Delta\chi}$ and 1/100 for only one sigma (Rossi et al., 2012). These are obtained respectively for a coherence greater than 0.95 and 0.8 for coherent cross-correlation and only for coherences close to 1.0 for speckle tracking. This is thus the limit to detect phase unwrapping errors for an individual patch.

Moreover, the CRLB given by eq. (3.14) is valid for uniform patches i.e. for more or less flat terrain meaning that the topographic phase has to be removed perfectly from the data so that any residual artefacts or non-Gaussian scatterers degrade the accuracy. Notwithstanding, several thousand (coherent) patches are averaged per scene to measure the global offset (typically more than N_{patches} =10,000, Rossi et al. (2012)). Hence, the achieved accuracy is improved by a factor of $\sqrt{N_{\mathrm{patches}}}$ as it can be seen from Fig. B.4b. For this reason, coregistration shift accuracy is not limiting the absolute phase offset estimation and the π-ambiguity coming from the synchronisation link can be solved for average coherences (see appendix A.5).

When PU errors happen, several local phase offsets appear. Their accuracy is lower because of the reduced number of patches to average. Consequently, the stereo-radargrammetric phase is not adapted to deal with PU problems. Another limiting factor is the size of the phase. Indeed, the shifts are computed on a grid which is about 13×13 down to 21×21 coarser than the interferometric phases (appendix B.3.2). The phase unwrapping check and a possible a fortiori correction is not possible pixel-wise. However, the coarse PU error detection is reliable for scene exhibiting a good coherence.

B.3.5.4 Back-up solution

The coregistration shifts are not always usable. Indeed, in very low coherent scenes or in scenes containing little landmass like small islands, coherent and incoherent shifts estimates are not in a sufficient amount to compute the absolute phase offset. In this case, it is computed by averaging phase differences between the unwrapped phase and a simulated phase from a reference DEM (SRTM or GLOBE). Nonetheless, the offset is not truly reliable since PU errors can bias the offset or the reference DEM can be erroneous. A map is also generated to *visually* check the consistency with the reference DEM. It gives an idea of phase unwrapping correctness in regions, where the reference data is reliable (see Fig. B.6b, notice the size difference between both maps due to the different samplings). Fig. B.5 depicts how this map should be interpreted. Areas in agreement with the reference DEM (the yellow continuous line) are displayed in green in the

map (the green continuous line in this plot). Discrepant regions are depicted according to their possibly wrong ambiguity band in red or blue depending on the sign. Note that artefacts in the reference DEM are also visible in this map like in Fig. B.7.

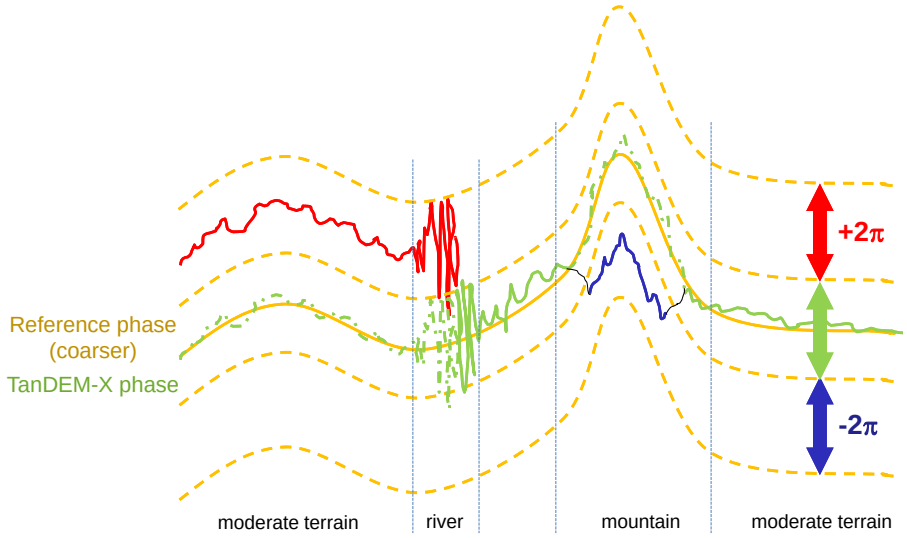

Fig. B.5. Explanation plot for the interpretation of the visual comparison map with the reference DEM.

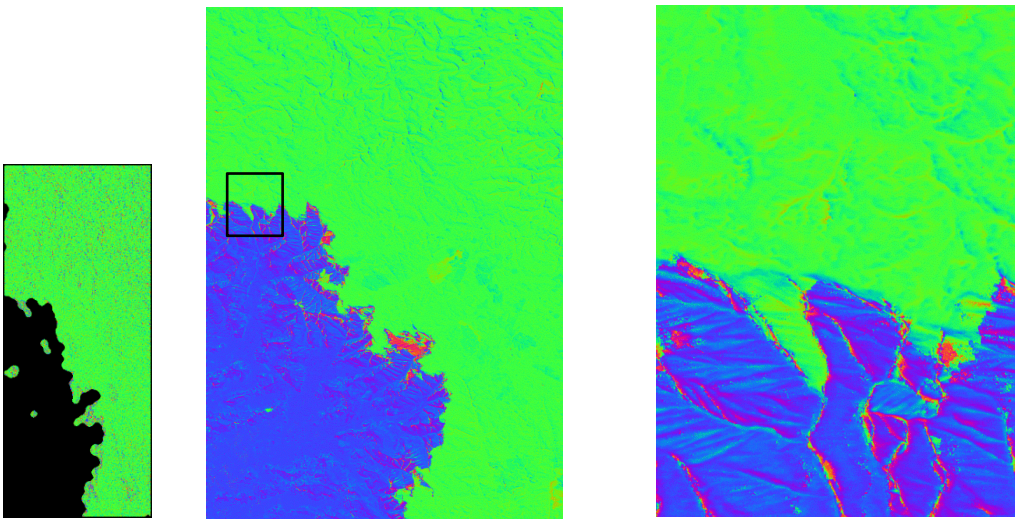

(a) (b) (c)

Fig. B.6. Comparison maps: (a) with respect to the stereo-radargrammetry (autonomous check, $q_{\text{ratio}} = 0.96$), (b) with respect to the reference DEM where (c) is the cropped area depicted previously.

B.3.6 Raw DEMs generation: geocoding

Geocoding refers to the generation of a DEM starting from the interferometric unwrapped phase. It involves the conversion to terrain height and the transformation from slant-range coordinates to an Earth-related reference frame. The algorithm is based on the technique described in Schwäbisch (1998). This concept allows to obtain the desired output in a single step, since it links all the parameters involved for geocoding: azimuth and range times, interferometric phase and terrain height (Rossi et al., 2010). During the processing, atmospheric path delay is taken into account. The ionospheric delay, which has a small impact on the geolocation accuracy at X-band, is modeled with a constant delay over the whole scene corresponding to 5 TECU (Breit et al., 2010a). Last but not least, the tropospheric delay, which is the dominant source of geolocation errors, is modelled by a height-dependent model (Breit et al., 2010a). The phase screen is also corrected for differential tropospheric propagation. The latter is caused by

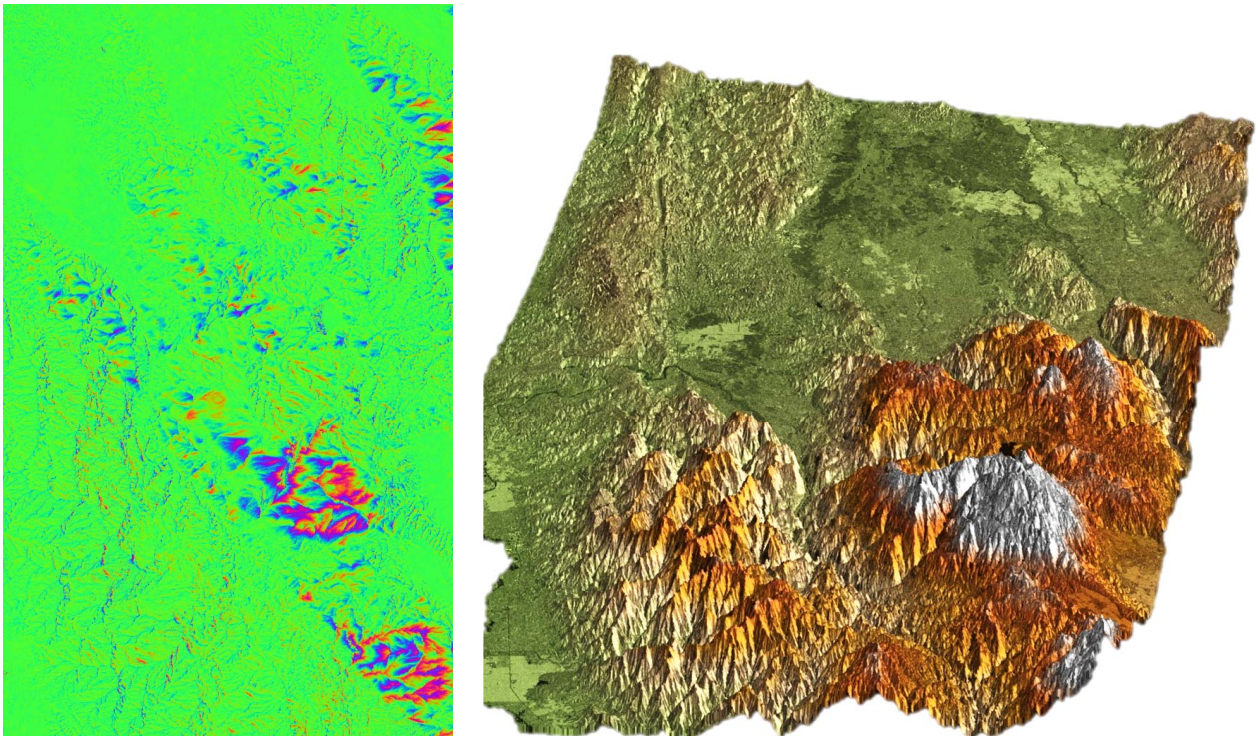

(a) (b)

Fig. B.7. Example of an error in mountainous terrain in SRTM DEM: (a) comparison of unwrapped phase with the simulated phase from SRTM DEM, (b) the 3-D scene.

the difference of local incidence angles between the two satellites, which imply small variations in the length of the signal (Breit et al., 2012). In a typical TanDEM-X scenario, for a height of ambiguity of 40 m/cycle and a point on ground at the sea level, the differential slant range correction is varying between about 0.5 and 1.5 millimetres for incidence angles varying between 30° and 45°, yielding an absolute height correction of 0.7 to 2.0 metres. These effects are only corrected during the geocoding and are thus still present in all CoSSC products.

Two quality maps assessing the generated Raw DEM are also delivered. The first map is the Height Error Map representing, for each pixel, the standard error of the corresponding elevation value in the DEM. The second quality map represents a coarse overview of possible problematic regions providing an indication about shadow, layover, water, phase unwrapping residues and branch-cuts (see Rossi et al. (2010) for more details).

Raw DEMs are finally stored in the archive from which they are ingested in the Mosaicking and Calibration Processor (MCP) (see appendix A.6) for further processing.

B.4 Dual-baseline phase unwrapping chain

Dual-baseline phase unwrapping is operationally applied to all incoming data from the second coverage on. Furthermore, Raw DEMs from the first global coverage exhibiting significant PU errors are automatically triggered for reprocessing. The following description of the chain is based on Lachaise et al. (2012a).

B.4.1 Key steps of the chain

The dual-baseline chain is activated as soon as some previously processed CoSSCs are provided to support the current interferometric processing (see Fig. B.1). The chain can handle as many supporting CoSSCs as available under the assumptions that they overlap, have a sufficiently

different baseline and the same acquisition geometry. In this sense, it can also be seen as a multi-baseline PU algorithm. Nonetheless, the whole processing is done for every CoSSC pair separately, hence referred to as dual-baseline. The interferometric data of the current processing are called *master* data and these from the supporting CoSSCs *slave* data.

The basic idea of the DB-PUC approach is to unwrap both interferograms separately using the MCF phase unwrapping (appendix B.3.4) and to compare them in slant range height domain to detect regions where the unwrapped phases differ significantly. These local discrepancies are then corrected pixel-wise for an integer multiple of 2π determined from the (corrected) unwrapped differential interferogram. This is described in details in chapter 5. More specifically, it consists of (Fig. B.8):

- coregistrating the *slave* CoSSC on the *master* interferogram (v_m);
- cropping to the common part;
- forming the *slave* interferogram v_s and unwrapping it;
- checking phase unwrapping consistency of both *master* and *slave* unwrapped phases (in slant range height domain);
- if phase unwrapping is inconsistent:
  - calculation of the *differential interferogram* (v_d);
  - possibly, correction with the stereo-radargrammetric phase;
  - correction of the *master* unwrapped phase.

A final overall step is the mosaicking of the different corrected *master* unwrapped phases coming from every overlap with a different *slave* interferogram.

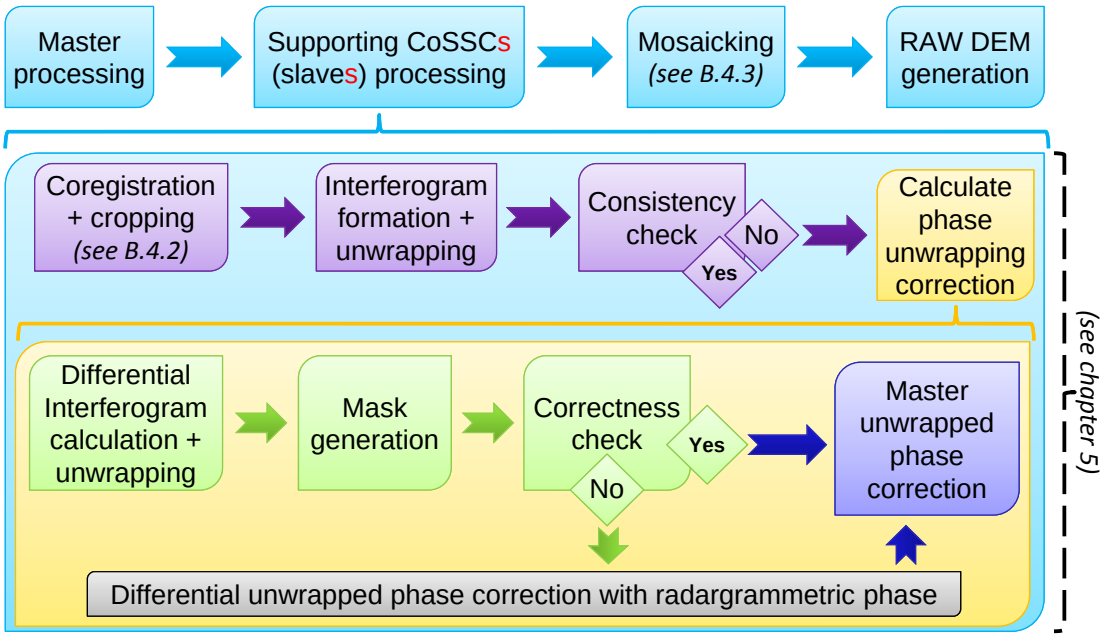

Fig. B.8. Overview block diagram of the dual-baseline InSAR chain inside the ITP.

B.4.2 Preparation of the supporting CoSSCs

Since the input of the dual-baseline chain (and as a result of the DB-PUC) are coregistered SSCs and a *master* interferogram (which is therefore already coregistered), only both master SSCs have to be coregistered. After that, the resampling matrix is applied to both channels of the supporting CoSSC. Nevertheless, since there is a large time span (typically of about one year) between both acquisitions, the usual ITP coregistration algorithm based on coherent cross-correlation (see appendix B.3.2) cannot be used because of the high temporal decorrelation. Notwithstanding, since all the data have the same acquisition geometry but different baselines,

it is possible to rescale the signal based coregistration shifts (equivalent to a coarse stereo-radargrammetric DEM) to the new baseline. When the *slave* bistatic data are coregistered to the *master* bistatic data, a repeat-pass monostatic pair is formed. As a result, the rescaling of the shifts has to take into account the different acquisition configuration with the help of the shifts coming from the simulated acquisition geometry. Thus, the relation between the signal *slave-master* monostatic shifts and the *master* bistatic shifts is the same as the relation between their respective geometrical estimates:

$$\frac{[\text{signal shifts}]^{slave\text{-}master}_{\text{monostatic}}}{[\text{signal shifts}]^{master}_{\text{bistatic}}} = \frac{[\text{geometrical shifts}]^{slave\text{-}master}_{\text{monostatic}}}{[\text{geometrical shifts}]^{master}_{\text{bistatic}}} \tag{B.1}$$

Consequently, the equivalent precise monostatic signal shifts can be derived as follows:

$$[\text{signal shifts}]^{slave\text{-}master}_{\text{monostatic}} = \frac{[\text{geometrical shifts}]^{slave\text{-}master}_{\text{monostatic}}}{[\text{geometrical shifts}]^{master}_{\text{bistatic}}} [\text{signal shifts}]^{master}_{\text{bistatic}} \tag{B.2}$$

These shifts are correct as long as the reference DEM used for the simulation or the *master* bistatic signal shifts do not exhibit significant errors.

The obtained shifts are then used to resample the *slave* data to the *master* geometry. Once both scenes are coregistered, the common part is cropped. Finally, the interferogram is calculated and unwrapped using the MCF algorithm (appendix B.3.4).

B.4.3 Mosaicking of the different corrected parts

The phases coming from the different overlapping *slave* interferograms, which were corrected by means of the DB-PUC framework explained in chapter 5, are finally mosaicked to rebuild the entire scene. Remaining offsets between the different parts are corrected. In the overlapping areas of the corrected phases, the corrected values can be either equal (straightforward) or different by a multiple of 2π. In this case, the final corrected phase is chosen according to the correction quality.

C Maps of the height of ambiguity slopes

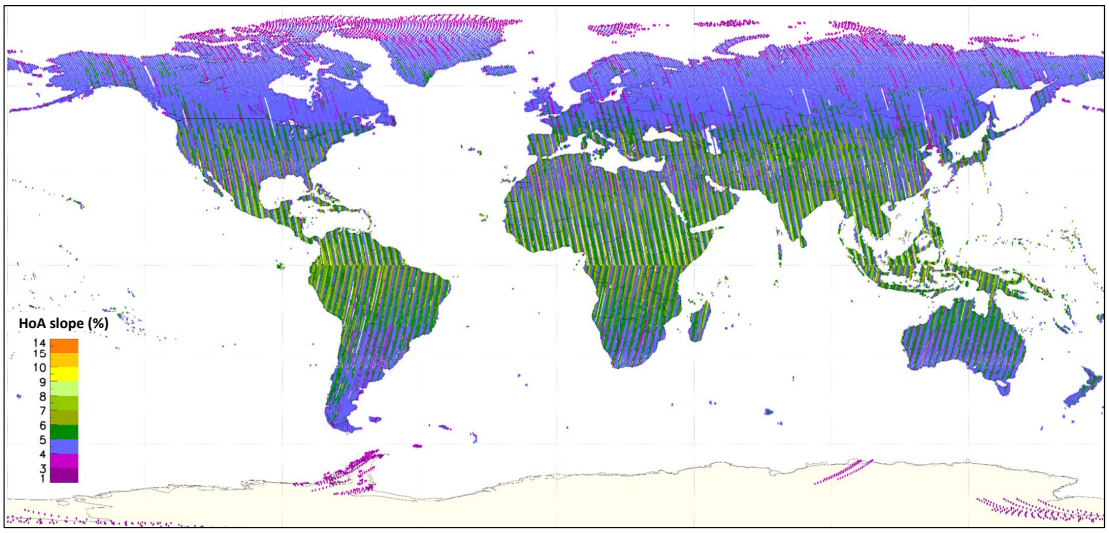

(a) First global coverage (acquired from end of December 2010 to March 2012)

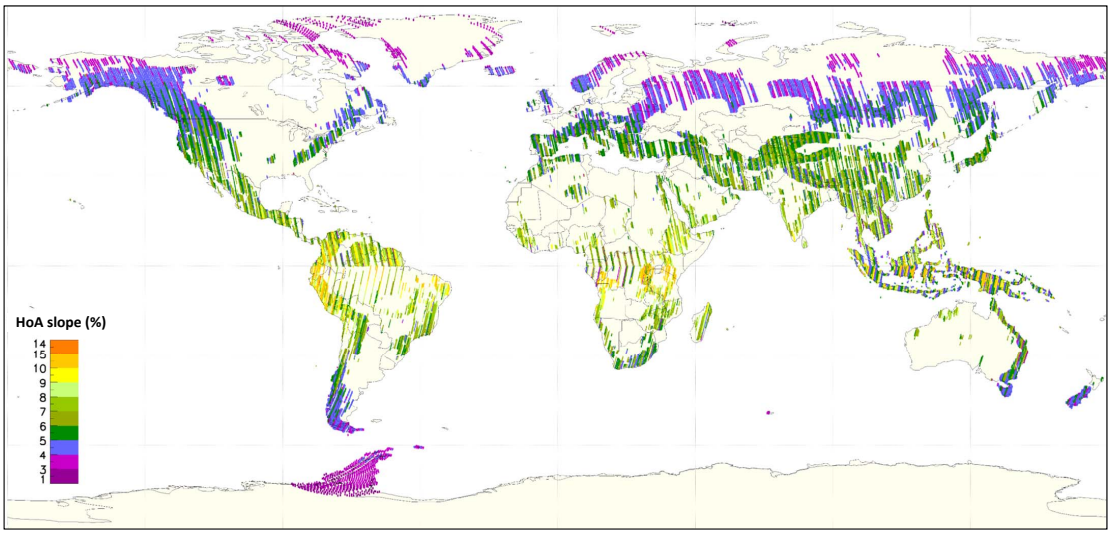

(b) Additional acquisitions (acquired from April 2011 to March 2012)

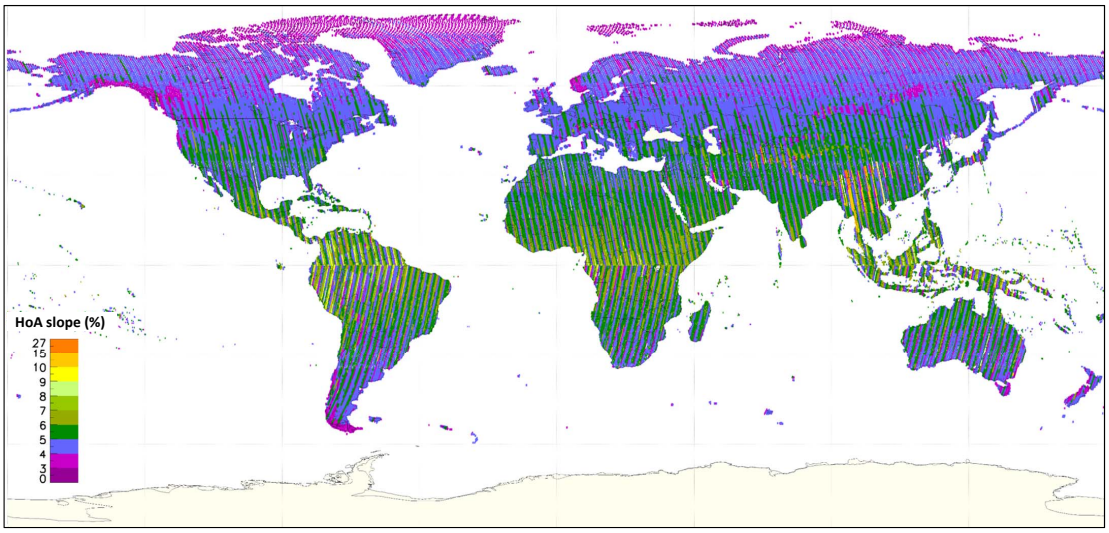

(c) Second global coverage (acquired from March 2012 to March 2013)

Fig. C.1. Maps of the height of ambiguity (HoA) slopes for the different coverages.

D Complex correlation of the differential interferogram

The complex correlation of the differential interferogram is (Papoulis, 1991):

$$\rho^d = \frac{\mathrm{E}\left[v^m v^{s*}\right] - \mathrm{E}\left[v^m\right]\mathrm{E}\left[v^{s*}\right]}{\sqrt{\left(\mathrm{E}\left[\left|v^m\right|^2\right] - \left|\mathrm{E}\left[v^m\right]\right|^2\right)\left(\mathrm{E}\left[\left|v^s\right|^2\right] - \left|\mathrm{E}\left[v^s\right]\right|^2\right)}} \tag{D.1}$$

where $v^m = u_1^m u_2^{m*}$ and $v^{s*} = u_1^{s*} u_2^s$, thus:

$$\rho^d = \frac{\mathrm{E}\left[u_1^m u_2^{m*} u_1^{s*} u_2^s\right] - \mathrm{E}\left[u_1^m u_2^{m*}\right]\mathrm{E}\left[u_1^{s*} u_2^s\right]}{\sqrt{\left(\mathrm{E}\left[\left|u_1^m u_2^{m*}\right|^2\right] - \left|\mathrm{E}\left[u_1^m u_2^{m*}\right]\right|^2\right)\left(\mathrm{E}\left[\left|u_1^{s*} u_2^s\right|^2\right] - \left|\mathrm{E}\left[u_1^{s*} u_2^s\right]\right|^2\right)}} \tag{D.2}$$

Following the moment theorem for four jointly circular Gaussian random values (Reed, 1962), an expression of the first term of the numerator of eq. (D.2) can be derived:

$$\mathrm{E}\left[u_1^m u_2^{m*} u_1^{s*} u_2^s\right] = \mathrm{E}\left[u_1^m u_2^{m*}\right]\mathrm{E}\left[u_1^{s*} u_2^s\right] + \mathrm{E}\left[u_1^m u_1^{s*}\right]\mathrm{E}\left[u_2^{m*} u_2^s\right] \tag{D.3}$$

Since the coherences of the two interferograms are (eq. (2.14)):

$$\gamma^m = \frac{\mathrm{E}\left[u_1^m u_2^{m*}\right]}{\sqrt{\mathrm{E}\left[\left|u_1^m\right|^2\right]\mathrm{E}\left[\left|u_2^m\right|^2\right]}} = \frac{\mathrm{E}\left[u_1^m u_2^{m*}\right]}{\overline{I^m}} \quad \text{and} \quad \gamma^s = \frac{\mathrm{E}\left[u_1^s u_2^{s*}\right]}{\sqrt{\mathrm{E}\left[\left|u_1^s\right|^2\right]\mathrm{E}\left[\left|u_2^s\right|^2\right]}} = \frac{\mathrm{E}\left[u_1^s u_2^{s*}\right]}{\overline{I^s}} \tag{D.4}$$

and the cross-interferograms coherences are defined as:

$$\gamma_1 = \frac{\mathrm{E}\left[u_1^m u_1^{s*}\right]}{\sqrt{\mathrm{E}\left[\left|u_1^m\right|^2\right]\mathrm{E}\left[\left|u_1^s\right|^2\right]}} = \frac{\mathrm{E}\left[u_1^m u_1^{s*}\right]}{\overline{I_1}} \quad \text{and} \quad \gamma_2 = \frac{\mathrm{E}\left[u_2^m u_2^{s*}\right]}{\sqrt{\mathrm{E}\left[\left|u_2^m\right|^2\right]\mathrm{E}\left[\left|u_2^s\right|^2\right]}} = \frac{\mathrm{E}\left[u_2^m u_2^{s*}\right]}{\overline{I_2}} \tag{D.5}$$

eq. (D.3) can be rewritten as:

$$\mathrm{E}\left[u_1^m u_2^{m*} u_1^{s*} u_2^s\right] = \overline{I^m I^s}\left(\gamma^m \gamma^{s*} + \gamma_1 \gamma_2^*\right) \tag{D.6}$$

The term $\mathrm{E}\left[\left|u_1^m u_2^{m*}\right|^2\right]$ of the denominator of eq. (D.2) is equal to:

$$\mathrm{E}\left[\left|u_1^m u_2^{m*}\right|^2\right] = \overline{I^m}^2\left(1 + \left|\gamma^m\right|^2\right) \tag{D.7}$$

Finally the complex correlation of the *differential interferogram* of eq. (D.2) is:

$$\rho^d = \frac{\overline{I^m I^s}\left(\gamma^m \gamma^{s*} + \gamma_1 \gamma_2^*\right) - \gamma^m \overline{I^m} \gamma^s \overline{I^s}}{\sqrt{\left(\overline{I^m}^2\left(1 + \left|\gamma^m\right|^2\right) - \left(\left|\gamma^m\right|\overline{I^m}\right)^2\right)\left(\overline{I^s}^2\left(1 + \left|\gamma^s\right|^2\right) - \left(\left|\gamma^s\right|\overline{I^s}\right)^2\right)}} = \gamma_1 \gamma_2 \tag{D.8}$$

In this way, the complex correlation coefficient of the *differential interferogram* is simply the product of the coherences of the two cross-interferograms.

References

Adi, K., Mengko, T. L. R., Suksmono, A. B., Gunawan, H., 2010. *Phase Unwrapping Using Energy Minimization Methods for MRI Phase Image*. International Journal of E-Health and Medical Communications 1 (3), 50–56.

Antony, J. W., Hueso González, J., Schwerdt, M., Bachmann, M., Krieger, G., Zink, M., 2013. *Results of the TanDEM-X Baseline Calibration*. IEEE Journal of Selected Topics in Applied Earth Observations and Remote Sensing 6 (3), 1495–1501.

Bachmann, M., Schulze, D., Ortega-Miguez, C., Polimeni, M. D., Boer, J., Hueso González, J., Walter Antony, J. M., Krämer, R., Brautigam, B., Schwerdt, M., Zink, M., 2012. *TanDEM-X acquisition status and calibration of the interferometric system*. In: Proceedings of IGARSS.

Bachmann, M., Schwerdt, M., Castellanos Alfonzo, G., Schrank, D., 2013. *Phase Pattern Calibration for Interferometric Applications in Spaceborne SAR Systems*. International Journal of Antennas and Propagation 2013, 1–8.

Balss, U., Cong, X. Y., Brcic, R., Rexer, M., Minet, C., Breit, H., Eineder, M., Fritz, T., 2012. *High precision measurement on the absolute localization accuracy of TerraSAR-X*. In: Proceedings of IGARSS.

Balss, U., Niedermeier, A., Breit, H., 2010. *TanDEM-X Bistatic SAR Processing*. In: Proceedings of EuSAR.

Bamler, R., 2000. *Interferometric Stereo Radargrammetry : Absolute Height Determination from ERS-ENVISAT Interferograms*. In: Proceedings of IGARSS.

Bamler, R., Adam, N., Davidson, G. W., Just, D., 1998. *Noise-induced slope distortion in 2-D phase unwrapping by linear estimators with application to SAR interferometry*. IEEE Transactions on Geoscience and Remote Sensing 36 (3), 913–921.

Bamler, R., Eineder, M., 2005. *Accuracy of Differential Shift Estimation by Correlation and Split-Bandwidth Interferometry for Wideband and Delta-k SAR Systems*. IEEE Geoscience and Remote Sensing Letters 2 (2), 151–155.

Bamler, R., Hartl, P., 1998. *Synthetic aperture radar interferometry*. In: Inverse Problems. Vol. 14. p. 54.

Bamler, R., Just, D., 1993. *Phase statistics and decorrelation in SAR interferograms*. In: Proceedings of IGARSS.

Bamler, R., Meyer, F., Liebhart, W., 2007. *Processing of Bistatic SAR Data From Quasi-Stationary Configurations*. IEEE Trans. on Geoscience and Remote Sensing 45 (11), 3350–3358.

Baselice, F., Budillon, A., Ferraioli, G., Pascazio, V., Schirinzi, G., 2014a. *Multibaseline SAR Interferometry from Complex Data*. IEEE Journal of Selected Topics in Applied Earth Observations and Remote Sensing 7 (7), 2911–2918.

Baselice, F., Ferraioli, G., Pascazio, V., Schirinzi, G., 2014b. *Contextual Information-Based Multichannel Synthetic Aperture Radar Interferometry: Addressing DEM reconstruction using contextual information*. IEEE Signal Processing Magazine 31 (4), 59–68.

Beutler, G., Bock, H., Dach, R., Fridez, P., Gaede, A., Hugentobler, U., Jaeggi, A., Meindl, M., Mervart, L., Prange, L., Schaer, S., Springer, T., Urschl, C., Walser, P., 2007. *Bernese GPS Software, Version 5.0*. Ph.D. thesis, University of Bern.

Bioucas-Dias, J. M., Leitao, J. M. N., 2002. *The ZpiM algorithm: a method for interferometric image reconstruction in SAR/SAS*. IEEE Transactions on Image Processing 11 (4), 408–22.

Bioucas-Dias, J. M., Valadão, G., 2007. *Phase unwrapping via graph cuts*. IEEE Transactions on Image Processing 16 (3), 698–709.

Borla Tridon, D., Bachmann, M., Schulze, D., Míguez, C. O., Polimeni, M. D., Martone, M., Böer, J., Zink, M., 2013. *TanDEM-X: DEM acquisition in the third year era*. International Journal of Space Science and Engineering 1 (4), 367.

Borla Tridon, D., Bachmann, M., Schulze, D., Polimeni, M. D., Martone, M., Böer, J., Zink, M., 2014. *TanDEM-X DEM Difficult Terrain & Antarctica Acquisitions towards the Planning of the Science Phase*. In: Proceedings of EuSAR.

Brcic, R., Eineder, M., Bamler, R., Steinbrecher, U., Schulze, D., Metzig, R., Papathanassiou, K. P., Nagler, T., Mueller, F., Suess, M., 2009. *Delta-K wideband SAR interferometry for DEM generation and persistent scatterers using TerraSAR-X*. In: Fringe Workshop.

Breit, H., Boerner, E., Mittermayer, J., Holzner, J., Eineder, M., 2004. *The TerraSAR-X Multi-Mode SAR Processor - Algorithms and Design Blocks SAR Focusing Algorithm*. In: Proceedings of EuSAR.

Breit, H., Fritz, T., Balss, U., Lachaise, M., Niedermeier, A., Vonavka, M., 2010a. *TerraSAR-X SAR Processing and Products*. IEEE Trans. on Geoscience and Remote Sensing 48 (2), 727–740.

Breit, H., Fritz, T., Balss, U., Niedermeier, A., Eineder, M., Yague-Martinez, N., Rossi, C., 2010b. *Processing of bistatic TanDEM-X data*. In: Proceedings of IGARSS.

Breit, H., Lachaise, M., Balss, U., Rossi, C., Fritz, T., Niedermeier, A., 2012. *Bistatic and Interferometric Processing of TanDEM-X Data*. In: Proceedings of EuSAR.

Breit, H., Younis, M., Balss, U., Niedermeier, A., Grigorov, C., Hueso González, J., Krämer, R., Eineder, M., Fritz, T., 2011. *Bistatic synchronization and processing of TanDEM-X data*. In: Proceedings of IGARSS.

Buckreuss, S., Schättler, B., 2010. *The TerraSAR-X Ground Segment*. IEEE Transactions on Geoscience and Remote Sensing 48 (2), 623–632.

Carballo, G. F., Fieguth, P. W., 2000. *Probabilistic cost functions for network flow phase unwrapping*. IEEE Transactions on Geoscience and Remote Sensing 38 (5), 2192–2201.

Carballo, G. F., Fieguth, P. W., 2002. *Hierarchical network flow phase unwrapping*. IEEE Transactions on Geoscience and Remote Sensing 40 (8), 1695–1708.

Castellanos, J., Gómez, S., Guerra, V., 2002. *The triangle method for finding the corner of the L-curve*. Applied Numerical Mathematics 43 (4), 359–373.

Chen, C. W., Zebker, H. A., 2000. *Network approaches to two-dimensional phase unwrapping: intractability and two new algorithms*. Journal of the Optical Society of America A 17 (3), 401.

Chen, C. W., Zebker, H. A., 2001. *Two-dimensional phase unwrapping with use of statistical models for cost functions in nonlinear optimization*. J. Optical Society of America A 18 (2), 338.

Chen, C. W., Zebker, H. A., 2002. *Phase unwrapping for large SAR interferograms: statistical segmentation and generalized network models*. IEEE Transactions on Geoscience and Remote Sensing 40 (8), 1709–1719.

Chirico, D., Schirinzi, G., 2013. *Multichannel interferometric SAR phase unwrapping using extended Kalman Smoother*. International Journal of Microwave and Wireless Technologies 5 (3), 429–436.

Cong, X. Y., Balss, U., Eineder, M., Fritz, T., 2012. *Imaging Geodesy-Centimeter-Level Ranging Accuracy With TerraSAR-X: An Update*. IEEE Geoscience and Remote Sensing Lett. 9 (5), 948–952.

Corsini, G., Diani, M., Lombardini, F., Pinelli, G., 1997. *Reduction of the phase-unwrapping drawbacks by the three-antenna interferometric SAR system*. In: Proceedings of IGARSS.

Corsini, G., Diani, M., Lombardini, F., Pinelli, G., 1999. *Simulated analysis and optimization of a three-antenna airborne InSAR system for topographic mapping*. IEEE Transactions on Geoscience and Remote Sensing 37 (5), 2518–2529.

Costantini, M., 1998. *A novel phase unwrapping method based on network programming*. IEEE Transactions on Geoscience and Remote Sensing 36 (3), 813–821.

Cumming, I., Wong, F. H., 2005. *Digital Processing Of Synthetic Aperture Radar Data: Algorithms And Implementation*. Artech house.

Curlander, J. C., McDonough, R. N., 1991. *Synthetic Aperture Radar: Systems and Signal processing*. Wiley-Interscience.

D'Amico, S., Arbinger, C., Kirschner, M., Campagnola, S., 2004. *Generation of an optimum target trajectory for the TerraSAR-X repeat observation satellite*. In: 18th International Symposium on

Space Flight Dynamics.

De Zan, F., 2014. *Accuracy of Incoherent Speckle Tracking for Circular Gaussian Signals*. IEEE Geoscience and Remote Sensing Letters 11 (1), 264–267.

De Zan, F., Krieger, G., López-dekker, P., 2013. *On Some Spectral Properties of TanDEM-X Interferograms Over Forested Areas*. Geoscience and Remote Sensing Letters, IEEE 10 (1), 71–75.

Deledalle, C.-a., Denis, L., Tupin, F., 2011. *NL-InSAR: Nonlocal Interferogram Estimation*. IEEE Transactions on Geoscience and Remote Sensing 49 (4), 1441–1452.

Denis, L., Tupin, F., Darbon, J., Sigelle, M., 2008. *Joint Filtering of SAR Interferometric and Amplitude Data in Urban Areas by TV Minimization*. In: Proceedings of IGARSS.

Dubois, C., Thiele, A., Hinz, S., 2013. *Pixel-based approach for building heights determination by SAR radargrammetry*. In: Proceedings of ISPRS City Models, Roads and Traffic.

Duque, S., Balss, U., Cong, X. Y., Minet, C., Fritz, T., 2014. *Accurate measurements using TerraSAR-X and TanDEM-X data without any reference*. In: Proceedings of IGARSS.

Eineder, M., 2003a. *Efficient simulation of sar interferograms of large areas and of rugged terrain*. IEEE Transactions on Geoscience and Remote Sensing 41 (6), 1415–1427.

Eineder, M., 2003b. *Ocillator clock drift compensation in bistatic interferometric SAR*. In: Proceedings of IGARSS.

Eineder, M., Adam, N., 2005. *A maximum-likelihood estimator to simultaneously unwrap, geocode, and fuse SAR interferograms from different viewing geometries into one digital elevation model*. IEEE Transactions on Geoscience and Remote Sensing 43 (1), 24–36.

Eineder, M., Hubig, M., Milcke, B., 1998. *Unwrapping large interferograms using the minimum cost flow algorithm*. In: Proceedings of IGARSS.

Eineder, M., Krieger, G., 2005. *Interferometric digital elevation model reconstruction - experiences from SRTM and multi channel approaches for future missions*. In: Proceedings of IGARSS.

Farr, T. G., Rosen, P. A., Caro, E., Crippen, R., 2007. *The shuttle radar topography mission*. Reviews of Geophysics (2005), 1–33.

Ferraioli, G., 2010. *Multichannel InSAR Building Edge Detection*. IEEE Transactions on Geoscience and Remote Sensing 48 (3), 1224–1231.

Ferraioli, G., Ferraiuolo, G., Pascazio, V., 2008. *Phase-Offset Estimation in Multichannel SAR Interferometry*. IEEE Geoscience and Remote Sensing Letters 5 (3), 458–462.

Ferraioli, G., Shabou, A., Tupin, F., Pascazio, V., 2009. *Multichannel Phase Unwrapping With Graph Cuts*. IEEE Geoscience and Remote Sensing Letters 6 (3), 562–566.

Ferraiuolo, G., Meglio, F., Pascazio, V., Schirinzi, G., 2009. *DEM Reconstruction Accuracy in Multichannel SAR Interferometry*. IEEE Trans. Geoscience and Remote Sensing 47 (1), 191–201.

Ferraiuolo, G., Pascazio, V., Schirinzi, G., 2004. *Maximum A Posteriori Estimation of Height Profiles in InSAR Imaging*. IEEE Geoscience and Remote Sensing Letters 1 (2), 66–70.

Ferretti, A., Prati, C., Rocca, F., Monti Guarnieri, A., 1997. *Multibaseline SAR interferometry for automatic DEM reconstruction*. In: 3rd ERS Symposium on Space at the service of our Environment.

Fiedler, H., Krieger, G., Zink, M., Geyer, M., Jäger, J., 2008. *The TanDEM-X Acquisition Timeline and Mission Plan*. In: Proceedings of EuSAR.

Flynn, T. J., 1997. *Two-dimensional phase unwrapping with minimum weighted discontinuity*. Journal of the Optical Society of America A 14 (10), 2692–2701.

Fornaro, G., Franceschetti, G., Lanari, R., 1996. *Interferometric SAR phase unwrapping using Green's formulation*. IEEE Transactions on Geoscience and Remote Sensing 34 (3), 720–727.

Fornaro, G., Franceschetti, G., Lanari, R., Sansosti, E., Tesauro, M., 1997. *Global and local phase-unwrapping techniques: a comparison*. J. Optical Society of America A 14 (10), 2702.

Fornaro, G., Monti Guarnieri, A., Pauciullo, A., De Zan, F., 2006. *Maximum likelihood multi-baseline SAR interferometry*. IEE Proceedings Radar Sonar and Navigation 153 (3), 279.

Frery, A. C., Correa, A., Rennò, C. D., 1999. *Models for synthetic aperture radar image analysis*.

Resenhas do Instituto de Matemática e Estatística da Universidade de Sao Paulo.

Fried, D. L., 1977. *Least-square fitting a wave-front distortion estimate to an array of phase-difference measurements.* Journal of the Optical Society of America 67 (3), 370.

Fritz, T., Breit, H., Rossi, C., Balss, U., Lachaise, M., Duque, S., 2012. *Interferometric processing and products of the TanDEM-X mission.* In: Proceedings of IGARSS.

Fritz, T., Rossi, C., Yague-Martinez, N., Rodriguez Gonzalez, F., Lachaise, M., Breit, H., 2011. *Interferometric processing of TanDEM-X data.* In: Proceedings of IGARSS.

Galli, L., 2001. *A new approach based on network theory to locate phase unwrapping unreliable results.* In: Proceedings of IGARSS.

Gatelli, F., Monti Guarnieri, A., Parizzi, F., Pasquali, P., Prati, C., Rocca, F., 1994. *The wavenumber shift in SAR inferometry.* IEEE Transactions on Geoscience and Remote Sensing 32 (4), 855–865.

Geman, S., Geman, D., 1984. *Stochastic relaxation, gibbs distributions, and the bayesian restoration of images.* IEEE transactions on pattern analysis and machine intelligence 6 (6), 721–41.

Gens, R., 2003. *Two-dimensional phase unwrapping for radar interferometry: Developments and new challenges.* International Journal of Remote Sensing 24 (4), 703–710.

Geudtner, D., 1995. *Die Interferometrische Verarbeitung von SAR-Daten des ERS-1.* Ph.D. thesis.

Ghiglia, D. C., Pritt, M. D., 1998. *Two-Dimensional Phase Unwrapping: Theory, Algorithms, and Software.* Wiley-Interscience.

Ghiglia, D. C., Romero, L. A., 1994. *Robust two-dimensional weighted and unweighted phase unwrapping that uses fast transforms and iterative methods.* J. Optical Society of America A 11 (1), 107.

Ghiglia, D. C., Romero, L. A., 1996. *Minimum Lp-norm two-dimensional phase unwrapping.* Journal of the Optical Society of America A 13 (10), 1999.

Ghiglia, D. C., Wahl, D. E., 1994. *Interferometric synthetic aperture radar terrain elevation mapping from multiple observations.* In: Proceedings of IEEE Digital Signal Processing Workshop.

Goldstein, R. M., Zebker, H. A., 1987. *Interferometric radar measurement of ocean surface currents.* Nature 928, 707–709.

Goldstein, R. M., Zebker, H. A., Werner, C. L., 1988. *Satellite radar interferometry- Two-dimensional phase unwrapping.* Radio Science.

Gonzalez, C., Bräutigam, B., Martone, M., Rizzoli, P., 2014. *Relative Height Error Estimation Method for TanDEM-X DEM Products.* In: Proceedings of EuSAR.

Goodman, N. R., 1963. *Statistical Analysis Based on a Certain Multivariate Complex Gaussian Distribution (An Introduction).* The Annals of Mathematical Statistics 34 (1), 152–177.

Gray, A., Mattar, K., Vachon, P. W., Bindschadler, R., Jezek, K., Forster, R., Crawford, J., 1998. *InSAR results from the RADARSAT Antarctic Mapping Mission data: estimation of glacier motion using a simple registration procedure.* In: Proceedings of IGARSS.

Gruber, A., Wessel, B., Huber, M., 2009. *TanDEM-X DEM calibration: Correction of systematic DEM errors by block adjustment.* In: Proceedings of IGARSS.

Gruber, A., Wessel, B., Huber, M., 2012. *Quality assessment of first TanDEM-X DEMs for different terrain types.* In: Proceedings of EuSAR.

Guerriero, L., Nico, G., Pasquariello, G., Stramaglia, S., 1998. *New regularization scheme for phase unwrapping.* Applied Optics 37 (14), 3053–8.

Hansen, C., O'Leary, D. P., 1993. *The Use of the L-Curve in the Regularization of Discrete Ill-Posed Problems.* SIAM Journal on Scientific Computing 14 (6), 1487–1503.

Hanssen, R. F., 2001. *Radar interferometry: data interpretation and error analysis.* Springer Science.

Hedley, M., Rosenfeld, D., 1992. *A new two-dimensional phase unwrapping algorithm for MRI images.* Magnetic Resonance in Medicine 24 (1), 177–181.

Höhle, J., Höhle, M., 2009. *Accuracy assessment of digital elevation models by means of robust statistical methods.* ISPRS Journal of Photogrammetry and Remote Sensing 64 (4), 398–406.

Homer, J., Longstaff, I., She, Z., 1997. *Improved digital elevation models via multi-baseline interferometric SAR.* In: Proceedings of IGARSS.

Huber, M., Gruber, A., Wendleder, A., Wessel, B., Roth, A., Schmitt, A., 2012. *The global TanDEM-X DEM: production status and first validation results.* In: Int. Arch. Photogramm. Remote Sens. Spatial Inf. Sci.

Huber, M., Wessel, B., Kosmann, D., Felbier, A., Schwieger, V., Habermeyer, M., Wendleder, A., Roth, A., 2009. *Ensuring globally the TanDEM-X height accuracy: Analysis of the reference data sets ICESat, SRTM and KGPS-tracks.* In: Proceedings of IGARSS.

Huber, S., Younis, M., Krieger, G., 2010. *The TanDEM-X mission: overview and interferometric performance.* International Journal of Microwave and Wireless Technologies 2 (3-4), 379–389.

Hubig, M., Suchandt, S., Eineder, M., 2000. *Automatic correction of baseline and phase unwrapping errors in SAR interferograms.* In: Proceedings of EuSAR.

Hudgin, R. H., 1977. *Wave-front reconstruction for compensated imaging.* Journal of the Optical Society of America 67 (3), 375.

Hueso González, J., Bachmann, M., Hofmann, H., 2010. *TanDEM-X commissioning phase status.* In: Proceedings of IGARSS.

Hueso González, J., Walter Antony, J. M., Bachmann, M., Krieger, G., Zink, M., Schrank, D., Schwerdt, M., 2012. *Bistatic system and baseline calibration in TanDEM-X to ensure the global digital elevation model quality.* ISPRS Journal of Photogrammetry and Remote Sensing 73, 3–11.

Ishikawa, H., 2000. *Global optimization using embedded graphs.* Ph.D. thesis.

Itoh, K., 1982. *Analysis of the phase unwrapping algorithm.* Applied Optics 21 (14), 2470.

Jakowatz, C. V., Wahl, D. E., Thompson, P. A., 1996. *Ambiguity resolution in SAR interferometry by use of three phase centers.* In: Zelnio, E. G., Douglass, R. J. (Eds.), Proc. SPIE 2757, Algorithms for Synthetic Aperture Radar Imagery III.

Joughin, I., Winebrenner, D., Percival, D., 1994. *Probability density functions for multilook polarimetric signatures.* IEEE Transactions on Geoscience and Remote Sensing 32 (3), 562–574.

Just, D., Bamler, R., 1994. *Phase statistics of interferograms with applications to synthetic aperture radar.* Applied Optics 33 (20), 4361.

Kay, S. M., 1993. *Fundamentals of Statistical Signal Processing, Volume I: Estimation Theory.* Pearson Education.

Kim, S., Kim, Y.-S., 2005. *Least squares phase unwrapping in wavelet domain.* IEE Proceedings - Vision, Image, and Signal Processing 152 (3), 261.

Kraus, T., Bachmann, M., Rizzoli, P., Brautigam, B., Krieger, G., 2012. *TanDEM-X performance: Impact on acquisition planning optimization.* In: 2012 13th International Radar Symposium. No. 1.

Krieger, G., De Zan, F., 2012. *Relativistic Effects in Bistatic SAR Processing and System Synchronization.* In: Proceedings of EuSAR.

Krieger, G., De Zan, F., Bachmann, M., Hueso González, J., Rodriguez Cassola, M., Zink, M., 2012. *Unexpected height offsets in TanDEM-X: Explanation and correction.* In: Proceedings of IGARSS.

Krieger, G., Moreira, A., Fiedler, H., Hajnsek, I., Werner, M., Younis, M., Zink, M., 2007. *TanDEM-X: A Satellite Formation for High-Resolution SAR Interferometry.* IEEE Transactions on Geoscience and Remote Sensing 45 (11), 3317–3341.

Krieger, G., Younis, M., 2006. *Impact of Oscillator Noise in Bistatic and Multistatic SAR.* IEEE Geoscience and Remote Sensing Letters 3 (3), 424–428.

Krieger, G., Zink, M., Bachmann, M., Bräutigam, B., Breit, H., Fiedler, H., Fritz, T., Hajnsek, I., Hueso González, J., Kahle, R., König, R., Schättler, B., Schulze, D., Ulrich, D., Wermuth, M., Wessel, B., Moreira, A., 2013. *TanDEM-X.* In: Distributed Space Missions for Earth System Monitoring. pp. 1–52.

Kroes, R., 2006. *Precise relative positioning of formation flying spacecraft using GPS.* Ph.D. thesis, TU Delft.

Kuttikkad, S., Chellappa, R., 2000. *Statistical modeling and analysis of high-resolution Synthetic Aperture Radar images.* Statistics and Computing 10 (8), 133–145.

La Prade, G., 1963. *An analytical and experimental study of stereo for radar.* Photogrammetric Engineering 29 (2), 294–300.

Lachaise, M., Balss, U., Fritz, T., Breit, H., 2012a. *The dual-baseline interferometric processing chain for the TanDEM-X mission.* In: Proceedings of IGARSS.

Lachaise, M., Bamler, R., 2010. *Minimum Cost Flow phase unwrapping supported by multibaseline unwrapped gradient.* In: Proceedings of EuSAR.

Lachaise, M., Bamler, R., Rodriguez Gonzalez, F., 2010. *Multibaseline gradient ambiguity resolution to support Minimum Cost Flow Phase Unwrapping.* In: Proceedings of IGARSS.

Lachaise, M., Eineder, M., Fritz, T., 2007. *Multi baseline SAR acquisition concepts and phase unwrapping algorithms for the TanDEM-X mission.* In: Proceedings of IGARSS.

Lachaise, M., Fritz, T., Balss, U., Bamler, R., Eineder, M., 2012b. *Phase unwrapping correction with dual-baseline data for the TanDEM-X mission.* In: Proceedings of IGARSS.

Lachaise, M., Fritz, T., Breit, H., 2014a. *InSAR processing and dual-baseline phase unwrapping for global TanDEM-X DEM generation.* In: Proceedings of IGARSS.

Lachaise, M., Fritz, T., Eineder, M., 2008. *A new dual baseline phase unwrapping algorithm for the TanDEM-X Mission.* In: Proceedings of EuSAR.

Lachaise, M., Fritz, T., Eineder, M., 2014b. *Dual-Baseline Phase Unwrapping Challenges in the TanDEM-X Mission.* In: Proceedings of EuSAR.

Lachaise, M., Fritz, T., Yague-Martinez, N., Breit, H., 2013. *Dual-baseline phase unwrapping correction for the TanDEM-X mission: After one year experience.* In: Proceedings of IGARSS.

Lanari, R., Fornaro, G., Riccio, D., Migliaccio, M., Papathanassiou, K. P., Moreira, J. R., Schwäbisch, M., Dutra, L., Puglisi, G., Franceschetti, G., Coltelli, M., 1996. *Generation of Digital Elevation Models by Using Interferometry : The Etna Case Study.* IEEE Transactions on Geoscience and Remote Sensing 34 (5), 1097–1114.

Leberl, F. W., 1979. *Accuracy analysis of stereo side-looking radar.* Photogrammetric Engineering and Remote Sensing.

Leberl, F. W., 1990. *Radargrammetric Image Processing.* Artech House.

Leberl, F. W., Domik, G., Raggam, J., Kobrick, M., 1986. *Radar Stereomapping Techniques and Application to SIR-B Images of Mt. Shasta.* IEEE Transactions on Geoscience and Remote Sensing GE-24 (4), 473–481.

Leberl, F. W., Maurice, K., Thomas, J. K., Millot, M., 1994. *Automated radar image matching experiment.* ISPRS Journal of Photogrammetry and Remote Sensing 49 (3), 19–33.

Lee, J.-S., Hoppel, K. W., Mango, S., Miller, A. R., 1994. *Intensity and phase statistics of multilook polarimetric and interferometric SAR imagery.* IEEE Transactions on Geoscience and Remote Sensing 32 (5), 1017–1028.

Leitao, J. M. N., Figueiredo, M. a., 1998. *Absolute phase image reconstruction: a stochastic nonlinear filtering approach.* IEEE Transactions on Image Processing 7 (6), 868–82.

Li, S. Z., 2009. *Markov random field modeling in image analysis.* Springer Science & Business Media.

Liu, H., Xing, M., Bao, Z., 2015. *A Cluster-Analysis-Based Noise-Robust Phase-Unwrapping Algorithm for Multibaseline Interferograms.* IEEE Transactions on Geoscience and Remote Sensing 53 (1), 494–504.

Loffeld, O., Nies, H., Knedlik, S., Yu, W., 2008. *Phase Unwrapping for SAR Interferometry-A Data Fusion Approach by Kalman Filtering.* IEEE Transactions on Geoscience and Remote Sensing 46 (1), 47–58.

Lombardini, F., 1996. *Absolute phase retrieval in a three-element synthetic aperture radar interferometer.* In: Proceedings of International Radar Conference.

Lombardini, F., 1998. *Optimum absolute phase retrieval in three-element SAR interferometer.* Elec-

tronics Letters 34 (15), 1522.

Lombardo, P., Lombardini, F., 1997. *Multi-baseline SAR interferometry for terrain slope adaptivity.* Proceedings of the IEEE National Radar Conference (2), 196–201.

Madsen, S. N., 1995. *Absolute phase determination techniques in SAR interferometry.* In: Giglio, D. A. (Ed.), Proc. SPIE 2487, Algorithms for Synthetic Aperture Radar Imagery.

Madsen, S. N., Zebker, H. A., 1992. *Automated Absolute Phase Retrieval in Across-Track Interferometry.* In: Proceedings of IGARSS.

Madsen, S. N., Zebker, H. A., Martin, J. M., 1993. *Topographic mapping using radar interferometry: processing techniques.* IEEE Transactions on Geoscience and Remote Sensing 31 (1), 246–256.

Marroquin, J. L., Rivera, M., 1995. *Quadratic regularization functionals for phase unwrapping.* Journal of the Optical Society of America A 12 (11), 2393.

Marroquin, J. L., Tapia, M., Rodriguez-Vera, R., Servin, M., 1995. *Parallel algorithms for phase unwrapping based on Markov random field models.* J. Optical Society of America A 12 (12), 2578.

Martinez-Espla, J. J., Martinez-Marin, T., Lopez-Sanchez, J. M., 2009. *A Particle Filter Approach for InSAR Phase Filtering and Unwrapping.* IEEE Transactions on Geoscience and Remote Sensing 47 (4), 1197–1211.

Martone, M., Bräutigam, B., Rizzoli, P., Gonzalez, C., Bachmann, M., Krieger, G., 2012. *Coherence evaluation of TanDEM-X interferometric data.* ISPRS Journal of Photogrammetry and Remote Sensing 73, 21–29.

Martone, M., Bräutigam, B., Rizzoli, P., Krieger, G., 2014. *TanDEM-X Performance over Sandy Areas.* In: Proceedings of EuSAR.

Martone, M., Rizzoli, P., Bräutigam, B., Krieger, G., 2013. *First 2 years of TanDEM-X mission: Interferometric performance overview.* Radio Science 48 (5), 617–627.

Massonnet, D., 2001. *Capabilities and limitations of the interferometric cartwheel.* IEEE Transactions on Geoscience and Remote Sensing 39 (3), 506–520.

Massonnet, D., Rabaute, T., 1993. *Radar interferometry: limits and potential.* IEEE Transactions on Geoscience and Remote Sensing 31 (2), 455–464.

Massonnet, D., Souyris, J., 2008. *Imaging with synthetic aperture radar.* CRC Press.

Massonnet, D., Vadon, H., Rossi, M., 1996. *Reduction of the need for phase unwrapping in radar interferometry.* IEEE Transactions on Geoscience and Remote Sensing 34 (2), 489–497.

Meglio, F., Pascazio, V., Schirinzi, G., 2006. *Joint Statistical Distribution of Multi-Baseline SAR Interferograms.* In: Proceedings of IGARSS.

Méric, S., Fayard, F., Pottier, E., 2009. *Radargrammetric SAR image processing.* In: Geoscience and Remote Sensing. In-Tech, pp. 421–454.

Miller, D., 2008. *The TanDEM-X Satellite.* In: Proceedings of EuSAR.

Moreira, A., 2003. *TanDEM-X: TerraSAR-X Add-On for Digital Terrain Elevation Measurements.* Mission Proposal for a Next Earth Observation Mission DLR Docume, No. 2003–3472739.

Moreira, A., Krieger, G., Hajnsek, I., Hounam, D., Werner, M., Riegger, S., Settelmeyer, E., 2004a. *TanDEM-X: a TerraSAR-X add-on satellite for single-pass SAR interferometry.* In: Proceedings of IGARSS.

Moreira, A., Krieger, G., Mittermayer, J., 2004b. *Satellite configuration for interferometric and/or tomographic remote sensing by means of synthetic aperture radar (SAR).* US Patent 6,677,884.

Mrowka, F., Geyer, M. P., Lenzen, C., Sporl, A., Gottfert, T., Maurer, E., Wickler, M., Schättler, B., 2011. *The joint TerraSAR-X / TanDEM-X mission planning system.* In: Proceedings of IGARSS.

Nico, G., Palubinskas, G., Datcu, M., 2000. *Bayesian approaches to phase unwrapping: theoretical study.* IEEE Transactions on Signal Processing 48 (9), 2545–2556.

Oliver, C., Quegan, S., 1999. *Understanding Synthetic Aperture Radar Images.* SciTech Publishing.

Ortega-Miguez, C., Schulze, D., Polimeni, M. D., Boer, J., Rizzoli, P., Bachmann, M., 2012. *TanDEM-X acquisition planner.* Proceedings of EuSAR.

Osmanoglu, B., Dixon, T. H., Wdowinski, S., 2014. *Three-Dimensional Phase Unwrapping for Satellite Radar Interferometry, I: DEM Generation.* IEEE Transactions on Geoscience and Remote Sensing 52 (2), 1059–1075.

Papoulis, A., 1991. *Probability, Random Variables, and Stochastic Processes.* McGraw-Hill.

Pascazio, V., Schirinzi, G., 2001. *Estimation of terrain elevation by multifrequency interferometric wide band SAR data.* IEEE Signal Processing Letters 8 (1), 7–9.

Pascazio, V., Schirinzi, G., 2002. *Multifrequency InSAR height reconstruction through maximum likelihood estimation of local planes parameters.* IEEE Trans. Image Processing 11 (12), 1478–89.

Pitz, W., Miller, D., 2010. *The TerraSAR-X Satellite.* IEEE Transactions on Geoscience and Remote Sensing 48 (2), 615–622.

Pritt, M. D., 1996. *Phase unwrapping by means of multigrid techniques for interferometric SAR.* IEEE Transactions on Geoscience and Remote Sensing 34 (3), 728–738.

Pritt, M. D., 1997. *Congruence in least-squares phase unwrapping.* In: Proceedings of IGARSS.

Pritt, M. D., Shipman, J. S., 1994. *Least-squares two-dimensional phase unwrapping using FFT's.* IEEE Transactions on Geoscience and Remote Sensing 32 (3), 706–708.

Rabus, B., Eineder, M., Roth, A., Bamler, R., 2003. *The shuttle radar topography mission: a new class of digital elevation models acquired by spaceborne radar.* ISPRS Journal of Photogrammetry and Remote Sensing 57 (4), 241–262.

Raggam, H., Gutjahr, K., Perko, R., Schardt, M., 2010. *Assessment of the Stereo-Radargrammetric Mapping Potential of TerraSAR-X Multibeam Spotlight Data.* IEEE Transactions on Geoscience and Remote Sensing 48 (2), 971–977.

Ramapriyan, H., Strong, J., Hung, Y., Murray, C., 1986. *Automated Matching of Pairs of SIR-B Images for Elevation Mapping.* IEEE Trans. Geoscience and Remote Sensing GE-24 (4), 462–472.

Raney, R., 1971. *Synthetic Aperture Imaging Radar and Moving Targets.* IEEE Transactions on Aerospace and Electronic Systems AES-7 (3), 499–505.

Reed, I., 1962. *On a moment theorem for complex Gaussian processes.* IEEE Transactions on Information Theory 8 (3), 194–195.

Rizzoli, P., Bachmann, M., Bräutigam, B., 2012a. *Global performance monitoring from TanDEM-X quicklook data.* In: Proceedings of EuSAR.

Rizzoli, P., Bräutigam, B., Kraus, T., Martone, M., Krieger, G., 2012b. *Relative height error analysis of TanDEM-X elevation data.* ISPRS Journal of Photogrammetry and Remote Sensing 73 (2012), 30–38.

Rizzoli, P., Martone, M., Bräutigam, B., 2014. *Global Mosaics from TanDEM-X Quicklook Data: First Results and Potentials.* In: Proceedings of EuSAR.

Robertson, A. E., 1998. *Multi-baseline interferometric SAR for iterative height estimation.* Ph.D. thesis, Brigham Young University, Hamburg , Germany.

Rodriguez, E., Martin, J. M., 1992. *Theory and design of interferometric synthetic aperture radars.* IEE Proceedings F Radar and Signal Processing 139 (2), 147.

Romeiser, R., Suchandt, S., Runge, H., Steinbrecher, U., Grunler, S., 2010. *First Analysis of TerraSAR-X Along-Track InSAR-Derived Current Fields.* IEEE Transactions on Geoscience and Remote Sensing 48 (2), 820–829.

Rosen, P. A., Hensley, S., Joughin, I., Li, F., Madsen, S. N., Rodriguez, E., Goldstein, R., 2000. *Synthetic aperture radar interferometry.* Proceedings of the IEEE 88 (3).

Rossi, C., Eineder, M., Fritz, T., Breit, H., 2010. *TanDEM-X Mission : Raw DEM Generation.* In: Proceedings of EuSAR.

Rossi, C., Rodriguez Gonzalez, F., Fritz, T., Yague-Martinez, N., Eineder, M., 2012. *TanDEM-X calibrated Raw DEM generation.* ISPRS Journal of Photogrammetry and Remote Sensing 73, 12–20.

Rudin, L. I., Osher, S., Fatemi, E., 1992. *Nonlinear total variation based noise removal algorithms.*

Physica D: Nonlinear Phenomena 60 (1-4), 259–268.

Sansosti, E., Berardino, P., Manunta, M., Serafino, F., Fornaro, G., 2006. *Geometrical SAR image registration*. IEEE Transactions on Geoscience and Remote Sensing 44 (10), 2861–2870.

Sarabandi, K., 1992. *Derivation of phase statistics from the Mueller matrix*. Radio Science 27 (5), 553–560.

Schättler, B., Kahle, R., Metzig, R., Steinbrecher, U., Zink, M., 2011. *The joint TerraSAR-X / TanDEM-X ground segment*. In: Proceedings of IGARSS.

Schmitt, K., Wiesbeck, W., 1997. *An interferometric SAR processor avoiding phase ambiguities*. In: Proceedings of IGARSS.

Schmitt, M., 2014. *Reconstruction of Urban Surface Models from Multi-Aspect and Multi-Baseline Interferometric SAR Dissertation*. Ph.D. thesis, TUM.

Schulze, D., Bachmann, M., Bräutigam, B., Borla Tridon, D., Rizzoli, P., Martone, M., Zink, M., Krieger, G., 2014. *Status of TanDEM-X DEM Acquisition , Calibration and Perfor- mance 2 DEM Acquisition Planning 3 Interferometric Performance*. In: Proceedings of EuSAR.

Schwäbisch, M., 1995. *Die SAR-Interferometrie zur Erzeugung digitaler Geländemodelle*. Ph.D. thesis.

Schwäbisch, M., 1998. *A fast and efficient technique for SAR interferogram geocoding*. In: Proceedings of IGARSS.

Schwerdt, M., Hueso González, J., Bachmann, M., Schrank, D., Doring, B., Tous Ramon, N., Walter Antony, J. M., 2011. *In-orbit calibration of the TanDEM-X system*. In: Proceedings of IGARSS.

Shabou, A., Baselice, F., Ferraioli, G., 2012. *Urban Digital Elevation Model Reconstruction Using Very High Resolution Multichannel InSAR Data*. IEEE Transactions on Geoscience and Remote Sensing 50 (11), 4748–4758.

Soergel, U., Michaelsen, E., Thiele, A., Cadario, E., Thoennessen, U., 2009. *Stereo analysis of high-resolution SAR images for building height estimation in cases of orthogonal aspect directions*. ISPRS Journal of Photogrammetry and Remote Sensing 64 (5), 490–500.

Suchandt, S., Eineder, M., 2003. *Experiences with SRTM/X-SAR phase unwrapping using the minimum cost flow method*. In: Proceedings of IGARSS.

Suchandt, S., Runge, H., 2012. *First results of TanDEM-X along-track interferometry*. In: Proceedings of IGARSS.

TanDEM-X Science Website.
URL `http://www.dlr.de/hr/en/desktopdefault.aspx/tabid-2317/3669_read-5492/`

Thompson, D., Robertson, A. E., Arnold, D., Long, D., 1999. *Multi-baseline interferometric SAR for iterative height estimation*. In: Proceedings of IGARSS.

Tough, R. J. a., Blacknell, D., Quegan, S., 1995. *A Statistical Description of Polarimetric and Interferometric Synthetic Aperture Radar Data*. Proceedings of the Royal Society A: Mathematical, Physical and Engineering Sciences 449 (1937), 567–589.

Toutin, T., 1995. *Radarsat for stereoscopy*. GIM International 13 (1), 6–9.

Toutin, T., 1996. *Opposite side ERS-1 SAR stereo mapping over rolling topography*. IEEE Transactions on Geoscience and Remote Sensing 34 (2), 543–549.

Toutin, T., 2010. *Impact of Radarsat-2 SAR Ultrafine-Mode Parameters on Stereo-Radargrammetric DEMs*. IEEE Transactions on Geoscience and Remote Sensing 48 (10), 3816–3823.

Toutin, T., Gray, L., 2000. *State-of-the-art of elevation extraction from satellite SAR data*. ISPRS Journal of Photogrammetry and Remote Sensing 55 (1), 13–33.

Touzi, R., Lopes, A., 1996. *Statistics of the Stokes parameters and of the complex coherence parameters in one-look and multilook speckle fields*. IEEE Transactions on Geoscience and Remote Sensing 34 (2), 519–531.

Touzi, R., Lopes, A., Bruniquel, J., Vachon, P. W., 1999. *Coherence estimation for SAR imagery*. IEEE Transactions on Geoscience and Remote Sensing 37 (1), 135–149.

Ulander, L., Frolind, P.-O., 1998. *Ultra-wideband SAR interferometry*. IEEE Transactions on Geo-

science and Remote Sensing 36 (5), 1540–1550.

Urkowitz, H., 1983. *Signal Theory and Random Processes*. Artech House.

Weigt, M., Rizzoli, P., Schulze, D., Bachmann, M., Bräutigam, B., 2012. *TanDEM-X mission - interferometric performance and global DEM acquisition status*. In: IET International Conference on Radar Systems (Radar 2012).

Wendleder, A., Wessel, B., Roth, A., Breunig, M., Martin, K., Wagenbrenner, S., 2013. *TanDEM-X Water Indication Mask: Generation and First Evaluation Results*. IEEE Journal of Selected Topics in Applied Earth Observations and Remote Sensing 6 (1), 171–179.

Wessel, B., Gruber, A., Huber, M., Breunig, M., Wagenbrenner, S., Roth, A., 2014. *Status of TanDEM-X DEM Calibration and Mosaicking towards the TanDEM-X DEM*. In: Proceedings of EuSAR.

Wessel, B., Gruber, A., Huber, M., Roth, A., 2009. *TanDEM-X: Block adjustment of interferometric height models*. Proceedings of ISPRS Hannover Workshop.

Wessel, B., Huber, M., Bachmann, M., Fritz, T., 2013. *TanDEM-X Products Specification Document*. Tech. rep.

Wessel, B., Marschalk, U., Gruber, A., Huber, M., Hahmann, T., Roth, A., Habermeyer, M., 2008. *Design of the DEM Mosaicking and Calibration Processor for TanDEM-X*. In: Proceedings of EuSAR.

Wildey, R. L., 1986. *Radarclinometry for the Venus radar mapper*. Photogrammetric Engineering and Remote Sensing 52, 41–50.

Wu, B.-I., Yeung, M. C., Hara, Y., Kong, J. A., 2009. *InSAR height inversion by using 3-D phase projection with multiple baselines*. Progress In Electromagnetics Research 91, 173–193.

Xu, W., Chang, E. C., Heng, A., 1994. *Phase-unwrapping of SAR interferogram with multi-frequency or multi-baseline*. In: Proceedings of IGARSS.

Yague-Martinez, N., Eineder, M., Brcic, R., Breit, H., Fritz, T., 2010a. *TanDEM-X Mission: SAR Image Coregistration Aspects*. In: Proceedings of EuSAR.

Yague-Martinez, N., Rossi, C., Lachaise, M., Rodriguez Gonzalez, F., Fritz, T., Breit, H., 2010b. *Interferometric processing algorithms of TanDEM-X data*. In: Proceedings of IGARSS.

Yu, H., Li, Z., Bao, Z., 2011. *A Cluster-Analysis-Based Efficient Multibaseline Phase-Unwrapping Algorithm*. IEEE Transactions on Geoscience and Remote Sensing 49 (1), 478–487.

Zebker, H. A., Chen, K., 2005. *Accurate Estimation of Correlation in InSAR Observations*. IEEE Geoscience and Remote Sensing Letters 2 (2), 124–127.

Zebker, H. A., Goldstein, R. M., 1986. *Topographic mapping from interferometric synthetic aperture radar observations*. Journal of Geophysical Research 91 (B5), 4993.

Zebker, H. A., Lu, Y., 1998. *Phase unwrapping algorithms for radar interferometry: residue-cut, least-squares, and synthesis algorithms*. Journal of the Optical Society of America A 15 (3), 586.

Zebker, H. A., Villasenor, J., 1992. *Decorrelation in interferometric radar echoes*. IEEE Transactions on Geoscience and Remote Sensing 30 (5), 950–959.

Zhang, K., Ge, L., Hu, Z., Ng, A. H.-M., Li, X., Rizos, C., 2011. *Phase Unwrapping for Very Large Interferometric Data Sets*. IEEE Trans. on Geoscience and Remote Sensing 49 (10), 4048–4061.

Zhu, S., Reigber, C., König, R., 2004. *Integrated adjustment of CHAMP, GRACE, and GPS data*. Journal of Geodesy 78 (1-2), 103–108.

Zink, M., 2014. *TanDEM-X: Key Features and Mission Status*. In: Proceedings of EuSAR.

Zink, M., Bachmann, M., Brautigam, B., Fritz, T., Hajnsek, I., Moreira, A., Wessel, B., Krieger, G., 2014. *TanDEM-X: The New Global DEM Takes Shape*. IEEE Geoscience and Remote Sensing Magazine 2 (2), 8–23.

Zwally, H., Schutz, B., Abdalati, W., Abshire, J., Bentley, C., Brenner, A., Bufton, J., Dezio, J., Hancock, D., Harding, D., Herring, T., Minster, B., Quinn, K., Palm, S., Spinhirne, J., Thomas, R., 2002. *ICESat's laser measurements of polar ice, atmosphere, ocean, and land*. Journal of Geodynamics 34 (3-4), 405–445.

List of Figures

List of Tables

Acknowledgement

The way to the end was long. It was not always easy but it was for sure a rich experience full of emotions. Throughout this adventure and all these years, many persons helped me and motivated me. Without them, I would certainly never have written the final point.

First of all, I would like to thank Prof. Richard Bamler and Prof. Michael Eineder who were my supervisors and advisers during this long adventure. They provided me a job at the DLR IMF-SAR department, the chance to be part of the ITP team for the TanDEM-X mission and the opportunity to do a PhD at the same time. Both have been always ready to give me advice and constructive comments and suggestions. I really appreciated their fast feedback especially during the last months of my writings.

I am sincerely grateful to Prof. Giampaolo Ferraioli who accepted to be my third reviewer. His elevation extraction method and various researches inspired me particularly during the first half of my PhD. He and Dr. Aymen Shabou kindly shared their own source code with me. My gratitude goes to Prof. Uwe Stilla who agreed to be the chairman for the oral examination.

My very special thanks have to go to Dr. Thomas Fritz, my team leader but also and especially someone I can rely on in any situations. He is always available and a considerate and attentive listener and advisor. During all these years, he supported me, cheered me on and up and let me gain self-confidence. He also proofread a significant part of my thesis and was a great help to me with the translation of the abstract in German. Besides his support at work, he is also always there to answer my questions about my every day life in Germany.

To all my colleagues, thank you for the productive work atmosphere. More particularly, thank you Fernando Rodriguez Gonzalez for your numerous recommendations and all the time you invested to explain me various theoretical points. I would also like to express my gratitude to the whole TanDEM-X team and more particularly to my colleagues of the ITP team, among them to Ulrich Balss for his translation in C of my IDL prototypes, to Andreas Niedermeier for his nice 3D views of the DEMs, to Nestor Yague Martinez for sharing his knowledge on the InSAR processor and coregistration, to Silke, Helko, Cristian, Birgit. I am also thankful to Xiaoxiang Zhu who was once my almost best friend, to Michael Bäßler who shared with me his experience with a “never ending” PhD, to Daniele Cerra, Ramon and many others. I am also grateful to Dr. Gianfranco Fornaro from the IREA, Naples for the constructive talks we had.

To Cyrille Marie, I am deeply and sincerely grateful for his invaluable help not only with respect to this thesis but for his presence and the way he helped me to acclimatise myself here. Regarding this thesis, he invested lot of time to proofread it completely and gave me very constructive feedback. His comments on my writing style made me smile again and again. During the last months, he really cheered me up.

I am thankful to Xiaoying Cong and I am glad to know her and have her as a colleague but also and especially as a caring friend. We shared uncountable moments and experiences, happy or less happy ones. She also guided me with her own experience to the end of my PhD. Thanks to our discussion, several ideas and plots became clear. She helped me to considerably improve the introduction and conclusion.

To all my friends, I am deeply grateful. You were there at my side. Especially, Pierre-Alexis, Soazic, my *Lieblingssilke*, Anaissa, Valérie, Grégory, Néstor, Fernando and many others. Without you, I would never have reached the end. You all supported me much more than you probably think. Xiaoying and Silke, I am looking forward our next Charlie’s Angels tour.

Finally, I would like to thank my family, my parents, especially my *moumoune*, who did everything possible so that I could achieve my goals, and express them all my love. They support me every day and always find the right word.